Plasma Physics Reports, Vol. 26, No. 8, 2000, pp. 633–640. Translated from Fizika Plazmy, Vol. 26, No. 8, 2000, pp. 675–682.

TOKAMAKS

Effect of Helical Magnetic Fields on Plasma Stability in Tokamaks

P. V. Savrukhin

Institute of Nuclear Fusion, Russian Research Centre Kurchatov Institute, pl. Kurchatova 1, Moscow, 123182 Russia

Received September 9, 1999

Abstract—Physical mechanisms for destabilization of MHD perturbations by external quasistatic magnetic fields and rotating helical magnetic fields in a tokamak plasma are identified using a numerical model of tearing modes in a viscous high-temperature plasma. The critical conditions for the onset of MHD perturbations and their dynamic model are compared with the experimental results from the JET tokamak. The model is used to predict how the stray magnetic fields will influence plasma stability in a tokamak reactor (ITER). © *2000 MAIK "Nauka/Interperiodica".*

1. INTRODUCTION

Recent tokamak experiments have revealed that stray magnetic fields have a significant impact on the stability of MHD modes in a high-temperature plasma [1–5]. The stray fields, which inevitably arise because of the asymmetry of electromagnetic systems in experimental devices and the nonuniform arrangement of the protection systems of the tokamak chamber (divertors and limiters), not only cause the MHD mode rotation to relax but can also, under certain conditions, destabilize quasistatic (locked) MHD perturbations, thereby leading to discharge disruption. Experiments in large tokamaks with a slowed plasma rotation and high gas-dynamic pressure revealed a significant reduction in the critical amplitude of the stray fields, which give rise to MHD modes. Such discharge regimes, which are typical of self-sustained fusion reactions in a tokamak reactor [6], place very demanding requirements on both the models aimed at predicting the behavior of locked MHD modes and the systems for stabilizing these modes.

Thorough experimental investigations of locked MHD modes in the COMPASS-C [4] and DIII-D [3] tokamaks made it possible to determine the characteristic features of the development of perturbations and to estimate the parametric relations (scalings) for the thresholds for mode destabilization in various plasma discharges. However, direct application of these scalings to predict the thresholds for the onset of locked modes in future experiments is hampered by such factors as the complicated nonlinear dynamics of plasma perturbations observed in previous experiments and the unsteady nature of the stray fields. An analysis shows that tracing the evolution of the locked modes requires an accurate and detailed numerical modeling of the physical processes associated with the effect of external helical magnetic fields on plasma stability in tokamaks.

Our objective here is to determine the parameters of the model aimed at comparing theoretical and experimental results and to apply the model to predict the evolution of locked MHD modes in the future ITER tokamak reactor. To make the estimates and predictions more realistic, the model parameters are determined from the JET experiments under conditions that are as close as possible to those of the operating regimes of a future reactor (a relatively low content of impurities, high plasma temperature and density near the boundary of the plasma column, relatively slow plasma rotation, etc.). The JET experiments that were described in detail in [5, 7, 8] made it possible to examine the conditions for mode excitation in Ohmically heated plasmas and auxiliary heated plasmas (neutral beam injection and RF heating) both in limiter and divertor discharges. To study how the conditions for mode generation depend on the machine dimensions, we also compare the model results with the experimental data from DIII-D [3] and COMPASS-C [4].

In the cited JET experiments, the external magnetic fields are excited by a set of four saddle coils located inside the vacuum chamber [5]. In contrast to the previous experiments [1–4], such coils make it possible to produce both quasistatic and rotating helical magnetic fields, thereby providing the basis for a more accurate description of the stability of MHD modes.

In Section 2, we describe the phenomenological model used to analyze MHD perturbations. In Section 3, we compare the model results with the experimental data from tokamaks and use the model to obtain predictions for ITER. In Section 4, we examine preliminary JET experiments with neutralization of the stray fields and with a delay in the time at which magnetic perturbations stop rotating before the density limit disruption. In Section 5, we discuss some assumptions underlying the model and numerical results.

1063-780X/00/2608-0633$20.00

2. DYNAMIC MODEL OF MHD PERTURBATIONS

We study the evolution of MHD perturbation modes and the effect of the external controlling magnetic fields on the mode dynamics using the PLASCON phenomenological model for regularization of the tearing modes [9]. This model is based on single-fluid MHD theory [10–12] and thus makes it possible to analyze electromagnetic, inertial, and viscous effects in high-temperature plasmas. We simulated a plasma column with a circular cross section at a large aspect ratio, assuming the plasma pressure to be low. The model plasma configuration is illustrated schematically in Fig. 1. In computations, the MHD perturbations and external magnetic fields were represented as superpositions of the helical harmonics: $B_{rm} = B_r \exp(jm\chi_m)$ and $B_{em} = B_e \exp(jm\chi_e)$, where χ_m and χ_e are the phases of the MHD modes and external magnetic field harmonics, $m\chi_m = m\vartheta - n\varphi + \int \omega_m dt$, $m\chi_e = m\vartheta - n\varphi + \int \omega_e dt$, ϑ and φ are the poloidal and longitudinal (toroidal) coordinates, ω_m and ω_e are the rotation frequencies, and m and n are the poloidal and toroidal wavenumbers. We also assumed that the magnetic perturbations only weakly distort the equilibrium plasma configuration.

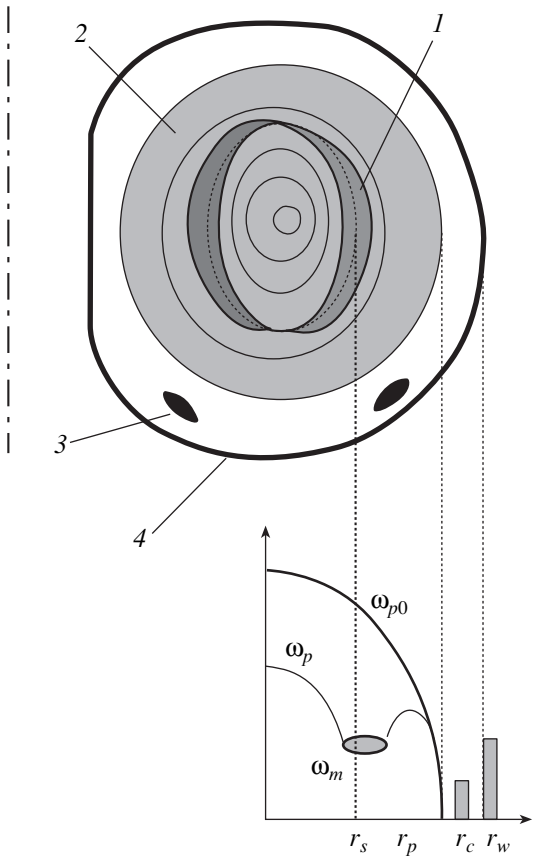

Fig. 1. Schematic drawing of the model for controlling MHD perturbations in a tokamak plasma with the help of external helical magnetic fields. Magnetic islands (*1*) are close to the resonant surfaces $r = r_s$ in a rotating viscous plasma (*2*). The external magnetic fields are produced by a set of magnetic coils (*3*) located inside the tokamak chamber (*4*). The minor radii of the plasma column, tokamak chamber, and magnetic coils are r_p, r_w, and r_c, respectively. The computed profiles of the angular frequencies of rotation of the magnetic islands and the plasma, ω_m and ω_p, are also shown schematically.

Following the theoretical analysis performed by Fitzpatrick [11], we simulated two regimes of the development of MHD perturbations, depending on the plasma parameters at the resonant magnetic surface $r = r_s$ and the amplitude B_r of the magnetic perturbations. The transition from one regime to another is described by the parameter [11]

$$\lambda \simeq (\delta_l / w_i)^{3/2}. \quad (1)$$

Here, $\delta_l \simeq \tau_H^{2/6} \tau_V^{-1/6} \tau_R^{-1/6} r_s$ is the width of a viscoresistive layer; $w_i = 4r_s \sqrt{B_r / sB_\vartheta m}$ is the magnetic-island width; $\tau_R = \mu_0 r_s^2 / \eta$, $\tau_V = \rho r_s^2 / \mu_\nu$, and $\tau_H = R_0 \sqrt{\mu_0 \rho} / sB_\varphi$ are skin, viscous, and Alfvén times, respectively; η is the specific resistivity; the magnetic shear s is defined as $(s = (r/q)dq/dr)$; μ_ν is the viscosity coefficient; ρ is the plasma mass density; and B_φ and B_ϑ are the longitudinal and poloidal components of the equilibrium magnetic field, respectively. A magnetic island is assumed to be suppressed if the amplitude of the magnetic perturbations becomes smaller than the threshold amplitude $B_l = c_l s \delta_l^2 B_\vartheta / 8 r_s^2$, where c_l is a numerical coefficient adjusted so as to achieve the best agreement with the experimental data.

In the nonlinear regime ($\lambda \ll 1$), the evolution of MHD perturbations is described by the theory of tearing modes [13–16]. The mode stability can be inferred by analyzing an MHD equilibrium [17], which is prescribed by both the current density profile and the boundary conditions governed by the external magnetic fields and the currents induced in the mechanical elements of a tokamak. In polar coordinates, the tearing mode amplitude B_r and the angular frequency $\omega_m = d\chi_m/dt$ of the rotation of MHD perturbations satisfy the equations [11, 12]

$$c_{mg1} \sqrt{B_r} dB_r/dt = \Delta'_{frb} B_r - c_{mg2} B_r (\omega_m \tau_w)^2 / (1 + \omega_m^2 \tau_w^2) + c_{mg3} B_e \cos(\chi_e - \chi_m), \quad (2)$$

$$c_{r1} d\omega_m/dt = c_{r2}(\omega_p - \omega_m) - c_{r3} B_r^2 \omega_m \tau_w / (1 - \omega_m^2 \tau_w^2) + c_{r4} B_e \sin(\chi_e - \chi_m), \quad (3)$$

where Δ'_{frb} is the stability parameter of a tearing mode in a free-boundary plasma, τ_w is the time constant of the tokamak chamber, the numerical coefficients $c_{mg(i)}$ and $c_{r(i)}$ depend on the plasma parameters [9], and ω_p is the

plasma rotation frequency around a magnetic island (see below).

In the linear regime ($\lambda \gg 1$), a tearing mode was assumed to be stabilized [11], in which case the interaction of vortex currents in a viscoresistive layer near a resonant surface with external magnetic fields gives rise to a constant (nonoscillating) moment of forces, which acts to reduce the plasma velocity with respect to the magnetic field [11]:

$$T_{bra} = c_{r5}B_e^2(\omega_e - \omega_l)\tau_{\rm rec}/(1 + (\omega_e - \omega_l)^2\tau_{\rm rec}^2). \quad (4)$$

Here, $\tau_{\rm rec}$ is the characteristic reconnection time ($\tau_{\rm rec} = 2.1\tau_H^{1/3}\tau_R^{5/6}\tau_V^{-1/6}/|\Delta'_{frb}\, r_s|$), ω_l is the plasma rotation frequency in a viscoresistive layer, and the numerical coefficient c_{r5} depends on the plasma parameters [9]. The angular rotation frequency ω_l satisfies the equation

$$c_{r6}d\omega_l/dt = c_{r4}(\omega_p - \omega_l) + T_{bra}, \quad (5)$$

where c_{r6} is the "phenomenological" moment of the plasma inertia in a viscoresistive layer.

The plasma rotation frequency ω_p around a magnetic island was determined from the balance between the moment of viscous forces near the resonant surface and the phenomenological moment of inertia, which was adjusted to achieve the best agreement between the computed and experimental rotation velocities. In simulations, the moment of viscous forces in a plasma volume V_p was modeled by the phenomenological friction at the surfaces between neighboring layers inside the plasma, $T_{V\alpha\beta} = c_{r8}(\omega_{p\beta} - \omega_{p\alpha})$, where α and β are the labels of the plasma layers ($\beta = \alpha \pm 1$), the friction coefficient c_{r8} has the form ($c_{r8} = 4\pi^2 R_0^3 r_s \rho\mu_\nu/d_\nu$), and d_ν is the width of a viscous layer (see [9, 18]). The angular plasma motion in the α-layer is described by the equation

$$c_{r7\alpha}d\omega_{p\alpha}/dt = \sum_\beta c_{r8\alpha}(\omega_{p\beta} - \omega_{p\alpha}) + c_{r9\alpha}(\omega_{p\alpha 0} - \omega_{p\alpha}), \quad (6)$$

where the numerical coefficients $c_{r7\alpha}$ and $c_{r9\alpha}$ depend on the plasma parameters and the parameter $\omega_{p\alpha 0}$ is obtained from the experimental data. The equation of plasma motion in a layer around the resonant surface $r = r_s$ accounts for the additional friction between plasmas on the outside and inside of a magnetic island,

$$c_{r7\alpha}d\omega_{p\alpha}/dt = c_{r4}(\omega_m - \omega_{p\alpha}) + \sum_\beta c_{r8\alpha}(\omega_{p\beta} - \omega_{p\alpha}) + c_{r9\alpha}(\omega_{p\alpha 0} - \omega_{p\alpha}). \quad (7)$$

3. CONDITIONS FOR DESTABILIZATION OF THE MHD PERTURBATIONS

The destabilization of internal MHD perturbations was studied in the JET experiments under different conditions ($R_0 = 2.9$–3.0 m and $r_p = 0.8$–0.9 m) with the help of external static magnetic fields and external rotating magnetic fields with a time-varying amplitude and/or time-varying rotation frequency [5, 7, 9]. Those experiments in JET, as well as previous experimental investigations [3, 4], revealed that the plasma parameters and factors such as the spatial structure of the external fields and the schemes for auxiliary plasma heating affect the thresholds for mode destabilization in a fairly complicated fashion. Consequently, numerical simulations of such experiments require that the dynamics of the external magnetic fields $B_e(t)$ be prescribed and the plasma parameters be predetermined for particular experimental conditions. In all versions of the simulations described here, we took the same values of the free parameters, which were chosen so as to achieve the best agreement between the computed evolution of the plasma perturbations and the experimental results. The PLASCON numerical model makes it possible to simultaneously trace the evolution of several coupled helical perturbation harmonics [18]. In this paper, we consider the dynamics of the perturbation mode with (m, n) = (2, 1), which dominated in the JET experiments [5, 9].

As in the previous JET experiments with static external fields [3, 4], the threshold for destabilization of the MHD modes decreased with the electron density, the parameters of the plasma discharge being fixed (Fig. 2). This is consistent with the results obtained in our numerical model, which predicts that the lower the

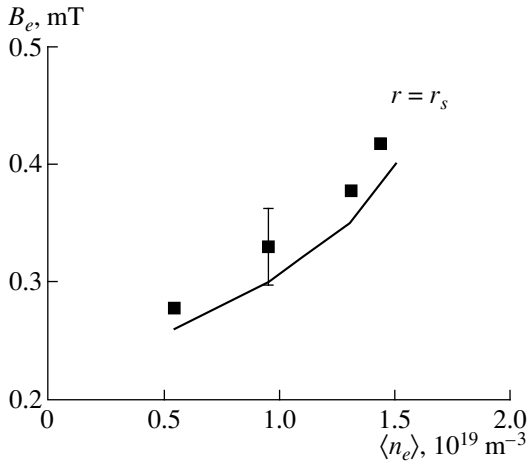

Fig. 2. Comparison between the computed amplitude of the external quasistatic magnetic fields destabilizing the locked MHD modes (solid curve) and the results of JET experiments [5, 7] (squares) in regimes with different plasma densities.

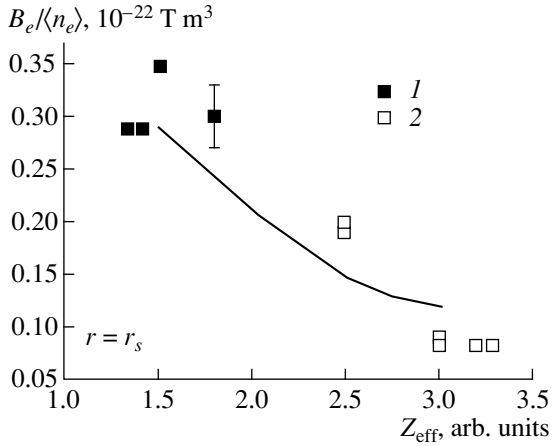

Fig. 3. Comparison between the computed thresholds for destabilization of the locked MHD modes in plasmas with different effective ion charge numbers (solid curve) and the results of JET experiments [2, 5, 7] with external quasistatic magnetic fields (squares): (*1*) divertor experiments [5, 7], (*2*) limiter experiments [2], and the model profile (solid curve).

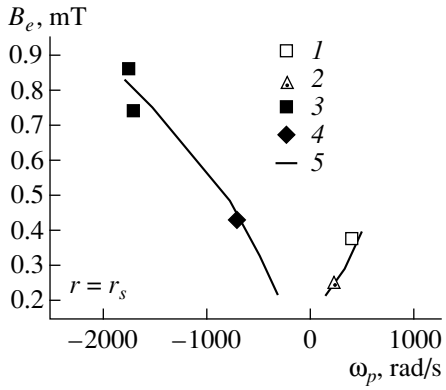

Fig. 4. Comparison between the computed thresholds for destabilization of the locked MHD modes (solid curve) and the results of JET experiments [5, 7] with external quasistatic magnetic fields in regimes with different angular rotation frequencies of the plasma. The plasma rotation frequency was measured experimentally by recording the charge exchange recombination (CXR) emission of spectral lines from the ^{6}C carbon ions: (*1*) Ohmic heating, $\delta_{\text{rippl}} = 2\%$; (*2*) Ohmic heating, $\delta_{\text{ripple}} = 0.1\%$; (*3*) neutral injection heating, $P_{NB} = 2.1$ MW and $\delta_{\text{ripple}} = 2\%$; (*4*) neutral injection heating plus RF heating, $P_{NB} = 0.8$ MW, $P_{RF} = 8$ MW, and $\delta_{\text{ripple}} = 0.1\%$; and (*5*) model profile.

plasma density, the smaller the viscous friction coefficient. A decrease in the viscous moments, which hinder the slowing of the plasma rotation, lowers the thresholds for destabilization of the MHD modes.

The JET experiments with a single-null divertor [5, 7] demonstrated that the thresholds for mode destabilization are higher than those in previous experiments with limiter plasmas [2]. According to our simulations, this discrepancy can be attributed primarily to a significantly lower content of impurities in divertor plasmas (in a divertor configuration, the effective ion charge number Z_{eff} is smaller than that in a limiter configuration by a factor of 1.5 to 2). The smaller the effective ion charge number, the longer both the skin times and the reconnection time τ_{rec}. As a result, with the plasma rotation frequency taken from experiments, the effect of the braking moment T_{bra} in (4) becomes less significant, thereby raising the threshold external fields. Figure 3 compares the experimental and computed thresholds for mode destabilization.

An analysis of the JET experiments with auxiliary heating (the RF heating power and the injected neutral beam power being $P_{rf} = 8$ MW and $P_{nb} = 0.8$–2.0 MW, respectively) and with different ripple amplitudes ($\delta_{\text{ripple}} = 0.1$–$2.0\%$) showed that the thresholds for destabilization of the MHD modes increase sharply with increasing the angular frequency of the plasma rotation with respect to the steady-state magnetic field (Fig. 4). According to our simulations, this is attributed to the fact that the braking moment T_{bra} in (4) decreases as the plasma rotation frequency ω_l increases ($\omega_e = 0$). To check the conclusion of the resonant dependence of the thresholds for mode destabilization on the frequency of the plasma rotation relative to the external magnetic field, we performed numerical calculations for a series of JET experiments with the generation of rotating MHD modes [5, 7]. These experiments were carried out with Ohmically heated plasmas and with external magnetic fields rotating at different rates, the plasma parameters being fixed. The relevant experimental and computed thresholds for mode destabilization are compared in Fig. 5. The numerical results are seen to agree with experiments when the prescribed rotation frequency of the main plasma is equal to $\omega_{p0} = 720$ Hz. The experimentally observed resonant frequency dependence of the thresholds for mode destabilization agrees qualitatively with the analytic scaling $B_e/B_\varphi \approx (\tau_H(\omega_e - \omega_l)^{2/5}$ derived in [10, 11]. However, because of the unsteady character of the external magnetic fields (whose amplitudes and frequencies vary in time), the MHD modes in JET are more difficult to calculate analytically.

To refine the dependence of the thresholds for destabilization of the locked MHD modes on the plasma dimensions, we applied the PLASCON model in order to numerically analyze the stability of MHD modes in the DIII-D ($R_0 = 1.67$ m and $r_p = 0.6$ m) and COMPASS-C ($R_0 = 0.56$ m and $r_p = 0.2$ m) tokamaks [3, 4]. Simulations carried out with the plasma parameters taken from the experiments of [3, 4] showed that, in larger tokamaks, the thresholds for destabilization of the MHD modes are lower. This is attributed primarily to the fact that, in large tokamaks, the plasma rotates at a slower rate (Fig. 6).

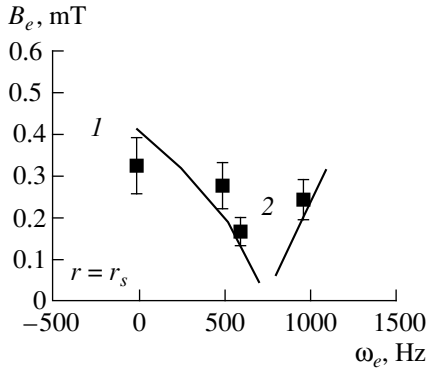

Fig. 5. Comparison between the computed thresholds for destabilization of the locked MHD modes (solid curve) and the results of JET experiments [5, 7] (closed squares) in regimes with different angular rotation frequencies of the external magnetic fields at fixed plasma discharge parameters for (*1*) a constant helical perturbation and (*2*) a rotating helical perturbation.

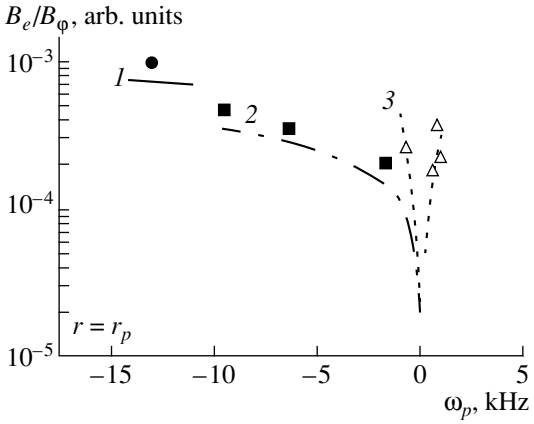

Fig. 6. Comparison between the thresholds for destabilization of the locked MHD modes computed for the (*1*) COMPASS-C, (*2*) DIII-D, and (*3*) JET tokamaks in regimes with different angular rotation frequencies of the plasma and the experimental results from JET [5, 7] (triangles), COMPASS-C [4] (circles), and DIII-D [3] (squares), respectively.

Our numerical model, which was calibrated by examining the cited JET experiments, allows us to estimate the possible thresholds for destabilization of the MHD modes in the future ITER tokamak reactor [6]. Our numerical analysis shows that, with the plasma parameters adopted for ITER, the reconnection time τ_{rec} is as long as $\tau_{rec} = 3.7$ s and, for the standard plasma rotation frequency $\omega_p = 170$ Hz [11], the threshold for mode destabilization is above the level $B_e/B_\varphi(r = r_p) \approx 2 \times 10^{-4}$. Simulations with the reconnection time τ_{rec} typical of the JET experiments ($\tau_{rec} = 0.1$ s) yielded significantly lower thresholds for mode destabilization in ITER, $B_e/B_\varphi(r = r_p) \approx 2 \times 10^{-5}$ (see also [3]). The results of our analysis and the predictions for ITER are illustrated in Fig. 7, which also presents the diagram obtained in [3].

4. NEUTRALIZATION OF THE STRAY FIELDS AND THE DELAY OF PLASMA DISRUPTION BY EXTERNAL MAGNETIC FIELDS

The predicted lowering of the thresholds for destabilization of the MHD modes in tokamak-reactor plasmas imposes strict requirements on the development and testing of both systems for neutralizing the stray magnetic fields and the methods for suppressing the instability. Preliminary JET experiments [5, 7, 19] showed that the external (saddle) coils can be used to determine the stray fields in a tokamak plasma and even to partially suppress them. Those experiments demonstrated that, under the same discharge conditions, the thresholds for destabilization of the MHD modes can differ by 25%, depending on the phase of the controlling currents in the saddle coils. Our calculations show that the difference in the thresholds for locked modes is governed by the orientation of the external magnetic fields relative to the stray fields [20], which are typical of experiments in the JET tokamak. With the given discharge conditions, i.e., $B_r \simeq (0.75–1) \times 10^{-4}$ T at the magnetic surface with $q = 2$, the neutralization of the internal stray fields increases the critical amplitude of the external fields required for destabilization of the MHD modes.

An analysis of the density limit disruptions in the JET tokamak [21], as well as previous investigations [22, 23], revealed that the mode with (m, n) = (2, 1)

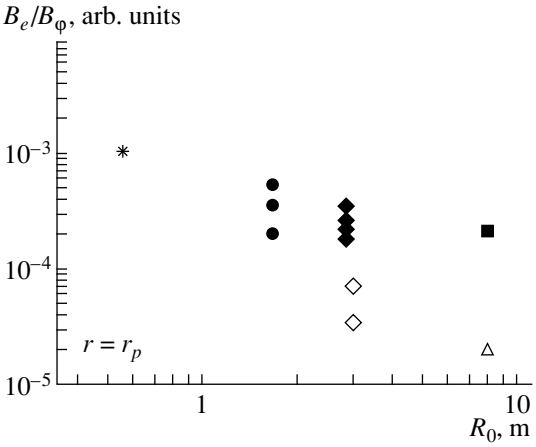

Fig. 7. Diagram of the stability thresholds for locked MHD modes [3] in tokamaks of different sizes [2–5, 7] and the computed thresholds for mode destabilization in the ITER tokamak reactor for the plasma rotation frequency $\omega_p \simeq 170$ Hz. Shown are the experimental results from COMPASS-C [4] (asterisk), DIII-D [3] (circles), and JET [5, 7] (closed diamonds) and [2] (open diamonds). The square and triangle reflect the results of simulations with two different τ_{rec} values: the one calculated from the plasma parameters in the ITER device [6], $\tau_{rec} = 3.7$ s (square), and the one used to simulate JET experiments, $\tau_{rec} = 0.1$ s (triangle).

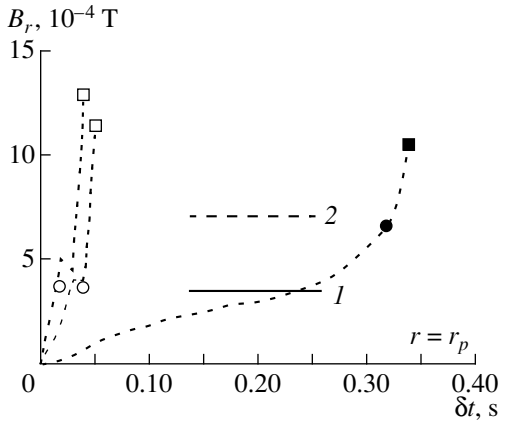

Fig. 8. Amplitude of the magnetic mode with $(m, n) = (2, 1)$ before the density limit disruption in the JET tokamak [5, 7] with (closed symbols) and without (open symbols) external rotating magnetic fields (δt is the time interval after the destabilization of the rotating magnetic perturbations). The circles and squares correspond to the mode amplitude at the time at which the mode stops rotating and just before the major disruption. Straight lines (*1*) and (*2*) are the computed amplitudes at the time at which the mode stops rotating in the cases without and with external magnetic fields, respectively.

plays a major role in the destruction of the plasma column. Just before the disruption, the magnetic perturbations were observed to rotate at a slower rate; moreover, in some cases, the perturbations stopped rotating or, in other words, the mode with $(m, n) = (2, 1)$ became completely locked. A numerical analysis carried out in [18] showed that preventing the mode locking may ensure a delayed onset of the disruption and safe shutdown of the discharge. The JET experiments with rotating magnetic fields [5, 7, 19] demonstrated that, in the predisruption stage, the time at which MHD modes stop rotating may be delayed and, in some cases, it is possible to lower the rate at which the perturbations grow. For the same power of the external magnetic fields used in the JET experiments, the MHD modes were observed to stop rotating when the amplitude of the magnetic perturbations doubled (Fig. 8). According to the results of our simulations, a decrease in the rate at which the perturbations decelerate is attributed to the accelerating moment of the forces exerted by an external magnetic field on a magnetic island.

5. DISCUSSION

An analysis of the JET experiments with quasistatic and rotating magnetic fields and a comparison of our numerical results with the experimental data from the COMPASS-C [4] and DIII-D [3] tokamaks allowed us to determine the parameters of the phenomenological model of MHD perturbations in the plasma of large tokamaks. Our model, which is based on the analysis of electromagnetic, viscous, and inertial effects near a given resonant magnetic surface, makes it possible to describe the experimentally observed thresholds for destabilization of the MHD perturbations and the evolution of the rotating modes and to predict the thresholds for MHD modes in the ITER tokamak reactor.

Our investigations show that the phenomenological parameters of the model affect the computation results in a fairly complicated manner. However, most of the model parameters are calculated from quantities that are either measured directly in experiments (T_e, n_e, $\omega_{p\alpha 0}$, A, Z_{eff}, r_s, r_w) or are reconstructed from experimental data (Δ'_{frb}, s, η, B_ϑ, τ_w, and μ_ν). The free parameters of the model, c_l and d_ν, are adjusted as necessary to achieve the best agreement between the computed evolution of the MHD modes and the experimentally observed perturbation dynamics. A detailed analysis of the experiments, which were carried out for a broad range of plasma parameters and machine dimensions, allowed us to determine the free model parameters with a relatively high degree of confidence.

The estimates of the thresholds for destabilization of the MHD modes in the future ITER tokamak reactor depend on the viscosity coefficient μ_ν. In analyzing the experiments performed in the JET, DIII-D, and COMPASS-C tokamaks with L-mode discharges, we calculated μ_ν using the ITER89-P scaling [24]. A future tokamak reactor is supposed to operate in an improved confinement regime (the H-mode) [6]. Although the experiments have not yet revealed any differences between the thresholds for destabilization of the MHD modes in the L- and H-regimes [25], the use of the ITER89-P scaling may introduce additional inaccuracies into the predicted thresholds for MHD modes in ITER.

In simulations, magnetic islands were treated as small perturbations of an equilibrium plasma configuration, as if they were surrounded by an incompressible "phenomenological plasma fluid" (see [11]). The analysis carried out by Fitzpatrick [11] showed that the single-fluid approximation can be applied to a multicomponent plasma (consisting of ions, electrons, and impurities) in order to calculate the relative change in the plasma velocity during the development of magnetic islands. In the standard operating regimes of a tokamak, the velocities of different plasma components are coupled through the condition that the given net plasma current be conserved. In the first approximation, the change in the velocity of one of the plasma components inevitably alters the velocities of the remaining components. In simulations, the toroidal rotation velocity of the phenomenological plasma fluid surrounding the magnetic island was assumed to be proportional to the angular velocity of the plasma ions. We adopted this approximation because the ion velocity may be comparable with the velocity of the ^{6}C ions, which was measured in the JET experiments. In order to model the rotation of the main plasma in more detail, it is necessary to take into account additional, more complicated

effects (see, e.g., [26]); this problem, however, goes beyond the scope of our paper.

Measurements from magnetic probes and saddle loops in the JET tokamak revealed that the perturbation mode with $(m, n) = (2, 1)$ plays a governing role in experiments with external helical magnetic fields (in which we are interested here). This circumstance enabled us only to trace the evolution of the mode with $(m, n) = (2, 1)$. On the other hand, the DIII-D experiments [27] showed that the contribution of the nearest satellite modes, specifically, those with $(m, n) = (3, 1)$ and (1, 1), to the threshold for destabilization of the MHD perturbations can be as large as 10–15%. To analyze in detail the effect of the nearest satellites on the plasma stability in JET requires further experimental investigation.

In the absence of external magnetic fields, the stability of MHD perturbations is governed by the stability parameter of the tearing mode, Δ'_{frb}, which is calculated from the equilibrium current density profile. In our model, the possible change in the current density profile during the growth of the MHD modes is incorporated through the tearing-mode saturation effect [16]. This approach, which is justified for the initial stage of the evolution of perturbations, should be refined in order to describe large-amplitude MHD modes, in which case the perturbations can be analyzed in detail only through a complete solution of the boundary-value problem of the tearing-mode stability [26, 28].

The simulations of experiments with a delayed onset of the density limit disruptions allowed us to outline possible ways of using the external rotating magnetic fields in order to make tokamak plasmas more stable. Note that the JET experiments described here are of a preliminary nature, so that a detailed analysis of the conditions under which MHD perturbations are stabilized requires further experimental investigations. Our simulations also showed that, for prescribed stray magnetic fields, plasma stability can be ensured by maintaining the rotation rate of the plasma column. This effect was demonstrated in experiments with auxiliary heating, with both NBI-heated [2, 5] and ECR-heated [29] plasmas.

6. CONCLUSIONS

Analyzing the JET experiments [5, 7], we have determined the thresholds for destabilization of quasistatic (locked) and rotating MHD perturbations in a plasma under fusion reactor conditions. Numerical simulations carried out for the ITER tokamak reactor predict that, depending on the plasma parameters, the thresholds for MHD modes may be very different, $B_r/B_\varphi(r = r_0) \simeq (0.2\text{–}2) \times 10^{-4}$. The conclusion that, in some operating regimes of the ITER device, the thresholds for destabilization of the MHD modes may be low necessitates steps to develop and construct systems for neutralizing the stray magnetic fields and systems for controlling MHD perturbations.

ACKNOWLEDGMENTS

I am grateful to K.A. Razumova, Yu.N. Dnestrovskiĭ, I.B. Semenov, S.V. Mirnov, N.V. Ivanov, and A.M. Kakurin for their interest in our work and fruitful discussions. I would like to thank G. D'Antona, M. DeBenedetti, R.J. LaHaye, E. Lazzaro, A. Santagiustina, A.W. Morris, A. Smolyakov, T. Hender, M.F. Nave, and B. Tubbing for stimulating consultations. I am especially grateful to D.J. Campbell and A. Tanga for the opportunity to participate in the JET experiments. This work was supported in part by the Russian Foundation for Basic Research, project no. 98-02-17382.

REFERENCES

1. J. A. Snipes, D. J. Campbell, P. S. Haynes, *et al.*, Nucl. Fusion **28**, 1085 (1988).
2. G. M. Fishpool and P. S. Haynes, Nucl. Fusion **34**, 109 (1994).
3. R. S. LaHaye, R. Fitzpatrick, T. C. Hender, *et al.*, Phys. Fluids B **4**, 2098 (1992).
4. A. W. Morris, P. Carolan, R. Fitzpatrick, *et al.*, Phys. Fluids B **4**, 413 (1992).
5. A. Santagiustina, S. Ali Arshad, D. J. Campbell, *et al.*, in *Proceedings of 22nd European Conference on Controlled Fusion and Plasma Physics, Bournemouth, 1995* [ECA **19C** (IV), 461 (1995)].
6. ITER-JCT and Home Teams (presented by G. Janeschitz), Plasma Phys. Controlled Fusion **37**, A19 (1995).
7. P. Savrukhin, S. Ali Arshad, D. J. Campbell, *et al.*, in *Proceedings of 23rd European Conference on Controlled Fusion and Plasma Physics, Kiev, 1996* [ECA **20C** (I), 187 (1996)].
8. R. J. Buttery, D. J. Campbell, M. DeBenedetti, *et al.*, in *Proceedings of 24th European Conference on Controlled Fusion and Plasma Physics, Berchtesgaden, 1997* [ECA **21A** (I), 265 (1997)].
9. P. V. Savrukhin, Preprint No. IAE-6152/7 (Russian Research Centre Kurchatov Institute, Moscow, 1999).
10. R. Fitzpatrick and T. C. Hender, Phys. Fluids B **3**, 644 (1991).
11. R. Fitzpatrick, Nucl. Fusion **33**, 1049 (1993).
12. G. Bosia and E. Lazzaro, Nucl. Fusion **31**, 1003 (1991).
13. P. H. Rutherford, Phys. Fluids **16**, 1903 (1973).
14. D. A. Monticello, R. B. White, and M. N. Rosenbluth, in *Proceedings of 7th International Conference on Plasma Physics and Controlled Nuclear Fusion Research, Innsbruck, 1978* (IAEA, Vienna, 1979), Vol. 1, p. 605.
15. V. V. Arsenin, in *Proceedings of 8th European Conference on Controlled Fusion and Plasma Physics, Prague, 1977*, Vol. I, p. 43.
16. R. B. White, D. A. Monticello, M. N. Rosenbluth, and B. V. Waddell, Phys. Fluids **20**, 800 (1977).
17. J. A. Wesson, Nucl. Fusion **18**, 87 (1978).

18. P. Savrukhin, D. J. Campbell, M. DeBenedetti, *et al.*, Report No. JET-R(95)-06 (JET Joint Undertaking, Abingdon, 1995).
19. M. DeBenedetti, S. AliArshad, D. J. Campbell, *et al.*, in *Proceedings of 23rd European Conference on Controlled Fusion and Plasma Physics, Kiev, 1996* [ECA **20C** (I), 191 (1996)].
20. R. J. Buttery, Report No. F/PL/WPA9.2a (UK Atomic Energy Authority, Culham, 1995).
21. D. J. Campbell, P. A. Duperrex, A. W. Edwards, *et al.*, in *Proceedings of 11th International Conference on Plasma Physics and Controlled Nuclear Fusion Research, Kyoto, 1986* (IAEA, Vienna, 1987), Vol. 1, p. 197.
22. S. V. Mirnov and I. B. Semenov, in *Proceedings of 4th International Conference on Plasma Physics and Controlled Nuclear Fusion Research, Madison, 1971* (IAEA, Vienna, 1971), Vol. II, p. 401.
23. F. C. Schuller, Plasma Phys. Controlled Fusion **37**, A135 (1995).
24. P. N. Yushmanov, T. Takizuka, K. S. Riedel, *et al.*, Nucl. Fusion **30**, 1999 (1990).
25. A. W. Morris, Plasma Phys. Controlled Fusion **34**, 1871 (1992).
26. D. Biscamp, *Nonlinear Magnetohydrodynamics* (Cambridge, Cambridge Univ. Press, 1997).
27. R. J. LaHaye, Report No. GA-A22468 (General Atomics, San Diego, CA, 1997).
28. A. I. Smolyakov, Plasma Phys. Controlled Fusion **35**, 657 (1994).
29. N. V. Ivanov, A. M. Kakurin, P. E. Kovrov, *et al.*, in *Proceedings of 22nd European Conference on Controlled Fusion and Plasma Physics, Bournemouth, 1995* [ECA **19C** (III), 77 (1995)].

Translated by O. Khadin

Plasma Physics Reports, Vol. 26, No. 8, 2000, pp. 641–645. Translated from Fizika Plazmy, Vol. 26, No. 8, 2000, pp. 683–687.

MAGNETIC CONFINEMENT SYSTEMS

Local Three-Dimensional MHD Stability in Equilibrium Optimized Coordinates

W. A. Cooper

Centre de Recherches en Physique des Plasmas, Association Euratom–Confédération Suisse, Ecole Polytechnique Fédérale de Lausanne, Lausanne, Switzerland

Received March 7, 2000

Abstract—The linear equation for ideal magnetohydrodynamic ballooning modes in three-dimensional configurations is derived in the coordinate system that is optimal for the representation of the equilibrium state. The magnetic field lines in this coordinate system, however, are not straight. The form of the Mercier criterion that is currently in use is recovered from the asymptotic analysis of the ballooning equation. To determine the parallel-current density, a magnetic differential equation expressed in the optimal coordinates must be inverted.

1. INTRODUCTION

The formulation of the linear MHD stability problem has been usually carried out in coordinate systems in which the magnetic field lines are straight. This has been motivated by the realization that the $\mathbf{B}\cdot\nabla$ operator acquires a very simple structure in such a class of coordinates. In three-dimensional (3D) configurations, a specific straight-field-line (SFL) coordinate system identified by Boozer [1] has been preferred because the poloidal and toroidal magnetic field components in the covariant representation correspond to the toroidal and negative poloidal current flux functions, respectively, enclosed within each magnetic flux surface. This permits a more transparent determination of the parallel current density and a clearer identification of the mechanisms for driving and suppressing the instability [2].

For the computation of the MHD equilibrium state, however, the SFL coordinates are inadequate and cumbersome. The optimal coordinate system for the equilibrium problem represents the magnetic field $\mathbf{B}$ as [3]

$$\mathbf{B} = \nabla v \times \nabla\psi + \nabla\Phi \times \nabla u + \nabla\Phi \times \nabla\lambda, \qquad (1)$$

where $\psi(s)$ and $\Phi(s)$ are the poloidal and toroidal flux functions, respectively. The magnetic flux surfaces are constrained to be nested. In this coordinate system, s labels the radial variable, u labels the poloidal angle, and v is the geometric toroidal angle. The function λ is an angular renormalization parameter, which, in the iterative procedure employed to minimize the energy of the system, is adjusted to minimize the spectrum of poloidal modes required to describe the equilibrium [3]. It is this spectral condensation property that makes the coordinate system optimal. It has been implemented in the 3D VMEC equilibrium code [4].

To correctly converge ballooning eigenstructures to sufficient accuracy, it has been our experience that, for robust configurations of the helias type [2] similar to the proposed Wendelstein VII-X (WVII-X) device [5], the 61 mode-pairs needed to represent the equilibrium in the VMEC coordinates must be increased to a still manageable 186 mode-pairs to reconstruct the equilibrium state in the Boozer magnetic coordinates at volume-averaged β values of up to 8% [6]. However, for more fragile configurations of the torsatron type that undergo large Shafranov shifts at moderate values of β, the 61 mode-pairs needed to represent the equilibrium in the VMEC coordinates explode to 681 mode-pairs for the reconstruction in Boozer coordinates at $\beta \simeq 2\%$ for the ballooning calculations [7]. For Mercier-type modes that have more extended structures along the field lines and for global modes, the mode-pair requirements in the Boozer coordinate space are less stringent, although still nonnegligible when compared with the spectra required for the ballooning computations. In low-aspect-ratio heliac configurations, the determination of the equilibrium state imposes an already very broad spectrum of modes. In the three-field-period H1 heliac [8], the equilibrium is obtained with 314 mode-pairs, which must be expanded to 597 mode-pairs for the ballooning calculations in Boozer coordinates for β up to 1.5% [9]. In the four-field-period TJ-II heliac [10], spectral requirements of 138 mode-pairs have been reported for the equilibrium state [10, 11], which, being expanded in Boozer space to 750 mode-pairs, yields reliable ballooning estimates only up to $\beta \sim 2\%$ [11].

The spectral broadening of the equilibrium reconstruction in the Boozer magnetic coordinate system as a function of β can unduly overtax or even overwhelm the computational resources of present-day computers for the modeling of a torsatron, a low-aspect-ratio heliac, and other stellarator devices. This motivates us to consider the formulation of the MHD stability problem in an optimized coordinate system such as that developed for the VMEC equilibrium code.

1063-780X/00/2608-0641$20.00

2. BALLOONING STABILITY

The equation for ideal MHD ballooning modes in 3D configurations [12, 13] in a coordinate-free representation in a form applicable for marginal stability analysis can be expressed as

$$(\mathbf{B}\cdot\nabla)\left[\frac{|\mathbf{k}_\perp|^2}{B^2}(\mathbf{B}\cdot\nabla\chi)\right] + (1-\Gamma)\left(\frac{2\mathbf{B}\times\mathbf{k}_\perp\cdot\nabla p}{B^2}\right)\left(\frac{\mathbf{B}\times\mathbf{k}_\perp\cdot\boldsymbol{\kappa}}{B^2}\right)\chi = 0, \quad (2)$$

where $\mathbf{k}_\perp$ is the wave vector, $\boldsymbol{\kappa} = (\mathbf{b}\cdot\nabla)\mathbf{b}$ is the magnetic field line curvature, $\mathbf{b} = \mathbf{B}/B$ is the unit vector along the magnetic field lines, Γ is the eigenvalue, and χ is the ballooning eigenfunction. In the ballooning representation, the eigenfunction is expressed as

$$\chi = \tilde{\chi}\exp(iS/\epsilon), \quad (3)$$

where $\tilde{\chi}$ is a slowly varying amplitude and the phase factor satisfies the condition $\mathbf{B}\cdot\nabla S = 0$. Assuming $\epsilon \ll 1$, the rapid cross-magnetic field variation is contained within the exponential factor. The magnetic field given by equation (1) can be rewritten as

$$\mathbf{B} = \nabla\alpha\times\nabla\psi, \quad (4)$$

where α is a function that labels the magnetic field lines, which, in the VMEC coordinate system, is expressed as

$$\alpha = v - q(s)[u + \lambda(s, u, v)], \quad (5)$$

where $q(s) = \Phi'(s)/\psi'(s)$ is the inverse rotational transform and the prime indicates the derivative with respect to s of a variable that is constant on a magnetic flux surface. The lines of constant α in the (u, v) space are not straight because λ is a function of u and v. The condition $\mathbf{B}\cdot\nabla S = 0$ implies $S = S(s, \alpha)$ [13]. We now consider the perturbation χ to have the functional dependence $\chi = \chi(s, u, \alpha)$. As a result, we obtain

$$\mathbf{B}\cdot\nabla\chi = B^u\frac{\partial\chi}{\partial u}\bigg|_{s,\alpha} = \frac{\psi'(s)}{\sqrt{g}}\left[1 - q(s)\frac{\partial\lambda}{\partial v}\right]\frac{\partial\chi}{\partial u}\bigg|_{s,\alpha}, \quad (6)$$

where $\sqrt{g}$ is the Jacobian of the transformation from Cartesian coordinates to the flux coordinates used. The wave vector $\mathbf{k}_\perp = \nabla S/(\partial S/\partial\alpha) = \nabla\alpha + \theta_k\nabla q$ acquires the form

$$\mathbf{k}_\perp = \nabla v - q(s)\nabla u - \left[q'(s)(u-\theta_k) + \frac{\partial(q\lambda)}{\partial s}\right]\nabla s, \quad (7)$$

where θ_k is the radial wavenumber [13]. In these coordinates, the wave fronts S = const twist in a much more complicated manner along a field line than in SFL coordinates because of the term $\partial(q\lambda)\partial s$ in Eq. (7). By defining the vector of the magnetic field line bending as $\mathbf{h} \equiv \psi'(s)\mathbf{B}\times\mathbf{k}_\perp/B^2$, we have in the contravariant representation

$$h^s \equiv \mathbf{h}\cdot\nabla s = 1, \quad (8)$$

$$h^u \equiv \mathbf{h}\cdot\nabla u = -\frac{B^u B_s}{B^2} - \frac{\psi'(s)B_v}{\sqrt{g}B^2}\left[q'(s)(u-\theta_k) + \frac{\partial(q\lambda)}{\partial s}\right], \quad (9)$$

$$h^v \equiv \mathbf{h}\cdot\nabla v = -\frac{B^v B_s}{B^2} + \frac{\psi'(s)B_u}{\sqrt{g}B^2}\left[q'(s)(u-\theta_k) + \frac{\partial(q\lambda)}{\partial s}\right]. \quad (10)$$

These equations contain all of the components of the magnetic field $\mathbf{B}$ in the covariant and contravariant representations. Using these equations and the relations of differential geometry, it is easy to obtain an expression for $|\mathbf{k}_\perp|^2$. When evaluating the term with the magnetic field line curvature that drives ballooning instabilities, it is useful to apply the radial component of the MHD equilibrium force balance relation $\nabla p = \mathbf{j}\times\mathbf{B}$ given by

$$\sqrt{g}\mathbf{B}\cdot\nabla B_s = \sqrt{g}p'(s) + \sqrt{g}B^u\frac{\partial B_u}{\partial s} + \sqrt{g}B^v\frac{\partial B_v}{\partial s}. \quad (11)$$

Furthermore, a consideration of the equations of charge conservation $\nabla\cdot\mathbf{j} = 0$, force balance, and $\mathbf{j}\cdot\nabla s = 0$ shows that

$$\sqrt{g}\mathbf{B}\cdot\nabla\left(\frac{\mathbf{j}\cdot\mathbf{B}}{B^2}\right) = p'(s)\left[\frac{\partial}{\partial v}\left(\frac{B_u}{B^2}\right) - \frac{\partial}{\partial u}\left(\frac{B_v}{B^2}\right)\right] = \frac{p'(s)}{B^4}\left(B_v\frac{\partial B^2}{\partial u} - B_u\frac{\partial B^2}{\partial v}\right). \quad (12)$$

Then, the ballooning mode equation in the VMEC coordinates optimal for describing the equilibrium state can be written as

$$\frac{\partial}{\partial u}\left\{\left\{C_p + C_s\left[q'(s)(u-\theta_k) - \frac{\partial(q\lambda)}{\partial s}\right] + C_q\left[q'(s)(u-\theta_k) + \frac{\partial(q\lambda)}{\partial s}\right]^2\right\}\frac{\partial\chi}{\partial u}\bigg|_{s,\alpha}\right\}\bigg|_{s,\alpha} + (1-\Gamma)\left\{d_p + d_s\left[q'(s)(u-\theta_k) + \frac{\partial(q\lambda)}{\partial s}\right]\right\}\chi = 0, \quad (13)$$

where the coefficients are

$$C_p = \left(\frac{g_{ss}}{\sqrt{g}} - \frac{B_s^2}{B^2}\right)\left[1 - q(s)\frac{\partial\lambda}{\partial\nu}\right], \quad (14)$$

$$C_s = \frac{2\psi'(s)}{\sqrt{g}B^2}\left(\frac{g_{s\nu}}{\sqrt{g}}B_u - \frac{g_{su}}{\sqrt{g}}B_\nu\right)\left[1 - q(s)\frac{\partial\lambda}{\partial\nu}\right], \quad (15)$$

$$C_q = \frac{[\psi'(s)]^2}{\sqrt{g}B^2}\left[\frac{g_{uu}g_{\nu\nu} - g_{u\nu}^2}{(\sqrt{g})^2}\right]\left[1 - q(s)\frac{\partial\lambda}{\partial\nu}\right], \quad (16)$$

$$d_p = \frac{p'(s)}{[\psi'(s)]^2\left[1 - q(s)\frac{\partial\lambda}{\partial\nu}\right]}\left[\frac{\sqrt{g}p'(s)}{B^2} - \frac{\partial\sqrt{g}}{\partial s}\right.$$

$$\left. + \frac{B_u}{B^2}\frac{\partial(\sqrt{g}B^u)}{\partial s} + \frac{B_\nu}{B^2}\frac{\partial(\sqrt{g}B^\nu)}{\partial s} + \sqrt{g}(\mathbf{B}\cdot\nabla)\left(\frac{B_s}{B^2}\right)\right], \quad (17)$$

$$d_s = \frac{-1}{\psi'(s)\left[1 - q(s)\frac{\partial\lambda}{\partial\nu}\right]}(\sqrt{g}\mathbf{B}\cdot\nabla)\left(\frac{\mathbf{j}\cdot\mathbf{B}}{B^2}\right). \quad (18)$$

It is a one-page exercise in differential geometry to demonstrate that $|\nabla s|^2 = (g_{uu}g_{\nu\nu} - g_{u\nu}^2)/(\sqrt{g})^2$.

3. ASYMPTOTIC ANALYSIS

The asymptotic analysis ($u - \theta_k \longrightarrow \infty$) of the ballooning mode equation yields the equation $(1-\Gamma)^2 D_2 + (1-\Gamma)D_1 - [q'(s)]^2/4 = 0$ for the conditions of marginal stability, which implies

$$\Gamma = 1 + \frac{D_1}{2D_2} - \frac{\{D_1^2 + [q'(s)]^2 D_2\}^{1/2}}{2D_2} \le 0 \quad (19)$$

for the stability of modes with an extended structure along the field lines. The coefficients are

$$D_1 = \langle h_q\rangle\left\langle\left[1 - q(s)\frac{\partial\lambda}{\partial\nu}\right]\left[d_p + d_s\frac{\partial(q\lambda)}{\partial s} + q'(s)\left(\frac{\mathbf{j}\cdot\mathbf{B}}{B^2}\right)\right]\right\rangle - \left\langle h_q q'(s)\left(\frac{\mathbf{j}\cdot\mathbf{B}}{B^2}\right)\right\rangle, \quad (20)$$

$$D_2 = \langle h_q\rangle\left\langle h_q\left(\frac{\mathbf{j}\cdot\mathbf{B}}{B^2}\right)^2\right\rangle - \left\langle h_q\left(\frac{\mathbf{j}\cdot\mathbf{B}}{B^2}\right)\right\rangle^2. \quad (21)$$

The standard form of the Mercier criterion [14] is obtained with $D_1 + D_2 \le [q'(s)]^2/4$, although expression (19) is sometimes preferable because it allows a more ready comparison with the eigenvalue of the ballooning equation. We define $h_q \equiv \sqrt{g}\,B^u/[\psi'(s)C_q]$ and $\langle A\rangle \equiv (L/4\pi^2)\int_0^{2\pi} d\nu \int_0^{2\pi} du A$, where L is the number of equilibrium field periods. It can be shown by performing an integration by parts and some algebraic manipulations that

$$\left\langle\left[1 - q(s)\frac{\partial\lambda}{\partial\nu}\right]\left[d_p + d_s\frac{\partial(q\lambda)}{\partial s}\right]\right\rangle = \frac{p'(s)}{[\psi'(s)]^2}\left[p'(s)\left\langle\frac{\sqrt{g}}{B^2}\right\rangle - V''(s) + \frac{\psi''(s)}{\psi'(s)}V'(s) + q'(s)\psi'(s)\left\langle\frac{B_\nu}{B^2}\right\rangle\right], \quad (22)$$

where $V'(s) = \langle\sqrt{g}\rangle$ is the differential volume. After expanding $\mathbf{j}\cdot\mathbf{B}/B^2$ by invoking Ampere's law and radial force balance, we obtain

$$\left\langle\left[1 - q(s)\frac{\partial\lambda}{\partial\nu}\right]q'(s)\left(\frac{\mathbf{j}\cdot\mathbf{B}}{B^2}\right)\right\rangle = \frac{q'(s)I'(s)}{\psi'(s)} - \frac{p'(s)q'(s)}{\psi'(s)}\left\langle\frac{B_\nu}{B^2}\right\rangle. \quad (23)$$

From the flux-surface average of the radial force balance relation, we derive $p'(s)V'(s) = \Phi'(s)I'(s) - \psi'(s)J'(s)$, where $I(s)$ and $J(s)$ are the poloidal and toroidal current flux functions, respectively. This allows us to reduce D_1 to

$$D_1 = \langle h_q\rangle\left\{\frac{p'(s)[p'(s)\langle\sqrt{g}/B^2\rangle - V''(s)]}{[\psi'(s)]^2}\right\} + \langle h_q\rangle\left[\frac{\Phi''(s)I'(s) - \psi''(s)J'(s)}{[\psi'(s)]^2}\right] - \left\langle h_q q'(s)\left(\frac{\mathbf{j}\cdot\mathbf{B}}{B^2}\right)\right\rangle, \quad (24)$$

which reproduces the contributions from the magnetic well (first term) and net current (remaining terms) to the Mercier criterion, while D_2 corresponds to the geodesic curvature contribution to the Mercier criterion in a form that is currently in widespread use [14–16]. It is instructive to note that, taking $\lambda = 0$, $B_u = J(s)$, and $B_\nu = -I(s)$, we recover the form of the ballooning equation and the Mercier criterion as derived in Boozer coordinates [3].

4. PARALLEL-CURRENT DENSITY

One of the principal issues in 3D MHD stability concerns the evaluation of the parallel current density, since this can be an important source of instabilities in nonsymmetric configurations [3, 14]. Ballooning calculations in devices with a low global magnetic shear like the WVII-X heliac [6] and the H1 heliac [9] or in devices with a high global magnetic shear like the torsatron [7] have demonstrated that these types of instabilities tend to be insensitive to singularities of the parallel-current density on rational surfaces because their structures are too localized along the magnetic field lines to detect the resonance condition. On the other

hand, the Mercier criterion [3] and localized low mode structures [17] depend critically on the correct evaluation of $\mathbf{j}\cdot\mathbf{B}/B^2$. In particular, Gardner and Blackwell demonstrated that, in a low shear heliac, the geometric (direct) determination of the parallel-current density in either VMEC coordinates or Boozer magnetic coordinates failed to reproduce the correct behavior near the dominant low-order rational surfaces, and this seriously impacted the predictions of the Mercier criterion [18]. What still remains to be established is whether the component of the parallel current density that varies on the flux surface and is evaluated in the VMEC coordinates according to the magnetic differential equation (12) can capture the resonance condition in the vicinity of rational surfaces with reasonable accuracy. In SFL coordinates, the Fourier decomposition of this magnetic differential equation yields an algebraic equation for the Fourier components of $(\mathbf{j}\cdot\mathbf{B}/B^2)$, in which the resonance condition appears explicitly. In non-SFL VMEC coordinates, the Fourier decomposition of equation (12) yields a matrix equation that has to be inverted on each flux surface to evaluate the surface-varying components of $(\mathbf{j}\cdot\mathbf{B}/B^2)$. Consequently, the resonance condition does not appear explicitly in the resulting expression. If the approach proposed for evaluating the parallel current density in the VMEC coordinates proves to be successful in correctly reproducing the predictions of the Mercier criterion near rational surfaces, we can consider extending the method to the problem of global MHD stability. The application of equation (12) is insufficient, however, to determine the component of $(\mathbf{j}\cdot\mathbf{B}/B^2)$ that is constant on each flux surface. This component has to be calculated from the direct evaluation of $(\mathbf{j}\cdot\mathbf{B}/B^2)$. This can be obtained by invoking Ampere's law and radial force balance to yield

$$\left(\frac{\mathbf{j}\cdot\mathbf{B}}{B^2}\right) = \frac{1}{\sqrt{g}B^u}\left[\frac{\partial B_s}{\partial \nu} - \frac{\partial B_\nu}{\partial s} - \frac{p'(s)B_\nu}{B^2}\right]. \qquad (25)$$

This form is used to derive equation (23).

5. SUMMARY AND DISCUSSION

In summary, we have derived an expression for the 3D ideal ballooning equation in the coordinate system that is optimal for the representation of the MHD equilibrium state. We have recovered the Mercier criterion from the asymptotic analysis of this equation. The main advantages of this approach for the local 3D MHD stability problem are the following:

(i) It obviates a mapping procedure to a different coordinate system and the inherent errors introduced in the reconstruction of the equilibrium.

(ii) The spectrum of modes remains under control, which has favorable implications for computational efficiency.

The main disadvantages are the following:

(i) The coefficients to evaluate stability may be more complicated to calculate. In particular, the parallel-current density is a matrix equation rather than the algebraic expression in SFL coordinates.

(ii) The resonance condition at the rational surfaces does not appear explicitly in the inversion of the magnetic differential equation for $(\mathbf{j}\cdot\mathbf{B}/B^2)$, which could potentially suppress an important driving mechanism for instabilities in 3D systems. It could provide a numerical detuning of the resonance that may not be altogether insidious because instabilities driven by current sheets may constitute a manifestation of the generation of magnetic island structures rather than the true violation of a stability criterion.

(iii) On a fixed field line, the determination of the toroidal angle ν becomes a transcendental equation through the inversion of equation (5). Alternatively, a field-line-tracing technique can be applied to obtain ν by transforming equation (5) into a differential equation that can be written as

$$\left.\frac{\partial \nu}{\partial u}\right|_{s,\alpha} = q(s)\frac{1+\left.\frac{\partial \lambda}{\partial u}\right|_{s,\nu}}{1-q(s)\left.\frac{\partial \lambda}{\partial \nu}\right|_{s,u}}. \qquad (26)$$

The subscripts denote the quantities that remain fixed during the calculation of a derivative. In any SFL coordinate system, the relation between the poloidal and toroidal angles on a field line is a simple linear expression.

However, even if these disadvantages manifest themselves seriously, they are more likely to affect the Mercier predictions than the ballooning predictions. In the Boozer coordinate system, the ballooning instabilities, on the one hand, do not appear to depend sensitively on the singular nature of $(\mathbf{j}\cdot\mathbf{B}/B^2)$ but, on the other hand, impose the strictest demands with respect to the width of the spectral requirements needed for accurate convergence. We therefore anticipate that it would be much more efficient to compute the ballooning stability in the optimal coordinates developed to represent the equilibrium state even in the case when these coordinates fail to deliver satisfactory Mercier predictions. The Mercier criterion can be accurately evaluated in Boozer coordinates with a much more condensed spectrum of modes than the ballooning instabilities, which require higher resolution due to their localization along the magnetic field lines. The 3D ballooning solvers currently in existence could be adapted quite straightforwardly to the optimized VMEC coordinates, because the coefficients expressed with equations (14)–(18) may be more difficult to evaluate only in appearance as a result of the gains realized through spectral condensation.

ACKNOWLEDGMENTS

I thank Dr. S.P. Hirshman for pointing out the potentialities of the field-line-tracing technique. This work was supported by the Fonds National Suisse pour la Recherche Scientifique and by Euratom.

REFERENCES

1. A. H. Boozer, Phys. Fluids **23**, 904 (1980).
2. J. Nührenberg and R. Zille, in *Theory of Fusion Plasmas*, Ed. by A. Bondeson, E. Sindoni, and F. Troyon (Compositori, Bologna, 1988), p. 3.
3. S. P. Hirshman and J. C. Whitson, Phys. Fluids **26**, 3553 (1983).
4. S. P. Hirshman and O. J. Betancourt, Comput. Phys. **96**, 99 (1991).
5. W. Lotz, J. Nührenberg, and C. Schwab, in *Proceedings of 13th International Conference on Plasma Physics and Controlled Nuclear Fusion Research, Washington, 1990* [Nucl. Fusion Suppl. **2**, 603 (1991)].
6. R. Moeckli and W. A. Cooper, Nucl. Fusion **33**, 1899 (1993).
7. R. Moeckli and W. A. Cooper, Phys. Plasmas **1**, 793 (1994).
8. S. M. Hamberger, B. D. Balckwell, L. E. Sharp, and D. B. Denton, Fusion Technol. **17**, 123 (1990).
9. W. A. Cooper and H. J. Gardner, Nucl. Fusion **34**, 729 (1994).
10. A. Varias, C. Alejaldre, A. L. Fraguas, *et al.*, Nucl. Fusion **30**, 2597 (1990).
11. C. Alejaldre, L. García, J. A. Jiménez, *et al.*, in *Proceedings of 14th International Conference on Plasma Physics and Controlled Nuclear Fusion Research, Würzburg, 1992* (IAEA, Vienna, 1993), Vol. 2, p. 431.
12. D. Correa-Restrepo, Z. Naturforsch. A **33**, 789 (1978).
13. R. L. Dewar and A. H. Glasser, Phys. Fluids **26**, 3038 (1983).
14. F. Bauer, O. Betancourt, and P. Garabedian, *Magnetohydrodynamic Equilibrium and Stability of Stellarators* (Springer-Verlag, New York, 1984).
15. N. Domínguez, J. N. Leboeuf, B. A. Carreras, and V. E. Lynch, Nucl. Fusion **29**, 2079 (1989).
16. K. Ichiguchi, N. Nakajima, M. Okamoto, *et al.*, Nucl. Fusion **33**, 481 (1993).
17. G. Y. Fu, W. A. Cooper, R. Gruber, *et al.*, Phys. Fluids B **4**, 1401 (1992).
18. H. J. Gardner and B. D. Blackwell, Nucl. Fusion **32**, 2009 (1992).

Translated by the author

Plasma Physics Reports, Vol. 26, No. 8, 2000, pp. 646–656. Translated from Fizika Plazmy, Vol. 26, No. 8, 2000, pp. 688–699.

PLASMA OSCILLATIONS AND WAVES

Emission of Low-Frequency Electromagnetic Waves by a Short Laser Pulse Propagating in a Plasma with Density Fluctuations

L. M. Gorbunov* and A. A. Frolov**

**Lebedev Institute of Physics, Russian Academy of Sciences, Moscow, 117924 Russia*

*** Institute for High Energy Densities, Associated Institute for High Temperatures, Russian Academy of Sciences, Izhorskaya ul. 13/19, Moscow, 127412 Russia*

Received November 12, 1999

Abstract—It is shown that a short laser pulse propagating in a plasma with electron density fluctuations can emit electromagnetic waves with frequencies much lower than the laser carrier frequency. Emissions with frequencies close to the plasma frequency and the doubled plasma frequency in a nonisothermal plasma, as well as emission generated in a turbulent plasma, are examined. The effects in question are related to the transformation of the laser pulse wakefield into electromagnetic radiation by electron density fluctuations. The phenomenon under study opens new possibilities for diagnostics of both plasma fields excited by laser pulses and electron density fluctuations in a plasma. © *2000 MAIK "Nauka/Interperiodica".*

INTRODUCTION

A short laser pulse propagating in an underdense plasma excites an electron density wave (a wake wave) whose electric field is localized near the pulse trajectory [1, 2]. Recently, this wakefield has been studied experimentally with the help of a probing laser pulse propagating behind the main pulse at a certain distance from it [3–5]. However, the first publication on recording the wakefield excited by a laser pulse in a plasma was based on the investigation of electromagnetic radiation emitted from the plasma [6]; in the emission spectrum, a spike of intensity was observed in the vicinity of the plasma frequency. The authors of [6] explained this phenomenon by the transformation of the wakefield into electromagnetic radiation by regular plasma inhomogeneities. A somewhat different mechanism for the transformation of the wakefield into electromagnetic radiation in a periodically inhomogeneous (stratified) plasma was recently proposed in [7].

Here, we consider electromagnetic radiation generated during the propagation of a short laser pulse in a plasma that is on average uniform but in which there are electron density fluctuations. Taking into account the fact that the frequency of the emitted radiation is much lower than the laser frequency, we will refer to this radiation as "low-frequency emission."

Based on the general relationships presented in the first and second sections, we study the spectrum of emission from a nonisothermal plasma near the plasma frequency (Section 3). It is shown that the radiation is emitted mainly perpendicularly to the propagation direction of the laser pulse. The emission spectrum depends strongly on the electron temperature and the transverse size of the pulse. The conditions under which the spectrum consists of either two closely spaced lines or a single line are determined. The energy lost by the pulse due to emission is estimated. In Section 4, the emission near the doubled plasma frequency is studied. With a turbulent plasma in mind, in Section 5 we consider the emission near the plasma frequency that appears in a plasma with given stationary electron density fluctuations. In the Conclusion, we discuss the physical processes governing the low-frequency emission of a laser pulse and possible applications of this emission to plasma and laser-pulse diagnostics.

1. BASIC EQUATIONS

We consider a short laser pulse propagating with the group velocity V_g along the z-axis in a plasma with the electron density

$$N_e(\mathbf{r}, t) = N_{0e} + \delta N_e(\mathbf{r}, t), \tag{1.1}$$

where N_{0e} is the space averaged homogeneous density and $\delta N_e(\mathbf{r}, t)$ are the density fluctuations, which are assumed to be small ($|\delta N_e| \ll N_{0e}$).

The pulse propagation is accompanied by the excitation of electron density perturbations and low-frequency (as compared to the laser frequency) electromagnetic fields. From the Maxwell equations and hydrodynamic equations for electrons in which the action of the laser field is accounted for through the ponderomotive force (see, e.g., [7, 8]), we obtain the following linearized equation for the low-frequency

1063-780X/00/2608-0646$20.00

electromagnetic field $\mathbf{E}(\mathbf{r}, t)$:

$$\frac{\partial^2}{\partial t^2}\mathbf{E} + (c^2 - 3V_{Te}^2)\nabla \mathrm{div}\mathbf{E} - c^2\Delta\mathbf{E} + \omega_{pe}^2\left(1 + \frac{\delta N_e(\mathbf{r}, t)}{N_{0e}}\right)\mathbf{E} = \omega_{pe}^2\left(1 + \frac{\delta N_e(\mathbf{r}, t)}{N_{0e}}\right)\nabla\left(\frac{\Phi}{e}\right), \quad (1.2)$$

where $\omega_{pe} = \sqrt{4\pi e^2 N_{0e}/m_e}$ is the plasma frequency; e and m_e are the electron charge and mass, respectively; T_e is the electron temperature; $V_{Te} = \sqrt{T_e/m_e}$ is the electron thermal velocity; and $\Phi = e^2|\mathbf{E}^0|^2/4m_e\omega_0^2$ is the averaged high-frequency potential of the laser field with the frequency ω_0 and complex amplitude $\mathbf{E}^0$.

Since electron density fluctuations are assumed to be small, we will solve Eq. (1.2) using the perturbation theory and representing the electric field in the form $\mathbf{E} = \mathbf{E}_0 + \mathbf{E}_1 + \ldots$. The potential nature of the ponderomotive force allows us to obtain from (1.2) the equation for a zero-order electric field:

$$\frac{\partial^2}{\partial t^2}\mathbf{E}_0 + \omega_{pe}^2\mathbf{E}_0 - 3V_{Te}^2\Delta\mathbf{E}_0 = \omega_{pe}^2\nabla\left(\frac{\Phi}{e}\right). \quad (1.3)$$

This equation describes the excitation of potential plasma waves by a laser pulse in a uniform plasma. The first-order field $\mathbf{E}_1$ arises due to electron density fluctuations. From (1.2), we obtain the following equation for this field:

$$\frac{\partial^2}{\partial t^2}\mathbf{E}_1 + c^2\mathrm{curlcurl}\mathbf{E}_1 + \omega_{pe}^2\mathbf{E}_1 - 3V_{Te}^2\nabla\mathrm{div}\mathbf{E}_1 = \omega_{pe}^2\frac{\delta N_e}{N_{0e}}\nabla\varphi, \quad (1.4)$$

where

$$\nabla\varphi(\mathbf{r}, t) = \nabla\left(\frac{\Phi}{e}\right) - \mathbf{E}_0(\mathbf{r}, t). \quad (1.5)$$

It is seen from (1.4) that the generation of a low-frequency electromagnetic field is related to both the direct interaction of a laser pulse with density fluctuations [the first term on the right-hand side of (1.5)] and the interaction between fluctuations and the plasma oscillations excited by the pulse [the second term on the right-hand side of (1.5)].

We solve Eq. (1.4) by passing over to the Fourier transform:

$$\mathbf{E}_1(\mathbf{r}, t) = \int_{-\infty}^{+\infty}\frac{d\omega}{2\pi}\exp(-i\omega t)\int\frac{d\mathbf{k}}{(2\pi)^3}\exp(i\mathbf{kr})\mathbf{E}_1(\omega, \mathbf{k}),$$
$$\mathbf{E}_1(\omega, \mathbf{k}) = \int_{-\infty}^{+\infty}dt\exp(i\omega t)\int d\mathbf{r}\exp(-i\mathbf{kr})\mathbf{E}_1(\mathbf{r}, t). \quad (1.6)$$

As a result, from (1.4), we obtain the expression for $\mathbf{E}_1(\omega, \mathbf{k})$:

$$E_1(\omega, \mathbf{k}) = -i\omega_{pe}^2\int\frac{d\omega' d\mathbf{k}'}{(2\pi)^4}\frac{\delta N_e(\omega', \mathbf{k}')}{N_{0e}} \times \frac{\varphi(\omega - \omega', \mathbf{k} - \mathbf{k}')}{\mathbf{k}^2}\left\{\frac{\mathbf{k}\cdot((\mathbf{k} - \mathbf{k}')\cdot\mathbf{k})}{\omega^2\varepsilon^l(\omega, \mathbf{k})} + \frac{[\mathbf{k}\cdot[(\mathbf{k} - \mathbf{k}')\cdot\mathbf{k}]]}{\omega^2\varepsilon^{tr}(\omega) - c^2\mathbf{k}^2}\right\}, \quad (1.7)$$

where $\varepsilon^l(\omega, \mathbf{k}) = 1 - \omega_{pe}^2/(\omega^2 - 3\mathbf{k}^2V_{Te}^2)$ and $\varepsilon^{tr}(\omega) \equiv \varepsilon(\omega) = 1 - \omega_{pe}^2/\omega^2$ are the longitudinal and transverse plasma permittivities in the range of phase velocities higher than the thermal electron velocity.

From the equation $\mathrm{curl}\mathbf{E} = -\partial\mathbf{B}/c\partial t$ and formula (1.7), we obtain the Fourier transform for the magnetic field:

$$\mathbf{B}_1(\omega, \mathbf{k}) = \frac{ic}{\omega}\frac{\omega_{pe}^2}{\omega^2\varepsilon(\omega) - c^2\mathbf{k}^2}\int\frac{d\omega' d\mathbf{k}'}{(2\pi)^4}[\mathbf{k}\mathbf{k}'] \times \frac{\delta N_e(\omega', \mathbf{k}')}{N_{0e}}\varphi(\omega - \omega', \mathbf{k} - \mathbf{k}'). \quad (1.8)$$

We will assume that the distribution of the energy density of the laser field is axially symmetric and the high-frequency potential is a function of the radial coordinate $\rho = \sqrt{x^2 + y^2}$ and longitudinal coordinate $\xi = z - V_g t$. From (1.3) and (1.5), we obtain the expression for the function $\varphi(\omega, \mathbf{k})$:

$$\varphi(\omega, \mathbf{k}) = \frac{2\pi}{\varepsilon^l(\omega, \mathbf{k})}\delta(\omega - k_Z V_g)\frac{\Phi(\mathbf{k})}{e}, \quad (1.9)$$

where

$$\Phi(\mathbf{k}) = \int d\xi d\boldsymbol{\rho}\exp(ik_Z\xi + i\mathbf{k}_\perp\boldsymbol{\rho})\Phi(\xi, \boldsymbol{\rho}). \quad (1.10)$$

Taking into account that the phase velocity of the excited plasma wave is close to the laser-pulse group velocity V_g (which in turn is close to the speed of light), we write the expression for $\varepsilon^l(\omega, \mathbf{k})$ in the form

$$\varepsilon^l(\omega, \mathbf{k}) = 1 - \frac{\omega_{pe}^2}{\omega^2}\left(1 + 3\frac{k^2V_{Te}^2}{\omega^2}\right) + i\mathrm{Im}\varepsilon^l(\omega, \mathbf{k}). \quad (1.11)$$

Here, we have introduced the imaginary part of the longitudinal plasma permittivity,

$$\mathrm{Im}\varepsilon^l(\omega, \mathbf{k}) = \frac{\omega_{pe}^2}{\omega^2}\left\{\frac{\nu_{ei}}{\omega} + \sqrt{\frac{\pi}{2}}\frac{\omega^3}{k^3V_{Te}^3}\exp\left(-\frac{\omega^2}{2k^2V_{Te}^2}\right)\right\}, \quad (1.12)$$

which accounts for both the damping of plasma waves due to the electron–ion collisions with the frequency

$$\nu_{ei} = \frac{4}{3}\frac{\sqrt{2\pi}Ze^4N_{0e}}{m_e^{1/2}T_e^{3/2}}\Lambda$$

(where Z is the ion charge number and Λ is the Coulomb logarithm) and the Landau damping by resonant electrons.

For a Gaussian laser pulse, when

$$\Phi(\xi, \boldsymbol{\rho}) = \Phi_0\exp\left(-\frac{\xi^2}{L^2} - \frac{\rho^2}{R^2}\right), \quad (1.13)$$

function (1.10) takes the form

$$\Phi(\mathbf{k}) = \frac{2\pi e^2 W}{m_e\omega_0^2}\exp\left(-\frac{k_Z^2L^2}{4} - \frac{k_\perp^2R^2}{4}\right), \quad (1.14)$$

where L and R are the characteristic longitudinal and transverse sizes of the pulse, respectively, and Φ_0 is the maximum value of the high-frequency potential, related to the pulse energy W by the expression

$$\Phi_0 = \frac{2\pi e^2}{m_e\omega_0^2\pi^{3/2}R^2L}\frac{W}{}. \quad (1.15)$$

Expressions (1.7) and (1.8) can be used to study the spectral characteristics of the low-frequency electromagnetic radiation emitted from the plasma under the action of a short laser pulse.

2. SPECTRAL CHARACTERISTICS OF LOW-FREQUENCY EMISSION OF A LASER PULSE

We will characterize low-frequency emission of a laser pulse by the time-integrated energy flux density at a certain point [7]:

$$\mathbf{P}(\mathbf{r}) = \int_{-\infty}^{+\infty} dt\frac{c}{4\pi}[\mathbf{E}(\mathbf{r}, t)\cdot\mathbf{B}(\mathbf{r}, t)]. \quad (2.1)$$

The vector $\mathbf{P}$ determines the emitted electromagnetic energy that passes through the unit area element located in the vicinity of the point $\mathbf{r}$ and oriented perpendicularly to the energy flow. This quantity can be also represented in the form of the integral over the frequency

$$\mathbf{P}(\mathbf{r}) = \int_0^\infty d\omega\mathbf{p}(\omega, \mathbf{r}), \quad (2.2)$$

where $\mathbf{p}(\omega, \mathbf{r})$ characterizes the spectral density of the electromagnetic energy that passes through the unit area element during the total time of the pulse propagation. This quantity can be expressed through the Fourier transforms of the electric and magnetic fields:

$$\mathbf{p}(\omega, \mathbf{r}) = \frac{c}{8\pi^2}\{[\mathbf{E}_1(\omega, \mathbf{r})\cdot\mathbf{B}_1^*(\omega, \mathbf{r})] + \text{c.c.}\}. \quad (2.3)$$

We will assume that fluctuations are described by a homogeneous time-independent random function, whose Fourier transform $\delta N_e(\omega, \mathbf{k})$ satisfies the relationship

$$\begin{aligned}&\langle\delta N_e(\omega, \mathbf{k})\delta N_e^*(\omega', \mathbf{k}')\rangle \\ &= (2\pi)^4\delta(\omega-\omega')\delta(\mathbf{k}-\mathbf{k}')(\delta N_e^2)_{\omega,\mathbf{k}},\end{aligned} \quad (2.4)$$

where the angular brackets denote the averaging over fluctuations and $(\delta N_e^2)_{\omega,\mathbf{k}}$ is the Fourier transform of the correlation function of the electron density fluctuations.

Substituting (1.7) and (1.8) into (2.3) and averaging the resulting expression over fluctuations with the help of (2.4), we obtain

$$\begin{aligned}\mathbf{p}(\omega, \mathbf{r}) = -\frac{\omega_{pe}^4}{8\pi^2e^2\omega}\Bigg\{&\int\frac{d\omega''d\mathbf{k}''}{(2\pi)^4}n(\omega'', \mathbf{k}'')\int\frac{d\mathbf{k}_\perp d\mathbf{k}_\perp'}{(2\pi)^4} \\ &\times\exp[i(\mathbf{k}_\perp-\mathbf{k}_\perp')\boldsymbol{\rho}] \\ &\times\frac{\Phi(\mathbf{k}-\mathbf{k}'')\Phi^*(\mathbf{k}'-\mathbf{k}'')}{\varepsilon^l(\omega-\omega'', \mathbf{k}-\mathbf{k}'')\varepsilon^{l*}(\omega-\omega'', \mathbf{k}'-\mathbf{k}'')} \\ &\times\frac{\mathbf{k}''([\mathbf{k}\cdot\mathbf{k}'][\mathbf{k}\cdot\mathbf{k}'']) - \mathbf{k}'[\mathbf{k}\cdot\mathbf{k}'']^2}{k^2[\omega^2\varepsilon(\omega)-c^2k^2][\omega^2\varepsilon(\omega)-c^2k'^2]} + \text{c.c.}\Bigg\},\end{aligned} \quad (2.5)$$

where $n(\omega, \mathbf{k}) = (\delta N_e^2)_{\omega,\mathbf{k}}/N_{0e}^2$, $\mathbf{k} = \mathbf{k}_\perp + \mathbf{e}_Zk_\parallel$, $\mathbf{k}' = \mathbf{k}_\perp' + \mathbf{e}_Zk_\parallel$, $k_\parallel = \frac{\omega-\omega''}{V_g} + k_Z''$, and $\mathbf{e}_Z$ is the unit vector directed along the z-axis.

The emission of electromagnetic waves is related to the vanishing of denominators in (2.5):

$$\frac{\omega^2}{c^2}\varepsilon(\omega) = k_\perp^2 + k_\parallel^2, \quad \frac{\omega^2}{c^2}\varepsilon(\omega) = k_\perp'^2 + k_\parallel^2. \quad (2.6)$$

Obviously, equalities (2.6) can hold only under the condition

$$\frac{\omega^2}{c^2}\varepsilon(\omega) > k_\parallel^2, \quad (2.7)$$

which determines the k_Z'' range that contributes to electromagnetic emission:

$$\begin{aligned}-\left[\frac{\omega-\omega''}{V_g} + \frac{\omega}{c}\sqrt{\varepsilon(\omega)}\right] &< k_Z'' \\ &< -\left[\frac{\omega-\omega''}{V_g} - \frac{\omega}{c}\sqrt{\varepsilon(\omega)}\right].\end{aligned} \quad (2.8)$$

For a Gaussian pulse (1.12), at large distances from the z-axis ($\rho \gg R$, c/ω_{pe}), the integral in (2.5) can be approximately evaluated by the saddle-point method. As a result, we obtain

$$\mathbf{p}(\omega, \mathbf{r}) = \frac{e^2}{8\pi\rho\omega}\frac{\omega_{pe}^4}{\omega_0^4}\left(\frac{W}{m_e c^2}\right)^2\frac{c^2}{\omega^2\varepsilon(\omega)}\int\frac{d\omega''d\mathbf{k}''}{(2\pi)^4} \times \frac{n(\omega'', \mathbf{k}'')}{\left|\varepsilon^l(\omega-\omega'', \boldsymbol{\chi})\right|^2}[\mathbf{k}'', \boldsymbol{\chi}]^2\left(\mathbf{e}_\rho + \mathbf{e}_Z\frac{k_\parallel}{q}\right) \times \exp\left(-\frac{(\omega-\omega'')^2\tau^2}{2} - \frac{\chi_\perp^2 R^2}{2}\right), \quad (2.9)$$

where $q^2 = \frac{\omega^2}{c^2}\varepsilon(\omega) - k_\parallel^2 > 0$, $\boldsymbol{\chi} = \boldsymbol{\chi}_\perp + \mathbf{e}_Z\frac{\omega-\omega''}{V_g}$, $\boldsymbol{\chi}_\perp = q\mathbf{e}_\rho - \mathbf{k}_\perp''$, $\tau = \frac{L}{V_g}$ is the laser pulse duration, and $\mathbf{e}_Z$, $\mathbf{e}_\rho$ is the radial unit vector.

Further analysis of the emission spectral density $\mathbf{p}(\omega, \mathbf{r})$ requires specifying the Fourier transform of the correlation function $n(\omega'', \mathbf{k}'')$ of the electron density fluctuations.

3. NONISOTHERMAL PLASMA. EMISSION NEAR THE PLASMA FREQUENCY

In a nonisothermal plasma, where the ion temperature T_i is not equal to the electron temperature T_e, the Fourier transform of the correlation function $n(\omega, \mathbf{k})$ has the form [10]

$$n(\omega, \mathbf{k}) = \frac{k^2}{2\pi e^2 N_{0e}^2\omega}\frac{T_e\left|1+\delta\varepsilon_i^l(\omega,k)\right|^2\mathrm{Im}\,\delta\varepsilon_e^l(\omega,k) + T_i\left|\delta\varepsilon_e^l(\omega,k)\right|^2\mathrm{Im}\,\delta\varepsilon_i^l(\omega,k)}{\left|\varepsilon^l(\omega,k)\right|^2}, \quad (3.1)$$

where $\delta\varepsilon_e^l(\omega, k)$ and $\delta\varepsilon_i^l(\omega, k)$ are the partial contributions from electrons and ions, respectively, to the longitudinal plasma permittivity.

Here, we will analyze electromagnetic emission with frequencies close to the plasma frequency. Therefore, we consider low-frequency fluctuations satisfying the inequalities $kV_{Ti} \ll \omega \ll kV_{Te}$ (the domain of existence of the ion sound), where $V_{Ti} = \sqrt{T_i/m_i}$ is the ion thermal velocity and m_i is the ion mass. We represent formula (3.1) in the form

$$n(\omega, \mathbf{k}) = \frac{F(\omega,k)}{N_{0e}}\frac{\gamma_S(\omega,k)}{\left(\frac{\omega^2-k^2V_S^2}{2\omega}\right)^2 + \gamma_S^2(\omega,k)}, \quad (3.2)$$

where $\gamma_S = 0.5\omega k^2 r_{De}^2\,\mathrm{Im}\,\varepsilon^l(\omega, k)$, $r_{De} = V_{Te}/\omega_{pe}$ is the electron Debye radius, $V_S = \sqrt{ZT_e/m_i}$ is the ion-acoustic velocity,

$$F(\omega, k) = \frac{\mathrm{Im}\left(\delta\varepsilon_e^l + \frac{T_i}{T_e}\delta\varepsilon_i^l\right)}{\mathrm{Im}(\delta\varepsilon_e^l + \delta\varepsilon_i^l)}, \quad (3.3)$$

$$\mathrm{Im}\,\delta\varepsilon_e^l(\omega, k) = \sqrt{\frac{\pi}{2}}\frac{\omega}{kV_{Te}(kr_{De})^2}, \quad (3.4)$$

$$\mathrm{Im}\,\delta\varepsilon_i^l(\omega, k) = \frac{\omega_{pi}^2}{\omega^2} \times\left\{\frac{8}{5}\frac{\nu_{ii}k^2V_{Ti}^2}{\omega^3} + \sqrt{\frac{\pi}{2}}\frac{\omega^3}{k^3V_{Ti}^3}\exp\left(-\frac{\omega^2}{2k^2V_{Ti}^2}\right)\right\}, \quad (3.5)$$

Here, $\nu_{ii} = \frac{4}{3}\frac{\sqrt{\pi}Z^3e^4N_{0e}}{m_i^{1/2}T_i^{3/2}}\Lambda$ is the ion–ion collision frequency and $\omega_{pi} = \sqrt{4\pi Ze^2N_{0e}/m_i}$ is the ion plasma frequency.

The interaction of the laser pulse with ion-acoustic fluctuations (3.2) gives rise to anisotropic emission (the emission intensity in the radial direction is higher than that in the axial direction by a factor of $(R/r_{De})^2$. According to (2.9), the emission spectral density is described by the expression

$$\mathbf{p}(\omega, \mathbf{r}) = \mathbf{e}_\rho\frac{e^2}{3\pi^2R^2\rho\omega_0}\frac{\omega_{pe}^2}{\omega_0^2} \times \frac{r_e}{R}\frac{c}{\omega_0 R}\left(\frac{W}{m_e c^2}\right)^2 I_S\left(\frac{\omega}{\omega_{pe}}\right), \quad (3.6)$$

where $r_e = e^2/m_e c^2$ is the classical radius of an electron. The dimensionless function $I_S(x)$ characterizes the spectral distribution of the emission intensity:

$$I_S(x) = x^3\sqrt{x^2-1}\exp\{(b-a)x^2\}\int_{x\sqrt{b}}^{\infty}dt\,t^3\exp(-t^2)F(t) \times\left\{\frac{1}{\left[\left(x+\frac{\alpha t}{\beta^2}\right)^2 - 1 - \frac{t^2}{\beta^2x^2}\right]^2 + \Gamma_S^2}\right. \quad (3.7)$$

$$+\frac{1}{\left[\left(x-\frac{\alpha t}{\beta^2}\right)^2-1-\frac{t^2}{\beta^2 x^2}\right]^2+\Gamma_S^2}\Bigg\}.$$

Here, $a = 0.5\omega_{pe}^2\tau^2$ and $b = 0.5k_p^2R^2$ are the parameters related to the longitudinal and transverse dimensions of the laser pulse; $\alpha = \frac{\sqrt{2}}{6}\frac{V_S R}{V_{Te}r_{De}}$ and $\beta^2 = \frac{R^2}{6r_{De}^2}$ are the parameters determining the ratios of the transverse pulse size to the characteristic plasma scales; $k_p = \frac{\omega_{pe}}{c}$ and $F(t) = F(\omega = \sqrt{2}\,V_S t/R,\ k = \sqrt{2}\,t/R) = \frac{1+(T_i/T_e)\psi(t)}{1+\psi(t)}$, where

$$\psi(t) = \sqrt{\frac{m_i}{Zm_e}}\left\{\frac{8}{5\sqrt{\pi}}\frac{\nu_{ii}}{V_S}\frac{R}{t}\frac{T_i}{ZT_e}+\left(\frac{ZT_e}{T_i}\right)^{3/2}\exp\left(-\frac{ZT_e}{2T_i}\right)\right\}.$$

The expression for Γ_S, which is governed by dissipation of both plasma and ion-acoustic waves, has the form

$$\Gamma_S(x,t) = \frac{\nu_{ei}}{\omega_{pe}x}+\frac{\sqrt{\pi}x^3R^3}{4t^3r_{De}^3}\exp\left(-\frac{x^2R^2}{4t^2r_{De}^2}\right)$$
$$+\frac{8}{5}\frac{\nu_{ii}}{\omega_{pe}}\frac{T_i}{ZT_e}x+\sqrt{\pi}xt\frac{V_S r_{De}}{V_{Te}R} \qquad (3.8)$$
$$\times\left[\sqrt{\frac{Zm_e}{m_i}}+\left(\frac{ZT_e}{T_i}\right)^{3/2}\exp\left(-\frac{ZT_e}{2T_i}\right)\right].$$

In order to simplify expressions (3.7) and (3.8), we assume that the inequalities $\ln\left[\frac{Zm_i}{m_e}\ln\left(\frac{Zm_i}{m_e}\right)\right] > \frac{ZT_e}{T_i} > 1$ are satisfied, the electron mean free path $\lambda_{ei} = V_{Te}/\nu_{ei}$ is less than $R\sqrt{m_i/Zm_e}\,(ZT_e/T_i)^{-3/2}\times\exp(ZT_e/2T_i)$ and $(c/\omega_{pe})\sqrt{m_i/Zm_e}\,(ZT_e/T_i)^{-3/2}\times\exp(ZT_e/2T_i)$, and the inequality $\ln\left(\frac{\omega_{pe}}{\nu_{ei}}\right) \ll \frac{R^2}{4r_{De}^2},\ \frac{1}{2(k_p r_{De})^2}$ is also fulfilled. Under these conditions, $F(t) \simeq T_i/T_e$ and the first term on the right-hand side of (3.8) plays a dominant role. As a result, expression (3.7) in the vicinity of the plasma frequency is simplified:

$$I_S(\omega) = I_+(\omega)+I_-(\omega)$$
$$= \beta^3\exp(b-a)\frac{T_i}{T_e}[J_+(\zeta)+J_-(\zeta)]. \qquad (3.9)$$

Here, $\zeta = 2\beta^2(x-1)$ and the functions $J_\pm(\zeta)$ are

$$J_\pm(\zeta) = \sqrt{\zeta}\int_{\sqrt{b}}^{\infty}du\frac{u^3\exp(-u^2)}{(u^2\pm 2\alpha u-\zeta)^2+\nu_S^2}, \qquad (3.10)$$

where $\nu_S = \beta^2\frac{\nu_{ei}}{\omega_{pe}}$. The plus and minus signs refer to anti-Stokes and Stokes emission lines, respectively. For sufficiently small ν_S, when the condition $\nu_S \ll \sqrt{b}\,|\sqrt{b}\pm 2\alpha|$ is fulfilled, the functions $J_+(\zeta)$ and $J_-(\zeta)$ have maxima in the regions $\zeta > \sqrt{b}\,(\sqrt{b}\pm 2\alpha)$, respectively, where they are described by the following approximate expressions:

$$J_\pm(\zeta) = \frac{(t\mp\alpha)^{7/2}(t\pm\alpha)^{1/2}\exp[-(t\mp\alpha)^2]}{2\nu_S t}$$
$$\times\left\{\frac{\pi}{2}+\arctan\left[\frac{t^2-(\sqrt{b}\pm\alpha)^2}{\nu_S}\right]\right\}, \qquad (3.11)$$

where $t = \sqrt{\zeta+\alpha^2}$. Near their maxima, functions (3.11) can be represented in an even simpler form. Equating the derivative of the functions $J_\pm(\zeta)$ to zero, we obtain equations from which we can determine the values of $t_\pm$ at which these functions are maximum:

$$\pi[t^2-(\sqrt{b}\pm\alpha)^2]^2[3t^2\pm 3\alpha t+\alpha^2$$
$$-2t(t\mp\alpha)(t^2-\alpha^2)]+2\nu_S t^2(t^2-\alpha^2) = 0. \qquad (3.12)$$

In the vicinities of the points $t_\pm$, the functions $J_\pm(\zeta)$ can be expanded in series. Then, taking into account (3.9), the functions $I_\pm(\omega)$ can be represented in the form

$$I_\pm(\omega) = I_{\pm\max}\left[1-\frac{(\omega-\omega_\pm)^2}{\Delta\omega_\pm^2}\right], \qquad (3.13)$$

where $I_{\pm\max}$ are the maximum values of the functions $I_\pm(\omega)$, $\omega_\pm$ are the frequencies at which the emission intensity is maximum, and $\Delta\omega_\pm$ are the widths of the corresponding spectral lines:

$$\Delta\omega_\pm = 3\omega_{pe}\frac{r_{De}^2}{R^2}\sqrt{\frac{-2J_{\pm\max}}{\left.\frac{d^2J_\pm}{d\zeta^2}\right|_{\zeta=\zeta_\pm}}}, \qquad (3.14)$$

where $\zeta_\pm = 2\beta^2\left(\frac{\omega_\pm}{\omega_{pe}}-1\right)$.

Based on these rather general considerations, we first examine the emission of a wide laser pulse whose transverse dimensions are much greater than c/ω_{pe} and

for which the inequality $b = 0.5k_p^2R^2 \gg 1$ is satisfied. In this case, it follows from (3.12) that

$$\omega_\pm = \omega_{pe}\left(1 + \frac{3}{2}k_p^2r_{De}^2\right) \pm k_pV_S. \quad (3.15)$$

These frequencies correspond to anti-Stokes (merging) and Stokes (decay) processes involving Langmuir and ion-acoustic waves with the wavenumber k_p. The maximum intensities and the corresponding line widths entering formula (3.13) are described by the expressions

$$I_{\pm\max} = \frac{\pi}{8}\frac{T_i}{T_e}\frac{\omega_{pe}}{\nu_{ei}}\left(\frac{R^2}{3r_{De}^2}\right)^{1/2}(k_pR)^3 \times \frac{\left(1 \pm \frac{2}{3}\frac{cV_S}{V_{Te}^2}\right)^{1/2}}{1 \pm \frac{1}{3}\frac{cV_S}{V_{Te}^2}}\exp\left(-\frac{\omega_{pe}^2\tau^2}{2}\right), \quad (3.16)$$

$$\Delta\omega_\pm = 3\omega_{pe}\left(\frac{r_{De}}{R}\right)^{3/2}\left(\frac{\nu_{ei}}{6\pi\omega_{pe}}\right)^{1/4}\left(1 \pm \frac{cV_S}{3V_{Te}^2}\right)^{3/4}. \quad (3.17)$$

For electron temperatures that are not too high, when the inequality

$$V_{Te}^2 < \frac{2}{3}cV_S \quad (3.18)$$

holds, there is only the anti-Stokes line with the frequency ω_+, width $\Delta\omega_+$, and intensity $I_{+\max}$ in the emission spectrum of the laser pulse. In this case, the Stokes line is absent because $\omega_- < \omega_{pe}$.

At higher electron temperatures, when the inequality opposite (3.18),

$$V_{Te}^2 > \frac{2}{3}cV_S, \quad (3.19)$$

is satisfied, both the anti-Stokes and Stokes lines with frequencies (3.15) can be present in the emission spectrum. However, these lines can be resolved only when the difference between their frequencies, $\omega_+ - \omega_- = 2k_pV_S$, is greater than their widths. This requirement leads to the inequality

$$1 > \frac{2}{3}\frac{cV_S}{V_{Te}^2} \gg \frac{c^2}{V_{Te}^2}\left(\frac{r_{De}}{R}\right)^{3/2}\left(\frac{\nu_{ei}}{\omega_{pe}}\right)^{1/4}. \quad (3.20)$$

Figure 1 shows the logarithm of the dimensionless spectral intensity of emission versus the dimensionless frequency calculated by formula (3.7) for helium plasma ($Z = 2$) with density $N_{0e} = 3.1 \times 10^{16}$ cm^{-3}, electron temperature $T_e = 100$ eV, electron-to-ion temperature ratio $T_e/T_i = 5$, and electron–ion collision frequency $\nu_{ei} = 1.8 \times 10^{-4}\ \omega_{pe}$. The parameters b and a were assumed to be 8 and 0.5, respectively. Two spectral maximums correspond to the Stokes and anti-Stokes lines.

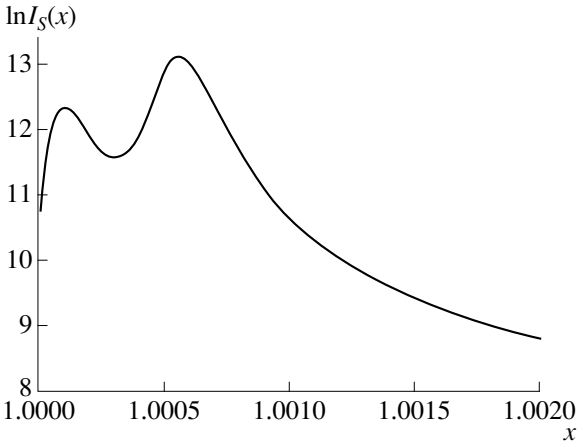

Fig. 1. Logarithm of the dimensionless spectral intensity of radiation emitted in the vicinity of the plasma frequency by a wide laser pulse ($b = 8$) in a relatively hot nonisothermal plasma ($\alpha = 0.14$). The remaining parameters are listed in the text.

When the inequality opposite (3.20) holds, the Stokes and anti-Stokes lines merge into one line, which is also described by expression (3.13) with a maximum intensity, frequency, and width equal to

$$I_{S\max} = I_{+\max} + I_{-\max} - \frac{I_{+\max}I_{-\max}(\omega_+ - \omega_-)^2}{I_{+\max}\Delta\omega_-^2 + I_{-\max}\Delta\omega_+^2}, \quad (3.21)$$

$$\omega_{\max} = \frac{I_{+\max}\omega_+\Delta\omega_-^2 + I_{-\max}\omega_-\Delta\omega_+^2}{I_{+\max}\Delta\omega_-^2 + I_{-\max}\Delta\omega_+^2}, \quad (3.22)$$

$$(\Delta\omega)^2 = \frac{I_{S\max}\Delta\omega_-^2\Delta\omega_+^2}{I_{+\max}\Delta\omega_-^2 + I_{-\max}\Delta\omega_+^2}, \quad (3.23)$$

respectively.

In a sufficiently hot plasma ($V_{Te}^2 \gg cV_S$), the intensity and width of the Stokes line are close to those of the anti-Stokes line: $I_{+\max} = I_{-\max} = I_1$ and $\Delta\omega_+ = \Delta\omega_- = \Delta\omega_1$. It follows from (3.21)–(3.23) that the emission intensity is maximum at the frequency $\omega_{\max} = \omega_{pe} \times \left(1 + \frac{3}{2}k_p^2r_{De}^2\right)$ and is proportional to $2I_1$, the line width being equal to $\Delta\omega_1$.

We turn now to the case of a narrow laser beam ($b = 0.5k_p^2R^2 \ll 1$) propagating in a relatively hot plasma ($\alpha \ll 1$). According to (3.12), in this case, the frequencies of the Stokes and anti-Stokes lines are equal to

$$\omega_\pm = \omega_{pe}\left(1 + \frac{9}{2}\frac{r_{De}^2}{R^2}\right) \pm \sqrt{3}\frac{V_S}{R}. \quad (3.24)$$

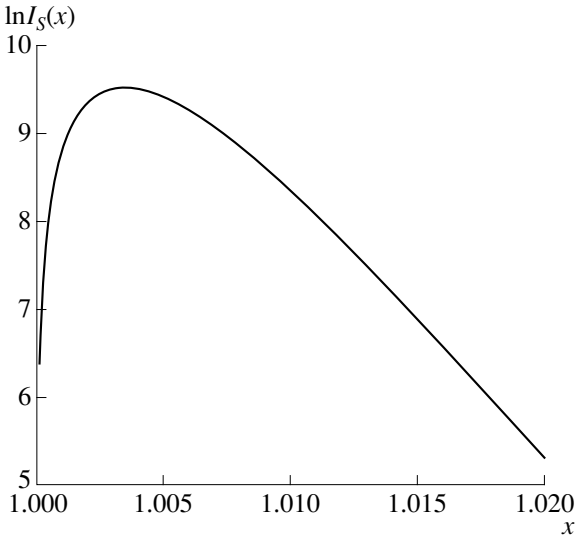

Fig. 2. Same as in Fig. 1 but for a narrow laser pulse (b = 0.125).

The intensities and widths are the same for both lines and are equal to

$$I_{\pm\max} = \frac{3\pi}{8}\frac{T_i}{T_e}\frac{\omega_{pe}}{\nu_{ei}}\frac{R}{r_{De}}\exp\left(-\frac{\omega_{pe}^2\tau^2}{2}-\frac{3}{2}\right),$$
$$\Delta\omega_{\pm} = 3\sqrt{3}\omega_{pe}\frac{r_{De}^2}{R^2}, \quad (3.25)$$

respectively. Although the frequencies of both the Stokes and anti-Stokes lines are higher than the plasma frequency, the distance between the lines is less than their widths. As a result, these lines merge into one whose intensity is the sum of the intensities of the Stokes and anti-Stokes lines.

Figure 2 shows the logarithm of the dimensionless spectral intensity of emission versus the dimensionless frequency calculated by formula (3.7) for the plasma with the same parameters as in Fig. 1 but for $b = 1/8$ and $a = 0.5$. It is seen that the spectrum has only one maximum.

The emission spectrum of a narrow laser pulse ($b \ll 1$) in a relatively cold plasma ($\alpha \gg 1$) has only the anti-Stokes line with the frequency

$$\omega_+ = \omega_{pe} + \sqrt{\frac{7}{2}}\frac{V_S}{R}. \quad (3.26)$$

The intensity and width of the line are

$$I_{+\max} = 0.86\frac{T_i}{T_e}\frac{\omega_{pe}}{\nu_{ei}}\left(\frac{V_{Te}}{V_S}\frac{R}{r_{De}}\right)^{1/2}\exp\left(-\frac{\omega_{pe}^2\tau^2}{2}\right),$$
$$\Delta\omega_+ = \frac{V_S}{R}, \quad (3.27)$$

respectively.

According to (3.9), at higher frequencies $\left(\frac{\omega-\omega_{pe}}{\omega_{pe}} \gg k_p^2 r_{De}^2, \left(\frac{r_{De}}{R}\right)^2, \frac{\nu_{ei}}{\omega_{pe}}\right)$, the spectral intensity is described by the expression

$$I_S(x) = \frac{x^3(1+bx^2)}{(x^2-1)^{3/2}}\exp(-ax^2). \quad (3.28)$$

If the length L of the pulse is greater than its transverse size R, then function (3.28) decreases monotonically as the frequency decreases to $\omega \simeq 2\omega_{pe}$, where the transformation of the wakefield into electromagnetic waves by thermal plasma waves becomes possible (see the next section). For a wide pulse ($R > L$), far away from the plasma frequency, there may be insignificant variations in the spectral intensity associated with the shape of the laser pulse.

It is also of interest to consider the energy emitted by the laser pulse over the unit length along the pulse trajectory:

$$\frac{dW_\perp}{dz} = 2\pi\rho\int_{\omega_{pe}}^{\infty} d\omega \mathbf{e}_\rho \mathbf{p}(\omega, \mathbf{r}). \quad (3.29)$$

According to formula (3.6), expression (3.29) can be rewritten in the form

$$\frac{dW_\perp}{dz} = \frac{2e^2}{3\pi R^2\omega_0}\frac{\omega_{pe}^2}{\omega_0^2}\frac{r_e}{R}\frac{c}{\omega_0 R}\left(\frac{W}{m_e c^2}\right)^2\int_{\omega_{pe}}^{\infty} d\omega I_S(\omega). \quad (3.30)$$

Note that the main contribution to the integral over frequency in (3.30) comes from a narrow region near the plasma frequency. Under the conditions listed before formula (3.9), this fact allows us to rewrite expression (3.30) in the form

$$\frac{dW_\perp}{dz} = \frac{e^2}{3R^2}\frac{\omega_{pe}^3}{\omega_0^3}\frac{r_e}{R}\frac{c}{\omega_0 R}\left(\frac{W}{m_e c^2}\right)^2\frac{T_i}{T_e}\frac{\omega_{pe}}{\nu_{ei}}\left(6\frac{r_{De}^2}{R^2}\right)^{1/2}$$
$$\times \exp(b-a)\int_{\sqrt{b}}^{\infty} dt t^3\exp(-t^2)\left(\sqrt{t^2+2\alpha t}+\sqrt{t^2-2\alpha t}\right).$$

For a narrow laser pulse ($k_p R < 1$) propagating in a relatively hot plasma ($V_{Te}^2 > cV_S$), the main contribution to the integral comes from the Stokes and anti-Stokes

lines. In this case, the energy of low-frequency radiation emitted by the pulse per unit length is

$$\frac{dW_\perp}{dz} = \frac{\sqrt{6\pi}e^2}{4R^2}\frac{\omega_{pe}^3}{\omega_0^3}\frac{r_e r_{De}}{R^2}\frac{c}{\omega_0 R} \times\left(\frac{W}{m_e c^2}\right)^2\frac{T_i}{T_e}\frac{\omega_{pe}}{\nu_{ei}}\exp\left(-\frac{\omega_{pe}^2\tau^2}{2}\right). \quad (3.31)$$

As an example, we consider a laser pulse propagating in a helium plasma. The laser frequency is $\omega_0 = 1.88\times10^{15}\ s^{-1}$, the pulse duration is $\tau = 100$ fs, the focal spot diameter is $2R = 30$ μm, and the pulse energy is $W = 1$ J. For these parameters, the main contribution to dissipation comes from the first term on the right-hand side in (3.8) ($\Gamma_S = (\nu_{ei}/\omega_{pe}) = 1.8\times10^{-4}$), the Debye radius is much less than the pulse radius ($r_{De}/R = 2.8\times10^{-2}$), and the electron mean free path is 0.23 cm. The dimensionless parameters introduced above are $\nu_S = \frac{R^2}{6r_{De}^2}\frac{\nu_{ei}}{\omega_{pe}} = 3.8\times10^{-2}$, $b = 0.125$, and $\alpha = 0.14$, so that the inequalities $1 > \sqrt{b} > 2\alpha$ hold. In this case, there is a single spectral line with the parameters determined by (3.25) in the vicinity of the plasma frequency; the total energy emitted by the pulse per unit length is $dW_\perp/dz \approx 10^{-4}$ erg/cm.

Note that expression (3.31) can be obtained accurate to a factor on the order of unity by summing the products of the maximum intensities of the Stokes and anti-Stokes lines with the corresponding line widths.

For a wide laser pulse ($k_pR > 1$), the calculation of the energy loss by formula (3.30) yields

$$\frac{dW_\perp}{dz} = \frac{e^2}{3R^2}\frac{\omega_{pe}^3}{\omega_0^3}\frac{r_e}{R}\frac{c}{\omega_0 R}\left(\frac{W}{m_e c^2}\right)^2 \times\frac{T_i}{T_e}\frac{\omega_{pe}}{\nu_{ei}}\left(6\frac{r_{De}^2}{R^2}\right)^{1/2}\left(\frac{k_p^2R^2}{2}\right)^{3/2}\exp\left(-\frac{\omega_{pe}^2\tau^2}{2}\right). \quad (3.32)$$

This loss is higher by a factor of $\left(\frac{r_{De}^2}{R^2}\frac{\nu_{ei}}{\omega_{pe}}\right)^{1/4}$ than the loss calculated taking into account only the Stokes and anti-Stokes lines by the approximate formulas (3.13) and (3.14). This difference is associated with the fact that the parabolic approximation (3.13) is only valid in the vicinities of the maximums, whereas the function $I_S(\omega)$ at $b \gg 1$ has a wide pedestal. In other words, not only the resonant density perturbations (for which the decay conditions are satisfied and which give rise to the Stokes and anti-Stokes lines) but also nonresonant perturbation contribute to the total emission power. Although the spectral intensity of the pedestal emission is relatively low, it is emitted in a rather wide frequency range, thus determining the total energy loss of a wide laser pulse.

4. EMISSION NEAR THE DOUBLED PLASMA FREQUENCY

Now, we consider fluctuations with higher frequencies: $\omega \gg kV_{Te}, kV_{Ti}$ (the domain of existence of Langmuir waves). In this case, spectral density (3.1) of the correlation function takes the form

$$n(\omega, \mathbf{k}) = \frac{k^2r_{De}^2}{N_{0e}}\frac{\gamma_L(\omega, k)}{\left[\frac{\omega^2-\omega_L^2(k)}{2\omega}\right]^2+\gamma_L^2(\omega, k)}, \quad (4.1)$$

where $\omega_L^2(k) = \omega_{pe}^2(1 + 3k^2r_{De}^2)$ and $\gamma_L(\omega, k) = 0.5\omega\mathrm{Im}\varepsilon^l(\omega, k)$ [with the imaginary part of the longitudinal permittivity determined by (1.12)].

From (2.9) and (4.1), we can find the spectral energy density of emission. For sufficiently narrow laser pulses $\left(b = \frac{1}{2}k_p^2R^2 \ll 1\right)$, it has a relatively simple form:

$$\mathbf{p}(\omega, \mathbf{r}) = \mathbf{e}_\rho\frac{e^2}{3\pi^2R^2\rho\omega_0}\frac{\omega_{pe}^2}{\omega_0^2}\frac{r_e}{R}\frac{c}{\omega_0 R}\left(\frac{W}{m_e c}\right)^2 I_L(x), \quad (4.2)$$

where

$$I_L(x) = \frac{\sqrt{x^2-1}}{3\beta^2x}\left\{\frac{(x+1)^4\exp[-a(x+1)^2]}{x^2(x+2)^2} + \frac{(x-1)^4\exp[-a(x-1)^2]}{2}\int_0^\infty\frac{dtt^2\exp(-t)}{\left[x(x-2)-\frac{2t}{\beta^2}\right]^2+\Gamma_L^2}\right\}. \quad (4.3)$$

Here, $x = \frac{\omega}{\omega_{pe}}$, $\beta^2 = \frac{R^2}{6r_{De}^2}$, and

$$\Gamma_L(t) = 2\frac{\nu_{ei}}{\omega_{pe}} + 3\sqrt{6\pi}\frac{\beta^{3/2}}{t^{3/2}}\exp\left(-\frac{3}{2}\frac{\beta^2}{t}\right).$$

Relationships (4.2) and (4.3) describe the electromagnetic emission that appears due to the transformation of the wakefield by thermal Langmuir fluctuations. Note that the intensity of emission in the radial direction is higher than that in the axial direction by a factor of b^{-1}.

Function (4.3) has a maximum near the frequency $2\omega_{pe}$, where it can be represented in the form

$$I_L(\eta) = \frac{\sqrt{3}}{48}\beta^2\exp(-a)\int_0^\infty \frac{dtt^2\exp(-t)}{(t-\eta)^2+\nu_L^2}, \quad (4.4)$$

where $\eta = \beta^2(x-2)$ and $\nu_L(t) = 0.5\beta^2\Gamma_L(t)$. At the frequency

$$\omega_{\max} = 2\omega_{pe}\left(1+6\frac{r_{De}^2}{R^2}\right), \quad (4.5)$$

the emission intensity described by (4.4) attains its maximum, approximately equal to

$$I_{L\max} = \frac{\sqrt{3}\pi}{6\nu_L(2)}\frac{R^2}{12r_{De}^2}\exp\left(-\frac{\omega_{pe}^2\tau^2}{2}-2\right). \quad (4.6)$$

At higher frequencies (i.e., at $x > 2$), function (4.4) decreases with increasing the frequency, and, under condition $|x-2| \gg \frac{\Gamma_L}{2}, \frac{1}{\beta^2}$ it takes the form

$$I_L(x) = 2\frac{r_{De}^2}{R^2}\frac{\sqrt{x^2-1}}{x^3}$$
$$\times\left\{\frac{(x+1)^4}{(x+2)^2}\exp[-a(x+1)^2]\right. \quad (4.7)$$
$$\left.+\frac{(x-1)^4}{(x-2)^2}\exp[-a(x-1)^2]\right\}.$$

The energy lost by the pulse due to the emission of radiation with frequencies close to $2\omega_{pe}$ can be calculated in the same way as was done above. As a result, for a narrow laser pulse, we obtain

$$\frac{dW_\perp}{dz} = \frac{e^2}{2\sqrt{3}R^2}\frac{\omega_{pe}^3}{\omega_0^3}\frac{r_e}{R}\frac{c}{\omega_0 R}\left(\frac{W}{m_e c^2}\right)^2$$
$$\times\frac{r_{De}^2}{R^2}\frac{\omega_{pe}}{\nu_{ei}}\exp\left(-\frac{\omega_{pe}^2\tau^2}{2}\right). \quad (4.8)$$

For a plasma and laser pulse with the above parameters, it follows from (4.8) that $dW_\perp/dz = 3.9\times10^{-6}$ erg/cm.

Note that, in a nonisothermal plasma, where the ion-acoustic waves are weakly damped, the maximum emission intensity near the plasma frequency is higher by a factor of R/r_{De} than the maximum emission intensity near the doubled plasma frequency.

5. LOW-FREQUENCY EMISSION OF A LASER PULSE IN A TURBULENT PLASMA

Usually, short laser pulses propagate in a nonequilibrium turbulent plasma, in which the level of density fluctuations is not expressed through the particle temperatures and is substantially higher than that determined by formula (3.1). With low-frequency plasma turbulence in mind, we will consider as an example the generation of low-frequency radiation by a laser pulse propagating in a plasma with stationary electron density fluctuations whose correlation function has the form

$$(\delta N_e^2)_{\mathbf{r}} = (\delta N_e^2)_0\exp\left(-\frac{r^2}{r_T^2}\right), \quad (5.1)$$

where the quantity r_T and $(\delta N_e^2)_0$ characterize the scale length and intensity of fluctuations. The Fourier transform of function (5.1) is

$$(\delta N_e^2)_{\omega,\mathbf{k}} = (2\pi)\delta(\omega)(\delta N_e^2)_0\pi^{3/2}r_T^3\exp\left(-\frac{k^2r_T^2}{4}\right). \quad (5.2)$$

We restrict ourselves to considering small scale fluctuations that satisfy the condition $r_T \ll k_p^{-1}$. According to (2.9) and (5.2), the spectral density of emission at large distances from the z-axis is determined by

$$\mathbf{p}(\omega,\mathbf{r}) = \mathbf{e}_\rho\frac{e^2}{3\sqrt{\pi}R_T^2\rho\omega_0}\frac{\omega_{pe}^2}{\omega_0^2}\frac{r_e}{R_T}\frac{c}{\omega_0 R_T}$$
$$\times\left(\frac{W}{m_e c^2}\right)^2\frac{(\delta N_e^2)_0}{N_{0e}^2}N_{0e}r_T^3 I_T(x), \quad (5.3)$$

where $R_T^2 = R^2 + (r_T^2/2)$ and the function $I_T(x)$ has the form

$$I_T(x) = x^3\sqrt{x^2-1}\exp[(b_T-a)x^2]$$
$$\times\int_{b_T x^2}^\infty \frac{dtt\exp(-t)}{\left(x^2-1-\frac{t}{\beta_T^2}\right)^2+\Gamma_T^2}. \quad (5.4)$$

Here, $b_T = \frac{1}{2}k_p^2R_T^2$, $\beta_T^2 = \frac{R_T^2}{6r_{De}^2}$, and

$$\Gamma_T(x,t) = \frac{\nu_{ei}}{\omega_{pe}x}+\frac{\sqrt{\pi}}{4}\frac{R_T^3x^3}{r_{De}^3t^{3/2}}\exp\left(-\frac{R_T^2x^2}{4r_{De}^2t}\right).$$

The emission intensity in the axial direction is higher than that in the radial direction by a factor of $(k_pr_T)^2$. The spectral intensity of emission is maximum in the

vicinity of the plasma frequency ($x \approx 1$), where expression (5.4) takes the form

$$I_T(x) = \sqrt{\zeta}\beta_T^3 \exp[(b_T - a)] \int_{b_T}^{\infty} \frac{dt t \exp(-t)}{(t-\zeta)^2 + \nu_T^2}, \quad (5.5)$$

where $\zeta = 2\beta_T^2(x-1)$ and $\nu_T(t) = \beta_T^2 \Gamma_T(x=1, t)$. It follows from (5.5) that the emission intensity vanishes at $\omega = \omega_{pe}$ ($x = 1$). This is explained by the fact that electromagnetic waves with a frequency equal to the plasma frequency cannot propagate in a plasma. At a higher frequency, under the condition $\nu_T \ll b_T$, there is a maximum in the emission spectrum. The position and magnitude of this maximum depend on the pulse width. For a sufficiently wide pulse ($k_p R \gg 1$), the maximum spectral intensity, which is attained at

$$\omega_{\max} = \omega_{pe}\left(1 + \frac{3}{2}k_p^2 r_{De}^2\right), \quad (5.6)$$

is equal to

$$I_{T,\max} = \frac{\pi}{\nu_T(b_T)}\left(\frac{k_p^2 R^4}{12 r_{De}^2}\right)^{3/2} \exp\left(-\frac{\omega_{pe}^2 \tau^2}{2}\right). \quad (5.7)$$

For a narrow pulse ($k_p R \ll 1$), the corresponding frequency and spectral intensity are

$$\omega_{\max} = \omega_{pe}\left(1 + \frac{9}{2}\frac{r_{De}^2}{R_T^2}\right), \quad (5.8)$$

$$I_{T,\max} = \frac{\pi}{\nu_T(3/2)}\left(\frac{R_T^2}{4 r_{De}^2}\right)^{3/2} \exp\left(-\frac{\omega_{pe}^2 \tau^2}{2} - \frac{3}{2}\right). \quad (5.9)$$

At higher frequencies, when the inequality $\frac{\omega - \omega_{pe}}{\omega_{pe}} \gg \frac{\Gamma_T}{2}, \frac{1}{2\beta_T^2}$ is satisfied, the function $I_T(x)$ has the form

$$I_T(x) = \frac{x^3(1 + b_T x^2)}{(x^2-1)^{3/2}} \exp(-a x^2). \quad (5.10)$$

If the pulse length is greater than its width ($L > R$), function (5.10) decreases monotonically with increasing its argument. In the opposite case ($L < R$), function (5.10) is nonmonotonic and has weakly marked maximums.

Figure 3 shows the logarithm of the dimensionless spectral intensity of emission versus the dimensionless frequency calculated by formula (5.4) for a narrow pulse ($k_{pe}^2 R^2 = 1/4$) propagating in a plasma with the electron Debye radius $r_{De} = 2.8 \times 10^{-2} R$ and effective collision frequency $\nu_{ei} = 1.8 \times 10^{-4} \omega_{pe}$; the pulse duration is $\tau = \omega_{pe}^{-1}$.

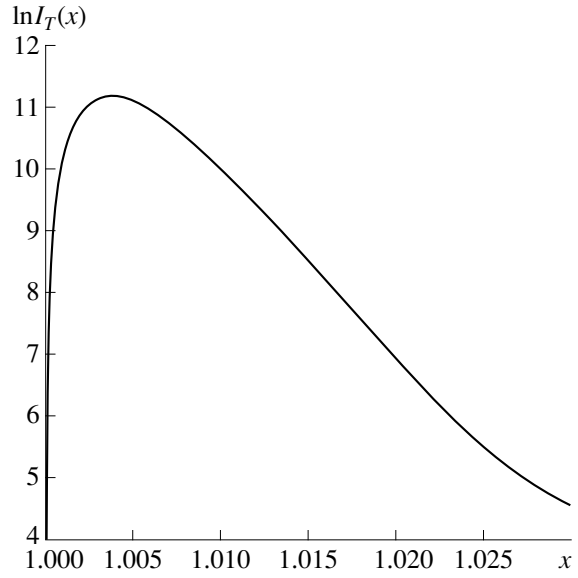

Fig. 3. Logarithm of the dimensionless spectral intensity of radiation emitted by a narrow ($b = 0.125$) and short ($L = k_p^{-1}$) laser pulse in a plasma with stationary electron density fluctuations for $(\delta N_e^2)_0/N_{0e}^2) = 0.01$, $r_T = 3 \times 10^{-4}$ cm, $r_{De} = 2.8 \times 10^{-2} R$, and $\nu_{ei} = 1.8 \times 10^{-4} \omega_{pe}$.

In conclusion, we estimate the energy of electromagnetic radiation emitted by the pulse per unit length, $dW_\perp/dz$. We integrate the spectral intensity over the frequency taking into account that the main contribution to the integral comes from frequencies close to the plasma frequency. As a result, for $k_p R \ll 1$ we obtain

$$\frac{dW_\perp}{dz} = \sqrt{\frac{3}{2}}\frac{\pi^2 e^2}{2R_T^2}\frac{\omega_{pe}^3}{\omega_0^3}\frac{r_e r_{De}}{R_T^2}\frac{c}{\omega_0 R_T}\left(\frac{W}{m_e c^2}\right)^2 \times \frac{(\delta N_e^2)_0}{N_{0e}} N_{0e} r_T^3 \frac{\omega_{pe}}{\nu_{ei}} \exp\left(-\frac{\omega_{pe}^2 \tau^2}{2}\right). \quad (5.11)$$

For estimates, we assume that the plasma and laser pulse have the same parameters as in previous sections. For $r_T = 3 \times 10^{-4}$ cm and $((\delta N_e^2)_0/N_{0e}^2) = 0.01$, from (5.11) we obtain $dW_\perp/dz = 5.2$ erg/cm. At such a low rate of energy loss, the total energy emitted by the pulse during its propagation through the plasma is small compared to the pulse energy; however, it is quite enough to be measured.

CONCLUSION

It is shown that a short laser pulse propagating in an underdense plasma with electron density fluctuations

can emit electromagnetic waves whose frequency is much lower than the frequency of laser radiation and is close to either the plasma frequency or the doubled plasma frequency. The mechanism for the generation of such an emission is related to the transformation of the excited wakefield by density fluctuations. This effect is usually treated using the planar wave approximation [10]. However, the wakefield excited by the pulse has a fairly complicated spatial structure strongly dependent on the ratio of the transverse pulse size to the wakefield wavelength $2\pi c/\omega_{pe}$. As a result, both the intensity and spectrum of the emitted radiation depend on the laser pulse parameters.

The estimates obtained in this paper refer to nonrelativistic laser intensities, when the electron oscillation velocity in the laser field is much less than the speed of light. The estimates show that the intensity of the emitted radiation is rather low. However, the emission energy is concentrated in narrow spectral intervals, which assists in measurements of this emission. It can be expected that the use of relativistically strong laser pulses (whose analysis, however, is beyond the range of applicability of the theory proposed) will allow one to significantly increase the intensity of low-frequency emission. In this case, additional lines at higher harmonics of the plasma frequency can also appear in the emission spectrum due to the nonlinearity of the excited wake wave.

The measurements of low-frequency electromagnetic radiation generated during the propagation of a short laser pulse in a plasma produced, e.g., in the interaction of another, longer laser pulse with a thin foil (see, e.g., [11, 12]) can open new possibilities for diagnosing both the wakefield and fluctuations by which the wakefield is transformed into electromagnetic radiation.

ACKNOWLEDGMENTS

This work was supported in part by the Russian Foundation for Basic Research, project nos. 97-02-16537 and 98-02-16263.

REFERENCES

1. L. M. Gorbunov and V. I. Kirsanov, Zh. Éksp. Teor. Fiz. **93**, 509 (1987) [Sov. Phys. JETP **66**, 290 (1987)].
2. E. Esarey, A. Ting, P. Sprangle, *et al.*, Appl. Phys. Lett. **53**, 2146 (1988).
3. J. R. Marques, J. P. Geindre, F. Amiranoff, *et al.*, Phys. Rev. Lett. **76**, 3566 (1996).
4. C. W. Siders, S. P. Leblanc, D. Fisher, *et al.*, Phys. Rev. Lett. **76**, 3570 (1996).
5. J. R. Marques, F. Dorchies, P. Audebert, *et al.*, Phys. Rev. Lett. **78**, 3463 (1997).
6. H. Hamster, A. Sullivan, S. Gordon, *et al.*, Phys. Rev. Lett. **71**, 2725 (1993).
7. L. M. Gorbunov and A. A. Frolov, Zh. Éksp. Teor. Fiz. **110**, 1757 (1996) [JETP **83**, 967 (1996)].
8. P. Mora and T. M. Antonsen, Jr., Phys. Plasmas **4**, 217 (1997).
9. A. F. Alexandrov, L. S. Bogdankevich, and A. A. Rukhadze, *Principles of Plasma Electrocdynamics* (Vysshaya Shkola, Moscow, 1978; Springer-Verlag, Berlin, 1984).
10. A. G. Sitenko, *Fluctuations and Non-Linear Wave Interactions in Plasmas* (Naukova Dumka, Kiev, 1977; Pergamon, Oxford, 1982).
11. G. Malka, J. Fuchs, F. Amiranoff, *et al.*, Phys. Rev. Lett. **79**, 2053 (1997).
12. M. Borghesi, A. J. Mackinnon, R. Gaillard, *et al.*, Phys. Rev. Lett. **80**, 5137 (1998).

Translated by A. Sakharov

Plasma Physics Reports, Vol. 26, No. 8, 2000, pp. 657–667. Translated from Fizika Plazmy, Vol. 26, No. 8, 2000, pp. 700–711.

NONLINEAR PHENOMENA

Spectra from Stimulated Raman Scattering of Short Relativistically Strong Laser Pulses in an Underdense Plasma

A. S. Sakharov

Institute of General Physics, Russian Academy of Sciences, ul. Vavilova 38, Moscow, 117942 Russia

Received December 23, 1999

Abstract—A set of equations describing large-angle stimulated Raman scattering (SRS) of a short, relativistically strong laser pulse propagating in an underdense plasma is derived and investigated numerically. It is shown that the SRS spectrum depends strongly on the pulse shape. If a pulse with a sharp leading edge excites a strongly nonlinear wake wave, the scattering occurs in relativistic electron flows and is accompanied by the Doppler frequency shift. When the electron flow is directed oppositely to the pulse propagation direction, the frequency upshift is maximum for the direct-backward SRS and decreases with decreasing scattering angle.

1. INTRODUCTION

For many years, the problem of stimulated Raman scattering (SRS) of high-power laser radiation in an underdense plasma ($\omega_{p0} \ll \omega_0$, where $\omega_{p0} = (4\pi e^2 n_0/m_e)^{1/2}$ is the electron plasma frequency and ω_0 is the laser frequency) has attracted much attention in connection with inertial confinement fusion research [1–6]. Recent interest in this problem has been motivated by the development of laser methods for charged-particle acceleration in a plasma [7–10]. Rapid progress in laser technology has resulted in creating lasers with an intensity of focused radiation higher than 10^{18} W/cm^2 [11–13]. In such a field, the oscillatory velocity of the plasma electrons is close to the speed of light. As a result, SRS acquires new features; in particular, backward and side scattering at the harmonics of the laser frequency starts to play an important role [14–17].

Due to the fairly strong focusing ($r_0 \sim 10$–100 μm) and extremely small duration of relativistically strong laser pulses ($\tau \sim 10^{-14}$–10^{-12} s), the instabilities of such pulses can be affected by finite pulse dimensions. Thus, for SRS at large angles, convective effects related to the withdrawal of perturbations from the region occupied by a pulse play an important role [18, 19]. If the duration of a relativistically strong pulse (or the duration of its leading edge) is comparable with or less than k_p^{-1} (where $k_p = \omega_{p0}/c$), the pulse excites a strongly nonlinear wake plasma wave [20] and the scattering occurs in an electron flow moving at the relativistic velocity. In this case, the backward SRS can be accompanied by a substantial change (upshift or downshift) of the frequency of the scattered radiation [21, 22].

Earlier, the effect of finite pulse duration on the SRS of relativistically strong laser pulses was examined only for cases of direct-forward [19, 23] or direct-backward [19, 21, 24] scattering. At the same time, from the point of view of diagnosing the processes occurring in the interaction of superintense laser radiation with plasmas, a study of the angular distribution of scattered radiation is of considerable interest [25].

The aim of this paper is to investigate (both analytically and numerically) the effect of a strongly nonlinear wake wave on the angular and frequency spectra from SRS of short relativistically strong laser pulses in an underdense plasma at the fundamental and higher harmonics. A set of equations describing the dynamics of the electron density perturbations and the amplitude of the scattered wave is derived and investigated numerically. It is shown that the excitation of a wake wave results in a strong frequency upshift of the radiation scattered into the backward hemisphere.

2. SRS IN A HOMOGENEOUS-AMPLITUDE PUMP WAVE

The problem of SRS spectra of a relativistically strong ($eE_0/m_e\omega_0 c \geq 1$), short ($\tau \sim \omega_{p0}^{-1}$) laser pulse exciting a strongly nonlinear wake wave can be substantially simplified if we assume that the characteristic temporal and spatial scales on which perturbations arising in the course of the SRS instability increase are much less than the temporal and spatial scales (ω_{p0}^{-1} and k_p^{-1}) on which the laser field amplitude and the parameters of the wake wave vary. Such an approximation seems to be justified for an underdense plasma with $\omega_{p0} \ll \omega_0$. In this case, the temporal and spatial growth rates of the SRS instability are on the order of $\Gamma \sim \omega_0^{1/3}\omega_{p0}^{2/3}$ [14–17]

1063-780X/00/2608-0657$20.00

and $K \sim \omega_0^{1/3}\omega_{p0}^{2/3}/c$ [21, 22], respectively. Therefore, for the parameter κ, characterizing the ratio between the above scales, we obtain $\kappa \sim (\omega_{p0}/\omega_0)^{1/3} \ll 1$.

Assuming the plasma to be highly underdense, we will consider the problem in the limit $\kappa \longrightarrow 0$. This limit corresponds to the locally homogeneous, quasi-steady approximation, in which the pump wave amplitude and the averaged (over high-frequency oscillations) density and hydrodynamic velocity of plasma electrons in the vicinity of a given point can be considered constant.

To analyze the linear stage of the instability associated with SRS of a homogeneous-amplitude pump wave in the presence of a homogeneous electron flow, we will use the results obtained in [17]. Let a relativistically strong, arbitrarily polarized electromagnetic wave propagate in a cold underdense plasma along the z-axis. The vector potential of the wave is described by

$$\mathbf{A}_0 \simeq \frac{1}{2}\frac{m_e c^2}{e}(a_0\mathbf{e}_\perp \exp(ik_0 z - i\omega_0 t) + \text{c.c.}), \qquad (1)$$

where ω_0, k_0, and a_0 are the frequency, wavenumber, and dimensionless pump wave amplitude, respectively (here, $\omega_0 \gg \omega_p = (4\pi e^2 \bar{n}_e/m_e)^{1/2}$, $k_0 \approx \omega_0/c$, and $\bar{n}_e$ is the plasma electron density averaged over high-frequency oscillations), and $\mathbf{e}_\perp = (\mathbf{e}_x + \mu\mathbf{e}_y)/\sqrt{1+|\mu|^2}$ is the unit polarization vector of the pump wave ($\mathbf{e}_\perp \cdot \mathbf{e}_\perp^* = 1$). In particular, the case $\mathrm{Im}\mu = 0$ corresponds to linear polarization and $\mu = \pm i$ corresponds to circular polarization.

Let the plasma electrons have a mean hydrodynamic velocity $\mathbf{V}$ = const. For definiteness, we assume that the vector $\mathbf{V}$ lies in the (x, z) plane. We pass over to the frame of reference in which the mean hydrodynamic velocity is equal to zero ($\mathbf{V}' = 0$; hereafter, the prime labels the quantities related to the frame associated with the electron flow). Let the z'-axis be directed along the vector $\mathbf{k}_0'$, the y'-axis coincide with the y-axis, and the x'-axis be perpendicular to the y'- and z'-axes. The amplitude of the vector potential of the pump wave and its polarization do not change when passing to the (x', y', z') coordinates: $a_0' = a_0$ and $\mathbf{e}_\perp' = (\mathbf{e}_x' + \mu\mathbf{e}_y')/\sqrt{1+|\mu|^2}$. The mean electron density in the frame of reference related to the electron flow is equal to $\bar{n}_e' = \bar{n}_e\sqrt{1-\beta^2}$, where $\beta = V/c$. Assuming that, in this frame, the plasma is also underdense ($\omega_0' \gg \omega_p'$), we have

$$k_0' \approx \omega_0'/c, \quad \omega_0' = \frac{\omega_0 - \mathbf{V}\mathbf{k}_0}{\sqrt{1-\beta^2}} \approx \omega_0\frac{1-\beta\cos\alpha}{\sqrt{1-\beta^2}},$$

where α is the angle between $\mathbf{V}$ and the z-axis. Thus, the vector potential of the pump wave in the new frame of reference is equal to

$$\mathbf{A}_0' \simeq \frac{1}{2}\frac{m_e c^2}{e}(a_0\mathbf{e}_\perp' \exp(ik_0' z' - i\omega_0' t') + \text{c.c.}). \qquad (1')$$

In the frame of reference related to the electron flow, the plasma is on average at rest ($\mathbf{V}' = 0$). Then, according to [17], the complex amplitude $\mathbf{a}_{s0}'$ of the vector potential of a daughter wave scattered at the Nth harmonic in the direction close to a given direction $\mathbf{e}_s'$ and the complex amplitude $\delta\tilde{N}_0'$ of the low-frequency (in Lagrangian coordinates related to an element of the electron fluid oscillating in the pump wave field) component of the relative perturbations of the electron density $\delta\tilde{N}' = \delta\tilde{n}_e'/n_e'$ arising in the course of the SRS instability are related by the expressions (note that the quantity $\delta\tilde{N}_0'$ does not change when passing over to the laboratory frame and, thus, is not further marked with a prime)

$$[\delta\omega' - c(\mathbf{e}_s' \cdot \delta\mathbf{k}')]\mathbf{a}_{s0}' = -\frac{\Omega_p'^2 a_0}{4N\omega_0'}[\mathbf{e}_s' \times [\mathbf{e}_s' \times \mathbf{F}_N'^*]]\delta\tilde{N}_0, \qquad (2)$$

$$(\delta\omega')^2\delta\tilde{N}_0 = \frac{2N^2\omega_0'^2 a_0}{\gamma_0^2}\sin^2(\theta'/2)(\mathbf{F}_N' \cdot \mathbf{a}_{s0}'). \qquad (3)$$

Here, $\delta\omega' = \omega_s' - N\omega_0'$, $\delta\mathbf{k}' = \mathbf{k}_s' - Nk_0'\mathbf{e}_s'$, ω_s' and $\mathbf{k}_s'$ are the frequency and the wave vector of the scattered radiation ($|\delta\omega'| \ll N\omega_0'$ and $|\delta\mathbf{k}'| \ll Nk_0'$), $\Omega_p'^2 = \omega_p'^2/\gamma_0$, $\gamma_0 = (1 + a_0^2/2)^{1/2}$, $\mathbf{e}_s' = (\sin\theta'\cos\varphi', \sin\theta'\sin\varphi', \cos\theta')$, θ' is the angle between $\mathbf{e}_s'$ and the propagation direction of the pump wave (the scattering angle), φ' is the angle between the x'-axis and the projection of the vector $\mathbf{e}_s'$ on the (x', y') plane (the azimuthal scattering angle),

$$\mathbf{F}_N'(\mathbf{e}_s') = \varepsilon_{N+1}\mathbf{e}_\perp' + \varepsilon_{N-1}\mathbf{e}_\perp'^* + \frac{a_0}{4\gamma_0}[\varepsilon_{N+2}(\mathbf{e}_\perp' \cdot \mathbf{e}_\perp')\mathbf{e}_\perp'^* + \varepsilon_{N-2}(\mathbf{e}_\perp'^* \cdot \mathbf{e}_\perp'^*)]\mathbf{e}_z', \qquad (4)$$

$$\varepsilon_N = \sum_m (-1)^m J_{N-2m}(\rho_\perp)J_m(\rho_\parallel)\exp[i\eta(2m-N) - im\delta], \qquad (5)$$

$$\rho_\perp = \frac{a_0}{\gamma_0}N|(\mathbf{e}_s' \cdot \mathbf{e}_\perp')|, \quad \rho_\parallel = \frac{a_0^2}{2\sqrt{2}\gamma_0^2}N\sin^2(\theta'/2)|(\mathbf{e}_\perp' \cdot \mathbf{e}_\perp')|, \qquad (6)$$

$$\eta = \arg(\mathbf{e}_s' \cdot \mathbf{e}_\perp'), \quad \delta = \arg(\mathbf{e}_\perp' \cdot \mathbf{e}_\perp'). \qquad (7)$$

We note that equations (2) and (3) correspond to the strong-coupling regime, when the growth rate of the instability is greater than Ω'_p and one can neglect the charge-separation field arising in the course of the SRS instability. From (2) and (3), we obtain the dispersion relation for the instability associated with SRS at the Nth harmonic [17]:

$$\{[\delta\omega' - c(\mathbf{e}'_s \cdot \delta\mathbf{k}')](\delta\omega')^2 - \Omega'^3_N\}\delta\tilde{N}_0 = 0, \quad (8)$$

where

$$\Omega'^3_N = \Omega'^2_p \omega'_0 \frac{Na_0^2}{2\gamma_0^2}\sin^2(\theta'/2)|[\mathbf{e}'_s \times \mathbf{F}'_N]|^2. \quad (9)$$

At a fixed scattering direction $\mathbf{e}'_s$, the maximum of the growth rate of the instability associated with SRS at the Nth harmonic corresponds to the zero detuning $\delta\mathbf{k}' = 0$ ($\omega'_s = N\omega'_0$) and is equal to $\Gamma'_N = (\sqrt{3}/2)\Omega'_N$. For $a_0 \ll 1$, $N = 1$, and $\mathbf{V} = 0$, we obtain from (8) the well-known nonrelativistic expression for the growth rate of the SRS instability in the strong-coupling regime ($\Gamma_1 = \Gamma'_1 \gg \omega_{p0}$) [6]:

$$\Gamma_1 = \frac{\sqrt{3}}{2}\left(\frac{\omega_{p0}^2 \omega_0 a_0^2}{2}\sin^2(\theta/2)|[\mathbf{e}_s \times \mathbf{e}_\perp]|^2\right)^{1/3}. \quad (10)$$

Since $\Omega'_N \longrightarrow 0$ (and, therefore, $\Gamma'_N \longrightarrow 0$) as $\theta' \longrightarrow 0$, the applicability condition of the strong-coupling approximation, $\Gamma'_N \gg \omega'_p$, means that dispersion relation (8) is valid at scattering angles that are not too small.

The dispersion relation for the SRS instability near a given direction $\mathbf{e}_s = (\sin\theta\cos\varphi, \sin\theta\sin\varphi, \cos\theta)$ in the laboratory frame can be obtained from (8) by means of relativistic transformations:

$$\delta\omega' = \frac{\delta\omega - (\mathbf{V}\cdot\delta\mathbf{k})}{\sqrt{1-\beta^2}},$$
$$2N\omega'_0[\delta\omega' - c(\mathbf{e}'_s \cdot \delta\mathbf{k}')] \approx (\omega'^2_s - c^2 k'^2_s) \quad (11)$$
$$= (\omega_s^2 - c^2 k_s^2) \approx 2\omega_N(\tilde{\theta})[\delta\omega - c(\mathbf{e}_s \cdot \delta\mathbf{k})],$$

where $\delta\omega = \omega_s - \omega_N(\tilde{\theta})$, $\delta\mathbf{k} = \mathbf{k}_s - k_N(\tilde{\theta})\mathbf{e}_s$, $k_N(\tilde{\theta}) = \omega_N(\tilde{\theta})/c$,

$$\omega_N(\tilde{\theta}) = \frac{1-\beta\cos\alpha}{1-\beta\cos\tilde{\theta}}N\omega_0, \quad (12)$$

$\tilde{\theta}$ is the angle between the scattering direction $\mathbf{e}_s$ in the laboratory frame and $\mathbf{V}$, and

$$\cos\tilde{\theta} = \cos\theta\cos\alpha + \sin\theta\cos\varphi\sin\alpha. \quad (13)$$

The angles θ' and φ' are related to θ and φ by the expressions

$$\theta' = \arccos(\cos\tilde{\theta}'\cos\alpha' - \sin\tilde{\theta}'\cos\tilde{\varphi}\sin\alpha'), \quad (14)$$

$$\varphi' = \arctan\left(\frac{\sin\tilde{\theta}'\sin\tilde{\varphi}}{\sin\tilde{\theta}'\cos\tilde{\varphi}\cos\alpha' + \cos\tilde{\theta}'\sin\alpha'}\right), \quad (15)$$

where

$$\cos\tilde{\theta}' = \frac{\cos\tilde{\theta}-\beta}{1-\beta\cos\tilde{\theta}}, \quad \cos\alpha' = \frac{\cos\alpha-\beta}{1-\beta\cos\alpha},$$
$$\tan\tilde{\varphi} = \frac{\sin\theta\sin\varphi}{\sin\theta\cos\varphi\cos\alpha - \cos\theta\sin\alpha}. \quad (16)$$

As a result, we obtain the dispersion relation in the laboratory frame:

$$\{[\delta\omega - c(\mathbf{e}_s \cdot \delta\mathbf{k})][\delta\omega - (\mathbf{V}\cdot\delta\mathbf{k})]^2 - \Omega_N^3\}\delta\tilde{N}_0 = 0, \quad (17)$$

where

$$\Omega_N^3 = (1-\beta^2)^{1/2}(1-\beta\cos\tilde{\theta})(1-\beta\cos\alpha) \times \omega_p^2\omega_0\frac{Na_0^2}{2\gamma_0^3}\sin^2(\theta'/2)|[\mathbf{e}'_s \times \mathbf{F}'_N(\mathbf{e}'_s)]|^2. \quad (18)$$

If the electron flow is aligned with the z-axis, i.e., directed along the wave vector of the pump wave ($\alpha = 0$) or oppositely to it ($\alpha = \pi$), expression (18) is somewhat simplified:

$$\Omega_N^3 = (1-\beta_z^2)^{3/2}\omega_p^2\omega_0\frac{Na_0^2}{2\gamma_0^3} \times \sin^2(\theta/2)|[\mathbf{e}'_s \times \mathbf{F}'_N(\mathbf{e}'_s)]|^2. \quad (18')$$

In this case, $\tilde{\theta} = \theta$, $\varphi' = \varphi$, $\cos\theta' = (\cos\theta - \beta_z)/(1 - \beta_z\cos\theta)$, and

$$\omega_N(\theta) = \frac{1-\beta_z}{1-\beta_z\cos\theta}N\omega_0. \quad (12')$$

The growth rate of the instability associated with SRS at the Nth harmonic is maximum at $\omega_s = \omega_N(\theta)$. Accordingly, at $\beta_z > 0$ the backward and side scattering is accompanied by a Doppler downshift (with respect to $N\omega_0$) and at $\beta_z < 0$ it is accompanied by a Doppler upshift. The frequency upshift is maximum for $\beta_z < 0$ and direct-backward scattering ($\theta = \pi$): $\omega_{N\max} = N\omega_0(1 + |\beta_z|)/(1 - |\beta_z|)$.

3. SRS OF A FINITE-SIZE PULSE

Let us consider a laser pulse with a finite duration τ propagating in an underdense plasma along the z-axis with the velocity $v_g \approx c$. We assume that the pulse shape

does not change in the course of propagation and the parameters of the pulse depend only on $\mathbf{r}_\perp$ and $\xi = z - ct$.

The instability associated with the backward and large-angle SRS ($\theta \sim 1$) is convective in character, because both the scattered radiation and the electron density perturbations arising in the course of the instability are carried backward with respect to the pulse. If we assume that the instability is seeded by short-wavelength ($k_e \sim k_0$) fluctuations of the electron density ahead of the pulse [8, 19, 21], then, in a time of about τ, a steady-state solution describing the growth of perturbations from the front of the pulse toward its trailing edge is established in the region occupied by the pulse.

Since, in this paper, we restrict ourselves to considering the linear stage of the instability, the seed electron-density perturbations contribute to the steady-state solution additively. Therefore, we will consider a solution arising from a single seed electron-density wave with a certain fixed wave vector $\mathbf{k}_e$. Assuming that the characteristic value of the instability growth rate is much greater than the plasma frequency, we can consider the seed perturbation to be time independent:

$$\delta N_e \approx \delta N_{e0} \exp(i\mathbf{k}_e\mathbf{r}). \tag{19}$$

The leading edge of a laser pulse propagating in an underdense plasma along the z-axis with the velocity $v_g \approx c$ undergoes the action of the seed electron-density wave at the frequency $\tilde{\omega} = -ck_{ez}$. The establishment of a steady-state solution means that, in the variables $\boldsymbol{\rho} \equiv (x, y, \xi)$ and t, all the perturbations inside the pulse depend on time as $\exp(-i\tilde{\omega}t)$.

We represent the field of the daughter wave scattered in the direction $\mathbf{e}_s$ in the form

$$\begin{aligned}\mathbf{a}_s &= \mathbf{a}_{s0}(\mathbf{r}, t)\exp(-i\omega_s t + i\mathbf{k}_s\mathbf{r}) \\ &= \mathbf{a}_{s0}(\boldsymbol{\rho})\exp(-i\tilde{\omega}t + i\mathbf{k}_s\boldsymbol{\rho}),\end{aligned} \tag{20}$$

where $\mathbf{a}_{s0}$ is the complex amplitude and $\mathbf{k}_s = \mathbf{e}_s\omega_s/c$ is the wave vector of the scattered wave, which satisfies the relationship $\mathbf{k}_s = \mathbf{e}_z k_s + \mathbf{k}_e$ (see Fig. 1). The latter means that the frequency of the scattered wave ω_s and scattering angle θ are related by the expressions

$$\omega_s(1 - \cos\theta) = -ck_{ez} = \tilde{\omega}, \quad \omega_s \sin\theta = ck_{e\perp}. \tag{21}$$

If the parameters of the pulse vary slowly on the characteristic length on which perturbations increase (which corresponds to the most interesting case of strong amplification of initial perturbations), the local variations of perturbations can be described with the help of Eq. (17), which we transform into a differential equation for $\delta\tilde{N}_0(\boldsymbol{\rho})$.

We represent $\delta\omega$ and $\delta\mathbf{k}$ in the vicinity of $\delta\omega_0 \equiv \omega_s - \omega_N(\tilde{\theta})$ and $\delta\mathbf{k}_0 \equiv \mathbf{k}_s - k_N(\tilde{\theta})\mathbf{e}_s$ in the form

$$\delta\omega \longrightarrow \delta\omega_0 + i\partial/\partial t, \quad \delta\mathbf{k} \longrightarrow \delta\mathbf{k}_0 - i\nabla.$$

Then, taking into account that $\partial\delta\tilde{N}_0(\boldsymbol{\rho})/\partial t = -c\partial\delta\tilde{N}_0(\boldsymbol{\rho})/\partial\xi$ and assuming that the parameters of the pulse and the excited wake wave vary slightly on the characteristic length on which perturbations increase ($\kappa \sim k_p|\partial \ln \delta\tilde{N}_0(\boldsymbol{\rho})/\partial\xi|^{-1} \ll 1$), we obtain from (17) the equation for $\delta\tilde{N}_0(\boldsymbol{\rho})$:

$$\begin{aligned}\left[\left(\frac{\partial}{\partial\xi} - \frac{(\mathbf{e}_s\cdot\nabla_\perp)}{1-\cos\theta}\right)\left(\frac{\partial}{\partial\xi} - \frac{(\mathbf{V}\cdot\nabla_\perp)}{c(1-\beta\cos\alpha)} + iq\right)^2\right. \\ \left. + iQ_N^3\right]\delta\tilde{N}_0 = 0,\end{aligned} \tag{22}$$

where $\beta(\boldsymbol{\rho})$, $\alpha(\boldsymbol{\rho})$, $\mathbf{V}(\boldsymbol{\rho})$,

$$\begin{aligned}q(\boldsymbol{\rho}) &= \left(\frac{\omega_s}{\omega_N(\tilde{\theta})} - 1\right)Nk_0, \\ Q_N^3(\boldsymbol{\rho}) &= \frac{\Omega_N^3(\mathbf{e}_s)}{c^3(1-\beta\cos\alpha)^2(1-\cos\theta)}\end{aligned} \tag{23}$$

are slowly varying (on a scale of k_p^{-1}) coefficients. The boundary conditions ahead of the pulse are

$$\delta\tilde{N}_0(\xi \longrightarrow \infty) = \delta N_{e0}\exp(-iq_0\xi), \tag{24}$$

where $q_0 = q(\xi \longrightarrow \infty) = k_s - Nk_0$.

Similarly, from (3) we obtain the equation for the evolution of $\mathbf{a}_{s0}(\rho)$:

$$\begin{aligned}&\left(\frac{\partial}{\partial\xi} - \frac{(\mathbf{e}_s\cdot\nabla_\perp)}{1-\cos\theta}\right)\mathbf{a}_{s0} \\ &= -\frac{i\omega_p^2(1-\beta^2)^{1/2}}{4c\omega_N(\tilde{\theta})(1-\cos\theta)}\frac{a_0}{\gamma_0}(R_\sigma\mathbf{e}_\sigma + R_\tau\mathbf{e}_\tau)\delta\tilde{N}_0,\end{aligned} \tag{25}$$

where

$$\begin{aligned}\mathbf{e}_\sigma &= [\mathbf{e}_s\times\mathbf{e}_V]/|[\mathbf{e}_s\times\mathbf{e}_V]|, \quad \mathbf{e}_\tau = [\mathbf{e}_s\times\mathbf{e}_\sigma], \\ R_\sigma &= ([\mathbf{e}'_s\times[\mathbf{e}'_s\times\mathbf{F}'^*_N]]\mathbf{e}'_\sigma) \equiv -(\mathbf{e}'_\sigma\cdot\mathbf{F}'^*_N), \\ R_\tau &= ([\mathbf{e}'_s\times[\mathbf{e}'_s\times\mathbf{F}'^*_N]]\mathbf{e}'_\tau) \equiv -(\mathbf{e}'_\tau\cdot\mathbf{F}'^*_N), \\ \mathbf{e}'_\sigma &= [\mathbf{e}'_s\times\mathbf{e}'_V]/|[\mathbf{e}'_s\times\mathbf{e}'_V]|, \quad \mathbf{e}'_\tau = [\mathbf{e}'_s\times\mathbf{e}'_\sigma], \\ \mathbf{e}_V &= \mathbf{V}/V, \quad \mathbf{e}'_V = (\sin\alpha', 0, \cos\alpha'), \\ \cos\alpha' &= \frac{\cos\alpha - \beta}{1-\beta\cos\alpha}.\end{aligned} \tag{26}$$

It follows from (25) that, behind the pulse, where $a_0 \longrightarrow 0$, the amplitude of the scattered wave is constant along the straight lines

$$\xi + \frac{(\mathbf{k}_{s\perp}\mathbf{r}_\perp)}{k_{s\perp}}\tan\frac{\theta}{2} = \text{const}. \tag{27}$$

Note that, strictly speaking, Eqs. (22) and (25) are applicable at $|\omega_s - \omega_N| \ll \omega_N$, i.e., in the resonant regions, where the detuning $q(\boldsymbol{\rho})$ is small ($|q| \ll Nk_0$) and the spatial growth rate of the instability associated with SRS at the Nth harmonic attains its maximum. It is these regions that make the main contribution to the SRS spectrum. Since the contribution from nonresonant regions is relatively small, we will use equations (22) and (25) in the entire range of q values when calculating the SRS spectrum.

To find the power P_N lost by the pulse due to SRS at the Nth harmonic, it is necessary to solve Eqs. (22) and (25) for $\delta\tilde{N}_0$ and $\mathbf{a}_{s0}$ and then integrate the square of the amplitude of the electric field of the scattered wave ($\mathbf{E}_{s0} = i(mc\omega_s/e)\mathbf{a}_{s0}$) over the plane $\xi = \xi_0 = \text{const}$ behind the laser pulse. Taking into account that $a_{s0} \propto \delta N_{e0}$, for P_N we obtain

$$P_N = G_N \frac{m_e^2 c^3 \omega_s^2}{8\pi e^2}(1 - \cos\theta)|\delta N_{e0}|^2, \tag{28}$$

where the proportionality factor G_N for the case of SRS at the Nth harmonic is equal to

$$G_N \equiv \int\limits_{\xi = \xi_0} \frac{|a_{s0}|^2}{|\delta N_{e0}|^2} dS. \tag{29}$$

Knowing the radiation power scattered at each harmonic for individual seed waves, we can express the spectral density of scattered radiation $P_\mathbf{k}$ through the spectral density of seed electron-density waves $\langle \delta N_{e0}^2 \rangle_{\mathbf{k}_e}$ ahead of the pulse:

$$P_\mathbf{k} = \frac{m_e^2 c^3 \omega_s^2}{8\pi e^2}(1 - \cos\theta)^2 \times (\langle \delta N_{e0}^2 \rangle_{\mathbf{k}_e} + \langle \delta N_{e0}^2 \rangle_{-\mathbf{k}_e}) G(\mathbf{k}), \tag{30}$$

where $\mathbf{k}_e = \mathbf{k} - \mathbf{e}_z k$, $k_e = 2\sin(\theta/2)k$, and $G(\mathbf{k}) = \sum_N G_N(\mathbf{k})$. (Note that, in the presence of relativistic electron flows in the region occupied by the pulse, the spectra of SRS at different harmonics can broaden or even overlap.) When deducing (30), we took into account that the ratio of the elementary phase volume of seed waves to that of scattered radiation is equal to $|d\mathbf{k}_e/d\mathbf{k}| = 1 - \cos\theta = 2\cos^2\theta_e$ and that, within the model at hand [i.e., neglecting the time dependence of the initial electron-density perturbations; see (19)], the seed perturbations with oppositely directed wave vectors ($\mathbf{k}_e$ and $-\mathbf{k}_e$) give the same contributions to the SRS spectrum.

Note that, when the growth rate of the SRS instability is much greater than the electron plasma frequency ($\Omega_N \gg \omega_p$), not only the oscillation at the frequencies close to ω_{p0} but all of the fluctuations in the frequency range $\omega_e \leq \Omega_N$ contribute to the scattering. Therefore, as

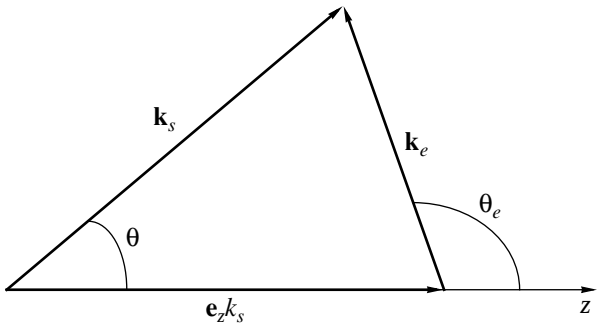

Fig. 1. Relation between the wave vector of a seed perturbation of the electron density $\mathbf{k}_e$ and the wave vector of scattered radiation $\mathbf{k}_s$.

$\langle \delta N_{e0}^2 \rangle_{\mathbf{k}_e}$, we must use the frequency-integrated spectral distribution of electron-density fluctuations, which, according to [26], is equal to

$$\langle \delta N_{e0}^2 \rangle_{\mathbf{k}_e} = \frac{1}{(2\pi)^3 n_0} \frac{1 + k_e^2 r_{De}^2}{2 + k_e^2 r_{De}^2}, \tag{31}$$

where r_{De} is the electron Debye radius. Accordingly, from (30) we obtain

$$P_\mathbf{k} = \frac{1}{(2\pi)^3} \frac{m_e c^3 \omega_s^2}{\omega_{p0}^2}(1 - \cos\theta)^2 \frac{1 + k_e^2 r_{De}^2}{2 + k_e^2 r_{De}^2} G(\mathbf{k}). \tag{32}$$

The spectral intensity (per unit solid angle) S_k of radiation scattered in a given direction is equal to

$$S_k \equiv \frac{dI_k}{d\Omega} = k^2 P_\mathbf{k} = \frac{1}{(2\pi)^3} \frac{m_e c \omega_s^4}{\omega_{p0}^2}(1 - \cos\theta)^2 \frac{1 + k_e^2 r_{De}^2}{2 + k_e^2 r_{De}^2} G(\mathbf{k}). \tag{33}$$

4. SRS OF A WIDE PULSE

The problem can be significantly simplified in the case of an ultrashort pulse whose transverse size r_0 is much greater than its longitudinal size $L = c\tau$ ($r_0 \gg L$). In this case, the electron flow excited by the pulse is almost parallel to the z-axis ($\mathbf{V} \approx V_z \mathbf{e}_z$) and the electron flow velocity V_z and the electron density $\bar{n}_e$ averaged over high-frequency oscillations are described by a set of quasi-one-dimensional equations [20]:

$$V_z = c\left(1 - \frac{n_0}{\bar{n}_e}\right),$$
$$\frac{\bar{n}_e}{n_0} - 1 = \frac{1}{2}\left(\frac{1 + a_0^2/2}{(1 + e\bar{\Phi}/m_e c^2)^2} - 1\right), \tag{34}$$
$$\frac{\partial^2 \bar{\Phi}}{\partial \xi^2} = 4\pi e(\bar{n}_e - n_0),$$

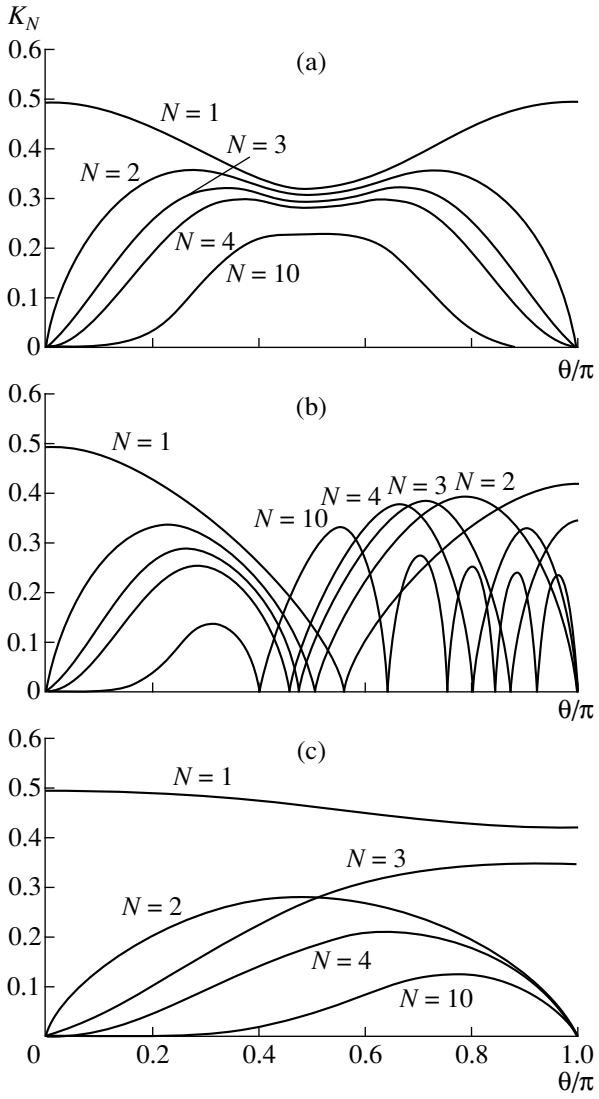

Fig. 2. The maximum spatial growth rate K_N (normalized to $k_p^{2/3}k_0^{1/3}$) of the instability associated with SRS at the fundamental and higher harmonics (N = 1, 2, 3, 4, and 10) as a function of the scattering angle at $a_0 = 2.5$ and $\beta_z = 0$ for (a) circular and (b, c) linear polarization of laser radiation at φ = (b) 0 and (c) $\pi/2$.

where $\bar{\Phi}$ is the electric potential averaged over the laser-field period. Moreover, for scattering angles that are not too small ($\theta \gg L/r_0$), we can neglect the term with $(\mathbf{e}_s \cdot \nabla_\perp)$ in (22) and (25). Accordingly, Eqs. (22) and (25) reduce to equations

$$\left[\frac{\partial}{\partial\xi}\left(\frac{\partial}{\partial\xi} + iq\right)^2 + iQ_N^3\right]\delta\tilde{N}_0 = 0, \tag{22'}$$

$$\frac{\partial}{\partial\xi}\mathbf{a}_{s0} = -\frac{i\omega_p^2(1-\beta^2)^{1/2}}{4c\omega_N(\theta)(1-\cos\theta)}\frac{a_0}{\gamma_0}(R_\sigma\mathbf{e}_\sigma + R_\tau\mathbf{e}_\tau)\delta\tilde{N}_0, \tag{25'}$$

whose solutions depend parametrically on $\mathbf{r}_\perp$. Here,

$$q = \frac{1-\beta_z\cos\theta}{1-\beta_z}k_s - Nk_0 = q_0 + \frac{2\beta_z}{1-\beta_z}\sin^2(\theta/2), \tag{35}$$

$$Q_N^3 = \frac{\Omega_N^3(\mathbf{e}_s)}{c^3(1-\beta_z)^2(1-\cos\theta)} = \frac{Na_0^2}{4\gamma_0^3}k_p^2k_0\left(\frac{1+\beta_z}{1-\beta_z}\right)^{3/2}|[\mathbf{e}_s' \times \mathbf{F}_N'(\mathbf{e}_s')]|^2. \tag{36}$$

For a circularly polarized laser pulse and direct-backward scattering ($\mathbf{e}_s = -\mathbf{e}_z$), Eqs. (22') and (25') pass over (accurate to terms on the order of $k_p|\partial\ln\delta\tilde{N}_0/\partial\xi|^{-1} \ll 1$) to the equations obtained in [21] (note that, in this case, $Q_{N>1} = 0$; i.e., the scattering occurs only at the first harmonic).

Figure 2 shows the angular dependences of the maximum spatial growth rate $K_N \equiv |\partial\ln|\delta\tilde{N}_0|/\partial\xi|_{q=0} = (\sqrt{3}/2)Q_N$ for $\beta_z = 0$, $a_0 = 2.5$, and (Fig. 2a) circular and (Figs. 2b, 2c) linear polarization of the pump wave at N = 1, 2, 3, 4, and 10. Figures 2b and 2c correspond to the scattering in the plane of polarization ($\varphi = 0$) and in the plane perpendicular to the plane of polarization of the pump wave ($\varphi = \pi/2$), respectively.

We emphasize that, in contrast to the temporal growth rate of the SRS instability, the spatial growth rate K_1 of the instability associated with SRS at the first harmonic is finite at small scattering angles. This effect (earlier pointed out in [18]) is related to the fact that the velocity with which scattered radiation is carried away from the region occupied by the pulse depends on the scattering angle as $(1 - \cos\theta)c$. At $\theta = \pi$, the scattered radiation is carried away with a maximum velocity equal to $2c$. As θ decreases, the time during which the scattered radiation stays inside the pulse increases, which results in a relative increase in the spatial growth rate of the SRS instability at small scattering angles.

It follows from (22') that, if β_z varies inside the pulse, then, at a given $\mathbf{r}_\perp$, the perturbations grow most rapidly in the vicinity of the resonance point $q(\xi_r) = 0$, where the frequency of scattered radiation ω_s coincides with the local value of the frequency ω_N: $\omega_s = N\omega_0(1 - \beta_z(\xi_r))/(1 - \beta_z(\xi_r)\cos\theta)$. Farther from the resonance point, the spatial growth rate of perturbations falls off. Apparently, perturbations for which the resonance point lies near the extreme of q ($\partial q/\partial\xi = 0$ at $\xi = \xi_r$) undergo the maximum amplification. Note that, at small scattering angles, the detuning q depends slightly on β_z [see (35)]; i.e., at small θ, the perturbations with $q_0 = k_s - Nk_0 = 0$ remain resonant throughout the entire pulse even in the presence of a fast electron flow inside the pulse.

5. NUMERICAL RESULTS

Equations (22') and (25') were used to compute the spectra from SRS of relativistically strong pulses. The pulse shape was specified as

$$a_0^2(\xi, r) = a_{\max}^2 \exp(r^2/r_0^2) f(\xi), \quad (37)$$

where

$$f(\xi) = \begin{cases} \frac{1}{2}\left[1 - \sin\left(\frac{\pi\xi}{2L_1}\right)\right] & \text{for } -L_1 < \xi < L_1, \\ 1 \text{ for } -L + L_2 < \xi < -L_1, & \\ \frac{1}{2}\left[1 + \sin\left(\frac{\pi(\xi + L)}{2L_2}\right)\right] & \text{for } -L - L_2 < \xi < -L + L_2 \end{cases} \quad (38)$$

and $f(\xi) = 0$ for $\xi > 0$ and $\xi < -L - L_2$. Here, L is the effective longitudinal size of the pulse ($\int a_0^2(\xi, 0)d\xi = a_{\max}^2 L$) and L_1 and L_2 are the lengths of the leading and trailing edges, respectively.

The calculations were performed for the following parameters of the pulse and the plasma: $\lambda_0 = 1$ μm, $a_{\max} = 2.5$ ($I_{\max} \approx 0.85 \times 10^{19}$ W/cm^2), $r_0 = 60$ μm ($P_{\max} \approx 10^{15}$ W), $\omega_0/\omega_{p0} = 10$ ($n_0 \approx 10^{19}$ cm^{-3}), $T = 10$ eV ($r_{De} \approx 0.7 \times 10^{-6}$ cm). Below, we present the results of calculations for two typical longitudinal profiles $f(\xi)$.

In the first case, the longitudinal size of the pulse is $L = 5k_p^{-1} \approx 8$ μm (the pulse duration is $\tau \approx 26$ fs). The pulse has a smooth leading edge ($L_1 = 4.9k_p^{-1}$) and a sharp trailing edge ($L_2 = 0.1k_p^{-1}$). In this case, the velocity of the electron flow inside the pulse is relatively low ($|\beta_z| \le 0.1$) (see Fig. 3a) and the scattering occurs almost as in an immobile plasma.

In the second case, $L = 7k_p^{-1} \approx 11$ μm (the pulse duration is $\tau \approx 37$ fs), $L_1 = 0.5k_p^{-1}$ and $L_2 = 1.5k_p^{-1}$. In this case (Fig. 3b), the leading edge of the pulse excites a strong electron-density wave ($|\beta|_{\max} \approx 0.6$).

Figure 4 shows the angular distributions of the spectral intensity S_k of scattered radiation for the pulses with the above parameters in the case of circular polarization. Figure 4a corresponds to the pulse with a smooth leading and sharp trailing edge, and Fig. 4b corresponds to the pulse with a sharp leading edge exciting a strongly nonlinear plasma wave. Figures 5 and 6 show similar distributions in the case of linear polarization for $\varphi = 0$ (Fig. 5) and $\varphi = \pi/2$ (Fig. 6). The spectra are cut off at $\theta < 0.1\pi$ because the model used is inapplicable at small scattering angles. It is seen that, when the longitudinal electron velocity inside the pulse is relatively low (Figs. 4a, 5a, 6a), the structure of the spectrum generally correlates with the angular dependence

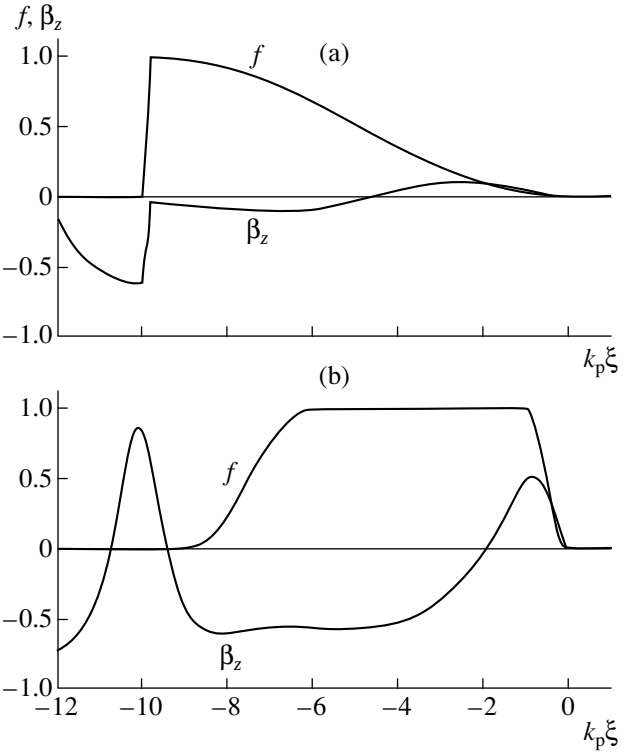

Fig. 3. The longitudinal profile $f(\xi)$ of the laser pulse intensity and the velocity of the electron flow $\beta_z = V_z/c$ on an axis of the pulse at $a_{\max} = 2.5$ and $\omega_0/\omega_{p0} = 10$ for (a) $L = 5k_p^{-1}$, $L_1 = 4.9k_p^{-1}$, and $L_2 = 0.1k_p^{-1}$ and (b) $L = 7k_p^{-1}$, $L_1 = 0.5k_p^{-1}$, and $L_2 = 1.5k_p^{-1}$.

of the spatial growth rate of the SRS instability in an immobile plasma at $a_0 = a_{\max} = 2.5$ (see Fig. 2).

In the case of a pulse with a sharp leading edge exciting a strongly nonlinear wake wave (Figs. 4b, 5b, 6b), the spectra of scattered radiation are substantially modified. In this case, in the main part of the pulse, the velocity of the electron flow is negative; as a result, the backward and side scattering is accompanied by a strong frequency upshift. In particular, in the case of circular polarization, a local maximum of the spectral intensity of backscattered radiation appears in the range $k \approx (3–4)k_0$, which corresponds to the Doppler shift of radiation scattered at the first harmonic ($k \approx k_0(1 - \beta_z)/(1 + \beta_z)$) in the presence of an electron flow with $|\beta_z|_{\max} \approx 0.6$ (Fig. 7a). Note that the absolute maximum of the spectral intensity of backscattered radiation nevertheless corresponds to frequencies close to ω_0. Numerical results show that the main contribution to this maximum comes from the peripheral part of the pulse ($r \ge 1.5r_0$), where the velocity of the excited electron flow is relatively low ($|\beta_z| \le 0.1$).

In the case of linear polarization, the effect of the frequency upshift of backscattered radiation is less pro-

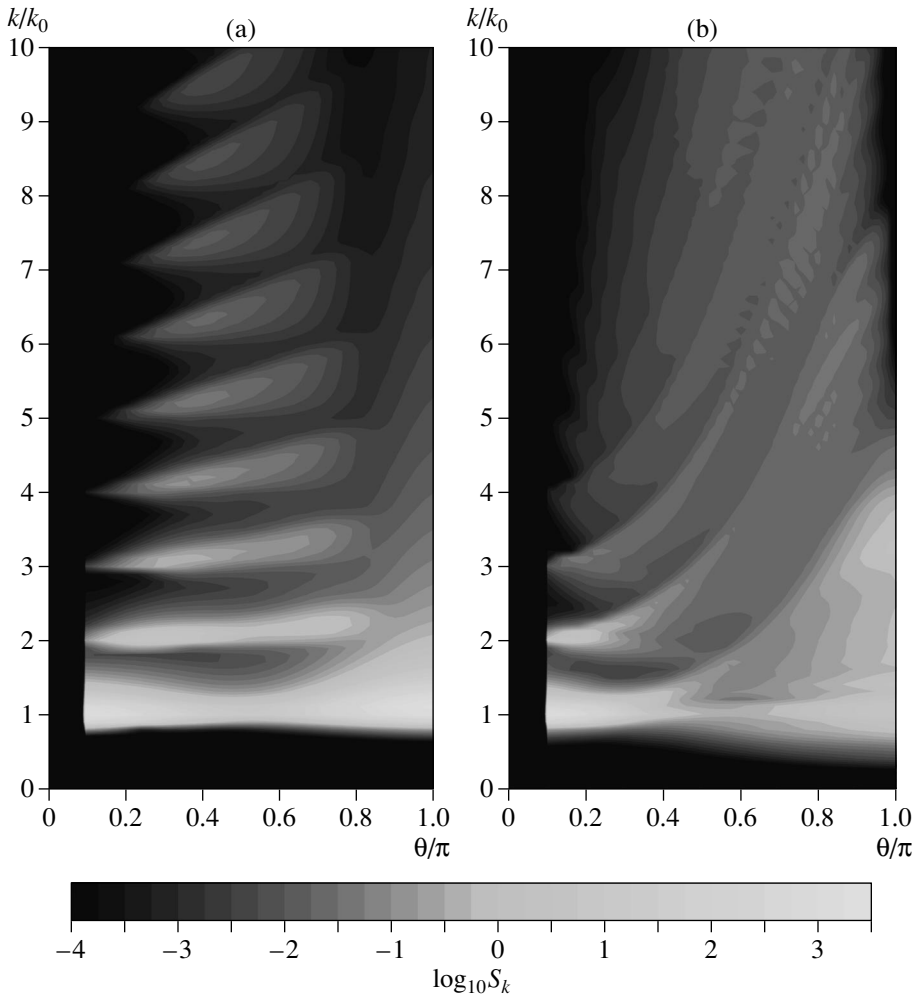

Fig. 4. Distribution of the spectral intensity S_k of scattered radiation (in units of W cm/sr) in the (θ, k) plane at $\lambda_0 = 1$ μm, $a_{max} = 2.5$, $r_0 = 60$ μm, $\omega_0/\omega_{p0} = 10$, and $T = 10$ eV for (a) a pulse with a smooth leading edge ($L = 5k_p^{-1}$, $L_1 = 4.9k_p^{-1}$, and $L_2 = 0.1k_p^{-1}$) and (b) a pulse with a sharp leading edge exciting a strongly nonlinear wake wave ($L = 7k_p^{-1}$, $L_1 = 0.5k_p^{-1}$, and $L_2 = 1.5k_p^{-1}$) for the case of circular polarization of laser radiation.

nounced. In this case, short-wavelength components corresponding to SRS at odd harmonics (particularly the third harmonic) of the laser frequency are present in the spectrum of backscattered radiation even in the absence of the excitation of a wake wave [14, 17] (Fig. 7b, solid curve). The excitation of a wake wave results in the frequency upshift of backscattered radiation at the first harmonic (up to $k \approx (3–4)k_0$). At the same time, the intensity of radiation scattered at higher harmonics decreases; as a result, the total intensity of backscattered radiation in the frequency range $\omega \geq 2\omega_0$ changes insignificantly (Fig. 7b, dashed curve).

It is seen from the figures that the frequency shift of scattered radiation decreases with decreasing the angle θ. The maximum of the intensity of radiation scattered at the first harmonic corresponds to small scattering angles because, as was mentioned above, at small θ the detuning of the resonant perturbations with $q_0 = k_s - k_0 = 0$ is small even in the presence of fast longitudinal motion of the electron component; i.e., the spatial growth rate of such perturbations is close to maximum throughout the entire pulse.

An analysis of angular and frequency spectra of scattered radiation for the above pulses shows that, when the amplitude of the excited wake wave is low, the radiation powers scattered into the forward and backward hemispheres are approximately the same in order of magnitude (~10^7 W). The power of scattered radiation with $k \geq 1.5k_0$ is about 1% of the total scattered power. The excitation of the wake wave weakly affects the power of radiation scattered into the forward hemisphere but leads to a substantial decrease (almost by two orders of magnitude) in the total power of radiation scattered into the backward hemisphere. This

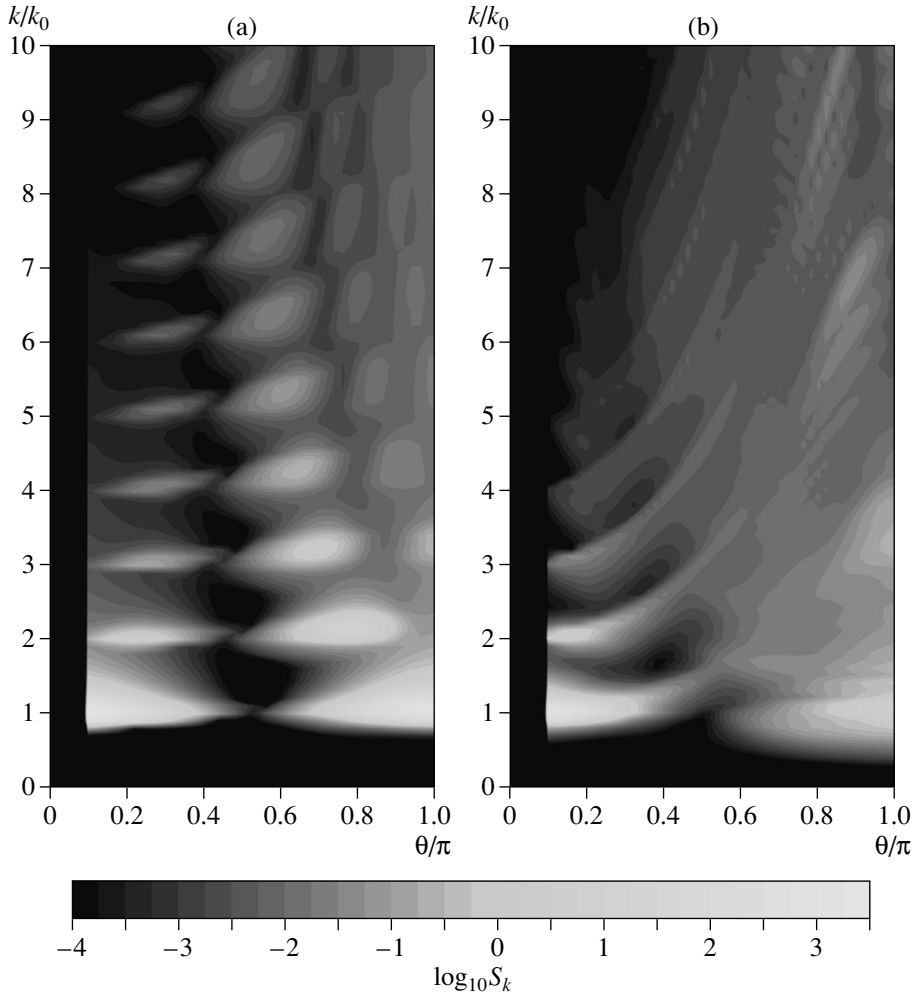

Fig. 5. Same as in Fig. 4, but for the case of linear polarization of laser radiation at $\varphi = 0$.

decrease is related mainly to suppression of SRS at frequencies close to the carrier frequency; as a result, the fraction of radiation with $k \geq 1.5k_0$ in the total power of radiation scattered into the backward hemisphere increases to several tens of percent.

For a relatively low total power of scattered radiation ($P_s \sim 10^7$ W), which is about $\sim 10^{-8} P_{\max}$, the total energy of radiation scattered during the time required for the pulse to cover a distance equal the length of the focal region (on the order of 1 cm) is also low and amounts to ~0.3 mJ (one-thousandth of a percent of the total energy of the pulse), which, however, is quite enough for diagnostic purposes. A relatively low scattering efficiency is related to the fact that the calculations were performed for the pulses with an extremely small length L satisfying the condition $L \ll r_0$, under which the quasi-one-dimensional approximation is valid. For actual pulses with duration $\tau \geq 0.1$ ps, the intensity of scattered radiation is expected to be much higher. In this case, the problem should be solved in terms of the complete set of Eqs. (22) and (25) because, for such pulses, the relation $L \geq r_0$ usually holds.

According to the results of numerical calculations, in the case at hand, the maximum value of the mean-square relative electron-density perturbation behind the pulse, $\overline{\delta N^2} = \int \langle \delta \tilde{N}_0^2 \rangle_{\mathbf{k}_e} k_e^2 \, dk_e d\Omega_e$ (the integral over k_e is taken over the region where the spectral density $\langle \delta \tilde{N}_0^2 \rangle_{\mathbf{k}_e}$ is close to its maximum), is on the order of 10^{-3}; i.e., the SRS instability is far from saturation, which occurs at $\overline{\delta N^2} \sim 1$. This means that, for longer pulses, the intensity of scattered radiation can be increased by three orders of magnitude under conditions when the instability is not yet saturated, i.e., when Eqs. (22) and (25) are applicable. In this case, the total energy of scattered radiation can amount to 1% of the total energy of the pulse.

Note that the calculations were carried out for the frequency ratio $\omega_0/\omega_{p0} = 10$. This value, in fact, lies on

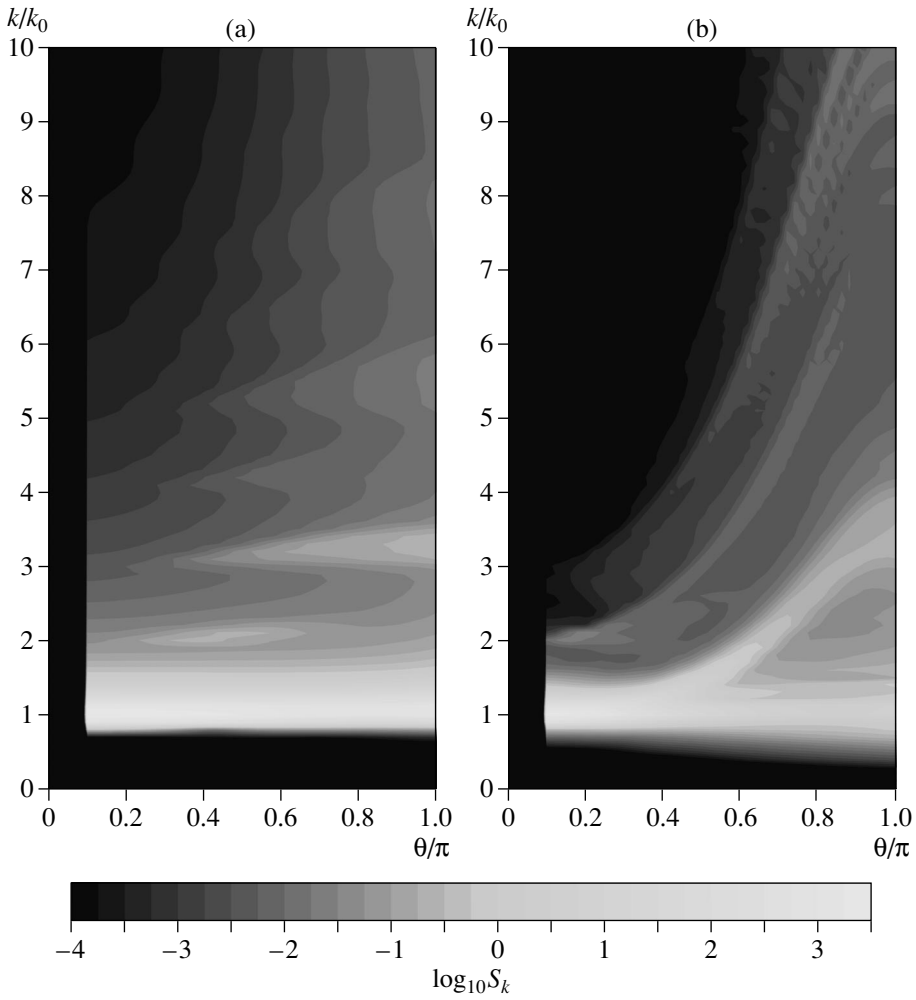

Fig. 6. Same as in Fig. 4, but for the case of linear polarization of laser radiation at $\varphi = \pi/2$.

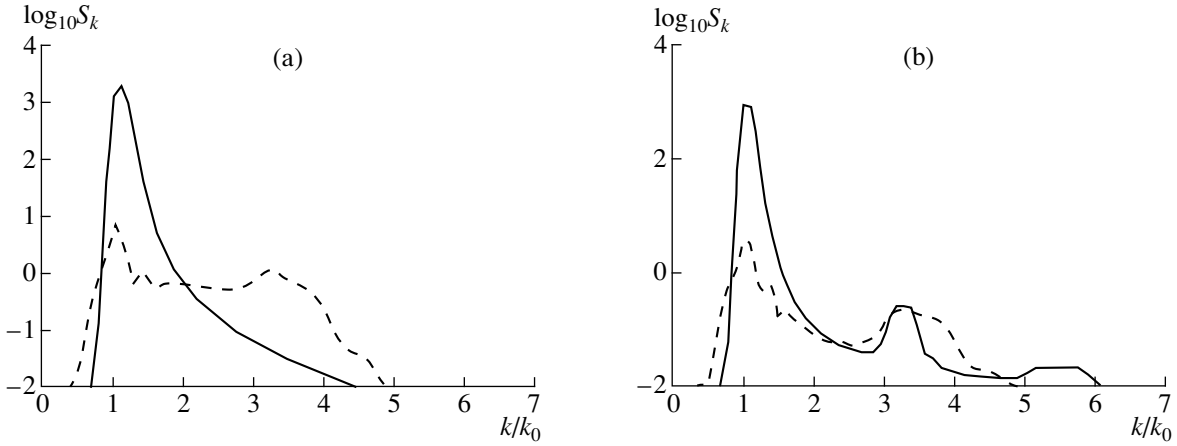

Fig. 7. Profiles of the spectral intensity S_k (in units of W cm/sr) of back-scattered radiation at $\lambda_0 = 1$ μm, $a_{\max} = 2.5$, $r_0 = 60$ μm, $\omega_0/\omega_{p0} = 10$, and $T = 10$ eV in the case of (a) circular and (b) linear polarization of laser radiation for a pulse with a smooth leading edge ($L = 5k_p^{-1}$, $L_1 = 4.9k_p^{-1}$, and $L_2 = 0.1k_p^{-1}$; solid curves) and a pulse with a sharp leading edge exciting a strongly nonlinear wake wave ($L = 7k_p^{-1}$, $L_1 = 0.5k_p^{-1}$, and $L_2 = 1.5k_p^{-1}$; dashed curves).

the boundary of the applicability region of the model used with respect to the parameter $\kappa \sim (\omega_{p0}/\omega_0)^{1/3}$ (see Section 2), which, in this case, can only roughly be considered small. Nevertheless, we can expect that the calculated SRS spectra will differ from the actual spectra mainly in the absolute values of the spectral density and total power of scattered radiation. At the same time, the model proposed is expected to correctly describe the general features of the SRS spectra even at not high values of the frequency ratio ω_0/ω_{p0}. In particular, the effect of a strong Doppler shift of back- and side-scattered radiation under conditions when a strongly nonlinear wake wave is excited should be described correctly, because this shift does not depend on ω_0/ω_{p0} at all.

5. CONCLUSION

In this paper, we have obtained and numerically investigated a set of equations describing the large-angle SRS of a short relativistically strong laser pulse propagating in an underdense plasma.

The results obtained show that the structure of the SRS spectrum of an ultrashort, relativistically strong laser pulse depends strongly on the pulse shape. When the pulse is smooth and the amplitude of the excited wake wave is relatively small, the structure of the SRS spectrum replicates the structure of the spatial growth rate of the instability associated with SRS at the fundamental and higher harmonics of the laser frequency in an immobile plasma.

If the pulse front excites a strongly nonlinear wake wave, the scattering occurs in relativistic electron flows and is accompanied by the Doppler frequency shift. In the presence of an electron flow directed oppositely to the pulse propagation direction, the scattering occurs with a frequency upshift. The frequency upshift is maximum for the direct-backward SRS and decreases with decreasing scattering angle.

The revealed dependence of the structure of the SRS spectrum on the amplitude of the excited wake wave can be applied to diagnosing the interaction of relativistically strong laser pulses with an underdense plasma.

ACKNOWLEDGMENTS

This work was supported by the Russian Foundation for Basic Research, project no. 98-02-17455.

REFERENCES

1. N. E. Andreev, Zh. Éksp. Teor. Fiz. **59**, 2105 (1970) [Sov. Phys. JETP **32**, 1141 (1971)].
2. L. M. Gorbunov, Usp. Fiz. Nauk **109**, 631 (1973) [Sov. Phys. Usp. **16**, 217 (1973)].
3. J. F. Drake, P. K. Kaw, Y. C. Lee, *et al.*, Phys. Fluids **17**, 778 (1974).
4. D. W. Forslund, J. M. Kindel, and E. L. Lindman, Phys. Fluids **18**, 1002 (1975); **18**, 1017 (1975).
5. L. M. Gorbunov, V. I. Domrin, and R. R. Ramazashvili, Zh. Éksp. Teor. Fiz. **70**, 2161 (1976).
6. W. L. Kruer, *The Physics of Laser Plasma Interaction* (Addison-Wesley, New York, 1988).
7. T. Antonsen, Jr. and P. Mora, Phys. Fluids B **5**, 1440 (1993).
8. N. E. Andreev, V. I. Kirsanov, and L. M. Gorbunov, Phys. Plasmas **2**, 2573 (1995).
9. E. Esarey, P. Sprangle, J. Krall, and A. Ting, IEEE Trans. Plasma Sci. **24**, 252 (1996).
10. N. E. Andreev and L. M. Gorbunov, Usp. Fiz. Nauk **169**, 53 (1999).
11. K. Nakajima, D. Fisher, Y. Kawakubo, *et al.*, Phys. Rev. Lett. **74**, 4428 (1995).
12. A. Modena, Z. Najmudin, A. E. Dangor, *et al.*, Nature **377**, 606 (1995).
13. D. Umstadter, S.-Y. Chen, A. Maksimchuk, *et al.*, Science **273**, 472 (1996).
14. P. Sprangle and E. Esarey, Phys. Rev. Lett. **67** (1991); Phys. Fluids B **4**, 2241 (1992).
15. A. S. Sakharov and V. I. Kirsanov, Fiz. Plazmy **21**, 632 (1995) [Plasma Phys. Rep. **21**, 596 (1995)].
16. B. Quesnel, P. Mora, J. C. Adam, *et al.*, Phys. Rev. Lett. **78**, 2132 (1997); Phys. Plasmas **4**, 3358 (1997).
17. A. S. Sakharov and V. I. Kirsanov, Phys. Plasmas **4**, 3382 (1997).
18. N. E. Andreev, L. M. Gorbunov, V. I. Kirsanov, *et al.*, Phys. Scr. **49**, 101 (1994).
19. A. S. Sakharov and V. I. Kirsanov, Phys. Rev. E **49**, 3274 (1994).
20. S. V. Bulanov, V. I. Kirsanov, and A. S. Sakharov, Fiz. Plazmy **16**, 935 (1990) [Sov. J. Plasma Phys. **16**, 543 (1990)].
21. A. S. Sakharov, N. M. Naumova, and S. V. Bulanov, Fiz. Plazmy **24**, 880 (1998) [Plasma Phys. Rep. **24**, 818 (1998)].
22. A. S. Sakharov, EM Waves Electron. Syst. **3**, 92 (1998).
23. W. B. Mori, C. D. Decker, D. E. Hinkel, and T. Katsouleas, Phys. Rev. Lett. **72**, 1482 (1994).
24. C. B. Darrow, C. Coverdale, M. D. Perry, *et al.*, Phys. Rev. Lett. **69**, 442 (1992).
25. K. Krushelnick, A. Ting, H. R. Burris, *et al.*, Phys. Rev. Lett. **75**, 3681 (1995).
26. *Plasma Electrodynamics*, Ed. by A. I. Akhiezer *et al.* (Nauka, Moscow, 1974; Pergamon, Oxford, 1975), Chap. 11.

Translated by the author

Plasma Physics Reports, Vol. 26, No. 8, 2000, pp. 668–681. Translated from Fizika Plazmy, Vol. 26, No. 8, 2000, pp. 712–726.

DUSTY PLASMA

One-Dimensional Nonlinear Self-Organized Structures in Dusty Plasmas

V. N. Tsytovich

Institute of General Physics, Russian Academy of Sciences, ul. Vavilova 38, Moscow, 117942 Russia

e-mail: tsytov@td.lpi.ac.ru

Received September 23, 1999; in final form, January 27, 2000

Abstract—Dusty plasmas, which are open systems, can form stable one-dimensional self-organized structures. Absorption of plasma by dust particles results in the plasma flux from the plasma regions where the dust is absent. It is found that, in a one-dimensional dust layer, this flux is completely determined by the number of dust particles per unit area of the layer surface. This number determines all of the other parameters of the steady-state dust structure; in particular, it determines the spatial distributions of the dust density, dust charge, electron and ion densities, and ion drift velocity. In these structures, a force and electrostatic balance is established that ensures the necessary conditions for confining the dust and plasma particles in the structure. The equilibrium structures exist only for subthermal ion flow velocities. This criterion determines the maximum possible number of dust particles per unit area in the steady-state structure. The structures have a universal thickness, and the dust density changes sharply at the edge of the structure. The structures with a size either less than or larger than the ion mean free path with respect to ion–neutral collisions, quasi-neutral and charged structures, and soliton- and anti-soliton-like structures are investigated. Laboratory experiments and observations in extraterrestrial plasma formation are discussed in relation to dust structures. © *2000 MAIK "Nauka/Interperiodica".*

1. INTRODUCTION

It is well known that dust particles efficiently absorb plasma particles and, therefore, a steady-state dusty plasma can exist either in the presence of plasma sources (e.g., introduced by volume ionization) or (in the absence of ionization) when dust-containing plasma regions are supported by plasma fluxes from dust-free regions. In the latter case, any dust inhomogeneity creates plasma flows directed toward the regions where the dust density is increased.

The aim of this paper is to investigate a simple one-dimensional distribution of the plasma and dust particles under the condition of a nonlinear electrostatic and hydrodynamic balance. We will assume that the dust-containing layer is surrounded on both sides by dust-free regions. The dust itself creates plasma flows directed toward this layer. In a steady state, these flows should compensate the plasma losses due to absorption of plasma particles by the dust. We will assume that the layer is symmetric and the plasma flows entering the layer from both sides are equal in magnitude. We will show that, within the hydrodynamic approach and with the dust pressure neglected, the boundary between the dust layer and the dust-free region is sharp in the sense that there exists a surface separating these two regions and the dust density is exactly zero outside this surface. This result will be proven valid only under the condition that the dust pressure is negligibly small, which appears to be satisfied in most cases of interest when the dust charges are large. The structures found are similar to solitons that are known in nonlinear plasma physics. They are exact nonlinear solutions to balance equations. An important difference from usual solitons is that dust structures exist only in the presence of plasma flows (which, in a sense, play the role of "food" supporting the structure). These flows are not external flows but are determined by the structure itself. Therefore, these structures should be regarded as self-organized structures. A number of observations indicate that structures with properties similar to those found in this paper (thin clouds with sharp boundaries) are indeed observed under various conditions in ionosphere, space, and laboratory experiments.

In this paper, which is the first attempt to treat these structures, we use a simple hydrodynamic description [1–6] based on the smallness of the ratio of the mean free path for ions and electrons with respect to collisions with dust particles to the size of the structure. A kinetic treatment is left for further investigation. The hydrodynamic approach for large dust charges is justified by an estimate showing that the frequency of dust–ion/electron collisions is much higher than the frequency of binary collisions between plasma particles (ions and electrons). This is correct even for sufficiently low dust densities (although $P \gg 1/Z_d$, see below).

Here, we will consider only steady-state equilibrium distributions and assume that, in equilibrium, the dust velocity is zero. Far away from both sides of the dust layer, the plasma, which is considered to be homogeneous and neutral, has the density n_0 and drift velocities $\pm u_0$ directed toward the layer. The absolute value of u_0 is governed by the parameters of the structure; in

1063-780X/00/2608-0668$20.00

particular, it is determined by the total number of dust particles per unit area of the layer surface.

2. GENERAL NONLINEAR BALANCE EQUATIONS FOR THE DUST STRUCTURES

In writing the balance equations, we will use dimensionless parameters. The ion density n, the electron density n_e, and the dust charge density $n_d Z_d$ (where Z_d is the dust charge in units of the electron charge) will be normalized to n_0:

$$n \equiv \frac{n}{n_0}, \quad n_e \equiv \frac{n_e}{n_0}, \quad P \equiv \frac{n_d Z_d}{n_0}. \tag{1}$$

The electric field E and distance x will be normalized as follows:

$$x \equiv \frac{xa}{d_i^2}, \quad E \equiv \frac{Ed_i^2}{aT_e}, \tag{2}$$

where a is the dust size (the dust radius; the dust particles are assumed to be spherical); d_i is the ion Debye radius for the parameters outside the structure,

$$d_i^2 \equiv T_i/4\pi n_0 e^2; \tag{3}$$

and T_e and T_i are the electron and ion temperatures (in energy units), respectively. The mathematical reason for normalization of the distance and the electric field according to relation (2) is that nonlinear equations in these units do not have any free parameters except τ and the ion drift velocity u:

$$\tau \equiv \frac{T_i}{T_e}, \quad u \equiv \frac{u}{\sqrt{2}v_{Ti}}, \tag{4}$$

where $v_{Ti} \equiv \sqrt{T_i/m_i}$ is the ion thermal velocity. Normalization of the electric field has a simple physical meaning: a unit of the normalized electric field corresponds to the value of the field in which the electron acquires the energy T_e over the characteristic distance determined by the first of expressions (2). The distances are normalized to a distance on the order of the ion mean free path with respect to ion–dust collisions. The electron and ion temperatures are assumed to be constant throughout both the dust-free and dust-containing regions.

We also introduce the parameter z as a dimensionless characteristic of the dust charge:

$$z \equiv \frac{Z_d e^2}{aT_e}. \tag{5}$$

In the balance equation, we take into account the electrostatic field force, pressure force, ram pressure force, and ion drag force acting on dust particles. The latter force, which arises due to momentum exchange between ions and dust particles and is proportional to the ion density, results in a decrease in the ion momentum proportional to the dust density. Absorption of electrons and ions by dust particles during dust charging is taken into account by the charging coefficient in the charging equation and continuity equation. The dust pressure is neglected, but, in order to prove the validity of this assumption, the equation for the dust force balance will also be written for the case when the dust pressure is taken into account.

Using the units defined above, we obtain a simple expression for the dust force balance, which contains only one new coefficient—the drag coefficient α_{dr}, which depends only on two dimensionless parameters already introduced in (4). In the case when the dust pressure is neglected, this equation describes the balance of the electrostatic field force and the ion drag force

$$E - \alpha_{dr} znu = 0, \tag{6}$$

where, for the Maxwell ion distribution with drift, the coefficient α_{dr} can be found in the form

$$\alpha_{dr}(t, u, a) = \frac{\mathrm{erf}(u)}{8u^3}\left[t(-1 + 4u^2 + 4u^4) + 2t(-1 + 2u^2) + 4\ln\left(\frac{1}{a}\right)\right] + \frac{\exp(-u^2)}{4\sqrt{\pi}u^2}\left[t(t(1 + 2u^2) + 2) - 4\ln\left(\frac{1}{a}\right)\right]. \tag{7}$$

Here, the parameters t and a are expressed through the parameters introduced above:

$$t \equiv \frac{\tau}{z}, \quad a \equiv \frac{a}{d_i}. \tag{8}$$

Expression (7) takes into account both the ion absorption by dust particles and the ion Coulomb scattering by dust charges.

We can also write the force balance equation with allowance for the dust pressure,

$$\tau_d \frac{d}{dx}\left(\frac{P}{z}\right) = P(E - \alpha_{dr} znu), \tag{9}$$

where the parameter τ_d, characterizing the dust pressure, is

$$\tau_d = \frac{T_d z}{Z_d T_e}. \tag{10}$$

For $\tau_d \ll 1$, we can neglect the left-hand side of equation (9). In this case, in addition to solution (6), we also obtain the solution $P = 0$. This fact will be used below to construct a solution such that, outside the structure, the solution is $P = 0$, but, inside the structure, relation (6) is satisfied. The condition $\tau_d \ll 1$ is easily satisfied in most of the laboratory and space conditions of interest, because Z_d is usually a large number.

The balance of forces for electrons is rather simple, because the electron inertia and the electron friction on dust particles are both negligible. The only forces left are the electrostatic force and the electron pressure force:

$$E = -\frac{1}{n_e}\frac{dn_e}{dx}. \tag{11}$$

This expression describes the adiabatic condition for electrons, and it can be used to exclude either the electric field or the electron density from the equation.

In the balance equation for ions, we take into account the electric field force, the ram pressure force, the pressure force, the force related to the momentum transfer to ions due to the interaction with dust particles, and the force due to the ion friction on neutral particles of the gas. This equation can be written in the form

$$\tau\left(\frac{du}{dx} + \frac{1}{n}\frac{dn}{dx}\right) + \frac{1}{n_e}\frac{dn_e}{dx} + Puz\alpha_{dr} + \nu u(1 + \alpha_u u) = 0, \tag{12}$$

where we used Eq. (11) for the electric field, wrote the force due to the ion friction on neutral atoms in the form (here, we use dimensional units with ν being the dimensional frequency of ion–neutral collisions)

$$F = -\nu n m_i u\left(1 + \frac{\alpha_u u}{\sqrt{2}v_{Ti}}\right), \tag{13}$$

and introduced a new nonlinear coefficient α_u. The form in which this nonlinearity is written satisfies both the existing experimental data and the theoretical models based on cross sections for ion–neutral collisions. Existing experimental data and simple physical considerations give the estimate $\alpha_u \approx 1$ (see below). We will show that the steady-state structures can exist in the range of the dimensionless parameter $u \le 1/\sqrt{2}$. Therefore, the contribution from the nonlinear term in the friction force (13) is not larger than that from the linear term. Nevertheless, we leave it because it can change the numerical coefficient by a factor on the order of unity.

In fact, the general equations will be valid for any ion drift velocity, including an ion drift velocity much higher than the thermal velocity. As will be shown, the structures in which the ion drift velocity substantially exceeds the ion thermal velocity cannot satisfy the conditions for the steady-state balance. However, the ion drift velocities can be rather close to the ion thermal velocity, in which case we need the exact expression for the linear friction force.

The coefficient α_u can be found from the known experimental data. The nonlinear dependence of the friction force in form (13) follows from elementary theoretical considerations. The momentum transferred from neutral atoms to ions should be on the order of $n\langle v\sigma\rangle u$, where u is the ion directed velocity and σ is the ion–neutral transport cross section; the brackets $\langle\rangle$ mean the averaging over the particle distribution. For small drift velocities, this averaging gives σv_{Ti}, whereas, for large drifts velocities, it gives σu (the latter is correct if the dependence of the cross section on u is not strong, which seems to be the case according to the existing data on cross sections). Thus, the theoretical arguments give the nonlinear dependence written in (13) with the coefficient α_u on the order of unity. In the computations described below, we use $\alpha_u = 1$, although it is not difficult to modify the computations using the existing experimental data for α_u.

The next equations for nonlinear structures are the ion continuity equation, which can be written in dimensionless units in the form

$$\frac{dnu}{dx} = -\alpha_{ch} P n, \tag{14}$$

and the charging equation, which can be written in the orbit motion limited approach (see [1]) in the form

$$\exp(-z) = z\alpha_{ch}2\sqrt{\pi}\frac{n_e}{n\sqrt{\tau\mu}}, \quad \mu = \frac{m_i}{m_e}. \tag{15}$$

The charging or capture coefficient α_{ch} enters both equations. It depends only on the parameters t and u (same as for the drag coefficient α_{dr}):

$$\alpha_{ch} = \frac{\mathrm{erf}(u)}{8u}(1 + t + 3u^2 t) - \frac{t\exp(-u^2)}{4\sqrt{\pi}}. \tag{16}$$

In the limit $u \ll 1$, the drag and charging coefficients have the following simple and well-known form:

$$\alpha_{dr} = \frac{2}{3\sqrt{\pi}}\left(\ln\frac{1}{a} + 2t + t^2\right), \quad \alpha_{ch} = \frac{1}{2\sqrt{\pi}}(1 + t). \tag{17}$$

For numerical calculations, it is useful to find from (15) the derivative dz/dx and include in the system of balance equations an additional equation for the dust charges using as an initial condition the solution to (15) for the initial values of parameters n and n_e. This procedure allows us to avoid the necessity of solving the transcendental charging equation for each step of the numerical calculations.

Finally, in dimensionless units, Poisson's equation will have the following form:

$$\frac{dE}{dx} = \frac{\tau}{a^2}(n - n_e - P), \tag{18}$$

where $a = a/d_i$ is the normalized dust size. We can substitute E from (6) into (18) and use the other equations to find the corresponding values of the derivatives with respect to x. This procedure leads to an exact solution to Poisson's equation in the dust region in the form of the expression for P as a function of the other variables:

$$P = \frac{\left[(n-n_e)\frac{\tau}{a^2} + u^2 n\alpha_{dr}\frac{z}{R}\frac{\partial(\alpha_{dr}z)}{\partial z} - zn_e\alpha_d\alpha_u\right](1-2u^2) + A}{\left(\frac{\tau}{a^2} - zn\alpha_{dr}\alpha_{ch}\right)(1-2u^2) - B}, \tag{19}$$

where

$$R = 1 + \frac{\mathrm{erf}(u)}{4uz\alpha_{ch}}, \tag{20}$$

$$A = \frac{nu}{R}\frac{\partial(z\alpha_{dr})}{\partial z}\left\{nuz\alpha_{dr} - \nu u(1+\alpha_u u) - \frac{1}{\alpha_{ch}}\left(\frac{\partial\alpha_{ch}}{\partial u}\right)[u^2 nz\alpha_{dr} - u^2\nu(1+\alpha_u u)]\right\} + nuz\left(\frac{\partial\alpha_{dr}}{\partial u}\right)\left\{\left[\frac{u^2 zn\alpha_{dr}}{\tau} - u^2\nu(1+\alpha_u u)\right]\right\}, \tag{21}$$

$$B = \frac{nu}{R}\frac{\partial(z\alpha_{dr})}{\partial z}\left[u\left(2\alpha_c - \frac{z}{\tau}\alpha_{dr}\right) - \frac{\partial\alpha_{ch}}{\partial u} + \frac{u^2 z\alpha_{dr}}{\tau\alpha_{ch}}\frac{\partial\alpha_{ch}}{\partial u}\right] + nuz\left(\alpha_{ch} - u^2\alpha_{dr}\frac{z}{\tau}\right)\frac{\partial\alpha_{dr}}{\partial u}. \tag{22}$$

The final set of nonlinear equations that are used in the next section to numerically calculate the dust structures is

$$\frac{dn}{dx} = n\left[\frac{2uP}{1-2u^2} + (n-P)\frac{uz\alpha_d}{\tau(1-2u^2)}\frac{\nu u(1+\alpha_u u)}{(1-2u^2)}\right], \tag{23}$$

$$\frac{dn_e}{dx} = -n_e nzu\alpha_{dr}, \tag{24}$$

$$\frac{du}{dx} = -\frac{1}{1-2u^2}\left[P\alpha_{ch} + u^2 z\alpha_{dr}(n-P)\frac{1}{\tau} - u^2\nu(1+u\alpha_u)\right], \tag{25}$$

$$\frac{dz}{dx} = \frac{1}{R}\left\{-nzu\alpha_{dr} - \frac{2u\alpha_{ch}P}{1-2u^2} - \frac{uz\alpha_{dr}(n-P)}{P\tau(1-2u^2)} + \frac{1}{\alpha_{ch}(1-2u^2)}\left(\frac{\partial\alpha_{ch}}{\partial u}\right)\left[P\alpha_c + \frac{u^2 z\alpha_{dr}(n-P)}{\tau}\right] + \frac{\nu u(1+\alpha_u u)}{1-2u^2} - n^2\nu(1+\alpha_u u)\right\}. \tag{26}$$

3. NUMERICAL RESULTS FOR ONE-DIMENSIONAL DUST STRUCTURES

3.1. Quasineutral Conservative Low-Flux Structures

The simplest type of dust structures can be found under the quasineutrality assumption, when, inside the structure, the following condition is locally satisfied:

$$n = n_e + P. \tag{27}$$

The condition under which the plasma flux in the structure can be considered low is defined by the condition

$$u \ll 1. \tag{28}$$

We will use the limiting expressions for the drag and charging coefficients given by (17).

Finally, we will assume that the structure is conservative (the ion–neutral collisions are weak), which corresponds to the condition

$$\nu \ll 1, \tag{29}$$

and consider the limiting case $\nu = 0$. In this case, the equations have an additional integral, which, together with the conditions far outside the structure, $n_e = 1$ and $n = 1$, yields the following relation:

$$n_e = 1 + (1+\tau)(n-1). \tag{30}$$

From (27), we obtain

$$P = (1+\tau)(n-1). \tag{31}$$

Then, the general set of equations reduces to the following equations:

$$\frac{dn}{dx} = nuz\frac{1+\tau-\tau n}{\tau}\alpha_{dr}\left(\frac{\tau}{z}\right), \tag{32}$$

$$\frac{du}{dx} = (n-1)(1+\tau)\alpha_{ch}\left(\frac{\tau}{z}\right) - u^2 z\frac{1}{\tau}\alpha_{dr}\left(\frac{\tau}{z}\right), \tag{33}$$

$$\frac{dz}{dx} = \frac{(1+\tau)(z+\tau)}{(1+z+\tau)\tau}uz\alpha_{dr}\left(\frac{\tau}{z}\right). \tag{34}$$

According to Poisson's Eq. (18), the quasineutrality condition means that

$$a \ll \sqrt{\tau}. \tag{35}$$

This condition requires that the size of the structure R be much larger than $a/\sqrt{\tau}$. For these scale lengths, the deviation from quasineutrality can also be neglected outside the structure, and, therefore, at the edge of the structure (taken here as $x = 0$), where $P = 0$,

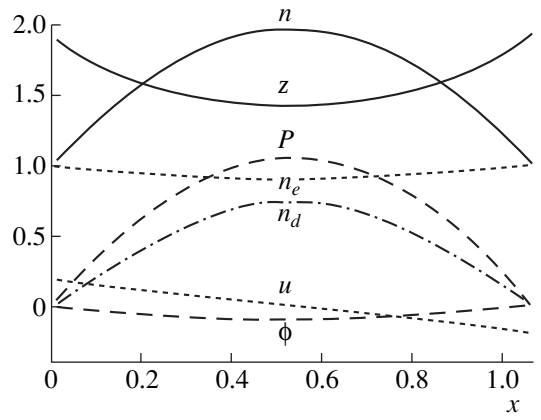

Fig. 1. Profiles of different quantities in a quasineutral dust structure in hydrogen plasma for $\tau = 0.1$.

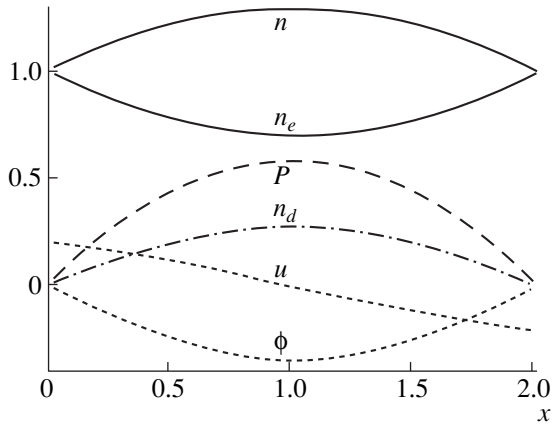

Fig. 2. Profiles of different quantities in a quasineutral dust structure in hydrogen plasma for $\tau = 1$.

we should impose the boundary condition $n(0) = 1$. Then, automatically, at $x = 0$, we have $n_e = 1$ and $P(0) = 0$. According to the existence of two equilibrium solutions, namely, $P = 0$ and relation (8), we use the first solution for $x < 0$ and solution (8) for $x > 0$. The structure is located at $x > 0$; all of its parameters can be found by numerically solving the set of nonlinear Eqs. (32)–(34). This numerical solution should give the value $x = R$ for which we again have $P(R) = 0$. This determines the size of the structure R. The initial value $z(0)$ can be found by numerically solving the charging equation for $n(0) = 1$. Due to the relations written in this section, this equation has the form

$$\exp[-z(0)] = \frac{1}{\sqrt{\mu\tau}}[z(0) + \tau]. \qquad (36)$$

For example, for hydrogen and $\tau = 0.1$, we find $z(0) = 1.91$. The numerical solutions for the distributions of different variables inside the structure are presented in Fig. 1 for $\tau = 0.1$ and in Fig. 2 for $\tau = 1$; in both cases, $u(0) = 0.2$ and $a = 0.1$. The results of these calculations allow us to determine the structure size, defined as the coordinate at which the density n again becomes equal to unity. For the above parameter values, these sizes are $R = 1.067$ (Fig. 1) and $R = 2.014$ (Fig. 2). At the boundary, the solution should be joined to the solution $P = 0$ at $x > R$. It is seen from the figures that the profiles of all the quantities are symmetric with respect to the center of the structure and that the drift velocity changes its sign at the center. From the physical standpoint, this seems to be natural in the absence of ion–neutral friction. Note that the ion density has a maximum at the center of the structure. The accumulation of ions at the center has a simple physical meaning: the flux brings ions to the center, but, due to ion absorption on dust particles, the ion density does not increase to infinity (which is the case if $u = 0$ at the center and the flux is conserved $nu = \text{const} = u(0)$). On the other hand, the ion scattering on dust is larger than absorption by a factor of the Coulomb logarithm, which leads to ion accumulation at the center. The electron density has a minimum at the center, which is related with absorption of electrons in the dust charging process. The parameter shown as n_d is equal to P/z and is proportional to the dust density, which has a maximum at the center of the structure. The potential drop shown in these figures was calculated from the value of the electric field determined by relation (5). The dimensionless potential ϕ is given by the expression

$$\phi \equiv \frac{e\phi}{T_e}. \qquad (37)$$

As is seen from Figs. 1 and 2, the potential has a minimum at the center of the structure. For the parameters used, the total potential drop is $\phi_{\text{center}} = -0.099$ for Fig. 1 and $\phi_{\text{center}} = -0.342$ for Fig. 2. This indicates that the potential well increases substantially with increasing the temperature ratio τ.

Numerical results allow us to determine the total number of dust particles in the structure per unit surface area (in dimensionless units):

$$N_d = \int_0^R \frac{P}{z} dx. \qquad (38)$$

For the parameters corresponding to Fig. 1, this number is $N_d = 0.493$, and for the parameters of Fig. 2 it is $N_d = 0.36$. Thus, for given τ, μ, and a, the structure is in fact determined by a single parameter, either $u(0)$ or N_d. In other words, the plasma flux is completely determined by the number of dust particles per unit surface area in the structure. The computations also show that an increase in τ, all other parameters being unchanged, increases the electron density depletion and the potential drop between the boundary and the center of the structure. The latter reaches a value of –0.342 at $\tau = 1$. In this case, the size of the structure increases to

2.014, while the number of dust particles per unit surface area decreases to 0.36. As the parameter τ decreases to 0.01, the size of the structure decreases to 0.53, the potential drop decreases to –0.002, and the number of dust particles per unit surface area decreases to 0.053. The decrease in the dust radius τ to 0.01, all other parameters being unchanged, decreases the size of the structure from 1.067 to 0.73, slightly decreases the number of dust particles from 0.493 to 0.459, and increases the potential drop from 0.099 to 0.127. A decrease in the drift velocity decreases both the number of dust particles and the potential drop. Note that, in these calculations, a substantial increase in the drift velocity is not allowed by virtue of restriction (28) used to simplify the general nonlinear equations. To illustrate the role of the type of gas, we also present the results obtained for an argon plasma for the same parameters as for Figs. 1 and 2 (where the gas was hydrogen). Calculations show that, in this case, the potential drop increases to –0.126 and to –0.374, the number of dust particles in the structure is 0.254 and 0.285; and the size of the structure is 0.783 and 1.889, respectively. Figure 3 describes the structure in hydrogen (Fig. 3a) and argon (Fig. 3b) for $\tau = 0.01$, the other parameters being the same as in Figs. 1 and 2. It is seen that a decrease in the temperature ratio leads to a decrease in the size of the structure and a larger concentration of dust particles at the center of the structure.

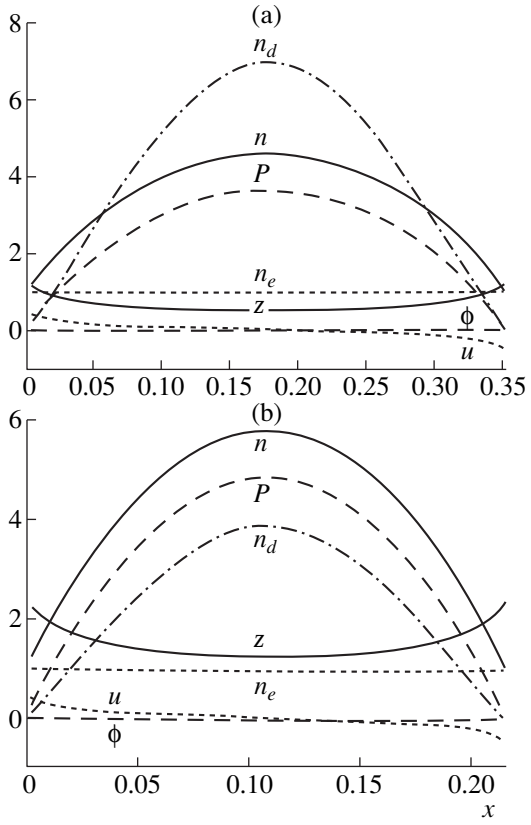

Fig. 3. Profiles of different quantities in dust structures for $\tau = 0.01$ in (a) hydrogen plasma and (b) argon plasma.

3.2. Limiting Value of a Plasma Flux

Here, we present the results of solving the exact set of equations with quasineutrality condition (17) imposed and for $\nu = 0$ but without any restrictions on u. We will assume that $u = 0$ at the center of the structure. By varying $u(0)$, we can find the maximum value $u(0)$ at which the balance equations can be satisfied. However, we will use a somewhat different approach, starting the calculations from the center of the structure, where the value of u is known. Here, we denote the coordinate of the center as $x = 0$. We will calculate only one-half of the structure for $x > 0$, which is sufficient taking into account the symmetry of the structure. We will also use the asymptotic expression for $u(x)$ at $x \longrightarrow 0$ (when $u \longrightarrow 0$) to start the calculations slightly away from the exact center of the structure (at small but finite values of x). We have

$$u \longrightarrow -\beta(n(0)n_e(0), z_0, \tau)x, \tag{39}$$

where

$$\beta(n, n_e, z, \tau) = \frac{(n - n_e)(z + \tau)}{6\sqrt{\pi}z}. \tag{40}$$

Starting with some initial value of $n(0)$ as a free parameter, we vary $n_e(0)$ and try to find the value of the electron density at the center until, at the border of the structure, where $P = 0$, we have $n = n_e = 1$. According to the quasineutrality assumption, at the point where $P = 0$, we should always have $n = n_e$, but, in the general case, this value is not equal to 1. We then vary $n_{e,0}$ until, at the point where $P = 0$, we obtain $n = n_e = 1$. If there is no such point, the equilibrium structure does not exist. The numerical calculations show that the steady-state structure does not exist for all values of $n(0)$. One can find the physical reason why the solution becomes impossible. The calculations show that an increase in $n(0)$ at the center of the structure requires a decrease in $n_e(0)$, which in turn leads to an increase in the value of u at the surface of the structure, until (for the largest possible value of n_0) the value of u at the surface reaches a value close to $1/\sqrt{2}$, when all the coefficients in the nonlinear equations change their signs and the balance becomes impossible (the solutions to the balance equations do not exist). The numerical results shown in Fig. 4 correspond to the case of parameters close to the limiting values at which no solutions exist for a further increase in the ion density at the center of the structure. The parameters used in computations were close to that often found in dusty clouds in space plasma and were taken to be $a = 10^{-9}$ and $\tau = 1$, the gas was hydrogen, the limiting value of $n(0)$ was found to be close to 2.2, the half-size of the structure was close to 0.343, and the number of dust particles per unit sur-

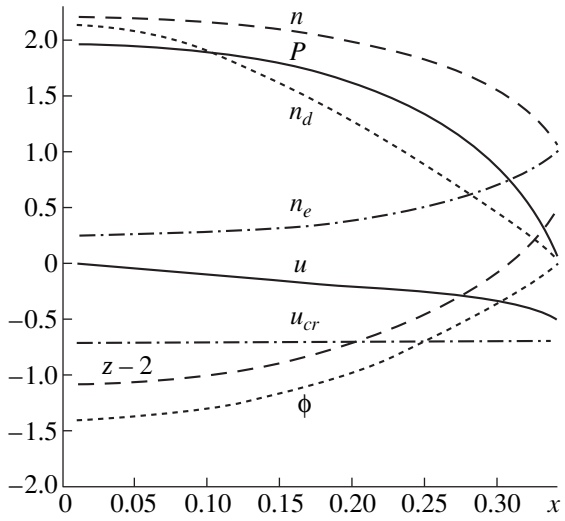

Fig. 4. Hydrogen plasma structure with parameters close to critical for $a = 10^{-9}$ and $\tau = 1$.

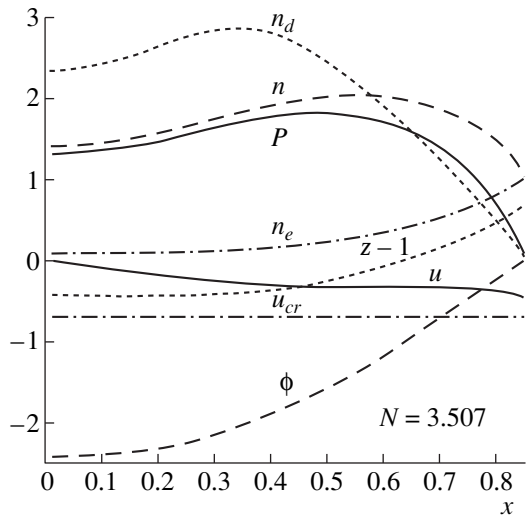

Fig. 5. Hydrogen plasma structure for the case where the ion–neutral collisions play an important role: $\nu = 10$, $\tau = 1$ and $a = 10^{-5}$. The ion density at the center of the structure is not maximum: $n = 1.4$.

face area in the structure was $N_d = 0.879$ (a factor of 2 was taken into account after calculating the number of dust particles in one-half of the structure). Calculations show that the quasineutrality condition is well satisfied for $a \ll \sqrt{\tau}$. In the case when the quasineutrality condition was violated, a procedure similar to that described in this section was used with β determined by an expression more general than (40):

$$\beta(n, n_e, z, \tau) = P_0(n, n_e, z, \tau)\frac{z+\tau}{6\sqrt{\pi z}}, \qquad (41)$$

where P_0 is the value of P at the center of the structure,

$$P_0(n, n_e, z, \tau) = \frac{n - n_e}{1 - \dfrac{a^2}{\tau}\left[zn\left(\ln\left(\dfrac{1}{a}\right) + \dfrac{\tau}{z} + 2\dfrac{\tau^2}{z^2}\right)\left(\dfrac{\tau}{z}+1\right)\dfrac{1}{3\pi}\right]}. \qquad (42)$$

The calculations are performed for some initial value of n_0 until the curves for n and n_e intersect the curve that relates n and n_e in the absence of dust. The limiting flux is again close to $1/\sqrt{2}$. For values of the dust sizes satisfying the quasineutrality condition, the method based on the intersection of the density curves with those curves in the absence of dust, when the electron and ion densities are related unambiguously by a certain analytical expression, gives values of n and n_e close to unity. However, this method is more general and allows one to calculate the distributions of the parameters in structures that are not quasineutral.

3.3. Influence of Ion–Neutral Collisions

In the case when the ion–neutral collision frequency ν cannot be neglected, the structure becomes dissipative. When calculating such structures, we again start from the center of the structure, but, instead of relations (41) and (42), we use equations in which all the terms with ν are retained. Calculations were performed for $a = 10^{-5}$ and $\tau = 1$ with the condition $P = 0$ at the surface of the structure; the gas was hydrogen. The condition that the ion and electron densities are equal to unity at the surface $x = R$ fixes the value of $n_e(0)$ for each value of $n(0)$. The structure does not exist if the calculations show that the drift velocity reaches the value $1/\sqrt{2}$ at any point between 0 and R. The limiting value of n_0 appears to be lower than in the absence of ion–neutral collisions. In all cases when the ion–neutral collisions strongly affect the distributions of the parameters in the structure, the ion- and dust-density profiles are found to be nonmonotonic and both the potential drop and the number of dust particles (per unit surface area) confined in the structure increase. The numerical results show that, for $\nu = 1$, ion–neutral collisions do not qualitatively change the distributions of the parameters in the structures, while, for $\nu = 10$, the distributions change noticeably. Figures 5 and 6 show the results of numerical calculations of such distributions for different values of the ion density at the center [$n(0) = 1.4$ (Fig. 5) and $n(0) = 2.0$ (Fig. 6)]; in both cases, $\alpha_u = 1$ and the other parameters are the same as in Fig. 1. The results presented in Figs. 5 and 6 correspond to rather large fluxes; however, in both cases, $u < u_{cr} = 1/\sqrt{2}$. Recall that we present only one-half of the structures; thus, the distributions of the ion and dust densities are depleted at the center of the structure. The potential drop does not change appreciably, while the

dust distribution changes with increasing the ion density at the center of the structure (see Figs. 5, 6). As the ion density at the center increases, the ion drift velocity increases rapidly toward the periphery of the structure and, for large values of the central density, approaches a plateau (Fig. 6). The appearance of this plateau is related to the fact that the electric and friction forces balance each other, which leads to a constant ion mobility. This effect is observed for large ion drift velocities; however, for lower central ion densities, the drift velocity at the boundary of the structure is closer to its critical value. The number of dust particles in the structure increases when the ion–neutral collisions play an important role (up to 4.16 for the parameters of Fig. 6).

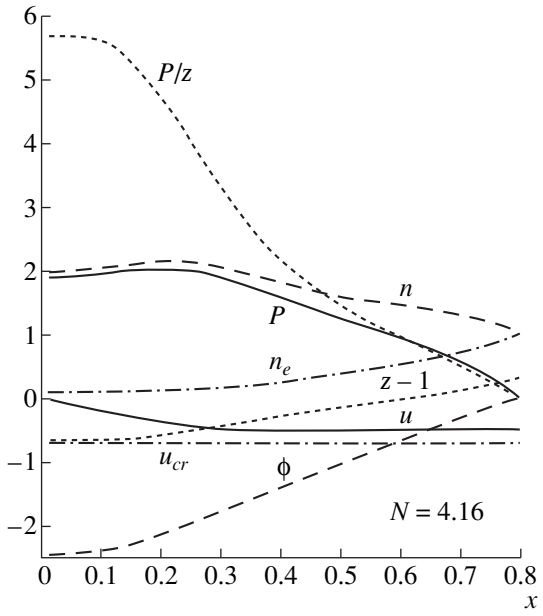

Fig. 6. Same as in Fig. 5, but for the ion central density close to its maximum value $n = 2.0$.

3.4. Boundary Values for Structures with Substantial Violation of the Quasineutrality Condition

When the quasineutrality condition is violated, the values of the electron and ion densities at the boundary of the structure are not equal to each other and are not equal to unity. It is possible to relate the values of the ion and electron densities at the boundary of the structures, as well as the other values at this boundary, to their values far from the structure, where $n = n_e = 1$ and $u = u_0$. Outside the structure, where the dust is absent, there exist several integrals of motion that can be considered as equations relating the surface parameters and the parameters far from the structure. Remember that, for quasineutral structures, the values of the parameters at the surface of the structure coincide with those far from the structure. The problem to be solved in this section is to determine the deviations of the parameters in the case when the quasineutrality condition is violated from those in quasineutral structures. The parameter that determines the degree to which the quasineutrality condition is violated (for brevity, this parameter will be referred to as the "quasineutrality parameter") has already been given above [see (35)]. However, it is desirable to find numerically how large this degree should be in order to produce a certain change in the structure; i.e., it is desirable to know how small the deviations are in the structure for small values of the quasineutrality parameter and what kind of structures can be created for large deviations from quasineutrality. For large deviations from quasineutrality, the values of n, n_e, and u at the surface of the structure and far from the structure turn out to be quite different and large jumps in the dust density and the value of the parameter P at the surface can appear, which leads to a rather sharp boundary of the structure. The presence of such jumps is a direct consequence of the balance equation and Poisson's equation, and naturally no surface charges or electrostatic discontinuity are present. The requirement of their absence gives the condition for the dust density jump at the structure surface. For quasineutral structures, these jumps are small, but the derivative of the dust density at the surface can undergo a large jump; therefore, the surface of the structure is also sharp in the sense that the value of P on one side of the surface is exactly zero, while, on the other side of the structure, it is small but not zero.

We denote the plasma parameters far from the structure by the subscript ∞. Taking into account the above-said, we can write $n_\infty = n_{e,\infty} = 1$ and $u_\infty = u_0$. We denote the values of parameters at the surface of the structure by $n(0)$, $n_e(0)$, and $u(0)$; i.e., the point $x = 0$ is placed at the surface of the structure (recall that, in Sections 3.2 and 3.3, the point $x = 0$ was placed at the center of the structure, whereas, in Section 3.1, it was placed at the surface of the structure). The values of $u(\infty)$ and $u(0)$ are different; the parameter that determines the structure is $u(\infty)$ (i.e., the flux far from the structure). An important problem is the distance from the structure surface at which the drift velocity and densities reach the values $n_\infty = n_{e,\infty} = 1$ and $u_\infty = u_0$, i.e., whether they are reached asymptotically at infinity or they are reached at a finite distance from the structure surface. For all of the cases under consideration, the numerical result is the same: the above parameters are reached at finite distances. The procedure of calculations was the following. For a given value of u_0 (the main parameter that determines the structure), the boundary conditions found from the conservation laws allow us to find all the important parameters at the surface of the structure. These parameters are then used as boundary values to numerically integrate Poisson's equation in the backward direction together with the ion balance equation in the absence of dust and to find the distance from the surface where the starting values $n_\infty = n_{e,\infty} = 1$ and $u_\infty = u_0$ are reached. In each case, this distance was finite and decreased with decreasing the quasineutrality

parameter. In the limit of quasineutral structures, this distance tends to zero and the parameter values on the structure surface coincide with those far from the surface, as was assumed above.

To explicitly find the boundary conditions, we will use the integrals of motion of the general set of nonlinear equations written above for the case where the dust is absent and the ion–neutral collisions are negligible ($\nu = 0$):

$$nu = \text{const} = u_0, \quad n_0 = 1, \tag{43}$$

$$\frac{E^2 a^2}{2\tau} - n_e - \tau n(1 + 2u^2) = \text{const} = -1 - \tau(1 + 2u_0^2). \tag{44}$$

Equation (44) can be interpreted as the pressure balance equation similar to that for magnetic confinement of a plasma. However, in the case at hand, the dust is confined by electrostatic fields that are not external but are produced by the structures themselves. Therefore, we are dealing with self-confinement of a structure that itself produces both the flux toward the structure and the electrostatic field near its boundary. The electrostatic field inside the structure also exists and has a dissipative nature, because, inside the structure, it is supported and created by the dust drag. Outside the structure, this dissipative drag is absent, because there is no dust; however, due to the continuity of the electric field at the surface of the structure, the field should also be created close to the structure surface in the region where the dust is absent. This field is obviously created by dust charges. Equation (44) indicates that, in the region where the dust is absent, the electrostatic field pressure [the first term in (44)] should be balanced by the electron pressure [the second term in (44)] and the sum of the thermal and the ram pressures of ions [the last term in (44)].

By using expression (43), we can rewrite relation (44) in the form

$$E^2 = \frac{2\tau}{a^2}\left[n_e - 1 + \tau(n-1) + 2\tau u_0^2\left(\frac{1}{n} - 1\right)\right]. \tag{45}$$

Relations (44) and (45) are an integral of Poisson's equation found by using the electron force balance equation, the ion force balance equation, and the ion continuity equation. The ion balance equation in the region where the dust is absent has a solution that allows us to relate the electron and the ion densities:

$$n_e = \frac{1}{n^\tau}\exp\left[-\tau u_0^2\left(\frac{1}{n^2} - 1\right)\right]. \tag{46}$$

After substituting this relation into (45), we find that the right-hand side of (45) contains only n and u_0. Due to the continuity of the electric field at the surface of the structure, the left-hand side of this expression is expressed through z and $u = u_0/n$. The equation for dust charging relates the charge of dust particles z with the ion and electron densities and is valid at the structure surface. As a result, we obtain two relations for the boundary values $z(0)$ and $n(0)$ as functions of the main parameter u_0 and the parameters a and τ:

$$\frac{u_0^2 a^2 z(0)^2 \alpha_{dr,0}^2}{2\tau} = \left\{\frac{1}{n(0)^\tau \exp\left[\tau u_0^2\left(\frac{1}{n(0)^2} - 1\right)\right]} - 1 + \tau\left[n - 1 + 2u_0^2\left(\frac{1}{n(0)} - 1\right)\right]\right\}, \tag{47}$$

$$\exp[-z(0)] = \frac{n(0)^{1+\tau}[z(0) + \tau]}{\sqrt{\mu\tau}\exp\left[-\tau u_0^2\left(\frac{1}{n(0)^2} - 1\right)\right]}, \tag{48}$$

where, for $\alpha_{dr,0}$, the approximate expression (17) with $z = z(0)$ should be used.

By numerically solving the set of Eqs. (47) and (48), we can find the values $n(0)$ and $z(0)$; $n_e(0)$ from (46); and, finally, using (19), the value of $P(0)$ on the dust side of the boundary. Since on the other side of the boundary the dust is absent, the value of $P(0)$ describes the jump in P at the boundary. As the charge $z(0)$ of the dust particles at the boundary is found, it is straightforward to find the dust density jump at the boundary. This scheme was used in all of the numerical calculations, whose results are presented below.

Figure 7 presents the results of numerical solution of the boundary problem for hydrogen plasma for the parameter τ varying in the range $0.02 < \tau < 1$ and the initial value of the Mach number $M_0 = \sqrt{2\tau}\,u_0$ varying in the range $0.005 < M_0 < 0.05$. The size of dust particles is $a = 0.1$. The quasineutrality condition is violated for small values of τ. The results are presented in the form of surface plots in which the values of τ are plotted along the x-axis and the values of the parameter M_0 are plotted along the y-axis (horizontal axis). On the vertical axis, the minimum and the maximum values of the parameter plotted along the z-axis are shown. The results obtained show that, when quasineutrality is violated, the ion density at the boundary is much higher than unity and that the jumps in the dust density and the parameter P can be rather big (for the range of parameters corresponding to the figure, the maximum jump in the parameter P is equal to 2.138 for hydrogen and is equal to 9.777 for argon). Also, when quasineutrality is violated, the ion drift velocity at the boundary $u(0)$ is substantially less than its value far from the boundary, u_0.

It should be noted that the boundary condition can be satisfied in both cases $P(0) < n(0)$ and $P(0) > n(0)$. The distributions of all the variables inside the structure

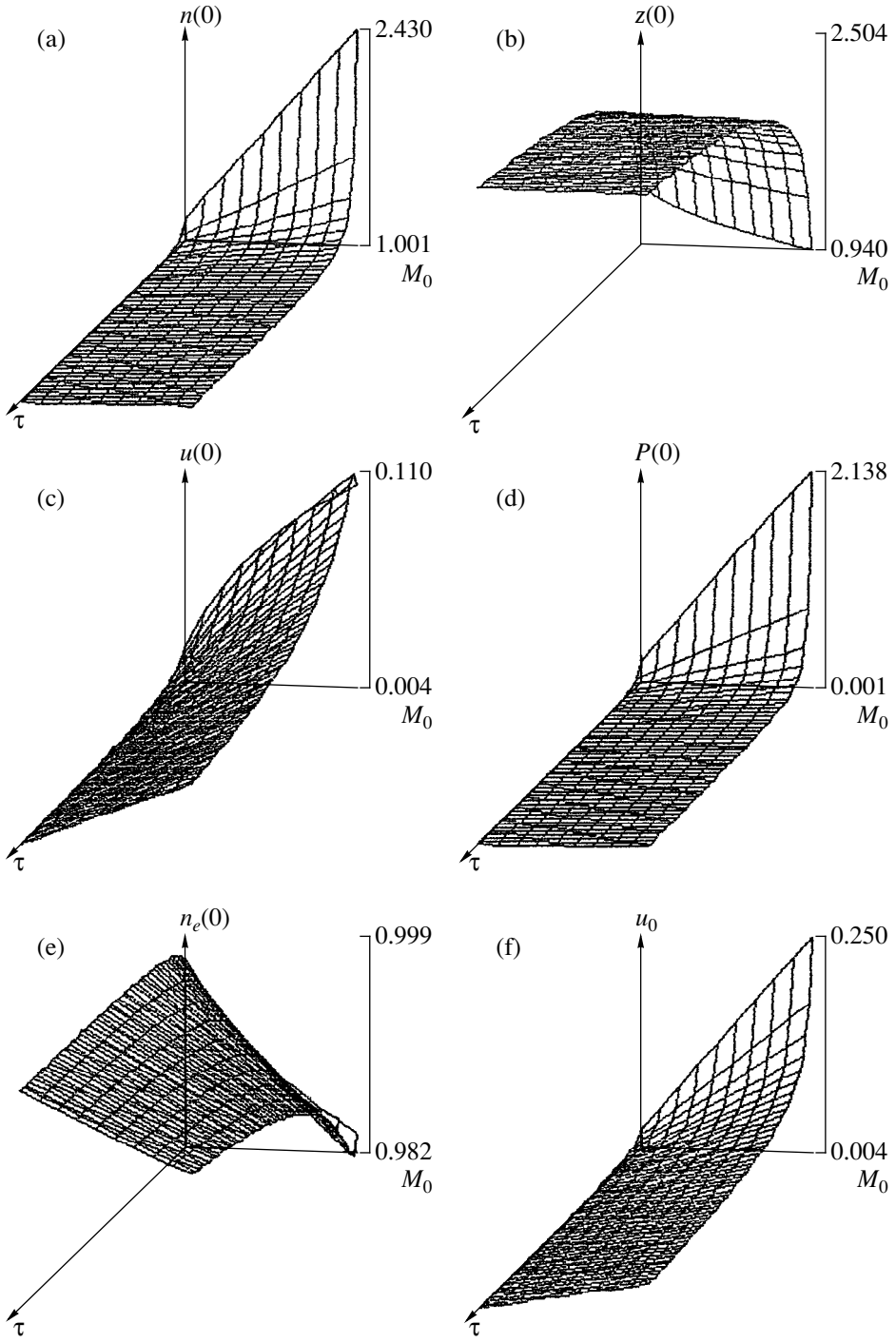

Fig. 7. Boundary values for hydrogen plasma structures.

for these two cases are qualitatively different. In the first case, the structure is of the soliton type with a characteristic maximum of the ion density at the center; however, as compared to quasineutral structures, the structure at hand might have an appreciable jump not only in the derivative of the dust density but also in the dust density itself accompanied by a subsequent increase in the dust density toward the center of the structure. We will refer to these structures as soliton-type structures. In the opposite case, when $P(0) > n(0)$, it is found that, after the dust density jump at the surface, the dust density decreases toward the center of the structure. These structures will be referred as antisoliton structures.

3.5. Almost Quasineutral Structures

The results presented above allow us to calculate the structures in which the violation of quasineutrality is small and to compare exact numerical calculations in which no assumption of quasineutrality is made with calculations in which the quasineutrality assumption is used as the starting point. As an example, we will consider a structure for $a = 0.01$ and $\tau = 0.1$, for which the quasineutrality parameter is sufficiently small: $a^2/\tau = 0.001$. The value of the ion drift velocity far from the structure is chosen to be $u_0 = 0.215$. Then, the solution of the boundary problem gives $u(0) = 0.2$ (which differs slightly from u_0), $n(0) = 1.072$ (which differs slightly from unity), and $n_e(0) = 0.994$ (which also differs slightly from unity). The calculated jump in P appears to be small: $P = 0.02$.

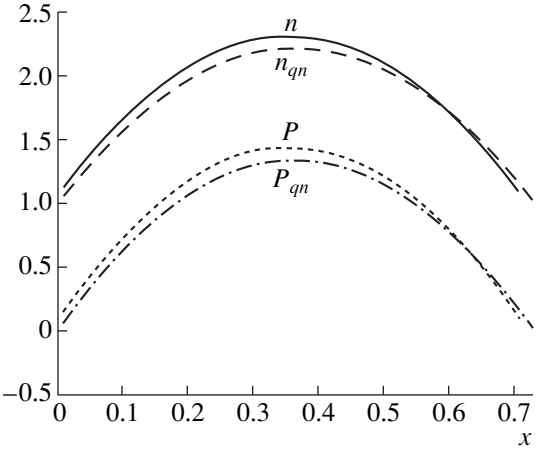

Fig. 8. Comparison of the solutions obtained under the quasineutrality assumption with exact solutions for the case when quasineutrality is slightly violated.

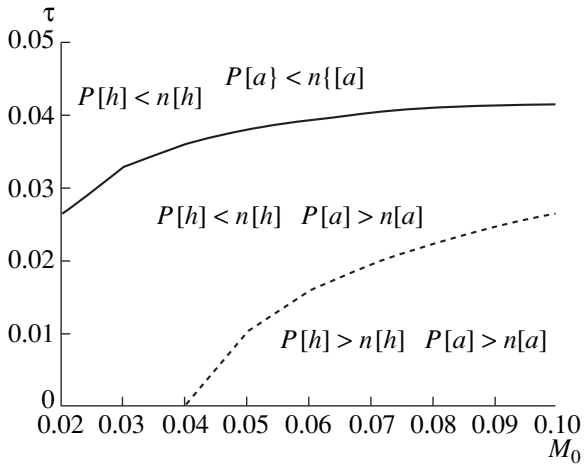

Fig. 9. Phase diagram showing the domains of existence of soliton-type solutions and antisoliton-type solutions for charged structures; $P[a]$ and $n[a]$ denote the values of P and n for argon plasma, and $P[h]$ and $n[h]$ denote the values for hydrogen plasma.

Figure 8 presents the distributions of the ion density and the parameter P for this structure obtained both without (the curves marked by n and P) and with (the curves marked by n_{qn} and P_{qn}) the quasineutrality assumption. One can see the difference in these solutions and the degree of their coincidence. The differences are most pronounced near the boundary, which is not surprising because, close to the boundary, the value of P is small and could be comparable with that related to the violation of quasineutrality (in the case at hand, the value of $P(0)$ is equal to 0.02). On the whole, exact solutions are well reproduced by quasineutral solutions, which shows the possibility of using quasineutral solutions for small values of the quasineutrality parameter.

3.6. Phase Diagrams

The boundary between the regions $P(0) < n(0)$ and $P(0) > n(0)$ can be obtained by calculating the curve that corresponds to $P(0) = n(0)$ on the phase plane (τ, M_0). Figure 9 presents such a diagram with two curves, one of which corresponds to a hydrogen plasma and the other corresponds to an argon plasma.

3.7. Charged Soliton Structures

The soliton-type structures are formed at $P(0) < n(0)$. This condition is also fulfilled for quasineutral structures; however, in this case, $P(0) \ll n(0) \approx 1$. As $P(0)$ increases, the structure changes qualitatively when the value of $P(0)$ becomes comparable with $n(0)$. For quasineutral structures, a small jump in the parameter P at the boundary is accompanied by a large increase in this parameter inside the structure. For charged structures, a large jump in the parameter P at the boundary is accompanied by an insignificant increase in this parameter inside the structure. Another difference of charged structures from quasineutral ones is that the charge density in charged structures is large, while in quasineutral structures, it is close to zero. The charge density in the structure is negative; i.e., the space charge created by electrons and dust dominates the charge produced by ions. In other aspects, charged structures are similar to quasineutral structures: the electron density is minimum at the center of the structure, the ion drift velocity at the center is zero, and the ion and dust densities are maximum at the center. For charged structures, the drop in the electrostatic potential between the center of the structure and its boundary is small, which indicates that the dust is confined in the structure not by this potential drop but by the drop in the potential in the regions adjacent on the outside to the dust region. The regions where the dust is absent (the dust voids) are essential parts of the structure itself and, as was already noted, they have a finite size. The dust voids are almost absent for quasineutral structures,

or, more exactly, they are very thin and the potential drop in them is small. Although charged structures differ qualitatively from quasineutral structures in the way the dust is confined, in both types of structures, both the flux and electrostatic field outside the dust-containing domain are created by dust particles themselves and, hence, these structures should be regarded as self-organized structures. As the parameter a^2/τ increases, quasineutral structures transform smoothly into charged structures.

All the results described above were obtained in a series of computations. As an example, in Fig. 10, we present the results obtained for the parameters $\tau = 0.06$ $a = 0.1$, $u_0 = 0.26$, $M_0 = 0.09$ for hydrogen plasma. Quasineutrality is violated because the corresponding parameter $a^2/\tau = 1/6$ is insufficiently small. The solution of the boundary problem gives $n(0) = 1.658 > P(0) = 0.84$ for hydrogen plasma and $n(0) = 2.234 > P(0) = 1.748$ for argon plasma; both cases correspond to the region on the phase diagram in which the structures are of the soliton type. The other parameters of the structures found in numerical calculations are the following: for hydrogen plasma, $u(0) = 0.157$, $z(0) = 1.424$, $n_e(0) = 0.973$, $R = 0.609$, $N_d = 0.653$, $\Phi = -0.029$, and $Q_d = -0.109$; for argon plasma, $u(0) = 0.116$, $z(0) = 2.434$, $n_e(0) = 0.956$, $R = 0.349$, $N_d = 0.308$, $\Phi = -0.048$, and $Q_d = -0.183$. The figure also shows the profile of the charge density determined by the relation $\rho = n - n_e - P$. The total dimensionless charge per unit surface area of the structure is defined by the relation

$$Q_d = \int \rho dx. \tag{49}$$

Finally, the above parameter Φ is defined as the total potential drop between the point $x = 0$ and the center of the structure $R/2$; i.e., the parameter ϕ does not take into account the potential drop in the dust voids surrounding the dust-containing region of the structure.

3.8. Charged Antisoliton Structures

The charged anti-soliton structures are formed at $P(0) > n(0)$. In such structures, the ion and dust densities at the center are depleted and the charge density inside the structure is highly inhomogeneous; however (similar to soliton-type structures), the ion drift velocity tends to zero at the center of the structure and the charge of the dust particles has a minimum at the center of the structure. In the antisoliton structures, the potential drop inside the structure is relatively small and the dust is confined by the fields of the dust voids adjacent to the dust-containing region. This is illustrated by numerical results for argon plasma (Fig. 11). As compared to Fig. 10, only the value of the parameter τ has been changed ($\tau = 0.02$), which substantially increases the value of the quasineutrality parameter a^2/τ. In this case, for hydrogen plasma, we have $n(0) = 3.491 < P(0) = 3.718$, and, for argon plasma, we have $n(0) = 6.674 < P(0) = 28.093$. The value $M_0 = 0.09$ is the same as for Fig. 10; however, due to the lower value of the temperature ratio $\tau = 0.02$, we have $u_0 = 0.45$ and $a^2/\tau = 1/2$. Other parameters of the structures obtained in numerical computations are the following: for hydro-

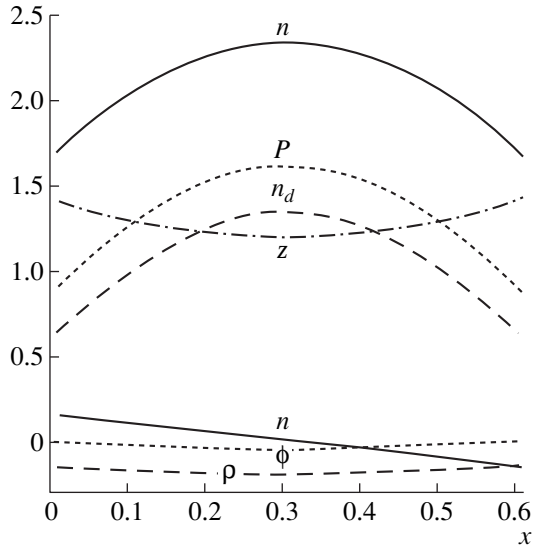

Fig. 10. Soliton-type charged structures in hydrogen plasma.

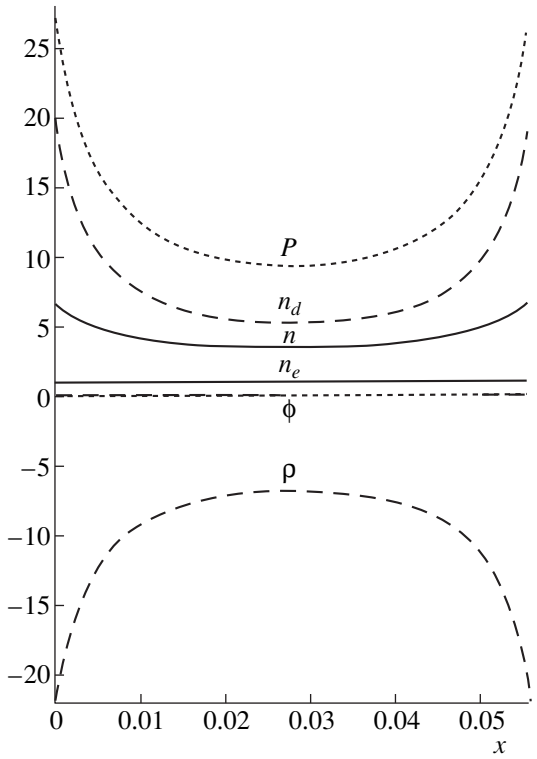

Fig. 11. Anti-soliton-type charged structures in argon plasma.

gen plasma, $z(0) = 0.718$, $u(0) = 0.129$, $n_e(0) = 0.967$, $R = 0.261$, $N_d = 1.187$, $\Phi = -0.0019$, and $Q_d = -0.303$ and, for argon plasma, $z(0) = 1.379$, $u(0) = 0.067$, $n_e(0) = 0.967$, $R = 0.056$, $N_d = 0.437$, $\Phi = -0.006$, and $Q_d = -0.536$.

4. DISCUSSION OF THE RESULTS

Three problems are still waiting to be investigated in more detail (at present, it is only possible to give some qualitative answers and fragmentary numerical results). These problems are the following.

4.1. Role of Dust Pressure

The equations that take into account the dust pressure have been written above. From a physics standpoint, we can expect that, if the dust pressure is taken into account, it smoothes the jumps in the dust density and its derivatives; however, the smoothing will occur at rather short distances (on the order of $\delta x = T_d z/Z_d T_e$ in dimensionless units), while the structure size R is on the order of unity. Note that, in most present laboratory experiments, $\delta x < 3 \times 10^{-3}$. In space plasma, δx is always small for $Z_d \gg 1$. The latter is always valid, except for the not very interesting case where the dust is almost uncharged. Numerical calculations were performed with the dust pressure taken into account for one set of the structure parameters; the results obtained confirm the expectations of smoothing the jumps. A more general investigation of this issue is of interest for several problems of space dusty plasma, such as the problem of the thickness of dust planetary rings.

4.2. Stability of Structures

The stability of structures can be analyzed in the frame of the hydrodynamic approach used in this paper to investigate steady-state structures. The problem of the structure stability against perturbations in which the velocity is aligned with the direction along which the parameters of the structure are changed can be considered by methods already used to investigate the void stability [2]. In [2], it was shown that ionization processes play an important role in the formation of voids. Here, in contrast to [2], we do not take into account the ionization processes, in which case the appearance of specific voids on both sides of the dust region is related to the structure self-organization. The method used in [2] was applied to the problem of the stability of structures considered in this paper; calculations were performed for a certain set of parameters determining the structure. The stability of the structure against such one-dimensional perturbations was demonstrated. However, in the general case, the numerical investigation of the structure stability needs a large amount of computational resources and should be the subject of a separate study, in which attention should be focused on the stability of charged structures. There are also calculations [3] showing that quasineutral structures are unstable against two-dimensional perturbations, which leads to dust convection in the nonlinear stage. Numerical calculations of quasineutral structures show that, in the nonlinear stage, convection is superimposed on the main steady-state distribution, which results in small perturbations of the above distributions in the direction of the initial ion drift. The perturbations perpendicular to the ion drift naturally cannot be considered weak because they are absent in the equilibrium structure. It is important that, in presence of convection, the distributions along the ion drift are, in the first approximation, the same as in the one-dimensional case. The generation of convection also has a threshold related to ion–neutral collisions.

4.3. Kinetic Effects

It was natural to start the investigation of structures using a hydrodynamic approach as was made in this paper. However, the necessity of applying a kinetic approach is obvious. It is interesting to note that the necessity of the appearance of sharp boundaries within a kinetic approach was demonstrated in [7]; this result agrees with the results obtained in the present paper. However, to obtain completely self-consistent distributions of the structure parameters, using a kinetic approach is much more complicated than the problem considered here.

Finally, we will shortly compare our results with other theoretical investigations of structures, as well as with experiments and observations. The distributions of the dust density and dust charge were previously calculated numerically in [8] using certain assumptions for either the plasma and field distributions or some other components of the system. Our investigation shows that, if the problem is formulated self-consistently, then there is no such freedom and all the distributions inside the structure are completely determined by a single parameter (if the size of dust particles and the temperature ratio are fixed as is often the case). This property of self-organized structures, which is very important in applications, substantially narrows the possibilities of comparing them with observations. One should have in mind that this narrowing was found only for the steady-state distributions considered above. During the structure formation, a variety of initial nonlinear evolutions are possible; however, finally, the self-organization process leads to a certain single solution. In this context, it is important to keep in mind an estimate for the time during which the structure is formed. For large-mass dust particles ($m_d > m_{d,cr}$, where $m_{d,cr} \approx (3m_i\tau)(n_n Z_d/n_0)$), this time is determined by the dust inertia and is on the order of the inverse dust-plasma frequency. For small-mass dust particles ($m_d < m_{d,cr}$), this time is determined by dust friction on neutral atoms. Estimates using these formulas show that the characteristic time during which steady-state dust structures are formed is quite short as

compared to the observation time both for laboratory experiments and space plasma. When comparing with laboratory experiments, one should keep in mind that, in this paper, gravity was not taken into account. There are laboratory experiments with small dust particles in which the Earth's gravity is unimportant [2] and in which ionization voids were observed. Further investigations can go both in the direction of variation of ionization rates in experiments similar to [2] with efforts in the experimental detection of structures investigated here and in the direction of theoretical computation of structures in the presence of a constant gravity field. The investigations carried out in the latter direction can answer the question of what the maximum thickness of a dust cloud should be after melting or evaporation of the plasma–dust crystal [9, 10] and indirectly can answer the question of how many layers of a dust crystal can be created. Note that, for the plasma parameters in a plasma–dust crystal, we have $a \approx 0.1$–0.15, $\tau \approx 0.02$, and the quasineutrality parameter is $a^2/\tau \approx 0.2$–1; therefore, all of the above results on charged structures can be applied to relevant dust–plasma crystal experiments if gravity is included to further generalize these results. For experiments with small dust particles such as [2], the condition of quasineutrality is satisfied but not with a large reserve, because the present investigation demonstrates that quasineutrality really occurs only when the parameter a^2/τ is less than 10^{-3}.

In regard to space observations, it should be mentioned that thin dust layers were observed in rocked probing of the upper atmosphere and in scattering of radio signals by the lower ionosphere [11, 12]. A detailed comparison with the results of the present investigation requires a special investigation; however, an estimate of the layer thickness based on the results of the this investigation shows that the observed thickness is on the order of that predicted for self-organized structures.

The results obtained show that, for given values of the parameters a, τ, and u_0, the structure should have a definite total (integrated across the layer) number of dust particles and a definite total charge per cm^2. These values were given above as dimensionless numbers N_d and Q_d. These numbers can be compared with experimental results and observations. For this purpose, we give here the expressions (in dimensional units) for the number of dust particles per unit area $N_{d,\,\mathrm{exp}}$ and the total charge per unit area $Q_{d,\,\mathrm{exp}}$:

$$N_{d,\,\mathrm{exp}} = N_d \frac{\tau}{4\pi a^2}, \quad Q_{d,\,\mathrm{exp}} = Q_d \frac{Z_d e \tau}{4\pi z a^2} = Q_d \frac{T_i}{4\pi a e}. \quad (50)$$

ACKNOWLEDGMENTS

I express deep thanks for my hosts' hospitality during my stay in the Max Plank Institute for Extraterrestrial Physics (Garching, Germany) and for support of Alexander von Humbold Foundation. This work was supported in part by INTAS, grant no. 97-2149.

REFERENCES

1. V. N. Tsytovich, Comments Plasma Phys. Controlled Fusion **1** (2), 54 (1999).
2. J. Goree, G. Morfill, V. N. Tsytovich, and S. V. Vladimirov, Phys. Rev. E **59**, 7055 (1999).
3. A. Bouchoule, G. Morfill, and V. N. Tsytovich, Comments Plasma Phys. Controlled Fusion **1** (3), 47 (1999).
4. V. N. Tsytovich, Y. Khodataev, R. Bingham, and D. Resendes, Comments Plasma Phys. Controlled Fusion **17**, 287 (1996).
5. V. N. Tsytovich, Usp. Fiz. Nauk **167**, 57 (1997) [Phys. Usp. **40**, 53 (1997)].
6. G. E. Morfill and E. Grun, Planet. Space Sci. **27**, 1282 (1979).
7. I. M. Ignatov, J. Phys. III **7**, C4–215 (1997).
8. T. Nitter and O. Havnes, Earth, Moon, Planets **56**, 7 (1992).
9. H. Thomas, G. E. Morfill, V. Demmel, *et al.*, Phys. Rev. Lett. **73**, 652 (1994).
10. G. E. Morfill, H. M. Thomas, U. Konopka, and M. Zuzic, Phys. Plasmas **6**, 1 (1999).
11. U. P. Hoppe, D. C. Fritts, I. M. Reid, *et al.*, J. Atmos. Sci. **37**, 1342 (1998); O. Havnes, in *Proceedings of 2nd International Conference on Physics of Dusty Plasmas, Hakone, 1999*, p. 28.
12. O. Havness, U. de Angelis, R. Bingham, *et al.*, J. Atmos. Terr. Phys. **52**, 637 (1990).

Translated by the author

Plasma Physics Reports, Vol. 26, No. 8, 2000, pp. 682–690. Translated from Fizika Plazmy, Vol. 26, No. 8, 2000, pp. 727–736.

DUSTY PLASMA

Ionization Instability and Dusty Plasma Structurization

G. Morfill* and V. N. Tsytovich**

**Max-Planck Institute for Extraterrestrial Physics, 85740 Garching, 1603 Germany*
e-mail: gem@mpe.mpg.de
***Institute of General Physics, Russian Academy of Sciences, ul. Vavilova 38, Moscow, 117942 Russia*
e-mail: tsytov@td.lpi.ac.ru

Received September 23, 1999; in final form, January 27, 2000

Abstract—In the presence of ionization processes, a homogeneous equilibrium dust distribution often appears as a balance between plasma generation by ionization and plasma absorption by dust particles. It is shown that such equilibrium, often present in laboratory plasmas, is generally unstable against the formation of dust clumps separated by dust-free regions (dust voids). The driving force that separates an initially homogeneous dusty plasma into dust clumps and dust voids is the drag force produced by ions flowing out from the regions with reduced dust density. The lower the dust density, the lower the electron absorption by dust particles and the larger the ionization rate proportional to the electron density. An increase in the ion drag force leads to a further decrease in the dust density and, thus, drives the instability. In the nonlinear stage, the instability creates structures—dust clouds separated by dust voids. The dependence of the instability growth rate on the wavenumber (or, in other words, on the size of the dust-free and dust-containing regions) is investigated. It is shown that, for sufficiently small wavenumbers, a homogeneous distribution is always unstable. An analogy with a gravitational-like instability related to shadowing of the plasma flux by dust particles is pointed out. This effect, which is due to collective shadowing of the plasma flux, dominates the shadowing by individual dust particles discussed previously. Similar to the usual gravitational instability, perturbations with the largest scales are always unstable. Contrary to the usual gravitational instability, the largest growth rate corresponds not to the largest possible scale but to the size close to the mean free path of plasma particles colliding with dust particles. A special investigation is undertaken to determine the influence of the ion–neutral collisions on the growth rate of the instability. © *2000 MAIK "Nauka/Interperiodica".*

1. INTRODUCTION

The term "dusty plasma" is often used for the state where the plasma components (electron, ions, and neutral atoms) are present together with solid grains. The latter, being highly charged, play an important role in the charge balance. The dusty plasma is not a usual multicomponent plasma, because the charges of dust particles are not fixed and depend on local plasma conditions and plasma currents that are responsible for dust charging. Since, in the charging process, the dust absorbs plasma particles, dusty plasmas are always open systems and need a source of ionization to sustain the ion and electron densities. The openness of the systems can support self-organization and structurization. A steady-state dusty plasma can occur when the absorption of plasma particles by dust is balanced by the creation of new plasma particles due to ionization. Such an equilibrium corresponds to a homogeneous state with constant densities of dust and plasma components. When speaking about dusty plasmas, one usually has this state in mind. However, up to the present time, this state has very rarely been found in experiments (see [1–3]). In this paper, we will show that the homogeneous dusty plasma formed due to the balance between ionization of neutrals and absorption of plasma particles by dust grains is always unstable against the creation of structures. In the nonlinear stage of the instability, these structures form dust clumps separated by dust voids. A general statement proven below is that dusty plasmas should exist, as a rule, in highly inhomogeneous structured states. It is these states for which the theory of dusty plasmas should be developed. The results of previous theoretical investigations, devoted mainly to homogeneous dusty plasmas, can be applied only to perturbations with a scale length shorter than the characteristic size of the dusty plasma structures. The latter can be estimated from the size for which the growth rate is maximum. Our aim here is to find this characteristic size and to show that, in many cases, it is of the order of the plasma-particle mean free path with respect to absorption by dust particles. This size can be rather small for many dusty plasma experiments: it is larger than the ion Debye radius d_i by a factor of only $d_i/a \gg 1$ (where a is the size of the dust particles).

Here, we examine the case in which the ionization rate is proportional to the electron density. Electron-impact ionization is one example where this condition is met. For instance, it is the most important ionization process in many laboratory experiments with RF-discharge dusty plasmas. Impact ionization is proportional to the electron density only when the degree of ionization is low and the neutral atom density is much higher

1063-780X/00/2608-0682$20.00 © 2000 MAIK "Nauka/Interperiodica"

than the electron or ion density. Most of the laboratory experiments with dusty plasmas satisfy this requirement. However, more advanced models should incorporate, for example, the balance of the number of neutral atoms in the ionization process. Under astrophysical conditions, different ionization mechanisms such as ionization by plasma flows or external radiation can be involved. The source of ionization can create fast electrons, which then take part in the ionization process. In this case, the ionization rate is also proportional to the electron density. The initial homogeneous dust-plasma state in which the ionization of neutral atoms is balanced by the plasma recombination by dust particles can be formed under astrophysical conditions, particularly, in dust–molecular clouds and protoplanetary clouds, in which ionization can be produced by cosmic and subcosmic rays or radioactivity. In all these examples, the gas-phase (volume) recombination is rather weak. Here, we concentrate our attention on the simplest case in which the gas-phase recombination is negligible; the plasma balance is established due to recombination of the plasma on the dust; and the ionization rate is proportional to the electron density, the proportionality factor being the function of the ionization source power.

It will be shown below that, under these conditions, the homogeneous plasma state is unstable against the creation of dust clumps separated by dust voids.

The mechanism for this instability is rather simple. Below, we describe it qualitatively. Let us assume that, in some spatial region, a fluctuation decreases the dust density. This should increase the electron density, because the absorption of electrons by dust particles is decreased. Both electrons and ions are produced by an ionization source. The ions created should form an ion flow directed toward the region with a higher dust density because the plasma particles are absorbed there more strongly. Due to the excess of negatively charged dust particles in the regions surrounding the dust rarefaction, an electric field is produced that accelerates the ions and decelerates the electrons. Since the momentum is transferred to dust particles mainly by ions, the ion flow creates a drag force acting on the dust particles. The enhanced drag force created by the dust rarefaction acts on the dust to increase this rarefaction. This is the reason why the instability develops. The nonlinear stage of this instability depends on what kind of new equilibrium can be established. A new equilibrium is possible if dust-free regions are formed, i.e., when the decrease in the dust density proceeds up to the stage in which no dust is left in the rarefaction region [2, 4, 5]. The process ends with approaching the state with many dust clumps (or dust structures) separated by dust voids.

It was shown in [4, 5] that, at the boundary between a dust-containing region and a dust void, a discontinuity of the dust density occurs, whereas the other plasma parameters (such as the electron and ion densities) remain continuous. The jump in the dust density at the boundary can be explicitly calculated (see [4, 5]). This result is obtained for small-size dust particles, when the dust inertia can be neglected.

Although the nonlinear stage of the instability is not the subject of the paper, it is worthwhile to qualitatively describe why the boundary between dust voids and dust clouds should be sharp, because, in [4, 5], such an explanation is lacking. The physics of this phenomenon is related to the presence of an ion flux from the void side toward the boundary and with the collective shadowing effect. An important point is that the ion flux is produced by collective effects, i.e., by many dust particles simultaneously. We can imagine the dust close to the boundary surface as being divided into several layers. The ion flux is partially absorbed by the first dust layer; the next dust layers are exposed to a lower flux, so that the drag force acting on these layers is smaller. As a result, the first dust layer moves more rapidly than the second one and, in equilibrium, the dust is squeezed at the surface to form a sharp boundary.

In the steady-state case, the force balance for the dust near the boundary incorporates an electrostatic force and the ion-drag force. In the force balance for ions, the ion ram pressure force, ion friction on dust, and electrostatic force play an important role. Together with the adiabaticity condition for electrons, the force balance equations are sufficient to calculate the jump of the dust density at the boundary [4, 5]. Collective shadowing of the particle fluxes also plays an important role in the linear stage of the instability, which is studied in this paper.

2. IONIZATION EQUILIBRIUM IN DUSTY PLASMAS

We consider a homogeneous state of dust and plasma in the presence of homogeneous ionization. The electrons and ions created in the ionization process are absorbed by dust particles at an equal rate. In this state, the dust charging process will keep some of the electrons on the dust when equilibrium is established; therefore, the electron and ion densities will not be equal—some of the negative charge will be on the surface of the dust particles. Electrons can also be created by photoelectric ionization processes on the surface of the dust particles. The following consideration will not depend on the mechanism of the equilibrium formation if the gas-phase ionization rate and the photoelectric emission rate on the dust surface do not change when the equilibrium is disturbed.

We will normalize the ion density n on its value in the equilibrium state. We denote all the values in the equilibrium state by the subscript 0. Thus, in equilibrium, we have $n_0 = 1$. The quasineutrality condition for the equilibrium state has the form

$$1 = n_{e,0} + P_0, \quad (1)$$

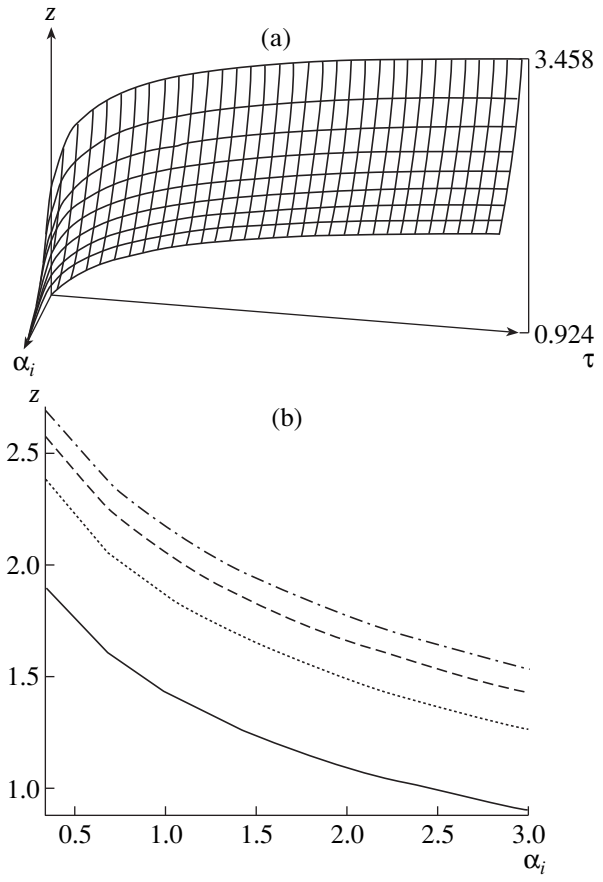

Fig. 1. (a) Dimensionless dust charge z_0 in the initial equilibrium state in argon plasma as a function of the ionization coefficient α_i and the temperature ratio τ. (b) Charge z_0 as a function of α_i for $\tau = 0.01$ (solid line), 0.04 (dotted line), 0.07 (dashed line), and 0.1 (dashed-and-dotted line).

where n_e is the electron density in units of the equilibrium ion density, $n_{e,0}$ is the electron density in the equilibrium state, $P = Z_d n_d/n_0$ is the minus dust charge density normalized on the ion charge density, $-Z_d$ is the dust charge in units of electron charge, n_d is the dust density, and $P_0 = Z_{d,0} n_{d,0}/n_0$ is the equilibrium value of P. We can express both $n_{e,0}$ and P_0 through the ionization rate α_i and the capture rate by dust particles α_c using as a unit of time $d_i^2 \sqrt{2}\, T_i/T_e a v_{Ti}$, where d_i is the equilibrium ion Debye radius; $d_i^2 = T_i/4\pi n_0 e^2$; T_i and T_e are the ion and electron temperatures, respectively; and a is the size of dust particles, which are assumed to be spherical. In these units, the ion continuity equation has the form

$$\frac{\partial n}{\partial t} + \frac{\partial \mathbf{u} n}{\partial \mathbf{r}} = -\alpha_c n P + \alpha_i n_e, \tag{2}$$

where the ion drift velocity $\mathbf{u}$ is given in units of the ion thermal velocity $\sqrt{2}\, v_{Ti}$, $v_{Ti} = \sqrt{T_i/m_i}$, and the distance $\mathbf{r}$ is given in units of d_i^2/a.

In equilibrium, the balance of volume ionization and recombination on dust can be written in the form ($n_{i,0} = 1$)

$$\alpha_c P_0 = \alpha_i n_{e,0}, \tag{3}$$

where, in the units used, the recombination rate is known to be (see [1])

$$\alpha_c = \frac{1}{2\sqrt{\pi}}\left(1 + \frac{\tau}{z}\right) \tag{4}$$

and

$$z \equiv = \frac{Z_d e^2}{a T_e}, \quad \tau = \frac{T_i}{T_e}. \tag{5}$$

The equilibrium condition for electrons is satisfied if the equilibrium condition (3) for ions is satisfied, because the electron and ions are created with equal rates in the ionization process and are recombined with equal rates on dust particles (in equilibrium, the dust charge does not change).

Relations (1) and (3) give

$$P_0 = \frac{\alpha_i}{\alpha_c + \alpha_i}, \quad n_{e,0} = \frac{\alpha_c}{\alpha_c + \alpha_i}. \tag{6}$$

The equilibrium dust charge can be determined, for example, from the orbit motion limited (OML) approach [4]. By using (5) and (6), we find

$$\exp(-z_0) = F + \frac{1}{\sqrt{\mu\tau}}[z_0(1 + \alpha_i 2\sqrt{\pi}) + \tau],$$
$$z_0 = \frac{Z_{d,0} e^2}{a T_e}, \quad \tau = \frac{T_i}{T_e}, \; \mu = \frac{m_i}{m_e}, \tag{7}$$

where F describes the process of photoelectron emission by dust particles. As soon as the ionization rate α_i and the parameter τ are fixed, Eq. (7) gives the dust charge for each type of gas (specified by the parameter μ). Then, relations (6) give the dust-to-ion density ratio and the electron-to-ion density ratio. For a fixed dust density, we obtain the electron and ion densities in the equilibrium state. Figure 1a gives the numerical results for the dust charge as a function of the ionization rate in the range $1/3 < \alpha_i < 3$ and the temperature ratio in the range $0.01 < \tau < 1$ for argon with singly ionized ions assuming $F = 0$. For hydrogen, the curves are similar in shape, but the charge values are lower (it is seen from Fig. 1a that the maximum value of z_0 is 2.058 instead of 3.458 for argon and the minimum value of z_0 is 0.278 instead of 0.924 for argon). The charge values decrease with increasing the ionization rate and decreasing the temperature ratio (see also Fig. 1b).

3. INSTABILITY OF THE EQUILIBRIUM STATE

For deviations from the equilibrium state, we use an additional sign δ for the corresponding quantity. We calculate the growth rate under several simplifying assumptions. These assumptions are (i) the quasineutrality of perturbation; (ii) the negligible role of electron inertia (by virtue of the small electron mass) and electron friction due to absorption and scattering by dust; (iii) the important role of collisions of ions with neutral atoms (if the plasma is weakly ionized) and momentum exchange with dust (dust drag); (iv) the important role of dust-ion drag and friction of dust on neutral gas; (v) ion inertia is taken into account; (vi) the dust inertia can be either small or large for small dust sizes or large dust sizes, respectively (note that the dust inertia is important only for dust sizes larger than a critical size related to dust friction on neutrals; a comparison of dust inertia and the neutral gas friction force acting on dust particles gives the critical value of this dust size); and (vii) the dust pressure term is negligible.

Both the cases where the dust inertia is negligible and where the dust inertia plays an important role will be considered. The quasineutrality assumption corresponds to large scales and low frequency (or a small growth rate) of perturbations. After finding the growth rate, we can find the range of validity of these assumptions. This range is fairly wide, so that, in fact, we will consider a rather general case.

For the perturbations, we write the momentum balance equation for electrons, ions, and dust; the continuity equations; and the quasineutrality condition.

The *quasineutrality condition* for the perturbations (which in general is expected to be valid for perturbations much longer than both electron and ion Debye radii) is

$$\delta n = \delta n_e + \delta P. \tag{8}$$

The *dust force balance equation* can be found from the following considerations. In the case of a partially ionized plasma, the dust–neutral collisions can play an important role in the onset of the instability. These collisions result in a dust friction force proportional to the dust velocity. In the case of a completely ionized plasma, the density of neutrals is zero and, hence, this friction force is also zero. In the initial equilibrium state, the dust and ion drift velocities are zero and the dust friction on neutrals and the drag by ions are zero as well. Thus, the friction force and the ion drag force act only on the perturbations. Since the ion velocity appears in the perturbation equations, the coefficient in front of the ion drag force is determined by the equilibrium values of the parameters in the linear approximation. Dust inertia is important only for large dust particles and can be treated as an additional effective friction force. The dust force balance equation for perturbation will have the form

$$\mathbf{E} - \alpha_{dr,0} z_0 n_0 \mathbf{u} + \frac{1}{z_0}\mathbf{v}_d(1 - m_d i\omega) = 0. \tag{9}$$

Here, $\mathbf{E}$ is the strength of the electric field in units of aT_e/ed_i^2 (since, in the initial equilibrium state, the electric field is absent, $\delta\mathbf{E}$ coincides with $\mathbf{E}$); $\alpha_{dr,0}$ is the ion drag force for the equilibrium values of the dust charge and density; $\mathbf{u}$ is the ion drift velocity in units of the ion thermal velocity $\sqrt{2}\,v_{Ti}$ (since, in the equilibrium state, the ion drift is absent, $\delta\mathbf{u}$ coincides with $\mathbf{u}$); $\mathbf{v}_d$ is the dust drift velocity in units of $n_0 v_{Tn}(T_i T_n/3T_e^2)/n_d$, where $v_{Tn} = \sqrt{T_n/m_n}$ is the neutral atom thermal velocity, T_n is the neutral temperature, and m_n is the neutral atom mass (since, in the equilibrium state, the dust has no drift, $\delta\mathbf{v}_d$ coincides with $\mathbf{v}_d$); z_0 is the equilibrium dimensionless dust charge determined by equation (4); m_d is the dust mass in units of $m_i\tau Z_d n_n/3n_0$, ω is the frequency of perturbations in units of $\omega_{pi}\sqrt{2}\,a/d_i$; and

$$\alpha_{dr} = \frac{2}{3\sqrt{\pi}}\left(\ln\frac{d}{a} + \frac{\tau}{z} + \frac{2\tau^2}{z^2}\right). \tag{10}$$

The first term in (9) describes the electric force acting on dust particles divided by the dust charge, the second term in (9) describes the ion drag force acting on dust particles (also divided by the dust charge), and the third term in (9) describes the dust–neutral friction force acting on dust particles and the dust inertia force (both divided by the dust charge, the reason why z_0 enters this term in the denominator). An additional factor $(1 - im_d\omega)$ describes the effective change in the friction force due to dust inertia. The reason why the last factor can be considered renormalization of the friction force is that, for a purely growing mode, when $\omega = i\Gamma$ (where $\Gamma > 0$ is the growth rate), this factor converts to $(1 + m_d\Gamma)$ and, indeed, corresponds to renormalization of the friction force. The value of m_d (dimensionless) is estimated as $m_d \approx (3m_d/m_i\tau)(n_0/Z_d n_n)$ (m_d is dimensional on the right-hand side). In existing experiments with low temperature plasmas, where $n_n/n_0 \approx 10^7$, the inertia becomes unimportant in comparison to friction for $a < (0.1\text{–}1)\mu$.

Let us turn to the *electron force balance* equation. The balance of the electric field force and the electron pressure force lead to the condition for electron adiabaticity:

$$\mathbf{E} = -\frac{1}{n_e}\frac{\partial n_e}{\partial \mathbf{r}}, \tag{11}$$

where r is in units of d_i^2/a (respectively, the wavenumber of perturbation k is in units of a/d_i^2). For harmonic

perturbations $\propto \exp(i\mathbf{k}\cdot\mathbf{r} - i\omega t)$, where ω is written in units of $\omega_{pi}\sqrt{2}\,a/d_i$ and $\omega_{pi} = \sqrt{4\pi n_0 e^2/m_i}$ is the ion plasma frequency, we find

$$\mathbf{E} = -\frac{i\mathbf{k}}{n_{e,0}}\delta n_e. \tag{12}$$

We use (12) to convert equation (9) to

$$\frac{\mathbf{k}\cdot\mathbf{v}_d(1+m_d\Gamma)}{z_0} = \alpha_{dr,0}z_0\mathbf{k}\cdot\mathbf{u} + \frac{i\mathbf{k}^2}{n_{e,0}}\delta n_e. \tag{13}$$

Let us now consider the *force balance equation for ions*. In this equation, we take into account the ion inertia, the pressure force, the electric force, the momentum transfer from ions to dust particles due to the ion drag force, and the friction on neutral atoms. The latter we write in the form $-\nu\tau\mathbf{u}$, where ν is the effective collision frequency. As a result, we obtain

$$i\mathbf{k}\left(\tau\delta n - i\omega\delta n + \frac{\delta n_e}{n_{e,0}}\right) + \mathbf{u}[z_0\alpha_{dr,0}P_0 + \tau(\nu - i\omega)] = 0. \tag{14}$$

The coefficient τ is introduced because the electric fields are, in fact, normalized to the electron temperature. The term with ω in the last brackets takes into account the ion inertia and, similar to the previous consideration for the dust inertia, can be regarded as an effective friction force for purely growing perturbations.

The next two equations are the *continuity equations for dust particles and ions*:

$$i\mathbf{k}\frac{P_0}{z_0}\cdot\mathbf{v}_d - i\nu^*\omega\delta\left(\frac{P}{z}\right) = 0, \tag{15}$$

$$i\mathbf{k}\cdot\mathbf{u} - i\omega\delta n = -\delta(\alpha_c P n) + \alpha_i\delta n_e. \tag{16}$$

Due to the normalization of the frequency and the dust velocity done above, the dust continuity equation contains an additional factor $\nu^* = \tau^2\sqrt{T_n/2T_i}\,(n_n/2n_0)$, which is the dust–neutral collision frequency. The frequency ν is related to ν by expression $\nu = \nu^* 2\sqrt{2T_n/T_i}\,(\bar{\sigma}\,Z_d/4\pi a^2\tau)$, where $\bar{\sigma}$ is the cross section for ion–neutral collisions averaged over the thermal ion and neutral atom distributions. For $\bar{\sigma} \approx 10^{-14}$ cm^{-2} and micron-size dust particles, the values of ν and ν^* are of the same order of magnitude.

The right-hand side of Eq. (16) contains the dust-charge variation of the capture coefficient:

$$\frac{\partial\alpha_c}{\partial z} = -\frac{\tau}{2\sqrt{\pi}z_0^2}. \tag{17}$$

The variation of the dust charge can be found from the charging equation [similar to Eq. (7) but for an arbitrary ion-to-electron density ratio]

$$\frac{\delta z}{z_0} = \frac{z_0+\tau}{z_0(z_0+\tau+1)}\left(\frac{\delta n_e}{n_{0,e}} - \delta n\right). \tag{18}$$

The written set of equations is sufficient to find the dispersion relation for the growth rate Γ defined by

$$\omega = i\Gamma. \tag{19}$$

This dispersion relation has the form

$$(\Gamma+\Gamma_n)\{\Gamma^2 - \Gamma_0\Gamma + (\Gamma+\alpha_c)(1+m_d\Gamma)\Gamma_1 k^2\} + \Gamma k^2\left[\Gamma_3 - \Gamma_1\frac{z_0}{\tau}(1+m_d\Gamma)\right] - k^2[\Gamma_4(1+m_d\Gamma)+\Gamma_5] + k^4(1+m_d\Gamma)\Gamma_1 = 0, \tag{20}$$

where

$$\Gamma_0 = \frac{P_0^2(z_0+\tau)^2}{2\sqrt{\pi}(z_0(z_0+\tau+1)(1-P_0)+P_0(z_0+\tau))}, \tag{21}$$

$$\Gamma_n = \nu + \frac{P_0 z_0\alpha_d}{\tau}, \tag{22}$$

$$\Gamma_1 = \frac{P_0 z_0}{n_{e0}\nu^*\left[1 + \dfrac{P_0(z_0+\tau)}{n_{e0}z_0(z_0+\tau+1)}\right]}, \tag{23}$$

$$\Gamma_3 = 1 + \frac{1}{\tau n_{e0}}\frac{1 + \dfrac{P_0(z_0+\tau)}{z_0}(z_0+\tau+1)}{1 + \dfrac{P_0(z_0+\tau)}{n_{e0}z_{z0}(z_0+\tau+1)}}, \tag{24}$$

$$\Gamma_4 = \Gamma_1\frac{\alpha_c z_0\alpha_d}{\tau}\left[1 + P_0\left(1 + \frac{\tau}{z_0(z_0+\tau+1)}\right)\right], \tag{25}$$

$$\Gamma_5 = \alpha_d z_0\left[\alpha_i + \alpha_c\left(1 + \frac{P_0\tau}{z_0(z_0+\tau+1)}\right)\right]\Gamma_1. \tag{26}$$

In the case where the dust inertia can be neglected, we can put $m_d = 0$ in (20). To take into account the dust inertia, it is sufficient to replace ν^* with $\nu^*/(1+\Gamma m_d)$ in the latter equation.

It is clear from expression (20) that Γ_0 gives the growth rate in the limit $k = 0$, and from (21) it is clear that Γ_0 is always positive, which means that the initial state is always unstable. In the case of low dust density or, more precisely, in the case when $P_0 \ll 1$, the growth rate is proportional to P_0^2. In the limit $P_0 \ll 1$ and $\tau \ll 1$, we have

$$\Gamma_0 \approx \frac{P_0^2 z_0}{z_0+1}. \tag{27}$$

The growth rate Γ_0 can also be expressed through the ionization rate by using expression (6) for P_0:

$$\Gamma_0 = \frac{2\sqrt{\pi}(z_0 + \tau)z_0\alpha_i^2}{[z_0\alpha_i 2\sqrt{\pi} + z_0 + \tau][\alpha_i 2\sqrt{\pi} + z_0 + \tau + 1]}. \quad (28)$$

Figure 2a shows the results of numerical calculations of the growth rate Γ_0 in the ranges of parameters $1/3 < \alpha < 3$ and $0.01 < \tau < 1$, and Fig. 2b shows the growth rate Γ_0 as a function of the ionization rate for $\tau = 0.01$, which is typical of most of the experiments. Both figures are evaluated for the argon plasma. In both computations, the dust inertia was neglected. It is seen that the maximum growth rate increases with τ and the maximum shifts to larger ionization rates with increasing τ. Substantial changes occur with a change in the type of gas, although the qualitative behavior is the same. In calculating the growth rate, the above results for dust charges (given in Fig. 1) were used.

The ion–neutral collision frequency and the drag force coefficient enter only expression (22) for Γ_n. This allows us to calculate the minimum value of the ion–neutral collision frequency ν_{min} when the ion–neutral collisions start to overcome the losses of ion momentum due to the dust drag. This occurs for two terms in (22) that are comparable in value. Figure 3 gives the values of ν_{min} in the same range of parameters as in Fig. 2a for argon. It is seen that the role of ion–neutral collisions increases with increasing τ.

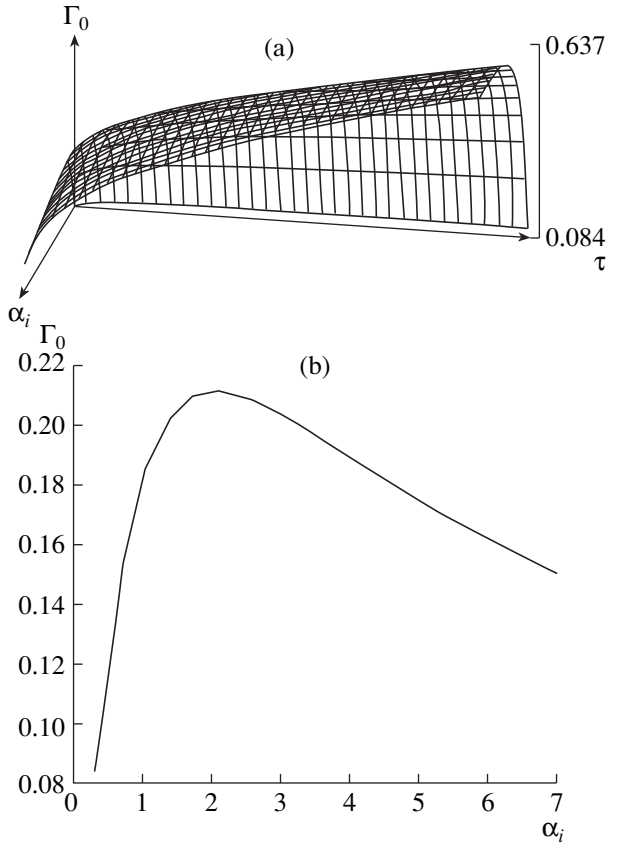

Fig. 2. (a) Dependence of Γ_0 on α_i and τ in argon plasma. (b) Dependence of Γ_0 on α_i for $\tau = 0.02$ in argon plasma.

4. RESULTS OF NUMERICAL SOLUTION OF THE DISPERSION RELATION

The aim of the numerical solution of the dispersion relation is to find the dependence of the growth rate on the wavenumber k. This dependence is not trivial, which can be seen from the analogy with gravitational instability.

The presence of an instability for $k = 0$ should be commented on because it means that the perturbations with the largest possible size in the system are unstable. It can be seen from the general dispersion relation that, for $\Gamma \gg 1$ and $k \gg 1$, the solution has the form $\Gamma = \pm ik$; i.e., the instability is absent (note that, in dimensional units, this growth rate is $\pm ikv_{Ti}$; i.e., it is similar to the sound-wave dispersion). This result resembles the known gravitation instability, for which

$$\Gamma = \sqrt{4\pi nmG - k^2 v_s^2}, \quad (29)$$

where v_s is the speed of sound and G is the gravitational constant. According to (29), the instability exists for $k = 0$, while for large k, there is a purely oscillating solution $\omega = \pm ikv_s$.

The physical reason for the gravitational instability to exist for the largest possible sizes of disturbances in the system is that the larger the size, the larger is the amount of matter involved in gravitational attraction.

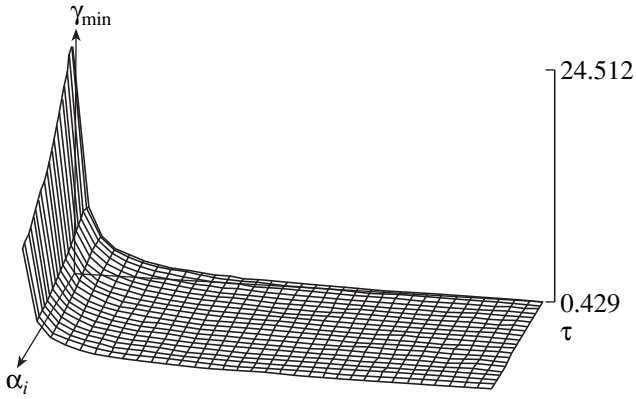

Fig. 3. Dependence of ν_{min} on the parameters in the ranges corresponding to Fig. 2a for argon plasma.

An attraction similar to gravitational attraction exists for two dust particles [6]; it appears as a result of mutual shadowing of plasma particle fluxes. The physics of this attraction is explained in detail in review [1]. Here, we are dealing with many dust particles. Apart from shadowing of a plasma flux by individual dust

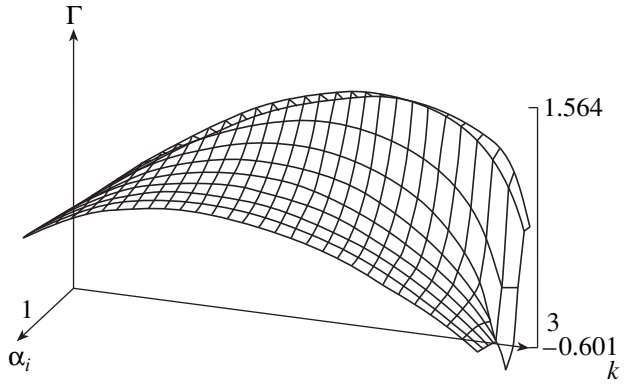

Fig. 4. Dependence of the growth rate of the instability on the wavenumber k and α_i for argon plasma in the parameter ranges $0 < k < 3$ and $0.1 < \alpha_i < 1$ for $a = 0.1$, $\tau = 0.1$, $\nu = 1$, $\nu^* = 1$, and $m_d \approx 0$.

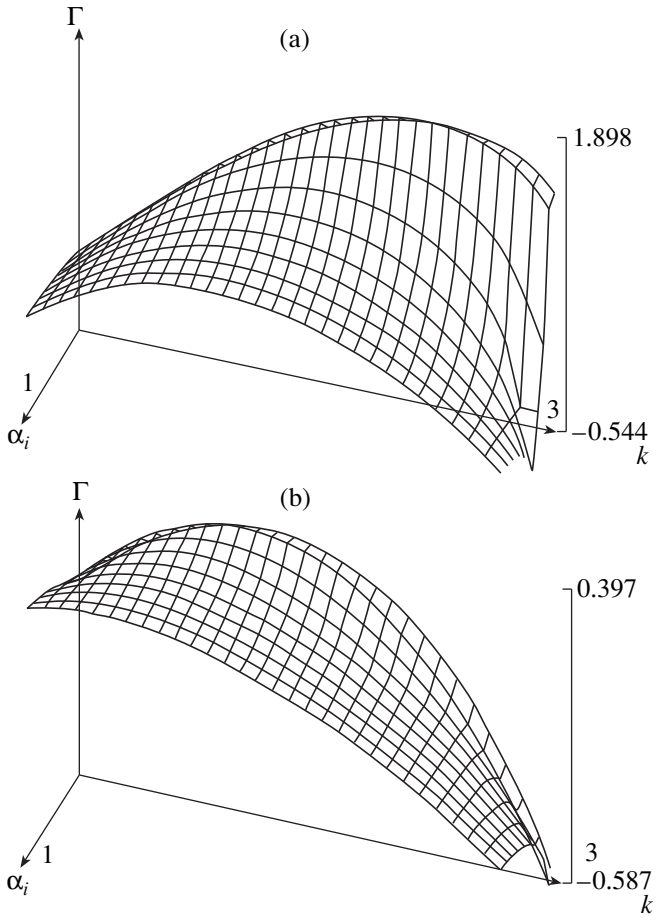

Fig. 5. Same as in Fig. 4, but for ν = (a) 10^{-2} and (b) 10.

particles, there exists the collective shadowing of the plasma flux by many dust particles (by a collective of dust particles). This collective shadowing should lead to an attraction similar to a single particle attraction but stronger than the latter due to coherency of the collective effects, which enhances the shadowing. This collective shadowing causes the existence of an instability for $k = 0$. Although there is an analogy with the gravitational instability, the physics included contains the interaction of dust particles with plasma particle and neutral atoms, which is determined by the correspondent mean free paths. In contrast to the gravitational instability, where the maximum growth rate corresponds to the largest possible size, we should expect that the instability we are considering here should be most pronounced for a wavelength on the order of the plasma particle mean free path, because, in this case, the maximum number of plasma particles take part in transferring the momentum to the dust and in collective shadowing. Thus, although the instability considered here should exist for $k = 0$, the maximum growth rate should occur at $k \approx 1$ (recall that, for the normalization used, $k = 1$ corresponds to the perturbation wavelength on the order of the ion mean free path with respect to collisions with dust particles).

This result is expected from a physical point of view. The aim of numerical calculations is to investigate the dependence of the growth rate on k and find the maximum value of the growth rate. We intend to investigate the role of neutral atoms, which participate through collision frequencies ν and ν^*, and also to find the influence of dust inertia on the instability growth rate.

Figure 4 gives the dependence of the growth rate on k and α_i for the argon plasma in the parameter ranges $0 < k < 3$ and $0.1 < \alpha_i < 1$ for $a = 0.1$, $\tau = 0.1$, $\nu = 1$, and $\nu^* = 1$ in the case when the dust inertia is negligible, $m_d \approx 0$. The growth rate has a pronounced maximum ($\Gamma_{max} = 1.564$) in this range of wavenumbers. The computations show that, as τ increases, the maximum value of Γ decreases and the interval of k in which Γ changes its sign (instability disappears) also decreases. It is found that, for $\tau = 1$ and other parameters unchanged, the maximum growth rate is $\Gamma_{max} = 1.215$. The growth rate increases with decreasing ν, and, for $\nu = 10^{-2}$ and 10 and other parameters unchanged, the maximum growth rate is $\Gamma_{max} = 1.898$ (Fig. 5a) and 0.397 (Fig. 5b), respectively. The increase in ν^* changes the growth rate in the opposite way, increasing it with decreasing ν^*. This is illustrated in Fig. 6, where $\nu^* = 0.1$ and the other parameters are the same as in Fig. 4. For astrophysical applications, the calculations were made for the case of hydrogen plasma and $a = 10^{-6}$, $\nu = 1$, $\nu^* = 1$, and $\tau = 1$. Figure 7 gives the results for $0.01 < \alpha_i < 0.1$. The maximum growth rate in this case is found to be $\Gamma_{max} = 2.464$. As ν^* decreases to 0.1, the growth rate increases to $\Gamma_{max} = 6.516$, and the increase in ν to 10 leads to a decrease in the maximum growth rate to $\Gamma_{max} = 0.91$.

The validity of neglecting the dust inertia can be found from the estimate of the growth rate $\Gamma \approx 1$. This

gives $(3m_d/m_i e^2/az_0^2 T_i)(n_0/n_n \ll 1)$. The left-hand side of the last inequality is proportional to a^2, because $m_d \propto a^3$. For a dust mass density on the order of unity and $T_i \approx 0.1$ eV, we obtain the estimate $a \ll (0.1–0.3)\mu$. For dust particles with larger sizes, the dust inertia is important.

In the case when the dust inertia plays an important role ($m_d \geq 1$), one has to renormalize the frequency ν^* by dividing it by $(1 + m_d\Gamma)$. Since the instability is anticipated to be a diffusive type and enhanced by a decrease in the collision frequency, one can expect that an increase in the dust inertia will increase the growth rate of the instability. This is confirmed by the numerical solution of the dispersion relation. The calculation of the growth rate for the same range of α_i as in Fig. 4 from 0.1 to 1 shows that changing m_d from 0 to 1 at $\alpha_i = 0.1$ increases the maximum growth rate from 1.564 to 13.025. For the same parameters but $m_d = 5$, the maximum growth rate increases to 17.936 and, for $m_d = 100$, it increases to 18.63. The larger α_i, the lower the growth rate (this tendency is the same as in the case when the dust inertia is negligible). For $m_d > 1$, the growth rate also exceeds 1 in the interval of much larger ionization rates $1 < \alpha_i < 10$. Figures 8a and 8b illustrate this effect for $m_d = 5$ and 50, respectively (the other parameters correspond to those of Fig. 4 except α_i and τ). One can see that, after the growth rate reaches its maximum, it decreases with growing k much more rapidly then in the case when the inertia is neglected.

5. DISCUSSION OF THE RESULTS

Let us discuss the validity of the above assumptions. The quasineutrality condition means that the characteristic wavenumber of disturbances should be less than the inverse Debye length. As the characteristic wavenumber, we can take the wavenumber corresponding to the maximum growth rate. The ion mean free path with respect to collisions with dust is on the order of

$$\lambda_{mfp} \approx d_i^2/aP_0. \quad (30)$$

With all variations of the parameters, we obtain that the maximum growth rate corresponds to $k \approx a/d_i^2$ (normalized k is on the order of unity). The condition for quasineutrality for dimensionless k reads

$$k \ll \frac{d_i}{a}, \quad (31)$$

which, for $d_i \gg a$, can indeed be satisfied for most of the numerical examples given above.

According to (31), the mean free path (30) can be obtained by dividing d_i^2/a by P_0 and the characteristic wavenumber can be obtained by multiplying (26) by P_0. For the range of parameters given in Fig. 5, this factor varies from 0.25 to 0.77. Thus, this factor makes the value of k for which the growth rate is maximum closer to that corresponding to the mean free path.

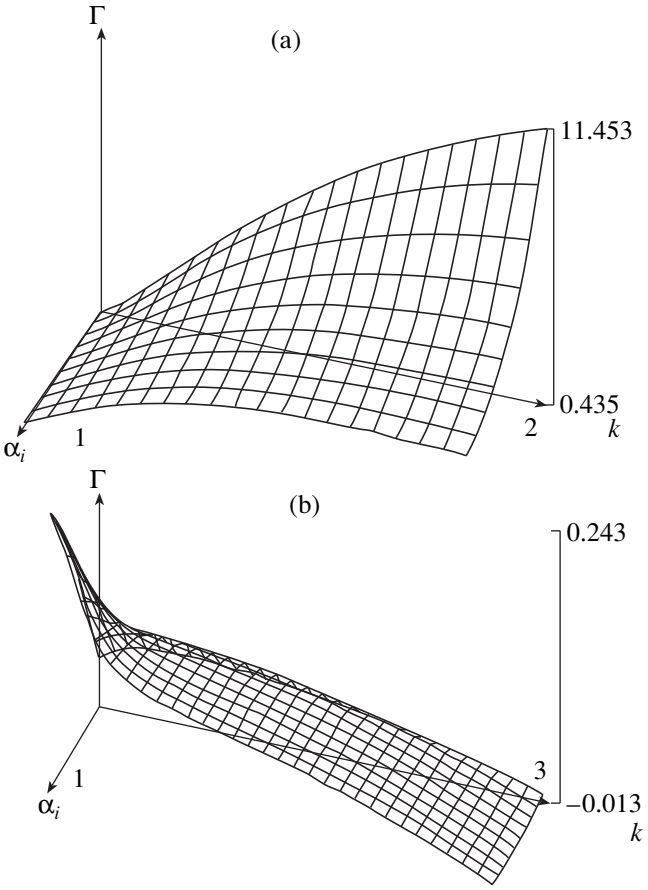

Fig. 6. Same as in Fig. 4, but for $\nu^* =$ (a) 0.1 and (b) 10.

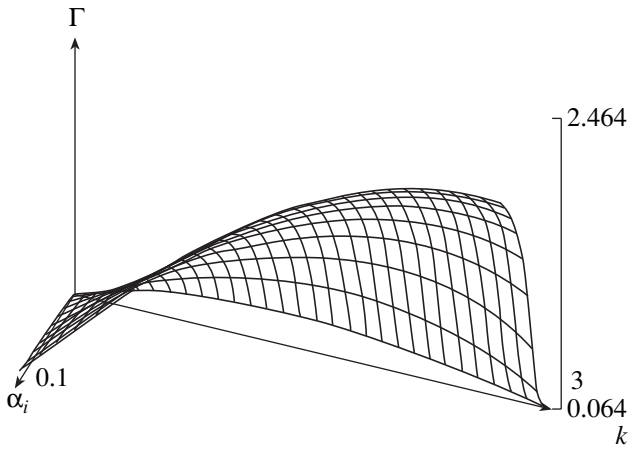

Fig. 7. Growth rate of the instability in the hydrogen plasma for $a = 10^{-6}$, $\nu = 1$, $\nu^* = 1$, $\tau = 1$, and $0.01 < \alpha_i < 0.1$.

To estimate the change in the characteristic wavenumber due to an increase in the ion–neutral collision frequency, one should consider the results presented in Fig. 5b. It is seen that the value of the characteristic

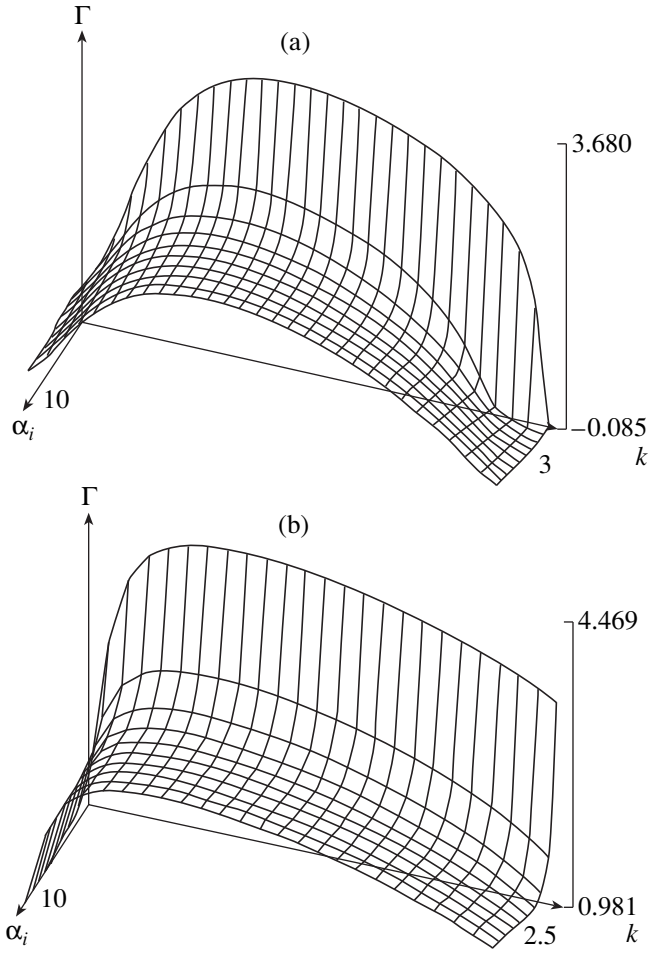

Fig. 8. Same as in Fig. 4, but for m_d = (a) 5 and (b) 50.

wavenumber changes insignificantly, although the value of $\nu = 10$ is much larger than ν_{min}. The nonlinear treatment of [4] also shows that the size of nonlinear structures is about 1 in dimensionless units.

The assumption of adiabaticity for electrons can be estimated from the condition of possible neglecting of the electron inertia and electron friction force due to the interaction of electrons with dust particles via charging them and scattering on their Coulomb fields. To obtain this estimate, one needs the above estimate of the characteristic size. As a result, we arrive at the condition

$$\tau \ll \left(\frac{m_i}{m_e}\right)^{1/3}, \tag{32}$$

which is usually satisfied.

The next condition is for neglecting the dust pressure. By using the estimate of the characteristic size, we obtain

$$T_d \ll \frac{T_e Z_d}{z}. \tag{33}$$

This condition is also easy to satisfy because of the large value of the dust particle charge.

Thus, the instability discussed in this paper applies to the parameters of a dusty plasma usually met under laboratory [2, 3] and astrophysical conditions. The linear stage of the instability does not indicate what the final nonlinear stage of its development or the characteristic size of nonlinear structures will be. However, it indicates that a homogeneous dusty plasma is always unstable against dust clumping and formation regions where the dust density is enhanced and the regions where the dust density is depleted. In some sense, this process resembles the modulational instability, which leads to the concentration of plasma oscillations in cavitons. Note that, unlike the modulational instability, the dust-clumping instability results in a stronger concentration of dust particles and the formation of dust-free regions.

ACKNOWLEDGMENTS

V. N. Tsytovich expresses his gratitude to his hosts' hospitality during his stay at the Max Plank Institute for Extraterrestrial Physics (Garching, Germany) and for support of Alexander von Humbold Foundation.

REFERENCES

1. V. N. Tsytovich, Usp. Fiz. Nauk **167**, 57 (1997) [Phys. Usp. **40**, 53 (1997)].
2. S. Samsonov and J. Goree, Phys. Rev. E **59**, 1047 (1999).
3. J. Goree, G. Morfill, V. N. Tsytovich, and S. V. Vladimirov, Phys. Plasmas **59**, 7055 (1999).
4. V. N. Tsytovich, Comments Plasma Phys. Controlled Fusion **1** (2), 54 (1999).
5. V. N. Tsytovich, Aust. J. Phys. **51**, 763 (1998).
6. V. N. Tsytovich, Y. Khodataev, R. Bingham, and D. Resendes, Comments Plasma Phys. Controlled Fusion **17**, 287 (1996).

Translated by V. Tsytovich

Plasma Physics Reports, Vol. 26, No. 8, 2000, pp. 691–700. Translated from Fizika Plazmy, Vol. 26, No. 8, 2000, pp. 737–746.

ELEMENTARY PROCESSES IN PLASMA

Analysis of the Differential Cross Sections for Bremsstrahlung during Collisions between Two Charged Particles in a Uniform Electric Field

V. I. Krylov and V. V. Pivkin

Institute of General Physics, Russian Academy of Sciences, ul. Vavilova 38, Moscow, 117942 Russia
Khabarovsk State Pedagogical University, ul. Karla Marksa 68, Khabarovsk, 680000 Russia

Received October 27, 1999

Abstract—Under the nonrelativistic Born approximation, differential cross sections are derived for elastic collisions between two point charged particles in an external constant uniform electric field and for bremsstrahlung during these collisions. An analysis of the cross sections obtained shows that, due to the interference of the wave functions of two colliding particles during their reflection from the potential barrier of an external electric field, the differential cross sections for elastic collisions and for unpolarized bremsstrahlung (i) are both oscillatory in character and (ii), instead of being linearly proportional to one another (as in the case without an external electric field), are related in a more complicated manner. © *2000 MAIK "Nauka/Interperiodica".*

1. In [1], it was shown that, even in an external uniform electric field weaker than the atomic field, the differential cross section for bremsstrahlung during a collision between two charged particles may differ significantly from that in the absence of a field.

Note that all of the calculations in [1] were based on the asymptotes of the wave functions, which describe either running or standing waves, depending on the longitudinal energy of the relative particle motion.

When an ionized gas in an external electric field is sufficiently rarefied, the longitudinal (field-aligned) component of the flux density of the relative motion of two colliding charged particles should be nonzero. Such a system is described by the wave functions corresponding to running waves at sufficiently large distances from the center of mass of two colliding particles.

Also, the pattern of the longitudinal motion of a charged particle in an external electric field changes qualitatively because the particle is reflected from the potential barrier formed by the field. In other words, the particle moves parallel or antiparallel to the external electric field in the region between the reflection point and the zone in which it interacts effectively with a scattering particle. In this spatial region, the longitudinal flux density of the relative momentum of two colliding particles should clearly be zero, so that the relevant wave function corresponds to a standing wave along the external field.

This circumstance was pointed out by Krylov [2], who proposed the asymptotes of the wave functions describing the scattering of charged particles in an external electric field.

Here, we use the asymptotes of such wave functions and the nonrelativistic Born approximation to derive the differential cross sections for bremsstrahlung during a collision between two charged particles in an external uniform electric field.

2. We consider the relative motion of two particles with charges e_1 and e_2 and masses m_1 and m_2 in an external electric field of strength $\boldsymbol{\varepsilon}$. We direct the z-axis of the Cartesian coordinates (x, y, z) along the field, so that $\boldsymbol{\varepsilon} = (0, 0, \varepsilon)$, where the sign of ε is determined by the condition $\varepsilon e_m > 0$, where $e_m = (e_1 m_2 - e_2 m_1)/(m_1 + m_2)$.

We assume that the external uniform electric field is nonzero in the half-space $z > -L$, where L is the distance from the center of inertia of a system of two interacting particles to the boundary of the field region.

With this choice of the field, we can construct a family of bounded functions $\psi_{\boldsymbol{\chi}}(\mathbf{r})$ that ensure that the longitudinal flux density of the relative particle motion is nonzero and time independent, assuming that the longitudinal energy of the relative motion satisfies the condition $E_z > e_m \varepsilon L$ (see [1] for details):

$$\psi_{\boldsymbol{\chi}}(\mathbf{r}) = \frac{A_{\boldsymbol{\chi}}}{S^{1/4}} \exp\left[i\left(\frac{2}{3}\frac{\chi_z}{|\chi_z|} S^{3/2} + \mathbf{k}_\perp \mathbf{r} \right)\right], \qquad (1)$$

where $S = \dfrac{z}{l} + \dfrac{E_z}{e_m \varepsilon l}$, $l = (\hbar^2/2m e_m \varepsilon)^{\frac{1}{3}}$, $E_z = \dfrac{\hbar^2 \chi_z^2}{2m} + e_m \varepsilon L$, $m = \dfrac{m_1 m_2}{m_1 + m_2}$, the vector $\boldsymbol{\chi} = (\mathbf{k}_\perp, \chi_z)$ determines the direction of the flux density of the relative particle motion at the boundary of the field region, and $A_{\boldsymbol{\chi}}$ is a normalization constant.

1063-780X/00/2608-0691$20.00 © 2000 MAIK "Nauka/Interperiodica"

For the range of longitudinal energies of the relative particle motion such that

$$e_m\varepsilon l \ll E_z \ll e_m\varepsilon L, \tag{2}$$

we choose the asymptotes of the wave functions in the region of allowed (in classical theory) motion in the form [2]

$$\psi_{\mathbf{k}} = A_{\mathbf{k}}\frac{e^{i\mathbf{k}_\perp\mathbf{r}}}{S^{\frac{1}{4}}}\begin{cases}\sin\left(\dfrac{2S^{\frac{3}{2}}}{3}+\alpha_1\right), & \text{for } z<0,\\ \exp\left(i\left[\dfrac{2S^{\frac{3}{2}}}{3}+\alpha_2\right]\right), & \text{for } z>0.\end{cases} \tag{3}$$

Here, the parameters α_1 and α_2 are close to $\pi/4$ and can be treated as adjustable parameters; presumably, they can only be determined from the exact solution to the Schrödinger equation for the problem at hand [2].

In order to solve for the differential cross section $d\sigma$ for bremsstrahlung in the nonrelativistic Born approximation, we start with the familiar expression [3]

$$d\sigma = \frac{1}{J}\left(\frac{\omega^3}{2\pi c^3\hbar}\right)|\mathbf{e}^*\mathbf{d}_{fj}|^2 d\mathrm{o}_{\mathrm{ph}}dn. \tag{4}$$

Here, $\omega = (E_j - E_f)/\hbar$; E_j and E_f are the energies of the initial and final states of the system; $\mathbf{e}$ is the polarization vector of an emitted photon; $d\mathrm{o}_{\mathrm{ph}} = \sin\theta_{\mathrm{ph}}d\theta_{\mathrm{ph}}d\varphi_{\mathrm{ph}}$ is the solid angle element in the wave vector space of the photon; dn is the number of states of the emitting system consisting of two colliding particles; the matrix element of the dipole moment of the system ($\mathbf{d}_{fj}$) is determined by the wave functions (1) and (3),

$$\mathbf{d}_{fj} = \frac{e_1e_2}{\omega^2}\left(\frac{e_1}{m_1}-\frac{e_2}{m_2}\right)\int_{-\infty}^{\infty}\int\psi_f^*\psi_j\nabla\frac{1}{r}d^3\mathbf{r},$$

where the functions of the initial and final states of the system, ψ_f and ψ_j, are chosen to be of the form of functions (1) or (3), depending on the range of the longitudinal energy E_z; $J = \dfrac{\hbar|A_{\chi 0}|^2}{lm}\dfrac{|\chi_0|}{|\chi_{0z}|}$ is the flux density of the relative particle motion in the initial state; and $A_{\chi 0}$ is a normalization constant for the functions (1) in the initial state.

We restrict ourselves to considering bremsstrahlung in the field direction over distances from the center of inertia of the system shorter than the distance $\dfrac{E_{0z}}{e_m\varepsilon}$, which, in turn, is much larger than the atomic distance in the range $\varepsilon \ll \dfrac{|e_m|}{a^2}$ (where $a = \dfrac{\hbar^2}{e_m^2 m}$). Given this condition, we can analyze how the external electric field "implicitly" affects bremsstrahlung from the colliding particles due to the redistribution of the interference pattern of their wave functions during the reflection from the potential barrier. Since the field strength $\boldsymbol{\varepsilon}$ is low, we can ignore photons emitted by the particles during acceleration in an external uniform electric field. Expanding the phases of the wave functions in powers of z and retaining terms up to first order, we represent the integral in the expression for $\mathbf{d}_{fj}$ in the range $E_z < e_m\varepsilon L$ as

$$\mathbf{e}\int_{-\infty}^{\infty}\int\int\psi_f^*\psi_j\nabla\frac{1}{r}dxdydz = 2\pi\frac{A_{\chi 0}A_{\mathbf{k}}^*}{\bar{S}_0^{\frac{1}{4}}\bar{S}^{\frac{1}{4}}}$$

$$\times\left\{\frac{1}{2iq_-^2}e^{i\gamma_1}[i\mathbf{e}q_- + \mathbf{e}\mathbf{u}_-] + \frac{1}{q_+^2}[ih_-\mathbf{e}\mathbf{q}_+ - h_+\mathbf{e}\mathbf{u}_+]\right\},$$

where

$$\mathbf{q}_\pm = \mathbf{k}_\pm - \mathbf{k}_0, \quad \mathbf{k}_\pm = \left(\mathbf{k}_\perp, \pm\frac{\sqrt{2mE_z}}{\hbar}\right),$$

$$\mathbf{k}_0 = \left(\mathbf{k}_{0\perp}, \frac{\chi_{0z}}{|\chi_{0z}|}\frac{\sqrt{2mE_z}}{\hbar}\right), \quad \bar{S}_0 = \frac{E_{0z}}{e_m\varepsilon l},$$

$$\bar{S} = \frac{E_z}{e_m\varepsilon l}, \quad \gamma_{1,2} = \alpha_{1,2} + \frac{2}{3}\left(\frac{E_z}{e_m\varepsilon l}\right)^{\frac{3}{2}},$$

$$h_\pm = \exp(-i\gamma_2) \pm \frac{1}{2i}(-i\gamma_1), \quad \mathbf{u}_\pm = (\mathbf{q}_\perp f_\pm, q_\perp),$$

$$f_\pm = \frac{q_\perp^2 - q_{z\pm}^2}{2q_{z\pm}^2}\left(\frac{\pi}{2}\frac{q_{z\pm}}{|q_{z\pm}|} - \arctan\frac{q_\perp}{q_{z\pm}}\right) - \frac{q_{z\pm}^2 + q_\perp^2}{2q_{z\pm}q_\perp}.$$

Note that, with function (3), this integral cannot be taken by parts, as is usually done in calculations for $\boldsymbol{\varepsilon} = 0$ (see, e.g., [3]). Taking into account the relationship

$$dn = \frac{|k_z|l}{8\pi^3|A_{\mathbf{k}}|^2}k^2dkd\mathrm{o},$$

where $d\mathrm{o} = \sin\theta d\theta d\varphi$ is the solid angle element containing the vector $\mathbf{k}$, we obtain from (4) the related cross section $d\sigma_{\mathbf{e}}$ for the emission of a photon during a collision between two charged particles in an external uniform electric field.

In Coulomb units with the scale length $a = \dfrac{\hbar^2}{e_m^2 m}$, in the range $\varepsilon^{\frac{2}{3}} \ll \dfrac{k_{z+}^2}{2} \ll \varepsilon L$, this cross section takes

the form

$$d\sigma_{\mathbf{e}} = \frac{1}{4\pi^2}\alpha^3\frac{|\chi_{0z}|}{|k_{0z}|}\frac{k}{\chi_0}(Z_1Z_2Z_m)^2|T_{\mathbf{e}}|^2\frac{d\omega}{\omega}d\mathrm{o}_{\mathrm{ph}}d\mathrm{o}, \quad (5)$$

where

$$k_+^2 = k_-^2 \equiv k^2,$$

$$|T_{\mathbf{e}}|^2 = \frac{1}{4q_-^4}[(\mathbf{e}^*\mathbf{q}_-)(\mathbf{e}\mathbf{q}_-) + i(\mathbf{e}\mathbf{q}_-)(\mathbf{e}^*\mathbf{u}_-) - i(\mathbf{e}^*\mathbf{q}_-)(\mathbf{e}\mathbf{u}_-) + (\mathbf{e}\mathbf{u}_-)(\mathbf{e}^*\mathbf{u}_-)]$$

$$+ \frac{i}{2q_-^2q_+^2}\{e^{i\gamma_1}[ih_+^*(\mathbf{e}\mathbf{q}_-)(\mathbf{e}^*\mathbf{u}_+) + ih_-^*(\mathbf{e}^*\mathbf{q}_+)(\mathbf{e}\mathbf{u}_-) + h_+^*(\mathbf{e}\mathbf{u}_-)(\mathbf{e}^*\mathbf{u}_+) - h_-^*(\mathbf{e}\mathbf{q}_-)(\mathbf{e}^*\mathbf{q}_+)]$$

$$+ e^{-i\gamma_1}[h_-(\mathbf{e}\mathbf{q}_+)(\mathbf{e}^*\mathbf{q}_-) + ih_-(\mathbf{e}\mathbf{q}_+)(\mathbf{e}^*\mathbf{u}_-) + ih(\mathbf{e}^*\mathbf{q}_-)(\mathbf{e}\mathbf{u}_+) - h_+(\mathbf{e}\mathbf{u}_+)(\mathbf{e}^*\mathbf{u}_-)]\}$$

$$+ \frac{1}{q_+^4}\{|h_-|^2(\mathbf{e}^*\mathbf{q}_+)(\mathbf{e}\mathbf{q}_+) + ih_-^*h_+(\mathbf{e}^*\mathbf{q}_+)(\mathbf{e}\mathbf{u}_+) - ih_-h_+^*(\mathbf{e}\mathbf{q}_+)(\mathbf{e}^*\mathbf{u}_+) + |h_+|^2(\mathbf{e}^*\mathbf{u}_+)(\mathbf{e}\mathbf{u}_+)\},$$

$Z_{1,2,m} = \frac{e_{1,2,m}}{|e|}$, e is the electron charge, α is the fine structure constant, $k^2 = k_0^2 - 2\omega$ (in Coulomb units $\gamma_{1,2} = \alpha_{1,2} + \frac{|k_{z+}|^3}{3\varepsilon}$, $\mathbf{k} = k(\sin\theta\cos\varphi, \sin\theta\sin\varphi, \cos\theta)$, and $\mathbf{k}_0 = k_0(\sin\theta_0, 0, \cos\theta_0)$.

Note that, in (5), the angle θ is in the interval $(0, \pi/2)$.

In the range $E_z > \varepsilon L$, the same procedure yields

$$d\sigma_{\mathbf{e}} = \frac{\alpha^3}{\pi^2}\frac{|\chi_{0z}|}{|k_{0z}|}\frac{k}{\chi_0}(Z_1Z_2Z_m)^2\frac{|\mathbf{e}\mathbf{q}_+|^2}{q_+^4}\frac{d\omega}{\omega}d\mathrm{o}_{\mathrm{ph}}d\mathrm{o}, \quad (6)$$

where $\theta \in (0, \pi)$.

For $E_z \gg \varepsilon L$, the coefficient $\frac{|\chi_{0z}|}{|k_{0z}|}$ in (6) is close to unity, so that, in the absence of an external field ($\boldsymbol{\varepsilon} = 0$), expression (6) passes over to the following formula for the differential cross section $d\sigma_{0\mathbf{e}}$ for bremsstrahlung during a collision between charged particles (see, e.g., [3]):

$$d\sigma_{0\mathbf{e}} = \frac{\alpha^3}{\pi^2}(Z_1Z_2Z_m)^2\frac{\chi}{\chi_0}\frac{|\mathbf{e}\mathbf{q}_\chi|^2}{q_\chi^4}\frac{d\omega}{\omega}d\mathrm{o}_{\mathrm{ph}}d\mathrm{o}, \quad (7)$$

where $\chi^2 = \chi_0^2 - 2\omega$, $\mathbf{q}_\chi = \boldsymbol{\chi} - \boldsymbol{\chi}_0$, $\boldsymbol{\chi}_0 = \left(\mathbf{k}_{0\perp}, \frac{k_{0z}}{|k_{0z}|}\sqrt{k_{0z}^2 - 2\varepsilon L}\right)$, $\boldsymbol{\chi} = \chi(\sin\theta\cos\varphi, \sin\theta\sin\varphi, \cos\theta)$.[1]

Summing (5)–(7) over the polarization vectors of the emitted photons, we arrive at the differential cross sections for the emission of unpolarized photons, $d\sigma_{\mathbf{n}}$ for $\boldsymbol{\varepsilon} \neq 0$ and $d\sigma_{0\mathbf{n}}$ for $\boldsymbol{\varepsilon} = 0$.

In the range $\varepsilon^{\frac{2}{3}} \ll E_z \ll \varepsilon L$, we obtain

$$d\sigma_{\mathbf{n}} = \frac{1}{4\pi^2}\alpha^3\frac{|\chi_{0z}|}{|k_{0z}|}\frac{k}{\chi_0}(Z_1Z_2Z_m)^2|T_{\mathbf{n}}|^2\frac{d\omega}{\omega}d\mathrm{o}_{\mathrm{ph}}d\mathrm{o}, \quad (8)$$

where

$$|T_{\mathbf{n}}|^2 = \frac{1}{4q_-^4}([\mathbf{q}_-, \mathbf{n}]^2 + [\mathbf{u}_-, \mathbf{n}]^2) + \frac{i}{2q_-^2q_+^2}$$

$$\times\{(e^{-i\gamma_1}h_- - h_-^*e^{i\gamma_1})[\mathbf{q}_-, \mathbf{n}][\mathbf{q}_+, \mathbf{n}] + i(h_+^*e^{i\gamma_1} + h_+e^{-i\gamma_1})[\mathbf{q}_-, \mathbf{n}][\mathbf{u}_+, \mathbf{n}] + i(h_-^*e^{i\gamma_1} - h_-e^{-i\gamma_1})[\mathbf{q}_+, \mathbf{n}][\mathbf{u}_-, \mathbf{n}] + (h_+^*e^{i\gamma_1} - h_+e^{-i\gamma_1})[\mathbf{u}_+, \mathbf{n}][\mathbf{u}_-, \mathbf{n}]\}$$

$$+ \frac{1}{q_+^4}\{|h_-|^2[\mathbf{q}_+, \mathbf{n}][\mathbf{q}_+, \mathbf{n}] + |h_+|^2[\mathbf{u}_+, \mathbf{n}][\mathbf{u}_+, \mathbf{n}] + i(h_-^*h_+ - h_-h_+^*)[\mathbf{q}_+, \mathbf{n}][\mathbf{u}_+, \mathbf{n}]\},$$

$$\mathbf{n} = \frac{\mathbf{k}_{\mathrm{ph}}}{k_{\mathrm{ph}}}, \quad \theta \in \left(0, \frac{\pi}{2}\right).$$

In the range $E_z > \varepsilon L$, we obtain

$$d\sigma_{\mathbf{n}} = \frac{\alpha^3}{\pi^2}\frac{|\chi_{0z}|}{|k_{0z}|}\frac{k}{\chi_0}(Z_1Z_2Z_m)^2\frac{[\mathbf{q}_+, \mathbf{n}]^2}{q_+^4}\frac{d\omega}{\omega}d\mathrm{o}_{\mathrm{ph}}d\mathrm{o}. \quad (9)$$

According to the energy conservation law, we have $k^2 = k_0^2 - 2\omega$ in expressions (8) and (9), as well as in (5) and (6).

In the absence of an external electric field ($\varepsilon = 0$), we obtain

$$d\sigma_{0\mathbf{n}} = \frac{\alpha^3}{\pi^2}\frac{\chi}{\chi_0}(Z_1Z_2Z_m)^2\frac{[\mathbf{q}_\chi, \mathbf{n}]^2}{q_\chi^4}\frac{d\omega}{\omega}d\mathrm{o}_{\mathrm{ph}}d\mathrm{o}. \quad (10)$$

Note that the mathematical expressions derived here for the cross sections at $\boldsymbol{\varepsilon} \neq 0$ are far more complicated than the corresponding expressions obtained in [1].

[1] The vectors $\boldsymbol{\chi}_0$, $\boldsymbol{\chi}$, and $\mathbf{q}_\chi$ in (7) may be replaced with $\mathbf{k}_0$, $\mathbf{k}$, and $\mathbf{q}_+$, in which case, however, the initial kinetic energy of the relative particle motion for $\boldsymbol{\varepsilon} = 0$ would be larger by an amount εL; for $\boldsymbol{\varepsilon} \neq 0$, this circumstance renders a comparison between (5), (6), and (7) impossible.

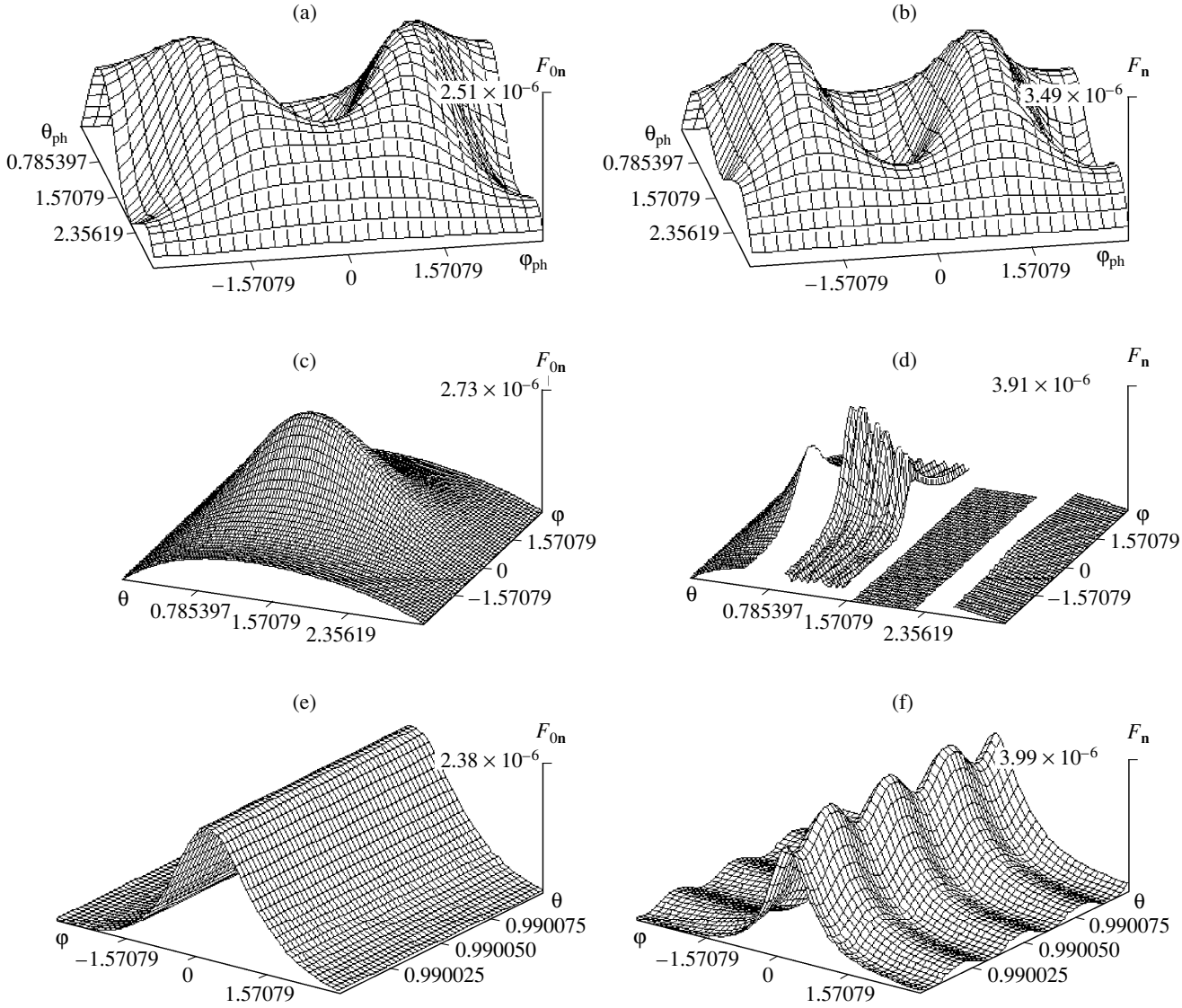

Fig. 1. Surfaces (a) $F_{0\mathbf{n}}(\theta_{ph}, \varphi_{ph})$, (b) $F_{\mathbf{n}}(\theta_{ph}, \varphi_{ph})$, (c) $F_{0\mathbf{n}}(\theta, \varphi)$, and (d) $F_{\mathbf{n}}(\theta, \varphi)$ for $\omega = 315$, $\theta_0 = 0.90$, $\theta = 1.07$, $\varphi = 0.36$, $\theta_{ph} = 1.57$, and $\varphi_{ph} = -1.88$ and portions of the surfaces (e) $F_{0\mathbf{n}}(\theta, \varphi)$ and (f) $F_{\mathbf{n}}(\theta, \varphi)$ in the interval $\theta \in (0.99, 0.9901)$.

The cross section $d\sigma_{\mathbf{n}}$ can be analyzed only numerically (in the same way as was done in [4]), because the expression for $|T_{\mathbf{n}}|^2$ is very lengthy. A numerical analysis showed that the biggest difference between $d\sigma_{\mathbf{n}}$ and $d\sigma_{0\mathbf{n}}$ is observed when the angular coordinates θ, φ of the points at which the surface

$$F_{\mathbf{n},0\mathbf{n}} = \frac{\pi^2}{\alpha^3 (Z_1 Z_2 Z_m)^2} \frac{d\sigma_{\mathbf{n},0\mathbf{n}}}{d\omega d\theta d\varphi d\theta_{ph} d\varphi_{ph}}$$

is most peaked lie in the interval satisfying the condition $k_z^2 < 2\varepsilon L$ in the θ, φ plane. This situation is illustrated in Fig. 1, which shows the surfaces $F_{\mathbf{n}}(\theta, \varphi)$, $F_{0\mathbf{n}}(\theta, \varphi)$, $F_{\mathbf{n}}(\theta_{ph}, \varphi_{ph})$, and $F_{0\mathbf{n}}(\theta_{ph}, \varphi_{ph})$ computed at $\varepsilon = 0.01$, $L = 10^4$, $k_0 = 30$, $\omega = 315$, and $\alpha_1 = \alpha_2 = 0.78 \approx \pi/4$, and at $\theta_0 = 0.90$, $\theta_{ph} = 1.57$, and $\varphi_{ph} = -1.88$ for $F_{\mathbf{n},0\mathbf{n}}(\theta, \varphi)$ and at $\theta = 1.07$ and $\varphi = 0.36$ for $F_{\mathbf{n},0\mathbf{n}}(\theta_{ph}, \varphi_{ph})$. Parenthetically, in this and other figures, the portions of the surface in the intervals where the angle θ is such that the k_z^2 values are close to $2\varepsilon L$ are left white, because expression (8) is meaningful only for $k_z^2 \ll 2\varepsilon L$.

The values of the angles θ_0, θ, φ, θ_{ph}, and φ_{ph} were obtained by analyzing the functions $F_{\mathbf{n}}(\theta, \theta_0)$, $F_{\mathbf{n}}(\theta_0, \varphi)$, $F_{\mathbf{n}}(\theta_{ph}, \theta_0)$, and $F_{\mathbf{n}}(\theta_0, \varphi_{ph})$ numerically and correspond to the highest peaks in the functions $F_{\mathbf{n}}(\theta, \varphi)$ and $F_{\mathbf{n}}(\theta_{ph}, \varphi_{ph})$ for the chosen values of ε, L, k_0, ω, α_1, and α_2.

From the shapes of the surfaces $F_{\mathbf{n}}(\theta_{ph}, \varphi_{ph})$ and $F_{0\mathbf{n}}(\theta_{ph}, \varphi_{ph})$, it is easy to establish that the angular dis-

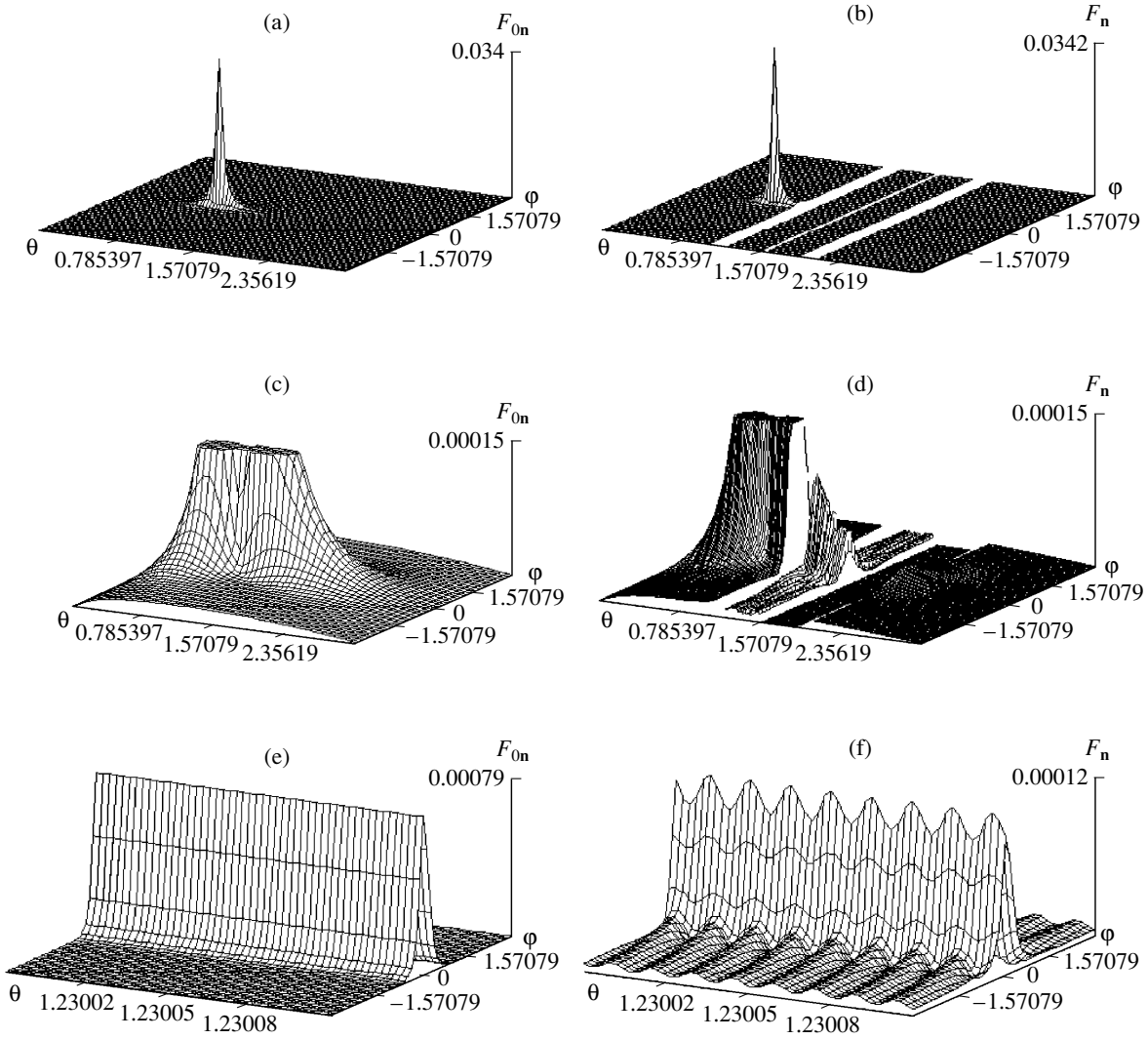

Fig. 2. Surfaces (a) $F_{0\mathbf{n}}(\theta, \varphi)$ and (b) $F_{\mathbf{n}}(\theta, \varphi)$ for $\omega = 25$, $\theta_0 = 0.82$, $\theta_{ph} = 1.69$, and $\varphi_{ph} = -1.47$; surfaces (c) $F_{0\mathbf{n}}(\theta, \varphi)$ and (d) $F_{\mathbf{n}}(\theta, \varphi)$ below the level 0.00015; and portions of the surfaces (e) $F_{0\mathbf{n}}(\theta, \varphi)$ and (f) $F_{\mathbf{n}}(\theta, \varphi)$ in the interval $\theta \in (1.23, 1.2301)$.

tribution of the emitted photons during collisions between the particles can differ markedly from that in the absence of an external field ($\boldsymbol{\varepsilon} = 0$).

The difference in the behavior of $d\sigma_{\mathbf{n}}$ and $d\sigma_{0\mathbf{n}}$ is even more significant for other directions of the wave vector $\mathbf{k}_+$, which governs the relative motion of colliding particles in the final state (at fixed θ_{ph} and φ_{ph}). Actually, the structure of the function $F_{\mathbf{n}}(\theta, \varphi)$, which characterizes the dependence of $d\sigma_{\mathbf{n}}$ on θ and φ, is oscillatory over the interval of the angles θ that satisfy the condition $k_z^2 \ll 2\varepsilon L$, whereas the surface $F_{0\mathbf{n}}(\theta, \varphi)$ does not exhibit oscillatory behavior. In Fig. 1, this can be seen more clearly from the portions of the surfaces $F_{\mathbf{n}}(\theta, \varphi)$ and $F_{0\mathbf{n}}(\theta, \varphi)$ in the interval (0.99, 0.9901) of the angle θ: over this interval, the function $F_{\mathbf{n}}$ varies periodically by more than 25% (at $\varphi \approx 0.25$, which corresponds to the maximum values of $F_{\mathbf{n}}$).

Figure 2 illustrates how the surfaces $F_{\mathbf{n}}(\theta, \varphi)$ and $F_{\mathbf{n}}(\theta_{ph}, \varphi_{ph})$ change when the frequency is changed from 315 to 25.

One can see that, in the range $\omega > 100$, the highest peak in the surface $F_{\mathbf{n}}(\theta, \varphi)$ is displaced toward the point $\theta = \pi/2$ while simultaneously becoming lower.

Analyzing the cross section for the emission of a photon with a frequency lower than 100 (at a fixed $k_0 = 30$), we can see that the highest peak in the surface $F_{\mathbf{n}}(\theta, \varphi)$ is shifted toward smaller values of θ, so that the bremsstrahlung is governed primarily by expression (9), which is valid under the condition $k_z^2 > 2\varepsilon L$. This is readily seen from Fig. 2, in which the surfaces $F_{\mathbf{n}}(\theta, \varphi)$ and $F_{0\mathbf{n}}(\theta, \varphi)$ computed for $\omega = 25$ are similar in shape.

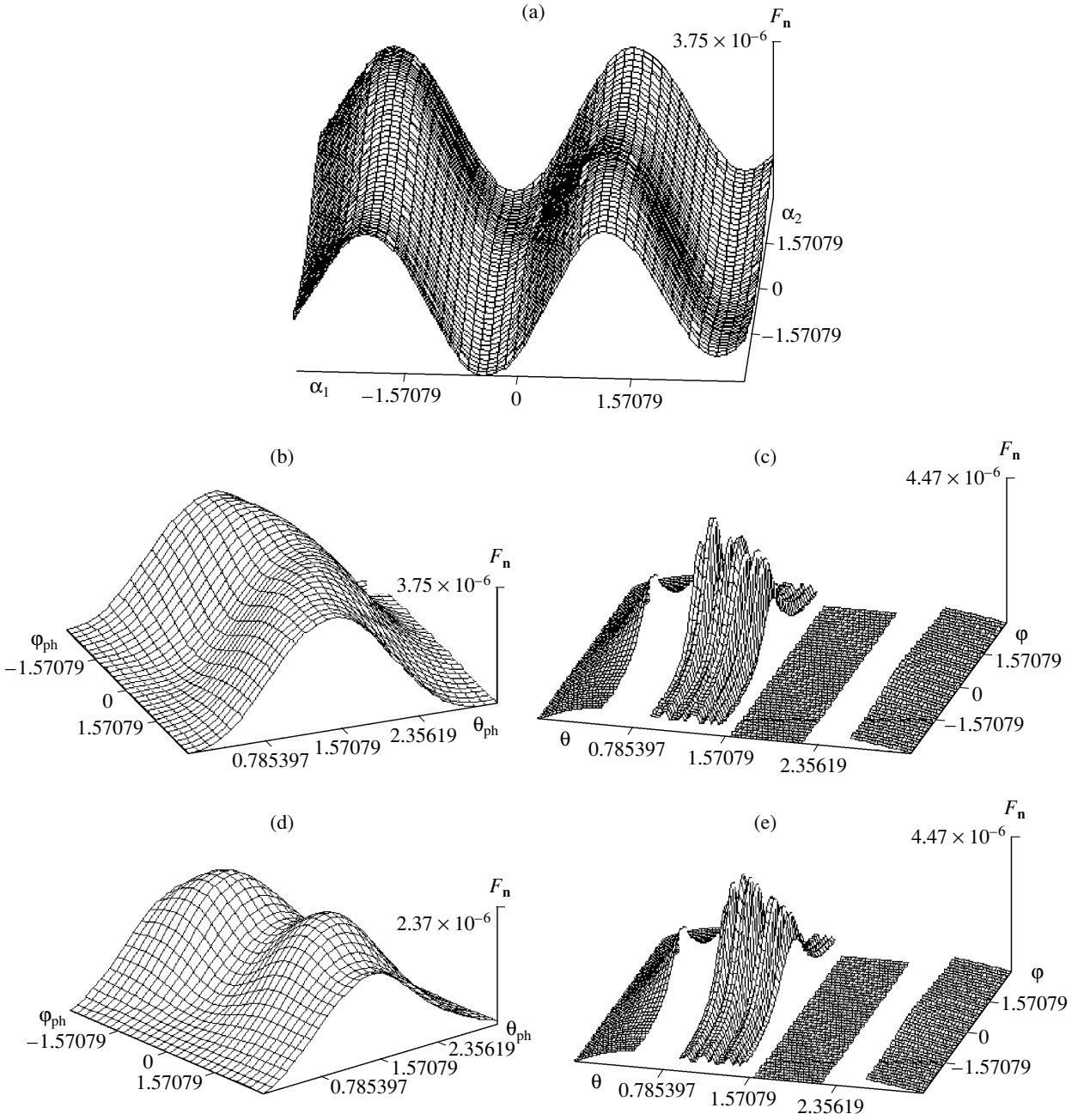

Fig. 3. Surface (a) $F_{0\mathbf{n}}(\alpha_1, \alpha_2)$ for $\omega = 315$, $\theta_0 = 0.90$, $\theta = 1.07$, $\varphi = 0.36$, $\theta_{ph} = 1.57$, and $\varphi_{ph} = -1.88$; surfaces (b) $F_{\mathbf{n}}(\theta_{ph}, \varphi_{ph})$ and (c) $F_{\mathbf{n}}(\theta, \varphi)$ for $\alpha_1 = 1.13$ and $\alpha_2 = -1.62$; and surfaces (d) $F_{\mathbf{n}}(\theta_{ph}, \varphi_{ph})$ and (e) $F_{\mathbf{n}}(\theta, \varphi)$ for $\alpha_1 = 2.64$ and $\alpha_2 = 0$.

However, in the range of angles θ satisfying the condition $k_z^2 \ll 2\varepsilon L$ (as well as in the range of high frequencies), the functions $F_{\mathbf{n}}(\theta, \varphi)$ and $F_{0\mathbf{n}}(\theta, \varphi)$ are different: in Fig. 2, this can be seen from the shapes of the surfaces $F_{\mathbf{n}}(\theta, \varphi)$ and $F_{0\mathbf{n}}(\theta, \varphi)$, which are plotted on different vertical scales.

Figure 2 also shows the portions of the surfaces $F_{\mathbf{n}}(\theta, \varphi)$ and $F_{0\mathbf{n}}(\theta, \varphi)$ in the interval (1.23, 1.2301) of angles θ satisfying the condition $k_z^2 \ll 2\varepsilon L$. It is seen that, as in the previous plots, these surfaces differ markedly in shape: at a fixed value of φ corresponding to the maximum values of $F_{\mathbf{n}}$, the function $F_{\mathbf{n}}$ varies periodically by more than 23% along the θ-axis.

In the theory presented here, the phases α_1 and α_2 are unknown parameters. We may only suggest that they do not differ markedly from $\pi/4$.

This uncertainty can be made somewhat smaller by examining the function $F_{\mathbf{n}}(\alpha_1, \alpha_2)$.

Figure 3 shows the surface $F_{\mathbf{n}}(\alpha_1, \alpha_2)$ computed in the interval $(2.36 \times 10^{-6}; 3.75 \times 10^{-6})$ at $\theta_0 = 0.90$, $\theta = 1.07$, $\varphi = 0.36$, $\theta_{ph} = 1.57$, and $\varphi_{ph} = -1.88$. This figure also displays the functions $F_{\mathbf{n}}(\theta, \varphi)$ and $F_{\mathbf{n}}(\theta_{ph}, \varphi_{ph})$ computed for the following values of the parameters α_1 and α_2, which determine certain characteristic points on the surface $F_{\mathbf{n}}(\alpha_1, \alpha_2)$: (i) $\alpha_1 = 1.13$ and $\alpha_2 = -1.62$, at which the function $F_{\mathbf{n}}(\alpha_1, \alpha_2)$ has an absolute maximum, and (ii) $\alpha_1 = 2.64$ and $\alpha_2 = 0$, at which the function $F_{\mathbf{n}}(\alpha_1, \alpha_2)$ has an absolute minimum.

One can see that, at different values of α_1 and α_2, the maxima of the function $F_{\mathbf{n}}(\theta_{ph}, \varphi_{ph})$ are close to one another, while the surfaces of this function can differ in shape. For example, the surface $F_{\mathbf{n}}(\theta_{ph}, \varphi_{ph})$ computed for the α_1 and α_2 values at which the function $F_{\mathbf{n}}(\theta_{ph}, \varphi_{ph})$ has an absolute maximum differs from the surface $F_{\mathbf{n}}(\alpha_1, \alpha_2)$ corresponding to the absolute minimum of this function.

Also shown in Fig. 3 are the surfaces $F_{\mathbf{n}}(\theta, \varphi)$, which correspond to different points of the function $F_{\mathbf{n}}(\alpha_1, \alpha_2)$. The heights of the peaks on these surfaces are approximately the same, but, in the range of angles θ satisfying the condition $k_z^2 \ll 2\varepsilon L$, the positions of the local maxima and local minima on different surfaces are different.

3. We integrate expression (8) over the angles θ_{ph} and φ_{ph}, which determine the direction of the wave vector of an emitted photon. As a result, in the range $\varepsilon^{2/3} \ll E_z \ll \varepsilon L$, we obtain the differential cross section $d\sigma_R$ for unpolarized bremsstrahlung during the evolution of the system from the initial state, described by the vector $\mathbf{k}_0$, to the final state, characterized by the vector $\mathbf{k}_+$ lying within the solid angle element $d\mathrm{o}$:

$$d\sigma_R = \frac{2}{3\pi}\alpha^3\frac{|\chi_{0z}|}{|k_{0z}|}\frac{k}{\chi_0}(Z_1Z_2Z_m)^2|T_R|^2\frac{d\omega}{\omega}d\mathrm{o}, \qquad (11)$$

where

$$|T_R|^2 = \frac{1}{4q_-^4}(q_-^2 + u_-^2) + \frac{i}{2q_-^2q_+^2}\{(e^{-i\gamma_1}h_- - h_-^*e^{i\gamma_1})\mathbf{q}_-\mathbf{q}_+$$
$$+ i(h_+^*e^{i\gamma_1} + h_+e^{-i\gamma_1})\mathbf{q}_-\mathbf{u}_+ + i(h_-^*e^{i\gamma_1} + h_-e^{-i\gamma_1})\mathbf{q}_+\mathbf{u}_-$$
$$+ (h_+^*e^{i\gamma_1} - h_+e^{-i\gamma_1})\mathbf{u}_+\mathbf{u}_-\}$$
$$+ \frac{1}{q_+^4}\{|h_-|^2q_+^2 + |h_+|^2u_+^2 + i(h_-^*h_+ - h_-h_+^*)\mathbf{q}_+\mathbf{u}_+\}.$$

Applying the same procedure to the range $E_z > \varepsilon L$, we get

$$d\sigma_R = \frac{8}{3\pi}\alpha^3\frac{|\chi_{0z}|}{|k_{0z}|}\frac{k}{\chi_0}(Z_1Z_2Z_m)^2\frac{1}{q_+^2}\frac{d\omega}{\omega}d\mathrm{o}. \qquad (12)$$

In the absence of an external electric field, integration of (10) over o_{ph} yields

$$d\sigma_0 = \frac{8}{3\pi}\alpha^3\frac{\chi}{\chi_0}(Z_1Z_2Z_m)^2\frac{1}{q_\chi^2}\frac{d\omega}{\omega}d\mathrm{o}. \qquad (13)$$

Let us consider the question of how the cross sections (11) and (12) are related to the differential cross section for elastic collisions between point charged particles in a constant uniform electric field.

We adopt the potential energy of Coulomb interaction between the particles, $\hat{V}$, as the perturbation operator $\hat{V} = e_1e_2/r$; use the wave functions (1) and (3); and turn to the nonrelativistic Born approximation. As a result, in Coulomb units, we obtain the differential cross section for elastic collisions in the range $\varepsilon^{2/3} \ll E_z \ll \varepsilon L$:

$$d\sigma_{el} = \frac{Z_1^2Z_2^2k_+}{Z_m^4k_0}|T_{el}|^2d\mathrm{o}, \quad k_+^2 = k_0^2, \qquad (14)$$

where

$$|T_{el}|^2 = \frac{1}{q_+^4}\left[|h_-|^2 + \frac{q_{z+}^2}{q_\perp^2}|h_+|^2 + i\frac{q_{z+}}{q_\perp}(h_-h_+^* - h_+h_-^*)\right]$$
$$+ \frac{1}{2q_+^2q_-^2}[i(h_-e^{-i\gamma_1} - h_-^*e^{i\gamma_1})$$
$$+ \frac{q_{z-}}{q_\perp}(h_-e^{-i\gamma_1} + h_-^*e^{i\gamma_1}) + \frac{q_{z+}}{q_\perp} \qquad (15)$$
$$\times (h_+e^{-i\gamma_1} + h_+^*e^{i\gamma_1}) + i\frac{q_{z+}q_{z-}}{q_\perp^2}(h_+^*e^{i\gamma_1} - h_+e^{-i\gamma_1}) + \frac{1}{4q_\perp^2q_-^2}.$$

Analogously, in the range $E_z > \varepsilon L$, we arrive at the expression

$$d\sigma_{el} = 4\frac{Z_1^2Z_2^2}{Z_m^4}\frac{k_+}{k_0}\frac{d\mathrm{o}}{q_+^4}, \quad k_+^2 = k_0^2, \qquad (16)$$

which coincides with the Rutherford formula.

Formulas (14) and (15) show that, because of the interference of the wave functions of colliding particles during their reflection from the potential barrier of the external electric field, the differential cross section for elastic collisions differs markedly from that in the case $\boldsymbol{\varepsilon} = 0$.

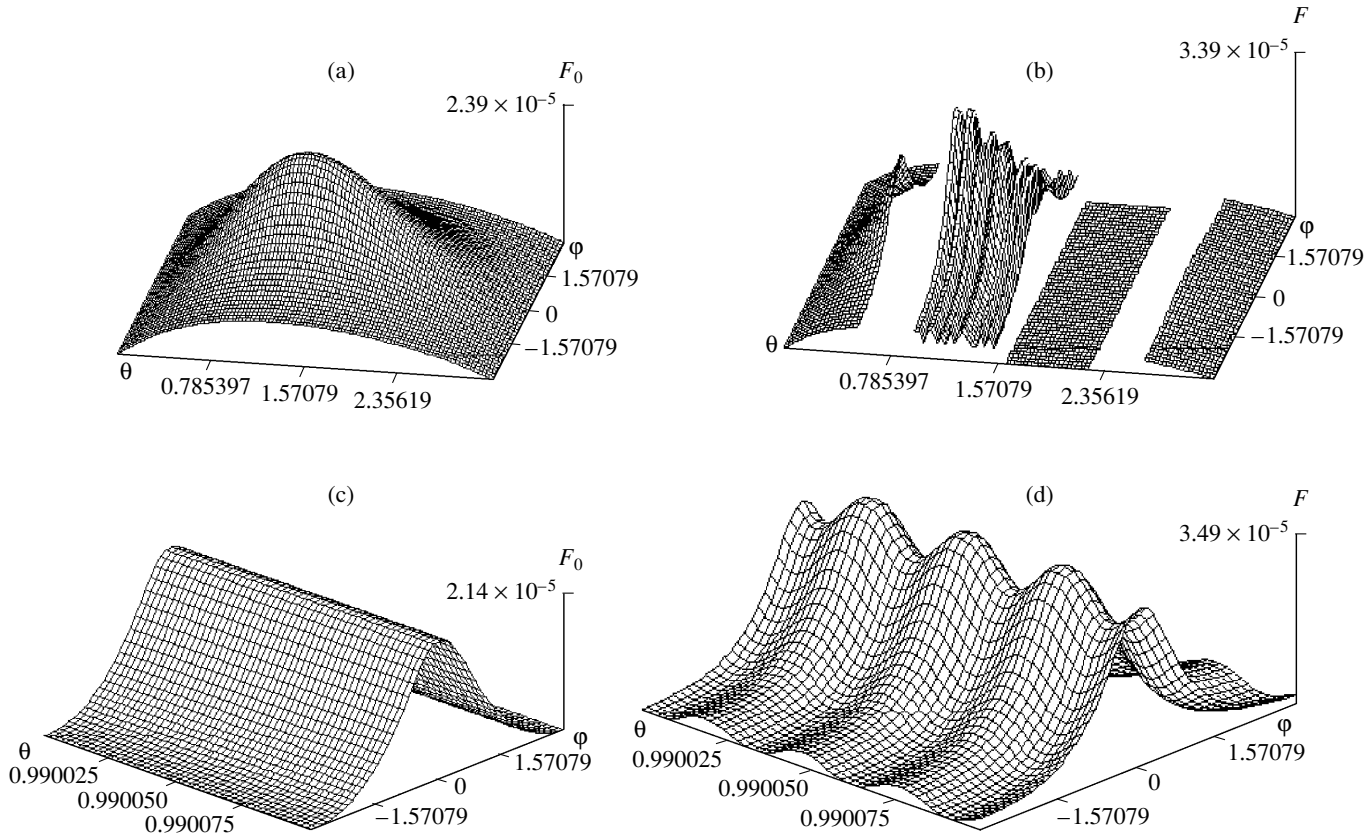

Fig. 4. Surfaces (a) $F_0(\theta, \varphi)$ and (b) $F(\theta, \varphi)$ for $\omega = 315$ and $\theta_0 = 0.88$ and portions of the surfaces (c) $F_0(\theta, \varphi)$ and (d) $F(\theta, \varphi)$ in the interval $\theta \in (0.99, 0.9901)$.

For real phases α_1 and α_2, the expression for $|T_{el}|^2$ may be written in a more illustrative form:

$$|T_{el}|^2 = \frac{1}{q_+^4}\left[\frac{5}{4}\left(1 + \frac{q_{z+}^2}{q_\perp^2}\right) + \left(1 - \frac{q_{z+}^2}{q_\perp^2}\right)\sin(\gamma_1 - \gamma_2)\right.$$

$$\left. - 2\frac{q_{z+}}{q_\perp}\cos(\gamma_1 - \gamma_2)\right] + \frac{1}{2q_-^2 q_+^2}\left[2\frac{q_{z-} + q_{z+}}{q_\perp}\cos(\gamma_1 + \gamma_2)\right.$$

$$+ \frac{q_{z-} - q_{z+}}{q_\perp}\sin 2\gamma_1 + 2\left(1 - \frac{q_{z-}q_{z+}}{q_\perp^2}\right)\sin(\gamma_1 + \gamma_2)$$

$$\left. - \left(1 + \frac{q_{z-}q_{z+}}{q_\perp^2}\right)\cos 2\gamma_1\right] + \frac{1}{4q_\perp^2 q_+^2},$$

which implies that the differential cross section for elastic collisions is oscillatory in character, as is the case with the cross section for bremsstrahlung in an external electric field.

Comparing (14)–(16) with the expression for $|T_R|^2$ and (12), we can readily see that, under the approximation adopted here, the differential cross sections for bremsstrahlung and elastic collisions are linearly proportional to one another in the range $E_z > \varepsilon L$.

On the other hand, although, in the range $\varepsilon^{2/3} \ll E_z \ll \varepsilon L$, the expressions for $|T_R|^2$ and $|T_{el}|^2$ are similar in structure, the cross sections (11) and (14) are not linearly proportional to one another (the proportionality coefficient being $\sim q_+^2$), but are related in a more complicated manner.

Although the substitutions

$$\frac{q_-^2 + u_-^2}{q_-^4} \longrightarrow \frac{q_+^2}{q_\perp^2 q_-^2}, \quad \frac{\mathbf{u}_+\mathbf{u}_-}{q_\perp^2} \longrightarrow \frac{q_{z+}q_{z-}}{q_\perp^2},$$

$$\frac{\mathbf{q}_+\mathbf{u}_-}{q_+^2} \longrightarrow -\frac{q_{z-}}{q_\perp}, \quad \frac{\mathbf{q}_-\mathbf{u}_+}{q_+^2} \longrightarrow -\frac{q_{z+}}{q_\perp}, \quad \frac{\mathbf{q}_-\mathbf{q}_+}{q_+^2} \longrightarrow 1,$$

$$\frac{\mathbf{q}_+\mathbf{u}_+}{q_+^2} \longrightarrow -\frac{q_{z+}}{q_\perp}, \quad \frac{u_+^2}{q_+^2} \longrightarrow \frac{q_{z+}^2}{q_\perp^2}$$

formally reduce the expression for $|T_R|^2$ to the expression for $q_+^2|T_{el}|^2$, they are inconsistent with the explicit expressions for $\mathbf{u}_\pm$.

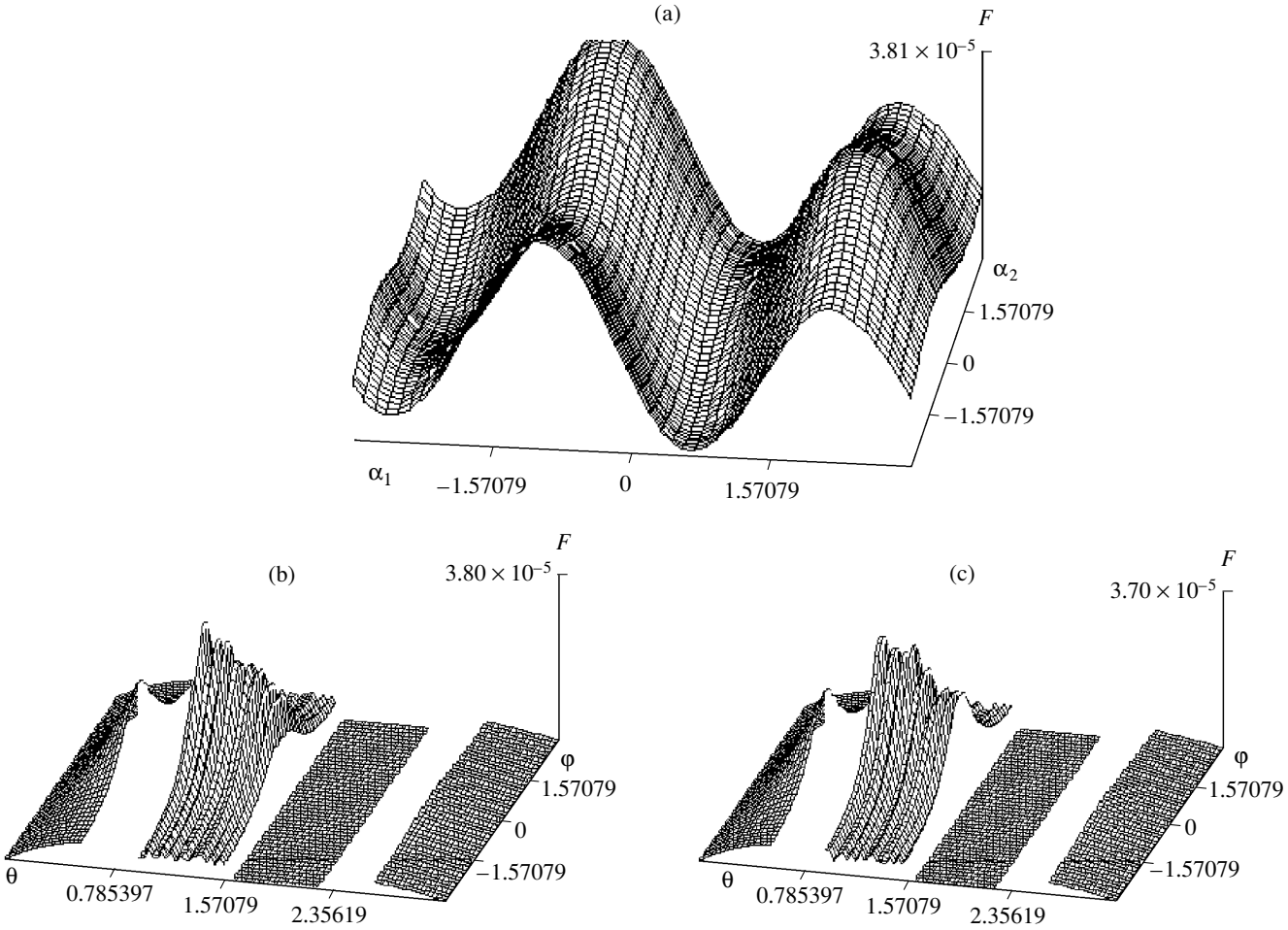

Fig. 5. Surfaces (a) $F(\alpha_1, \alpha_2)$ for $\omega = 315$ and $\theta_0 = 0.88$ and surfaces $F(\theta, \varphi)$ for (b) $\alpha_1 = -1.01$ and $\alpha_2 = 2.64$ and (c) $\alpha_1 = -2.58$ and $\alpha_2 = 0.75$.

As in the previous section, we analyze the cross sections (11)–(13) numerically, representing the functions

$$F = \frac{\pi^2}{\alpha^3}\frac{1}{(Z_1 Z_2 Z_m)^2}\frac{d\sigma_R}{d\omega d\theta d\varphi}$$

and

$$F_0 = \frac{\pi^2}{\alpha^3}\frac{1}{(Z_1 Z_2 Z_m)^2}\frac{d\sigma_0}{d\omega d\theta d\varphi}$$

as the surfaces on the (θ, φ) and (α_1, α_2) planes.

Numerical analysis of the functions $F(\theta, \theta_0)$ and $F(\theta_0, \varphi)$ at $\varepsilon = 0.01$, $L = 10^4$, $k_0 = 30$, $\omega = 315$, and $\alpha_1 = \alpha_2 = 0.78 \approx \frac{\pi}{4}$ allowed us to determine the angle $\theta_0 = 0.88$ at which the height of the highest peak on the surface $F(\theta, \varphi)$ is as close as possible to the maximum height.

This value of the angle θ_0 was used to compute the surfaces $F(\theta, \varphi)$ and $F_0(\theta, \varphi)$ presented in Fig. 4 and their portions in the interval (0.99, 0.9901) of angles θ, over which the function F is seen to vary periodically by more than 24% (at the value of φ at which this function is most peaked).

Finally, we analyze how the cross sections depend on the parameters α_1 and α_2. This dependence is characterized by the surfaces $F(\alpha_1, \alpha_2)$ shown in Fig. 5. The function $F(\alpha_1, \alpha_2)$ is seen to be similar in shape to $F_{\mathbf{n}}(\alpha_1, \alpha_2)$ and to vary in the range $(2.50 \times 10^{-5}; 3.81 \times 10^{-5})$.

Figure 5 illustrates how the function $F(\theta, \varphi)$ changes depending on the parameters α_1 and α_2. The surfaces $F(\theta, \varphi)$ are computed for (i) $\alpha_1 = -1.01$ and $\alpha_2 = 2.64$, which correspond to the absolute maximum of the function $F(\alpha_1, \alpha_2)$, and (ii) $\alpha_1 = -2.58$ and $\alpha_2 = 0.75$, which correspond to the absolute minimum of the function $F(\alpha_1, \alpha_2)$.

We can easily see that the surfaces are similar in shape and the heights of their peaks are nearly the same, although the values of α_1 and α_2 were chosen to correspond to the absolute maximum and absolute minimum of the function $F(\theta, \varphi)$.

4. Our results show that the differential cross sections for bremsstrahlung during collisions between two charged particles in an external electric field can differ markedly from those in the absence of a field ($\boldsymbol{\varepsilon} = 0$) both in magnitude and in the way they depend on the angles (θ, φ) and (θ_{ph}, φ_{ph}): the cross sections derived are oscillatory in character and, as a result of the spatial anisotropy in the presence of an external field ($\boldsymbol{\varepsilon} \neq 0$), depend on $q_\perp$ and $q_{z\pm}$.

Also, the external electric field substantially changes the differential cross section for elastic collisions between charged particles. Although the mathematical expressions for $d\sigma_R$ and $q_+^2 d\sigma_{el}$ are similar in structure, the differential cross sections for bremsstrahlung and elastic collisions are not linearly proportional to one another, as is the case with $\boldsymbol{\varepsilon} = 0$.

Physically, the change in the differential cross sections for bremsstrahlung and elastic collisions between point charged particles in a uniform electric field is attributed to a redistribution (in comparison with the case $\boldsymbol{\varepsilon} = 0$) of the mean charge density of the colliding particles as a result of the interference of their wave functions during the reflection from the potential barrier of the uniform external electric field.

Presumably, this redistribution will occur not only over such distances from the center of inertia of the particles that are much longer than the atomic distance ($\hbar^2/e_m^2 m$) but also over significantly shorter distances: the exact wave function, which explicitly incorporates the interaction between the particles, should be evaluated with allowance for the boundary conditions that describe particle reflection from the potential barrier of the external electric field. Clearly, these conditions differ from the boundary conditions imposed on the wave function at infinity in the case $\boldsymbol{\varepsilon} = 0$.

Note also that, in formulating the model problem, we introduced the boundary of the region occupied by the external uniform electric field. However, the cross sections derived with allowance for the interference of the wave functions of colliding particles during their reflection from the potential barrier of the external electric field turn out to be almost independent of this boundary. In fact, the flux of colliding particles with a nonzero longitudinal energy of their relative motion can be modeled by assuming that the particles from an infinitely remote region $z = -\infty$ penetrate through a sufficiently high potential barrier of a uniform electric field. In this case, the differential cross sections for bremsstrahlung and elastic collisions are only described by formulas (5), (8), (11), (14), and (15), which do not contain the parameter L and depend exclusively on E_{0z}, E_z, $\mathbf{k}_{0\perp}$, and $\mathbf{k}_\perp$.

We should, however, emphasize that, since the cross sections were derived based on the theory of steady-state scattering, they are meaningful only under the following two conditions: (i) the characteristic scale length of the problem of collisions between the particles should be much longer than the distance between the point at which the particles are reflected from the potential barrier of an external field of strength $\boldsymbol{\varepsilon}$ and the center of the mass of the system, and (ii) the mean transit time over this distance should be much shorter than the characteristic time scale of the problem.

On the other hand, introducing the model parameter L allowed us to obtain elastic collision cross sections for which these conditions are satisfied ($\varepsilon^{2/3} \ll E_z \ll \varepsilon L$) and the cross sections for which they fail to hold ($E_z > \varepsilon L$).

The effects under discussion are expected to manifest themselves, e.g., in ionized gases with a sufficiently large fraction of particles with longitudinal energies in the range $E_z < e_m \varepsilon n^{-1/3}$ (where n is the density of gas particles) in a quasi-steady and quasi-uniform electric field of strength $\boldsymbol{\varepsilon}$ such that the time scale on which this field varies is much longer than the mean time $\sqrt{m_e E_z}/|e|\varepsilon$ required for an electron to pass the distance $E_z/|e|\varepsilon$ (along the external field of strength $\boldsymbol{\varepsilon}$) between the ion and the point at which it is reflected from the potential barrier of the external field: $\sqrt{m_e E_z}/|e|\varepsilon \ll \tau$.

ACKNOWLEDGMENTS

We are grateful to A.A. Rukhadze for his interest in our study. This work was supported in part by the Council on the Federal Program "Government Support of the Integration between Higher Education and Basic Research for 1997–2000" (under the subprogram "A0028FTsP Integration").

REFERENCES

1. V. I. Krylov, Izv. Vyssh. Uchebn. Zaved. Fiz., No. 7, 46 (1994).
2. V. I. Krylov, Kr. Soobshch. Fiz., No. 8, 90 (1995).
3. V. B. Berestetskii, E. M. Lifshitz, and L. P. Pitaevskii, *Quantum Electrodynamics* (Nauka, Moscow, 1980; Pergamon, Oxford, 1982).
4. V. I. Krylov and V. V. Pivkin, Fiz. Plazmy **26**, 478 (2000) [Plasma Phys. Rep. **26**, 446 (2000)].

Translated by O. Khadin

Plasma Physics Reports, Vol. 26, No. 8, 2000, pp. 701–709. Translated from Fizika Plazmy, Vol. 26, No. 8, 2000, pp. 747–756.

LOW-TEMPERATURE PLASMA

Mechanism for Electric Breakdown in a Chemically Nonequilibrium System and the Influence of the Chain Oxidation Reaction in an H_2–Air Mixture on the Breakdown Threshold

I. N. Kosarev and A. Yu. Starikovskiĭ

Moscow Institute for Physics and Technology, Institutskiĭ proezd 9, Dolgoprudnyĭ, Moscow oblast, 141700 Russia

Received September 23, 1999; in final form, November 25, 1999

Abstract—A mathematical model is developed and a numerical analysis is performed for an electric breakdown in a hydrogen–air mixture with a low concentration of H_2. It is shown that, at sufficiently low pressures $p < 10^{-2}$ atm, a small molecular-hydrogen additive ($\eta = 5 \times 10^{-5}$–5×10^{-3}) decreases the reduced field of an electric breakdown in air by a factor of more than 2 because of the appearance of an additional detachment process associated with the chain hydrogen-oxidation reaction. Detailed calculations are performed for the mean number density of negative oxygen ions $[O_2^-] = 10^3$ cm^{-3} and the hydrogen concentration in air $[H_2] = 0.5$, 0.05, and 0.005%. It is found that, for $[H_2] = 0.005\%$, the breakdown can develop under the action of a geoelectric field of 1.3 V/cm at $p \simeq 10^{-4}$ atm. © *2000 MAIK "Nauka/Interperiodica".*

1. INTRODUCTION

In recent years, the intensification of combustion in gas-phase systems with the use of various types of gas discharge has attracted considerable interest [1, 2] primarily in connection with the development of technologies for creating combustion chambers operating at high gas-flow velocities.

Of particular interest is the use of self-sustained volume discharges that have a high propagation velocity and high spatial homogeneity and provide almost simultaneous controllable ignition of the mixture throughout the entire discharge volume [3].

When generating a highly homogeneous discharge, the phase of the discharge initiation is of crucial importance. In schemes for producing a uniform breakdown, high-power external preionization sources are traditionally used [4]. Such schemes usually require the creation of a rather complicated system of additional discharge gaps or the injection of a pulsed electron beam into the discharge volume.

An alternative method for producing a highly uniform breakdown is the use of fast ionization waves (FIWs) [5]. The discharge develops in the form of an FIW when the voltage at the discharge gap grows so rapidly that, during the characteristic time of the development of an electron avalanche, the electric field near the ionization-wave front becomes higher than the threshold field for the generation of runaway electrons [6].

In this case, the discharge homogeneity is determined by the ratio between the characteristic time of gas ionization and the time during which the field grows from the breakdown threshold to the threshold for the generation of runaway electrons. Hence, the investigation of mechanisms governing the combustion in moderate and strong electric fields involves the study of the breakdown dynamics and the determination of the critical fields in chemically nonequilibrium gas-phase systems.

Another interesting direction of investigation is related to discharges in the upper atmosphere, where the low total gas pressure and the absence of limitations on the characteristic dimensions of the processes involved can facilitate the discharge ignition.

Pulsed optical bursts above the upper boundary of a storm cloud have been observed for almost a century. However, only modern satellite diagnostics have made it possible to determine the position and size of such objects and to qualitatively study their internal structure [7–12]. At present, the understanding of the initiation phase of such processes is lacking. It is of interest to study the possibility of the development of a discharge under the action of the geoelectric field $E_0 = 1.3$ V/cm at high altitudes in the presence of small fluctuations in the H_2 content.

In [13], the problem was considered of the reduction of the breakdown field due to the detachment associated with the change in the chemical composition of a gas and a mechanism was proposed for the reduction related to the destruction of negative O^- ions by atmospheric ozone. In [14], it was shown that a small H_2 additive to oxygen almost completely eliminates stable negative oxygen ions. Later, a qualitative explanation

1063-780X/00/2608-0701$20.00

for the change in the first Townsend coefficient α^* in hydrogen–oxygen mixtures was put forward in [15].

In this paper, we analyze the development of breakdown in a hydrogen–air mixture at high pressures with the aim of investigating the breakdown dynamics and determining the critical electric field for different values of the hydrogen concentration and gas pressure.

2. NUMERICAL MODEL OF THE IONIZATION PROCESS IN A CHEMICALLY NONEQUILIBRIUM GAS IN A NEAR-BREAKDOWN ELECTRIC FIELD

The breakdown reduced electric field E/n in an electronegative gas usually depends on the ratio between the rates of electron-impact ionization and dissociative electron attachment [16]. Its value for the N_2–O_2 airlike mixture is equal to $E/n \simeq 41$ V/(cm torr). At such values of the reduced electric field, almost all the possible mechanisms contribute to ionization because of the relatively long breakdown time. These mechanisms are direct electron-impact ionization, step ionization with the participation of electronically excited states, and ionization through the collision of heavy particles (the Penning effect and associative ionization). For the same reason, it is necessary to take into consideration a large number of processes leading to electron loss—among these are dissociative and three-body recombination and electron attachment [17].

A process in some sense inverse to attachment is negative-ion destruction through associative attachment, by electron impact, or during collisions with excited particles. The process competing with the above processes leading to loss of negative ions is ion–ion recombination.

Hence, the kinetic scheme used to describe the mechanism for an electric breakdown in a chemically nonequilibrium system must incorporate balance equations (as full as possible) for charged and excited particles and radicals.

The kinetic scheme developed in this paper includes 83 particle species:

H, H_2, HO_2, H_2O_2, H_2O, OH, O, O_2, O_3, N, N_2, NO, N_2O, N_2O_4, N_2O_5, NO_2, NO_3, HNO, $HONO$, $HONO_2$, HO_2NO_2, NOH_2O, NH, NH_2, $N(^2D)$, $N(^2P)$, $N_2(a'^1\Sigma_u^-)$, $N_2(A^3\Sigma_u^+)$, $N_2(B^3\Pi_g)$, $N_2(C'^3\Pi_u)$, $N_2(C^3\Pi_u)$, $N_2(W^3\Delta_u)$, $N_2(a^1\Pi_g)$, $O(^1D)$, $O(^1S)$, $O(^5P)$, $O(^5S)$, $O_2(a^1\Delta_g)$, $O_2(b^1\Sigma_g^+)$, $O_2(A^3\Sigma_u)$, N^+, N_2^+, N_3^+, N_4^+, NO^-, NO^+, N_2O^-, N_2O^+, NO_2^-, NO_2^+, NO_3^-, NO_3^+, N_3O^+, $N_2O_2^+$, $N_2O_3^-$, $N_2O_3^+$, O^-, O^+, O_2^-, O_2^+, O_3^+, O_3^-, O_4^+, O_4^-, H^-, H^+, H_2^+, H_3^+, OH^+, OH^-, H_2O^+, H_2O^-, $H_2O_2^-$, $H_2O_3^-$, $H_4O_2^+$, NOH_2O^+, HO_2^+, $H_2O_3^+$, H_3O^+, $H_5O_2^+$, $H_2O_4^-$, e^-.

The scheme also includes the following processes with the participation of electrons: the excitation of the states $N_2(a'^1\Sigma_u^-)$, $N_2(a^1\Pi_g)$, $N_2(A^3\Sigma_u^+)$, $N_2(B^3\Pi_g)$, $N_2(C^3\Pi_u)$, $N_2(W^3\Delta_u)$, $O_2(a^1\Delta_g)$, $O_2(b^1\Sigma_g^+)$; dissociation and ionization of nitrogen, oxygen, and hydrogen; dissociative attachment to oxygen; and ozone dissociation. The rates of these processes were calculated using the conventional two-term approximation for the electron energy distribution function [18–20].

In addition to the electron-impact excitation processes, the kinetic model incorporates the processes of associative and Penning ionization (eight reactions), recombination of negative ions and electrons (52 reactions), electron attachment to atoms (27 reactions), electron detachment (44 reactions), interaction between neutral unexcited components (156 reactions), interaction between neutral excited and neutral unexcited components (148 reactions including radiative transitions), conversion of positive (126 reactions) and negative (56 reactions) ions, and recombination of positive and negation ions (169 reactions).

Since the full scheme of processes is rather cumbersome, only the part of the scheme that is directly related to the electron balance in the system is presented in this paper (Table 1).

To construct the right-hand side of the set of kinetic equations, we used the algorithm of the ChemKin code. The set of kinetic equations was solved by the Gear method.

To calculate the electron energy distribution function and the rates of the processes with the participation of electrons, we used the cross sections from [21–23] for hydrogen, from [21, 24, 25, 26–31] for nitrogen, and from [32–38] for oxygen. The other incorporated processes (and their rate constants) determining the evolution of radicals and excited components and the ion–ion reactions are listed in [39].

3. THE RESULTS OF CALCULATIONS

The calculations showed that, at a sufficiently low pressure p and low H_2 concentration, the breakdown can develop at a reduced electric field lower than 20 V/(cm torr). (Note that, in calculations, the initial concentration of charged particles was determined by O_2^- ions with a number density of 10^3–10^6 cm^{-3}.)

It turned out that there are three distinguishable stages of the breakdown. In the first stage (delay stage), a relatively slow exponential growth of the degrees of ionization and dissociation is observed during a time t_d. Then, after a short transient stage, the process goes into the phase of extremely rapid growth of the degrees of ionization and dissociation, which is accompanied by an increase in the gas temperature.

The calculations for an initial gas temperature of T = 300 K, calculation times $t_{calc} < 2 \times 10^3$ s, and molecular

Table 1. Processes with the participation of electrons that are incorporated into the model

Electron-impact excitation	$e^- + N_2 \longrightarrow e^- + N_2(a'^1\Sigma_u^-)$	$N(^2P^0) + O \longrightarrow NO^+ + e^-$
$e^- + H_2 \longrightarrow e^- + H_2(v = 1)$	$e^- + N_2 \longrightarrow e^- + N_2(a^1\Pi_g)$	$N_2(a^1\Pi_g) + N_2(A^3\Sigma_u^+) \longrightarrow N_4^+ + e^-$
$e^- + H_2 \longrightarrow e^- + H_2(v = 2)$	$e^- + N_2 \longrightarrow e^- + N_2(a''^1\Sigma_g)$	$N_2(a^1\Pi_g) + N_2(a^1\Pi_g) \longrightarrow N_4^+ + e^-$
$e^- + H_2 \longrightarrow e^- + H_2(v = 3)$	$e^- + N_2 \longrightarrow e^- + N_2(B^{13}\Sigma_u^-)$	$N_2(a'^1\Sigma_u^-) + N_2(a'^1\Sigma_u^-) \longrightarrow N_2 + N_2^+ + e^-$
$e^- + H_2 \longrightarrow e^- + H_2(\text{rot})$	$e^- + N_2 \longrightarrow e^- + N_2(B^1\Pi_u)$	$N_2(a'^1\Sigma_u^-) + N_2(A^3\Sigma_u^+) \longrightarrow N_2 + N_2^+ + e^-$
$e^- + H_2 \longrightarrow e^- + H_2(d^3\Pi_u)$	$e^- + N_2 \longrightarrow e^- + N_2(E^3\Sigma_g^+)$	Recombination
$e^- + H_2 \longrightarrow e^- + H_2(a^3\Sigma_g^+)$	$e^- + N_2 \longrightarrow e^- + N_2(\text{Rydberg})$	$O_2^+ + e^- \longrightarrow O + O(^1S)$
$e^- + H_2 \longrightarrow e^- + H_2(b^2\Sigma_g)$	$e^- + N_2 \longrightarrow N_2^- \longrightarrow e^- + N(^4S^0) + N(^4S^0)$	$O_2^+ + e^- \longrightarrow O + O(^1D)$
$e^- + H_2 \longrightarrow e^- + H_2(c^3\Pi_u)$	$e^- + N_2 \longrightarrow N + N$	$O_2^+ + e^- \longrightarrow O + O$
$e^- + H_2 \longrightarrow e^- + H_2(B^{1'}\Sigma_u^+)$	$e^- + N_2 \longrightarrow e^- + e^- + N_2^+$	$N_2^+ + e^- \longrightarrow N + N$
$e^- + H_2 \longrightarrow e^- + H_2(B^1\Sigma_u^+)$	$e^- + N_2 \longrightarrow N(4S^0) + N^+(^3P) + e^- + e^-$	$NO^+ + e^- \longrightarrow N + O$
$e^- + H_2 \longrightarrow e^- + H_2(E^1\Sigma_g^+)$	$e^- + N_2(j = 0) \longrightarrow e^- + N_2(j = 2, 4, 6, 8)$	$N_4^+ + e^- \longrightarrow N_2 + N_2$
$e^- + H_2 \longrightarrow e^- + H_2(C^1\Pi_u)$	$e^- + O_2 \longrightarrow e^- + O_2(v = 1)$	$N^+ + e^- \longrightarrow N$
$e^- + H_2 \longrightarrow e^- + H_2(e^3\Sigma_u^+)$	$e^- + O_2 \longrightarrow e^- + O_2(v = 2)$	$N_2O_2^+ + e^- \longrightarrow NO + NO$
$e^- + H_2 \longrightarrow e^- + H + H$	$e^- + O_2 \longrightarrow e^- + O_2(v = 3)$	$N_3O^+ + e^- \longrightarrow N_2 + NO$
$e^- + H_2 \longrightarrow e^- + e^- + H_2^+$	$e^- + O_2 \longrightarrow e^- + O_2(v = 4)$	$NO_3^+ + e^- \longrightarrow NO + O_2$
$e^- + H_2 \longrightarrow H^- + H$	$e^- + O_2 \longrightarrow e^- + O_2(a^1\Delta_g)$	$N_2O_2^+ + e^- \longrightarrow N_2 + O_2$
$e^- + N_2 \longrightarrow e^- + N_2(v = 1)$	$e^- + O_2 \longrightarrow e^- + O_2(b^1\Sigma_g^+)$	$NO_2^+ + e^- \longrightarrow NO + O$
$e^- + N_2 \longrightarrow e^- + N_2(v = 2)$	$e^- + O_2 \longrightarrow e^- + O_2(B^3\Sigma_u^-)$	$N_2O^+ + e^- \longrightarrow N_2 + O$
$e^- + N_2 \longrightarrow e^- + N_2(v = 3)$	$e^- + O_2 \longrightarrow e^- + O_2(A^3\Sigma_u^+)$	$N_3^+ + e^- \longrightarrow N + N_2$
$e^- + N_2 \longrightarrow e^- + N_2(v = 4)$	$e^- + O_2 \longrightarrow e^- + O_2(A^3\Sigma_u^+, C^3\Delta_u)$	$N_2^+ + e^- \longrightarrow N + N(^2D^0)$
$e^- + N_2 \longrightarrow e^- + N_2(v = 5)$	$e^- + O_2 \longrightarrow e^- + O_2(9.9\ \text{eV})$	$NO^+ + e^- \longrightarrow N(^2D^0) + O$
$e^- + N_2 \longrightarrow e^- + N_2(v = 6)$	$e^- + O_2 \longrightarrow e^- + O_2(\text{Rydberg})$	$N_2^+ + e^- + e^- \longrightarrow N_2 + e^-$
$e^- + N_2 \longrightarrow e^- + N_2(v = 7)$	$e^- + O_2 \longrightarrow O^-(^2P^0) + O(^3P)$	$O_2^+ + e^- + e^- \longrightarrow O_2 + e^-$
$e^- + N_2 \longrightarrow e^- + N_2(v = 8)$	$e^- + O_2 \longrightarrow e^- + O + O$	$NO^+ + e^- + e^- \longrightarrow NO + e^-$
$e^- + N_2 \longrightarrow e^- + N_2(v = 9)$	$e^- + O_2 \longrightarrow e^- + O^+ + O^-$	$N^+ + e^- + e^- \longrightarrow N + e^-$
$e^- + N_2 \longrightarrow e^- + N_2(v = 10)$	$e^- + O_2 \longrightarrow e^- + e^- + O_2^+$	$O^+ + e^- + e^- \longrightarrow O + e^-$
$e^- + N_2 \longrightarrow e^- + N_2(A^3\Sigma_u^+)$	$e^- + O_2 \longrightarrow e^- + e^- + O(^3P) + O^+(^4S)$	$N_2 + N_2^+ + e^- \longrightarrow N_2 + N_2$
$e^- + N_2 \longrightarrow e^- + N_2(B^3\Pi_g)$	Collisions of heavy particles	$N_2 + O_2^+ + e^- \longrightarrow N_2 + O_2$
$e^- + N_2 \longrightarrow e^- + N_2(C^3\Pi_u)$	$N_2(a'^1\Sigma_u^-) + N_2(A^3\Sigma_u^+) \longrightarrow N_4^+ + e^-$	$N_2 + NO^+ + e^- \longrightarrow N_2 + NO$
$e^- + N_2 \longrightarrow e^- + N_2(w^1\Delta_u)$	$N_2(a'^1\Sigma_u^-) + N_2(a'^1\Sigma_u^-) \longrightarrow N_4^+ + e^-$	$N^+ + N_2 + e^- \longrightarrow N + N_2$
$e^- + N_2 \longrightarrow e^- + N_2(w^3\Delta_u)$	$N(^2D^0) + N(^2P^0) \longrightarrow N_2^+ + e^-$	$N_2 + O^+ + e^- \longrightarrow N_2 + O$

Table 1. (Contd.)

$N_2^+ + O_2 + e^- \longrightarrow N_2 + O_2$	$N_2 + NO_2 + e^- \longrightarrow N_2 + NO_2^-$	$N + O^- \longrightarrow NO + e^-$
$O_2 + O_2^+ + e^- \longrightarrow O_2 + O_2$	$NO_2 + O_2 + e^- \longrightarrow NO_2^- + O_2$	$O + O_3^- \longrightarrow O_2 + O_2 + e^-$
$NO^+ + O_2 + e^- \longrightarrow NO + O_2$	$NO_2 + e^- \longrightarrow NO + O^-$	$NO_2^- + O \longrightarrow NO_3 + e^-$
$N^+ + O_2 + e^- \longrightarrow N + O_2$	$N_2 + N_2O + e^- \longrightarrow N_2 + N_2O^-$	$N_2(A^3\Sigma_u^+) + O^- \longrightarrow N + NO + e^-$
$O^+ + O_2 + e^- \longrightarrow O + O_2$	$N_2O + e^- \longrightarrow N_2 + O^-$	$O^- + O_3 \longrightarrow O_2 + O_2 + e^-$
$N_3^+ + e^- \longrightarrow N + N_2(B^3\Pi_g)$	$O_2 + O_2 + e^- \longrightarrow O_2 + O_2^-$	$H_2 + O^- \longrightarrow H_2O + e^-$
$N_3^+ + e^- \longrightarrow N + N_2(A^3\Sigma_u^+)$	$NO + NO + e^- \longrightarrow NO + NO^-$	$H_2O + O^- \longrightarrow H_2O_2 + e^-$
$O_4^+ + e^- \longrightarrow O_2 + O_2$	$N_2O + NO + e^- \longrightarrow N_2O + NO^-$	$H + O_2^- \longrightarrow HO_2 + e^-$
$H_3^+ + e^- \longrightarrow H + H_2$	$NO_2 + O + e^- \longrightarrow NO_2 + O^-$	$H^- + O_2 \longrightarrow HO_2 + e^-$
$H_2^+ + e^- \longrightarrow H + H$	$N_2 + O + e^- \longrightarrow N_2 + O^-$	$H + H^- \longrightarrow H_2 + e^-$
$NH^+ + e^- \longrightarrow H + N$	$NO + O_2 + e^- \longrightarrow NO + O_2^-$	$OH^- + O \longrightarrow HO_2 + e^-$
$OH^+ + e^- \longrightarrow H + O$	$O + O + e^- \longrightarrow O + O^-$	$H + OH^- \longrightarrow H_2O + e^-$
$H_3^+ + e^- \longrightarrow H + H + H$	$NO + O + e^- \longrightarrow NO + O^-$	$O(^1S) + O^- \longrightarrow O_2 + e^-$
$H^+ + e^- \longrightarrow H$	$H_2 + NO + e^- \longrightarrow H_2 + NO^-$	$O(^1D) + O^- \longrightarrow O_2 + e^-$
$H_3O^+ + e^- \longrightarrow H_2 + OH$	$NH_4 + NO + e^- \longrightarrow NH_4 + NO^-$	$O(^1S) + O_2^- \longrightarrow O_3 + e^-$
$O_3^+ + e^- \longrightarrow O + O_2$	$H_2O + O_2 + e^- \longrightarrow H_2O + O_2^-$	$O(^1D) + O_2^- \longrightarrow O_3 + e^-$
$O_4^+ + e^- \longrightarrow O + O(^1D) + O_2$	$H_2 + O_2 + e^- \longrightarrow H_2 + O_2^-$	$O(^1S) + O_3^- \longrightarrow O_2 + O_2 + e^-$
$OH^+ + e^- \longrightarrow H + O(^1S)$	$H + O_2 + e^- \longrightarrow H^- + O_2$	$O(^1D) + O_3^- \longrightarrow O_2 + O_2 + e^-$
$HO_2^+ + e^- \longrightarrow H + O_2(a^1\Delta_g)$	$H + N_2 + e^- \longrightarrow H^- + N_2$	$H^- + HO_2 \longrightarrow H_2O + O + e^-$
$H_2O^+ + e^- \longrightarrow H + OH$	$OH + O_2 + e^- \longrightarrow OH^- + O_2$	$H^- + H_2O_2 \longrightarrow H_2O + OH + e^-$
$H_2O^+ + e^- \longrightarrow H_2 + O$	$OH + N_2 + e^- \longrightarrow OH^- + N_2$	$H^- + O_3 \longrightarrow OH + O_2 + e^-$
$H_2O^+ + e^- \longrightarrow H + H + O$	Electron detachment	$H^- + O(^1S) \longrightarrow H + O + e^-$
$H_3O^+ + e^- \longrightarrow H + H_2O$	$O + O^- \longrightarrow O_2 + e^-$	$H^- + O(^1D) \longrightarrow H + O + e^-$
$H_4O_2^+ + e^- \longrightarrow H + H_2O + OH$	$O^- + O_2(a^1\Delta_g) \longrightarrow O_3 + e^-$	$OH^- + HO_2 \longrightarrow H_2O + O_2 + e^-$
$H_5O_2^+ + e^- \longrightarrow H + H_2O + H_2O$	$O_2(a^1\Delta_g) + O_2^- \longrightarrow O_2 + O_2 + e^-$	$OH^- + O(^1S) \longrightarrow HO_2 + e^-$
$H_2O_3^+ + e^- \longrightarrow H_2O + O + O$	$O_2(b^1\Sigma_g^+) + O_2^- \longrightarrow O_2 + O_2 + e^-$	$OH^- + O(^1D) \longrightarrow HO_2 + e^-$
Electron attachment	$N_2(A^3\Sigma_u^+) + O_2^- \longrightarrow N_2 + O_2 + e^-$	$H + O^- \longrightarrow OH + e^-$
$N_2 + O_2 + e^- \longrightarrow N_2 + O_2^-$	$N_2(a'^1\Sigma_u^-) + O_2^- \longrightarrow N_2 + O_2 + e^-$	$OH + O^- \longrightarrow HO_2 + e^-$
$O + O_2 + e^- \longrightarrow O + O_2^-$	$N_2(B^3\Pi_g) + O_2^- \longrightarrow N_2 + O_2 + e^-$	$HO_2 + O^- \longrightarrow OH + O_2 + e^-$
$O + O_2 + e^- \longrightarrow O^- + O_2$	$O^- + O_2(b^1\Sigma_g^+) \longrightarrow O + O_2 + e^-$	$H_2O_2 + O^- \longrightarrow H_2O + O_2 + e^-$
$O_2 + O_3 + e^- \longrightarrow O_2 + O_3^-$	$N_2(A^3\Sigma_u^+) + O^- \longrightarrow N_2 + O + e^-$	$H_2 + O_3^- \longrightarrow H_2O + O_2 + e^-$
$O_3 + e^- \longrightarrow O + O_2^-$	$N_2(B^3\Pi_g) + O^- \longrightarrow N_2 + O + e^-$	$H^- + NO \longrightarrow HNO + e^-$
$O_3 + e^- \longrightarrow O^- + O_2$	$N + O_2^- \longrightarrow NO_2 + e^-$	

hydrogen concentration $[H_2] = 5\%$ showed the following:

(i) For the reduced electric field $E/p = 10$ V(cm torr), the breakdown is absent over a wide range of pressures $p = 0.0005$–1 atm and relative concentrations of negative oxygen ions $\delta = [O_2^-]/N = 10^{-16}$–$10^{-12}$.

(ii) For $E/p = 15$ V/(cm torr), the development of the breakdown during the time $t = t_{calc}$ is observed only for the lowest pressures under study ($p = 0.0005$ atm) and the highest concentrations of negative oxygen ions.

(iii) For $E/p = 20$ V/(cm torr), the breakdown develops at the pressures $p = 0.0005$ and 0.005 atm and concentrations of negative oxygen ions $\delta = [O_2^-]/N = 10^{-13} - 10^{-12}$.

(iv) For $E/p = 30$ V/(cm torr), the breakdown is observed within the pressure range $p = 0.0005$–0.05 atm for the concentrations of negative oxygen ions $\delta = [O_2^-]/N = 10^{-16}$–$10^{-12}$.

The important feature of this type of breakdown is that it develops even if the initial hydrogen concentration in the mixture is very low. For $E/p = 20$ V/(cm torr), $\delta = 10^{-13}$, and $p = 0.005$ atm, the breakdown occurs at $[H_2] = 0.3\%$. For $E/p = 15$ V/(cm torr), $\delta = 8 \times 10^{-13}$, and $p = 0.0005$ atm, the H_2 concentration needed for the breakdown can be reduced to 0.4%.

Hence, in the mixture under study, the breakdown occurs at the reduced electric field at which the electron-impact ionization rate is much less than the attachment rate. Apparently, this can occur only if there exist efficient mechanisms for the destruction of negative ions at rates comparable with the electron-attachment rate. Such mechanisms are discussed in the next section.

4. DISCUSSION

Before thoroughly analyzing the breakdown mechanism, let us examine in more detail the regime with $E/p = 20$ V/(cm torr), $p = 0.005$ atm, $[H_2] = 5\%$, and $\delta = [O_2^-]/N = 2 \times 10^{-12}$.

The calculated duration of the breakdown-delay stage is equal to 90.6 s. Figure 1 shows the kinetic curves for the chemically active components O, H, OH, and O_3. Among the negative ions, the OH^- ions have the highest concentration, which remains almost unchanged throughout the delay stage and is equal to the initial concentration of O_2^- ions. Among the positive ions, the O_3^+ ions have the highest concentration.

The study of the time dependence of the concentration of electronically excited states $N_2(A^3\Sigma_u^+)$ and $N_2(a'^1\Sigma_u^-)$ plays an important role, because the collisions between these states lead to the ionization of molecular nitrogen. However, as will be shown below, this ionization process is not of primary importance for the type of breakdown under study. Among the electronically excited components, the $O_2(a^1\Delta_g)$ concentration is the highest. The gas temperature T remains constant during the delay stage.

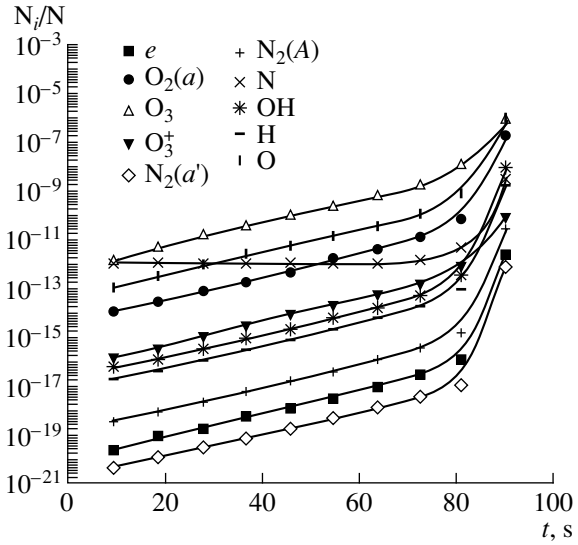

Fig. 1. Kinetic curves for the main components in the first breakdown stage for $E/p = 20$ V/(cm torr), $p = 0.005$ atm, relative hydrogen concentration $\eta_{H_2} = 5 \times 10^{-2}$, and relative O_2^- concentration $\eta_{O_2^-} = 2 \times 10^{-12}$.

In the next stage, the characteristic time scale of the process decreases significantly (Fig. 2). The degree of ionization becomes equal to 10^{-6} by the end of the second stage and the temperature increases by a factor of 2. The concentration of molecular hydrogen remains almost unchanged; consequently, the temperature growth cannot be attributed to combustion. The gas temperature grows due to collisional dissipation of the energy acquired by electrons in the electric field. The main dissipation process is the vibrational relaxation of the gas, because vibrational states of N_2 are effectively excited by electron impact in the near-breakdown field. The relaxation of the vibrational energy was calculated using the τ-approximation.

In a time less than 0.05 s, the characteristic time scale of chemical processes decreases again (Fig. 3). The third stage is characterized by a substantial increase in the temperature (by nearly one order of magnitude), high degrees of ionization and dissociation, and rapid growth of the NH concentration.

An analysis of the kinetic scheme shows that the OH^- ions arise through the conversion reaction

$$H_2 + O_2^- \longrightarrow OH^- + OH, \qquad (1)$$

whose rate constant is $k_1 = 0.4 \times 10^{-10}$ cm^3 s^{-1}. (The rate constants for reactions (1)–(16) [40–48] are listed in Table 2.)

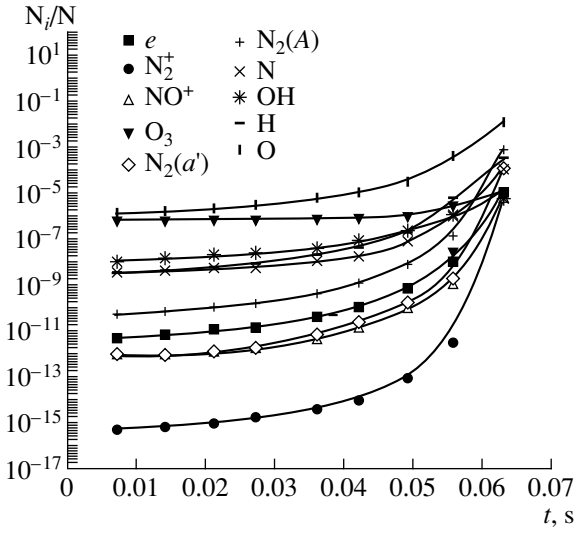

Fig. 2. Same as in Fig. 1, but in the second breakdown stage. The time is counted from the end of the curves in Fig. 1.

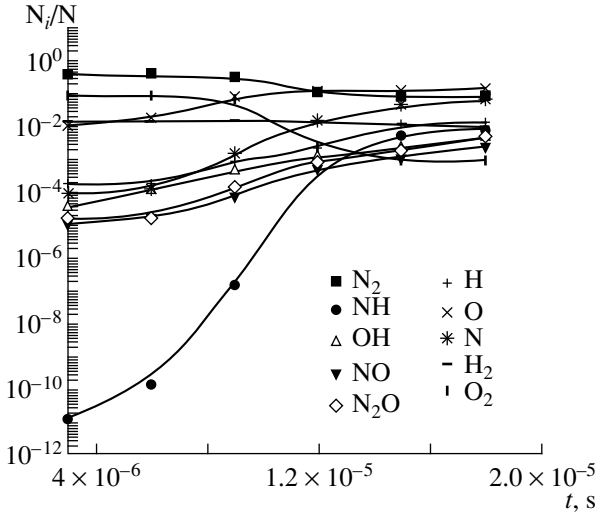

Fig. 3. Same as in Fig. 1, but in the third breakdown stage. The time is counted from the end of the curves in Fig. 2.

The O_2^- negative molecular ions are converted into OH^- stable ions via reaction (1) to form OH radicals. The most rapid process of OH destruction is the reaction

$$OH + H_2 \longrightarrow H_2O + H \quad (2)$$

extending the chain of hydrogen oxidation.

Atomic hydrogen H, which is a product of reaction (2), has the highest probability of reacting with O_2 via the three-body reaction

$$H + O_2 + M \longrightarrow HO_2 + M \quad (3)$$

which breaks the chain.

Free electrons arise due to detachment from OH^- in the reactions

$$OH^- + H \longrightarrow H_2O + e^-, \quad (4)$$

$$OH^- + HO_2 \longrightarrow H_2O + O_2 + e^-. \quad (5)$$

The following electron-balance reactions also play an important role in the development of the breakdown:

$$O_2 + e^- + M \longrightarrow O_2^- + M, \quad (6)$$

with $k_6 = 1.4 \times 10^{-29}\,(300/T_e)\exp(-600/T)\exp(700(T_e - T)/(T_eT))$ cm^6 s^{-1}, where $T_e = (2\varepsilon_e)/(3k)$ is the electron temperature, ε_e is the mean electron energy, and k is the Boltzmann constant;

$$OH^- + O \longrightarrow HO_2 + e^-; \quad (7)$$

$$OH^- + HO_2 \longrightarrow H_2O + O_2 + e^-; \quad (8)$$

$$H_2 + O_3^- \longrightarrow H_2O + O_2 + e^-; \quad (9)$$

$$H_2 + O^- \longrightarrow H_2O + e^-; \quad (10)$$

$$O_2 + e^- \longrightarrow O + O^-; \quad (11)$$

$$O_2 + e^- \longrightarrow O_2^+ + e^- + e^-; \quad (12)$$

$$N_2 + e^- \longrightarrow N_2^+ + e^- + e^-. \quad (13)$$

OH^- ions are also destroyed in the conversion reaction

$$OH^- + O_3 \longrightarrow OH + O_3^-. \quad (14)$$

Exclusion of any of the detachment reactions (7)–(11) or ionization reactions (12) or (13) makes the breakdown impossible. The exclusion of attachment reaction (6) decreases the delay stage significantly. A simplified model that incorporates only the electron-balance processes (6)–(13) describes well the behavior of the gas mixture during the delay stage of the breakdown. The duration of this stage is about 100 s. Almost throughout the entire delay period ($t < 80$ s), the concentrations of the main components (e^-, O, H, OH, HO_2, O_3, O^-, and O_3^-) and positive ions are less by nearly one-half in comparison with those calculated by the full model. The breakdown disappears at nearly the same minimum value of E/n as for the full model.

It is seen from Fig. 1 that the OH^- concentration is equal to the initial concentration of negative O_2^- ions. Consequently, the O_2^- ions are rapidly converted into OH^- ions to form OH radicals, which initiate the chain process of hydrogen oxidation.

The basic processes governing the electron balance are the ionization reactions (12) and (13), three-body attachment reaction (1), dissociative attachment reaction (11), and detachment reaction (10).

In a real situation, there is one more branch in the chain of electron reproduction. This branch consists of the reactions of three-body attachment to molecular oxygen; conversion of the molecular negative oxygen ions to OH^- ions; and detachment of electrons from the last ions in reactions (7) and (8), conversion reaction (14), and detachment reaction (9). From reactions (7)–(9) and (14), it is seen that this chain for the reproduction of electrons is connected with the chain reaction of hydrogen oxidation, electron-impact dissociation of oxygen and hydrogen, and the reactions of ozone reproduction.

Let us examine the development of the breakdown at various pressures and the same initial number density of molecular oxygen ions $[O_2^-] = 10^3$ cm^{-3}. Figures 4 and 5 show the breakdown-delay times calculated for the hydrogen concentrations $[H_2] = 0.5$ and 0.005% and the reduced electric fields of E/p = 15, 20, 25, and 30 V/(cm torr). Figure 6 shows the lower and upper critical breakdown pressures for the same values of the reduced electric field and hydrogen concentration. The breakdown occurs at pressures above the upper and below the lower critical pressure. The existence of the upper limit for the breakdown pressure indicates the important role of three-body processes.

As the hydrogen concentration decreases, reaction (10) slows down and the other processes of O^- ion destruction,

$$O^- + N_2 \longrightarrow N_2O + e^-, \quad (15)$$

$$O^- + O_2 + (N_2, O_2) \longrightarrow O_3^- + (N_2, O_2), \quad (16)$$

Table 2. Rate constants of the key processes, cm^3 s^{-1}, cm^6 s^{-1}

$k_1 = 0.4 \times 10^{-10}$
$k_2 = 0.8 \times 10^{-11}\exp(-2100/T)$
$k_3 = 0.5 \times 10^{-31}(300/T)^{1.6}$
$k_4 = 10^{-9}$
$k_5 = 10^{-9}$
$k_6 = f(T, T_e)$
$k_7 = 1.5 \times 10^{-9}$
$k_8 = 10^{-9}$
$k_9 = 10^{-9}$
$k_{10} = 0.6 \times 10^{-9}$
$k_{11} = f(T_e)$
$k_{12} = f(T_e)$
$k_{13} = f(T_e)$
$k_{14} = 10^{-9}$
$k_{15} = 10^{-12}$
$k_{16} = 0.3 \times 10^{-27}(T)^{-1}$

become more efficient. Further, the electrons detach from O_3^- ions when the latter interact with hydrogen in reaction (9).

The reactions of electron-impact ionization of oxygen (12), nitrogen (13), and hydrogen are chain-branching reactions during the discharge development. The reactions of dissociative attachment (11) and three-body attachment (6) can be considered chain-breaking reactions during the breakdown. However, the breakdown restarts due to the detachment of electrons from

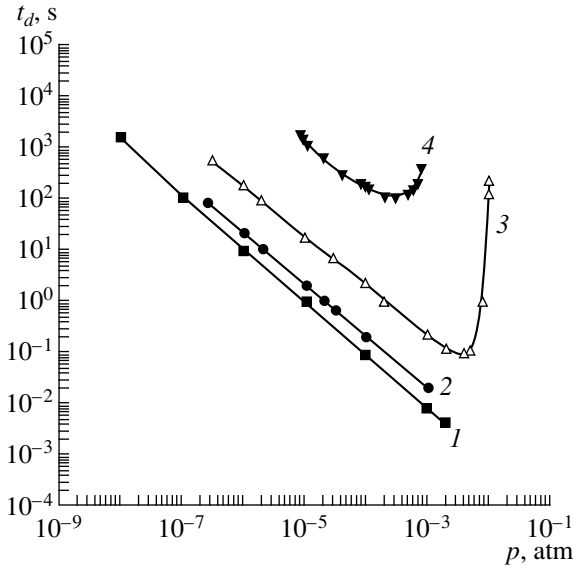

Fig. 4. The delay time as a function of pressure for the initial hydrogen concentration $[H_2] = 0.5\%$ at E/p = (*1*) 30, (*2*) 25, (*3*) 20, and (*4*) 15 V/(cm torr).

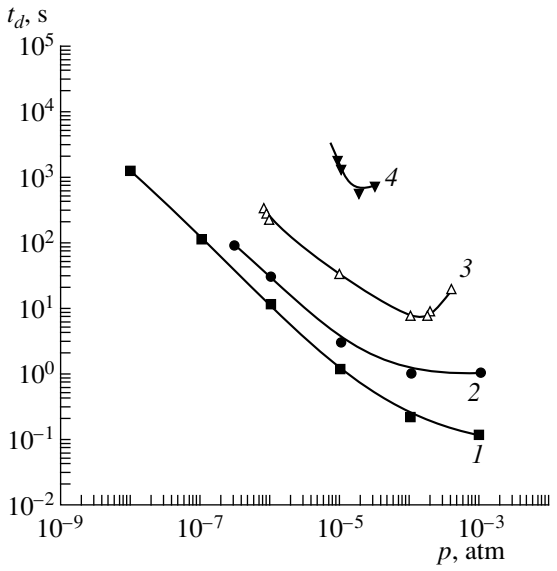

Fig. 5. The delay time as a function of pressure for the initial hydrogen concentration $[H_2] = 0.005\%$ at E/p = (*1*) 30, (*2*) 25, (*3*) 20, and (*4*) 15 V/(cm torr).

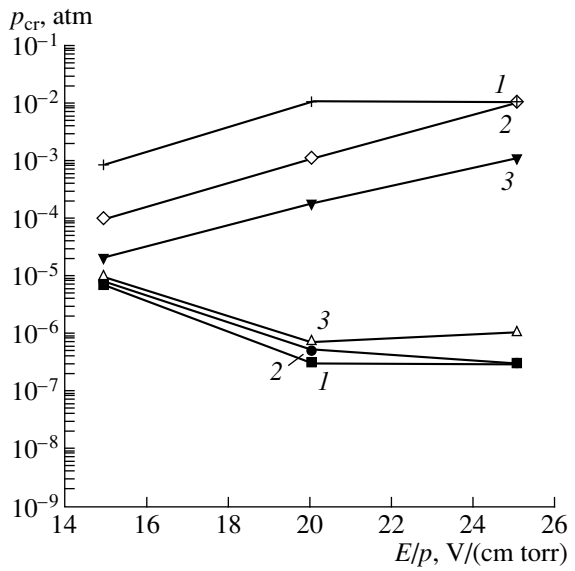

Fig. 6. The critical breakdown pressure as a function of the reduced electric field for a molecular hydrogen concentration of (*1*) 0.5%, (*2*) 0.005%, and (*3*) 0.05%.

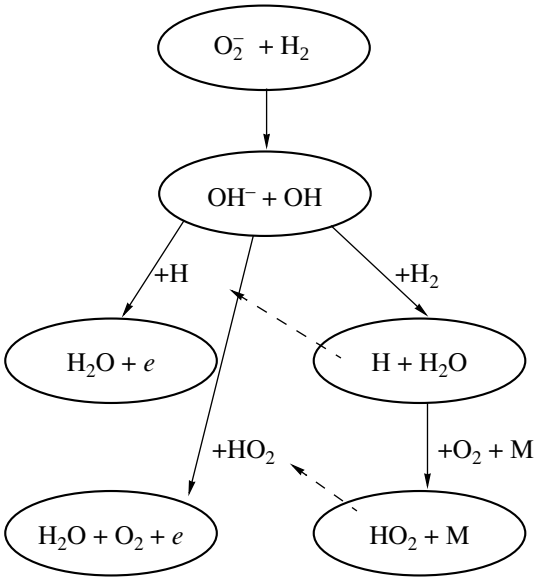

Fig. 7 Scheme of the basic processes during the breakdown.

positive ions. The electrons detach from O^- ions in reactions (10) and (15) either directly or through conversion into O_3^- via reaction (16) followed by the detachment reaction (9). The detachment from negative molecular oxygen ions is a more complicated process. First, the O_2^- ions are converted into OH^- ions via reaction (1). Then, the electrons detach from OH^- ions by the H atoms, HO_2 radicals, or O atoms [reactions (4), (8), and (7), respectively]; the latter is produced primarily by the electron-impact dissociation of oxygen. The electron detachment from OH^- ions also occurs through conversion into O_3^- ions [reaction (14)] followed by detachment [reaction (9)]. The scheme of the basic processes during development of the breakdown is illustrated in Fig. 7.

It follows from the above analysis that the initiation of the gas breakdown can be attributed to the presence of H, HO_2, and O components, which are produced in the reactions of hydrogen oxidation and electron-impact dissociation of O_2 and H_2, as well as due to ozone production and the presence of molecular hydrogen [see (9) and (14)]. In turn, OH production [see (1) and (14)] initiates the hydrogen oxidation.

5. GAS BREAKDOWN IN LOW GEOELECTRIC FIELDS

Finally, we consider the question of whether the breakdown under study can be initiated by the geoelectric field with a strength of $E_0 \simeq 1.3$ V/cm. As was shown above, the breakdown in air with a small addition of molecular hydrogen can occur even at E/p = 15 V/(cm torr). This value of the reduced electric field is attainable at a pressure of $p = 1.2 \times 10^{-4}$ atm corresponding to an altitude of 60 km. The breakdown can develop at the number density of negative oxygen ions of $[O_2^-] = 2 \times 10^3$ cm^{-3}, which is typical of the upper atmosphere. For the molecular-hydrogen number density $[H_2] = 1.5 \times 10^{12}$ cm^{-3} (0.04%), the breakdown time is $\tau_{ind} \simeq 1600$ s.

6. CONCLUSION

It is shown that the electric breakdown in a N_2–O_2 airlike mixture at low (0.005–5%) concentrations of H_2 and O_2^- (the admixture number density is on the order of 10^3–10^6 cm^{-3}) can occur via two mechanisms for electron reproduction: (i) the detachment from negative atomic oxygen ions and (ii) the detachment from negative molecular oxygen ions through conversion reactions. These mechanisms are associated with the reactions of hydrogen oxidation, electron-impact dissociation of oxygen, and ozone production. This type of breakdown can occur at the values of the reduced electric field at which the ionization rate is much lower than the electron-attachment rate.

Detailed numerical calculations were performed for the number density of negative oxygen ions $[O_2^-] = 10^3$ cm^{-3}, which corresponds to the mean ion concentration in the atmosphere. It is found that, at a sufficiently low pressure $p \simeq 10^{-4}$ atm, the breakdown can occur at E/p = 20 V/(cm torr) and hydrogen concentration $[H_2]$ = 0.005%. At a pressure corresponding to an altitude of

$h \simeq 60$ km, this value of the reduced field is attained at a mean geoelectric field of $E_0 = 1.3$ V/cm. Hence, this breakdown mechanism may contribute to the initiation of electric discharges in the upper atmosphere.

ACKNOWLEDGMENTS

This work was supported in part by the Russian Foundation for Basic Research (project no. 99-03-32237), INTAS (grant no. 96-2120), the US Force Research Laboratory's Office of Scientific Research, European Office of Aerospace and Development (London, UK).

REFERENCES

1. R. A. Morris, A. A. Viggiano, S. T. Arnold, *et al.*, in *Proceedings of 27th International Symposium on Combustion, Boulder, 1998*, WIP Abstracts, p. 343.
2. S. M. Starikovskaia, A. Yu. Starikovskii, and D. V. Zatsepin, in *Proceedings of 27th International Symposium on Combustion, Colorado, Boulder, 1998*, WIP Abstracts, p. 4.
3. S. M. Starikovskaia, A. Yu. Starikovskii, and D. V. Zatsepin, J. Phys. D: Appl. Phys. **31**, 1118 (1998).
4. Yu. D. Korolev and G. A. Mesyats, *Physics of Pulsed Gas Discharges* (Nauka, Moscow, 1991).
5. L. M. Vasilyak, S. V. Kostyuchenko, N. N. Kudryavtsev, and I. V. Filyugin, Usp. Fiz. Nauk **164**, 263 (1994) [Phys. Usp. **37**, 247 (1994)].
6. N. B. Anikin, S. V. Pancheshnyi, S. M. Starikovskaia, and A. Yu. Starikovskii, J. Phys. D: Appl. Phys. **31**, 826 (1998).
7. D. D. Sentman and E. M. Wescott, Phys. Plasmas **2**, 2514 (1995).
8. D. D. Sentman, E. M. Wescott, D. L. Osborne, *et al.*, Geophys. Res. Lett. **22**, 1205 (1995).
9. E. M. Wescott, D. D. Sentman, D. L. Osborne, *et al.*, Geophys. Res. Lett. **22**, 1209 (1995).
10. E. M. Wescott, D. D. Sentman, M. J. Heavner, *et al.*, Geophys. Res. Lett. **23**, 2153 (1996).
11. H. Fukunishi, Y. Takahashi, M. Kubota, *et al.*, Geophys. Res. Lett. **23**, 2157 (1996).
12. U. S. Inan, C. Barrington-Leigh, S. Hansen, *et al.*, Geophys. Res. Lett. **24**, 583 (1997).
13. A. V. Eletskiĭ and B. M. Smirnov, Inzh.-Fiz. Zh. **62**, 661 (1992).
14. D. A. Price, J. Lucas, and J. L. Morussi, J. Phys. D **5**, 1249 (1972).
15. R. J. Corbin and L. Frommhold, Phys. Rev. A **10**, 2273 (1974).
16. Yu. P. Raĭzer, *Gas Discharge Physics* (Nauka, Moscow, 1987; Springer-Verlag, Berlin, 1991).
17. V. D. Rusanov and A. A. Fridman, *Physics of Chemically Active Plasma* (Nauka, Moscow, 1984).
18. N. L. Aleksandrov, F. I. Vysikaĭlo, R. Sh. Islamov, *et al.*, Teplofiz. Vys. Temp. **19**, 22 (1981).
19. I. A. Kossyi, A. Yu. Kostinski, A. A. Matveev, and V. P. Silakov, Plasma Sources Sci. Technol. **1**, 207 (1992).
20. É. E. Son, *Electrons in a Low-Temperature Plasma* (Vsesoyuzn. Politekh. Inst., Moscow, 1990).
21. Y. Itikawa, At. Data Nucl. Data Tables **14** (1) (1974).
22. V. E. Gal'tsev *et al.*, Preprint No. 3156, IAE (Kurchatov Institute of Atomic Energy, Moscow, 1979).
23. D. A. Erwin and J. A. Kunc, IEEE Trans. Plasma Sci. **11**, 266 (1983).
24. G. J. Schulz, Phys. Rev. **135**, A938 (1964).
25. M. J. W. Boness and G. J. Schulz, Phys. Rev. A **8**, 2883 (1973).
26. D. C. Cartwright *et al.*, Phys. Rev. A **16** (3) (1977).
27. Y. Itikawa *et al.*, J. Phys. Chem. Ref. Data **15**, 985 (1986).
28. D. Spence and P. D. Burrow, J. Phys. B **12**, 179 (1979).
29. H. F. Winters, J. Chem. Phys. **44**, 1472 (1966).
30. D. Rapp and P. Englander-Golden, J. Chem. Phys. **43** (5) (1965).
31. K. Onda, J. Phys. Soc. Jpn. **54**, 4544 (1985).
32. O. A. Gordeev and D. V. Khmara, in *Proceedings of IX Conference on Physics of Gas Discharge, Ryazan, 1998*, p. 91.
33. R. D. Hake and A. V. Phelps, Phys. Rev. **158**, 70 (1967).
34. R. Sh. Islamov, I. V. Kochetov, and V. G. Pevgov, Preprint No. 169, FIAN (Lebedev Institute of Physics, USSR Academy of Sciences, Moscow, 1977).
35. Y. Itikawa *et al.*, J. Phys. Chem. Ref. Data **18**, 23 (1989).
36. D. Rapp and D. D. Briglia, J. Chem. Phys. **43**, 1480 (1965).
37. D. Rapp and P. Englander-Golden, J. Chem. Phys. **43**, 1464 (1965).
38. D. Rapp, P. Englander-Golden, and D. D. Briglia, J. Chem. Phys. **42**, 4081 (1965).
39. D. V. Zatsepin, S. M. Starikovskaya, and A. Yu. Starikovskiĭ, Khim. Fiz. (in press).
40. A. Yu. Kostinskiĭ, Preprint No. 87, IOFAN (Institute of General Physics, USSR Academy of Sciences, Moscow, 1990).
41. C. M. Ferreira *et al.*, IEEE Trans. Plasma Sci. **19**, 229 (1991).
42. L. I. Virin, *Ion–Molecular Reactions in Gases* (Nauka, Moscow, 1979).
43. V. L. Bychkov and V. A. Yurovskiĭ, Teplofiz. Vys. Temp. **31**, 8 (1993).
44. *Combustion Chemistry*, Ed. by W. Gardiner, Jr. (Springer-Verlag, New York, 1984; Mir, Moscow, 1988).
45. W. G. Mallard *et al.*, *NIST Chemical Kinetic Database, Ver. 6.0* (1994)
46. T. J. Millar, J. M. C. Rawlings, A. Bennett, *et al.*, Astron. Astrophys., Suppl. Ser. **87**, 585 (1991).
47. T. J. Millar, P. R. A. Farquhar, and K. Willacy, Astron. Astrophys., Suppl. Ser. **121**, 139 (1997).
48. E. F. van Dishoeck, in *Rate Coefficients in Astrochemistry*, Ed. by T. J. Millar and D. A. Williams (Kluwer, Dordrecht, 1988), p. 49.

Translated by N. Larionova

Plasma Physics Reports, Vol. 26, No. 8, 2000, pp. 710–714. Translated from Fizika Plazmy, Vol. 26, No. 8, 2000, pp. 757–762.

LOW-TEMPERATURE PLASMA

Population of Vibrational Levels of Krypton Excimer States Excited by an Electric Discharge

A. V. Loginov

Vavilov State Optical Institute, Birzhevaya liniya 12, St. Petersburg, 199034 Russia

Received March 12, 1999; in final form, November 28, 1999

Abstract—The effect of admixtures and excitation conditions on the population distribution of the vibrational levels of krypton excimer states is investigated. The emission spectra of a krypton discharge plasma in a supersonic jet, an extended capillary discharge, and a barrier discharge are considered. It is found that the population distribution in a barrier discharge best fits the equilibrium conditions. © *2000 MAIK "Nauka/Interperiodica".*

1. INTRODUCTION

The emission spectra of rare-gas plasmas excited by an electric discharge have been studied in experiments with a dc discharge in a krypton supersonic jet [1]; barrier discharge in both pure krypton and Kr–Xe mixtures [2]; and dc discharge in a krypton capillary both at room temperature and under cooling the capillary wall with liquid nitrogen [3]. One of the most important results of the studies is that all the above spectra are similar in shape, which enables their unified interpretation and modeling. At the same time, it is also of interest to compare the results of such an interpretation and reveal specific features of each type of discharge.

The spectra discussed are well known as molecular continuums of rare-gas dimers originating due to the bound–free transitions from the lowest electronic states 0_u^+ and 1_u to the repulsive ground electronic state 0_g^+ (see, e.g., [4] and references therein). Short-wavelength and long-wavelength wings of a molecular continuum (the so-called first and second continuums) are attributed to the transitions from the high-lying and low-lying vibrational levels of the upper electronic states, respectively. A distinguishing feature of the spectra in question is a clearly defined second continuum, whereas the first continuum is much weaker and less pronounced [1–3]. For this reason, below, we only consider the second continuum and, consequently, the low-lying vibrational levels.

Since the spectra are similar in shape [1–3], we will treat them in a unified manner, following our previous papers [5, 6]. The procedure enables us to evaluate the contribution of any vibrational level to the spectral distribution of the emission energy by fitting the calculated spectrum to the measured one. In such a way, both the number of involved levels and their relative populations can be determined. Based on these data and the values of the vibrational energy, we can find the vibrational temperature and reveal how the discharge mode and the presence of admixtures affect the shape of the distribution of the vibrational level populations.

2. METHOD FOR EVALUATING THE LEVEL POPULATION

Let us recall the procedure proposed in [5, 6]. The method is based on the numerical calculation of the spectral distribution $I_v(\lambda)$ of the radiant energy emitted via the bound–free transition $v \longrightarrow \varepsilon$ from the vibrational level v of the bound electronic state to the repulsive state. Having a set of $I_v(\lambda)$ functions for different vibrational quantum numbers v, we can approximate the measured distribution $I(\lambda)$ by expanding it into a series

$$I(\lambda) = \sum_v C_v I_v(\lambda), \qquad (1)$$

where the weighting factors C_v, which are treated here as relative populations of the vibrational levels v, are calculated by the least-squares method (LSM) with the help of the BARSIC numerical code [7].

The dependence of the spectral distribution of radiant energy on the wavelength is determined (accurate to a constant factor) by the expression

$$I_v(\lambda) = (1/\lambda^6)\left|\int \psi_v(R)\mu(R)\psi_\varepsilon(R)dR\right|^2, \qquad (2)$$

where λ is the wavelength of the bound–free transition $v \longrightarrow \varepsilon$; $\psi_v(R)$ is a vibrational wave function of the v level of the upper bound state 1_u; $\mu(R)$ is the dipole moment of the $1_u \longrightarrow 0_g^+$ transition, which is substituted here by a constant; and $\psi_\varepsilon(R)$ is a vibrational wave function of the lower repulsive state 0_g^+ corresponding to the positive value of the energy ε (the amplitude of $\psi_\varepsilon(R)$ is normalized to $1/(\sqrt{\pi}\sqrt{\varepsilon})$ at large R). Taking into account that only the vibrational levels $v \le 6$ are

ultimately involved in the calculation, such an approximation seems quite appropriate. In other words, since the internuclear distance in integral (2) varies only slightly, substituting the quantity $\mu(R)$ with a constant should not result in a drastic change of the integral value.

To find the wave functions, we numerically integrate the Schrödinger equation for the vibrational states,

$$d^2\psi/dR^2 + [E - U(R)]\psi = 0, \quad (3)$$

by applying a modified Numerov's method [8]. The proper internuclear potentials $U(R)$ of the upper 1_u and lower 0_g^+ states of a krypton dimer were taken from [9] and [10], respectively. We consider these potentials to be reliable because they satisfy the main criterion for closely fitting the experimental spectrum; namely, there is a good agreement between the maxima of the $I_0(\lambda)$ function and the measured peak of the second continuum.

Assuming that the population distribution is close to equilibrium, i.e.,

$$C_v/C_0 = \exp(-E_v/kT), \quad (4)$$

where E_v is the energy gap between the v and zero vibrational levels and the vibrational temperature T can be estimated from the values of C_v and C_0. Note that E_v values are derived from the Schrödinger equation (3).

Obviously, to apply the above approach, we have to assume that the measured spectrum can be accurately approximated by the transitions from only one of the two (1_u or 0_u^+) states. This is related to the fact that it is difficult to evaluate the partial contribution of a certain state to the measured spectrum $I(\lambda)$. Moreover, the energy gap between the $^3P_2$ and $^3P_1$ atomic levels to which the potential curves of the 1_u and 0_u^+ states tend is insufficiently wide for the functions $I_v(\lambda)$ [which are obtained by solving Eqs. (2) and (3) with potentials 1_u and 0_u^+] to be well separated and not overlap. Therefore, a mere combination of the two function sets in formula (1) would not provide a proper approximating basis for the LSM procedure in the BARSIC code [7]. In other words, it is impossible to separate the partial contributions from the excimer states based on the LSM only; some additional data are necessary. Since such data are unavailable, we assume the above contributions to be comparable. Therefore, the results obtained here for the 1_u state may also be assigned to the 0_u^+ state.

3. RESULTS

3.1. Preliminary Notes

Like any other LSM-based fitting procedure, the BARSIC code includes no inherent physical criteria for one or another parameter to be involved in the fitting procedure [7]. As applied to our problem, this means that we need certain auxiliary reasons to cut the summation on the right-hand side of (1). Keeping in mind the physical meaning of the C_v coefficients, we assume that they monotonically decrease with increasing v. Recall that, in our case, the object of fitting is the second continuum emitted from the low-lying vibrational levels. This means that, in the course of the fitting procedure, the number of fit functions $I_v(\lambda)$ in formula (1) is being increased as long as the C_v coefficients match the above assumption. The values of C_v normalized to C_0 for each of the populated levels and the corresponding values of the vibrational energy and temperature calculated according to (3) and (4), respectively, are presented in Tables 1–3. Note again that the E_v values are derived from the Schrödinger equation (3) with the internuclear potentials taken from [9, 10]. The data from Tables 1 and 2 were used to plot $\ln C_v$ versus E_v (Figs.1, 2). The better this dependence is approximated by a straight line, the closer the population distribution is to the equilibrium one. The slope of the straight line determines the vibrational temperature. For the highest vibrational levels from Tables 1–3, the C_v values fall out of the monotonic dependence. This was the reason to cut the series on the right-hand side of Eq. (1), thus determining the number of vibrational levels populated in the given type of discharge. In other words, we assume that the above nonmonotonic behavior has no physical sense; it merely reflects the features of the computing procedure [7]. For this reason, the corresponding points are not presented in Figs. 1 and 2.

3.2. Capillary DC Discharge

To examine the population distribution in this type of discharge, we used the spectra obtained in [1] at a pressure of 120 torr, a discharge current of 10 mA, and voltage of 1.4 kV at room temperature and under cooling with liquid nitrogen. The results are presented in Table 1 and Fig.1.

3.3. Barrier Discharge

To examine the population distribution in a barrier discharge, we used the spectra obtained in [2] at a krypton pressure of 400 torr. Discharges in both pure krypton and a Kr–Xe mixture with a Xe content of 0.01 and 0.04% were examined.

Note that, in this case, the main specific feature of the discharge emission spectra is the presence of an extremely narrow and intense peak in the vicinity of a Xe atomic resonant line against the Kr continuum background. The study of this feature was the main goal of [2]. For the above Xe concentrations, the krypton continuum can be easily separated out of the emission spectrum of the discharge. The procedure described above was applied to calculating the popula-

Table 1. Population C_v of krypton excimer vibrational v levels and vibrational temperature T [K] in a capillary dc discharge at room temperature and under cooling with liquid nitrogen

v		Room temperature		Cooling with liquid nitrogen	
	E_v, au	$C_v \pm \Delta C_v$	$T \pm \Delta T$	$C_v \pm \Delta C_v$	$T \pm \Delta T$
0	0	1.000 ± 0.048		1.000 ± 0.028	
1	0.000639	0.635 ± 0.058	445 ± 88	0.455 ± 0.034	256 ± 24
2	0.001269	0.377 ± 0.060	410 ± 66	0.205 ± 0.036	253 ± 29
3	0.001891	0.262 ± 0.060	445 ± 76	0.124 ± 0.035	286 ± 38
4	0.002505	0.212 ± 0.059	508 ± 92	0.099 ± 0.035	342 ± 51
5	0.003111	0.204 ± 0.057	619 ± 107	0.089 ± 0.033	406 ± 63
6	0.003708	0.299 ± 0.050		0.133 ± 0.029	

Table 2. Population C_v of krypton excimer vibrational v levels and vibrational temperature T [K] in a dc barrier discharge

v		Pure Kr		Kr–0.01% Xe mixture		Kr–0.04% Xe mixture	
	E_v, au	$C_v \pm \Delta C_v$	$T \pm \Delta T$	$C_v \pm \Delta C_v$	$T \pm \Delta T$	$C_v \pm \Delta C_v$	$T \pm \Delta T$
0	0	1.000 ± 0.047		1.000 ± 0.074		1.000 ± 0.109	
1	0.000639	0.649 ± 0.027	467 ± 45	0.631 ± 0.044	437 ± 66	0.489 ± 0.080	282 ± 64
2	0.001269	0.373 ± 0.043	407 ± 48	0.448 ± 0.061	499 ± 85	0.302 ± 0.106	335 ± 98
3	0.001891	0.194 ± 0.051	364 ± 58	0.343 ± 0.068	558 ± 103	0.171 ± 0.119	338 ± 133
4	0.002505	0.183 ± 0.048	467 ± 72	0.228 ± 0.074	535 ± 118	0.159 ± 0.117	430 ± 172
5	0.003111	0.121 ± 0.050	466 ± 91	0.084 ± 0.082	396 ± 156	0.109 ± 0.117	444 ± 215
6	0.003708	0.066 ± 0.061	430 ± 146	0.070 ± 0.097	441 ± 230	0.075 ± 0.142	451 ± 329
7	0.004297	0.145 ± 0.056		0.167 ± 0.088		0.126 ± 0.133	

Table 3. Population C_v of krypton excimer vibrational v levels and vibrational temperature T [K] in a supersonic jet discharge

		P = 536 torr T_g = room temperature I = 25 mA		P = 536 torr T_g = room temperature I = 50 mA		P = 350 torr T_g = 161 K I = 15 mA	
v	E_v, au	$C_v \pm \Delta C_v$	$T \pm \Delta T$	$C_v \pm \Delta C_v$	$T \pm \Delta T$	$C_v \pm \Delta C_v$	$T \pm \Delta T$
0	0	1.00 ± 0.19		1.00 ± 0.24		1.00 ± 0.17	
1	0.000639	0.29 ± 0.23	165 ± 111	0.30 ± 0.29	170 ± 139	0.31 ± 0.21	171 ± 98
2	0.001269	0.22 ± 0.21		0.32 ± 0.27		0.21 ± 0.20	

tions of the vibrational levels of krypton excimer states. The results are presented in Table 2 and Fig. 2.

An increase in the Xe content results in the appearance of continuums emitted by both heteronuclear KrXe molecules and Xe_2 molecules. Under these conditions, the procedure of separating out the part of the measured spectrum related exclusively to krypton molecular transitions becomes incorrect and, hence, our method fails. The effect of the Xe content on the discharge emission spectrum in Kr–Xe mixtures was studied in detail in [11].

3.4. DC Discharge in a Supersonic Jet

The emission spectra of a dc discharge in a supersonic krypton jet were measured in [1]. To calculate the level populations, we used three spectra under different discharge conditions. The discharge parameters, as well as the calculated populations and vibrational temperature, are presented in Table 3. Here, I, P, and T_g are the discharge current, gas pressure, and temperature upstream of the supersonic jet nozzle, respectively.

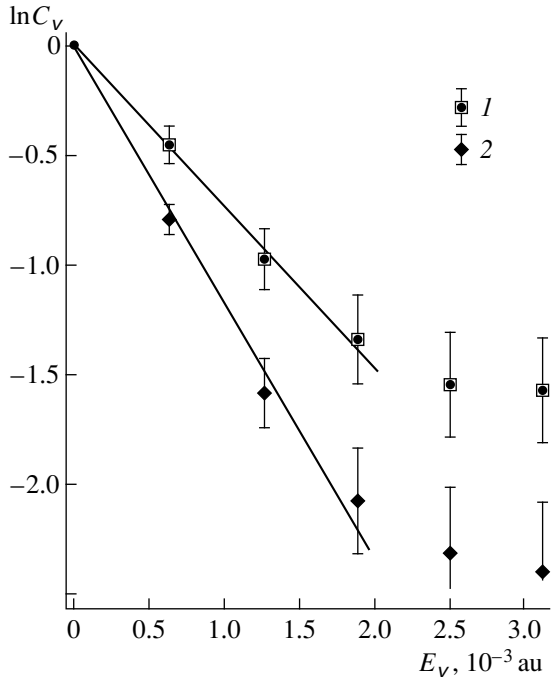

Fig. 1. Logarithm of the population C_v of krypton excimer vibrational levels vs. the level energy E_v in a capillary dc discharge (*1*) at room temperature and (*2*) under cooling with liquid nitrogen. Solid lines show the equilibrium population distribution for the first four levels.

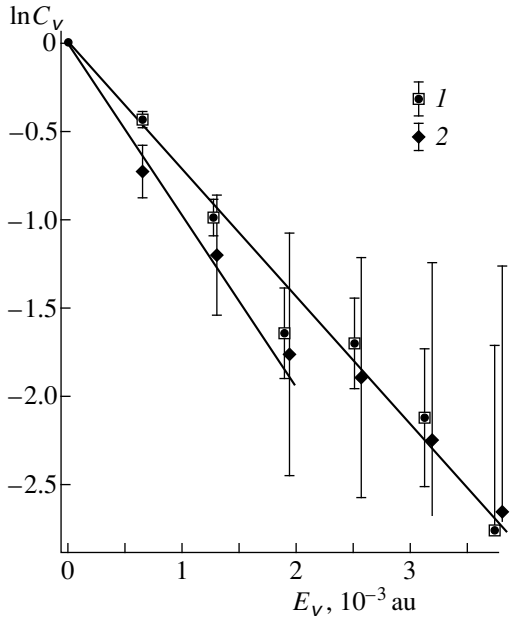

Fig. 2. Logarithm of the population C_v of krypton excimer vibrational levels vs. the level energy E_v in a barrier discharge in (*1*) pure krypton and (*2*) a Kr–0.04% Xe mixture. Solid lines show the equilibrium population distribution for pure krypton and the two-temperature population distribution over the $v = 0$–3 and $v = 4$–6 levels in the Kr–0.04% Xe mixture.

4. DISCUSSION

According to the model adopted, seven vibrational levels of electronically excited krypton dimer states are assumed to be populated in a capillary discharge. The same is for a barrier discharge. The situation is quite different in the case of a supersonic jet discharge, where only three vibrational levels are populated.

As for the results of computing the vibrational temperature, we note that the temperature T in Eq. (4) is a characteristic of a quantum ensemble as a whole. In the case under consideration, such a quantum ensemble is the system of krypton excimer vibrational levels. Therefore, the temperature T calculated according to (4) should be the same for all of the populated levels. In other words, the degree to which T is the same for all of the populated vibrational levels represented in Tables 1–3 can be regarded as the degree to which the system is in equilibrium. From this point of view, the barrier discharge in pure krypton, in which T is the same for all of the populated vibrational levels within the calculation accuracy (Table 2), matches the equilibrium state best of all. Accordingly, all the points in Fig. 2 fit a straight line.

It is noteworthy that the ΔT error stems from the existence of the ΔC_v error. The latter, in turn, is calculated according to the well-known LSM formulas (see, e.g., [12]) and characterizes the accuracy to which the method is realized within the adopted physical model. As for the question of whether the model is realistic, the values of ΔC_v and ΔT can only be regarded as supplementary evidence.

Under capillary discharge conditions (Table 1), the first four populated levels correspond to the equilibrium state. It is also seen in Fig.1, in which the first four points fit a straight line well. For subsequent levels, the T value obviously shows a tendency to increase. Finally, under conditions of a supersonic jet discharge (Table 3), the above criterion is not valid at all, taking into account the amount of populated levels and the ΔC_v error value. From the viewpoint of the LSM theory, large ΔC_v values for $v = 1$, 2 (Table 3) prove that the role of the $I_v(\lambda)$ functions ($v = 1$, 2) in describing discharge spectra in a supersonic jet is quite negligible. Perhaps there is no need at all to use these functions for spectrum fitting and it is better to consider the rotational structure of the zero vibrational level, using as an approximating set the $I_0(\lambda)$ functions obtained for different values of the rotational quantum number J ($J = 0$, 1 …). In doing so, the rotational temperature can be determined.

It is of interest to compare the population distribution in a barrier discharge in pure krypton and Kr–Xe mixtures (Table 2). As was mentioned above, the krypton continuum is easily separated out of the discharge spectrum at such a minor Xe content. An admixture of 0.01% Xe (Table 2, second column) hardly affects the

population distribution of krypton excimer vibrational levels, the C_v and T values being almost identical to those for pure krypton. However, at a higher Xe content of 0.04%, the population of the $v = 1$–3 levels corresponds to a significantly lower value of T. For higher levels ($v > 3$), the T value is the same as for pure krypton. This is clearly illustrated in Fig. 2, in which the $\ln C_v$ values for a discharge in krypton with an 0.04% Xe admixture could be fitted well by two straight lines; one of them refers to the $v = 0$–3 levels, whereas the other one refers to the $v = 4$–6 levels. The slope of the latter line coincides with the slope of the line approximating the dependence of $\ln C_v$ on E_v for a discharge in pure krypton. It seems that there is some threshold value of Xe concentration above which a depopulation mechanism for lower krypton excimer vibrational levels becomes involved. A more detailed examination of the energy transfer processes in a Kr–Xe plasma excited by an electric discharge is performed in [11].

5. CONCLUSIONS

(i) The distribution of vibrational level populations of krypton excimer states excited in the plasma of a barrier discharge in pure krypton is equilibrium.

(ii) The features of the distribution of vibrational level populations of krypton excimer states excited by a barrier discharge in a Kr–Xe mixture indicate the existence of a selective depopulation mechanism for lower vibrational levels.

ACKNOWLEDGMENTS

I am grateful to G.A. Volkova and B.E. Krylov for kindly providing me with the measured spectra.

REFERENCES

1. G. N. Gerasimov, B. E. Krylov, A. V. Loginov, and S. A. Shchukin, Opt. Spektrosk. **73**, 1075 (1992) [Opt. Spectrosc. **73**, 639 (1992)].
2. G. A. Volkova and G. N. Gerasimov, Kvantovaya Élektron. (Moscow) **23**, 219 (1996).
3. G. N. Gerasimov, B. E. Krylov, G. N. Zvereva, *et al.*, Opt. Spektrosk. **81**, 935 (1996) [Opt. Spectrosc. **81**, 857 (1996)].
4. A. Gedanken, J. Jortner, B. Raz, and A. Szoke, J. Chem. Phys. **57**, 3456 (1972).
5. A. V. Loginov, Opt. Spektrosk. **82**, 547 (1997) [Opt. Spectrosc. **82**, 505 (1997)].
6. A. V. Loginov, Z. Phys. **41**, 245 (1997).
7. V. V. Monakhov and A. V. Kozhedub, in *Proceedings of the Conference on Theoretical, Applied, and Computational Celestial Mechanics, St. Petersburg, 1993*, p. 68.
8. F. Y. Hajj, J. Phys. B **13**, 4521 (1980).
9. C. W. Werner, E. V. George, P. W. Hoff, and C. K. Rhodes, IEEE J. Quantum. Electron. **13**, 769 (1977).
10. K. K. Docken and T. P. Schafer, J. Mol. Spectrosc. **46**, 454 (1973).
11. G. N. Gerasimov, R. Khallin, and B. E. Krylov, Opt. Spektrosk. **88**, 210 (2000).
12. Yu. V. Linnik, *Method of Least Squares and Principles of the Theory of Observations* (Fizmatgiz, Moscow, 1962; Pergamon, Oxford, 1961).

Translated by N. Ustinovskiĭ

Plasma Physics Reports, Vol. 26, No. 8, 2000, pp. 715–719. Translated from Fizika Plazmy, Vol. 26, No. 8, 2000, pp. 763–768.

LOW-TEMPERATURE PLASMA

Measurements of a Negative Ion Flux in Plasma Thruster Tests in a Vacuum Chamber

A. I. Bugrova*, A. V. Desyatskov*, A. I. Morozov, and V. K. Kharchevnikov***

**Moscow State Institute of Radioengineering, Electronics, and Automation (Technical University), pr. Vernadskogo 78, Moscow, 117454 Russia*

***Nuclear Fusion Institute, Russian Research Centre Kurchatov Institute, pl. Kurchatova 1, Moscow, 123182 Russia*

Received June 24, 1999; in final form, December 6, 1999

Abstract—The dynamics of negative ions created in the interaction of a plasma jet with a target is investigated experimentally. The experiments were carried out with a stationary plasma thruster. A multigrid probe was used to record negative ions. © *2000 MAIK "Nauka/Interperiodica".*

1. INTRODUCTION

An unusual dusting of the inner wall of the ATON stationary plasma thruster (SPT) [3] was found in the course of thruster tests in a vacuum chamber in which a metal surface was used as a collector of the plasma jet [1, 2]. A sharp drop in the thruster characteristics was observed during the first 1–15 min of its operation [4, 5]. Narrow strips of a deposited substance produced in the channel of the thruster indicated the deposition of a well-focused particle flow. It was supposed that, in the vacuum chamber, there were negative ions that moved under the action of the electric field towards the thruster channel, where they were accelerated and focused [6].

The purpose of our study is to record negative ions at the entrance and exit of the thruster channel.

2. EXPERIMENTAL SETUP

The ATON SPT, whose schematic is presented in Fig. 1, was installed in a $60 \times 60 \times 250$-cm vacuum chamber. The thruster jet was directed along the axis of the chamber; because of a small divergence of the jet, it hardly touched the chamber wall [7]. The ion beam was decelerated by a residual gas (the so-called "gas target") near the pumps. There were no metal crumbs (usually formed during bombardment of a chamber wall with the SPT ion beam) even after a 200-hour resource test of the thruster.

In the normal operation mode of the thruster, the residual air pressure in the vacuum chamber was kept at the level $P \sim (2–3) \times 10^{-4}$ torr and the xenon mass flow rate was $\dot{m}_a$ = 1–2.5 mg/s; the pumping was produced by diffusion pumps filled with VM–5 oil. In this case, the integral thruster characteristics such as the mean discharge current and thrust were high and stable.

To cause a drop in the thruster characteristics, a quartz target 15×15 cm in size was placed on the axis of the thruster at a distance of 25 cm from the thruster exit; the target was tilted 30° with respect to the axis. As a result, the discharge current increased from 2.07 to 2.21 A and the current fluctuations grew from 10 to 40% (with the anode voltage U and Xe mass flow rate kept constant). After 40 min of running the thruster, the operating conditions became stabilized at this level.

To record charged particles, we used a probe consisting of two grids and a collector placed behind the grids; the distance between the grids was 2 mm. The collector was installed at a distance of 2 mm from the last grid. The collector diameter was 6 mm, which corresponded to the inner diameter of the ceramic working channel of the probe. An advantage of the probe measurements is the possibility to determine the distribution function of charged particles by the collector current–voltage characteristic and estimate their density and energy. A disadvantage of the method is that it is somewhat cumbersome, which makes it impossible to determine the local parameters of charged particles with good spatial resolution.

To determine the energy spectrum of the particles entering the thruster channel, we set the probe at a distance z = 140 mm from the thruster exit and 30 mm away from its axis. The entrance window of the probe was oriented along the plasma jet, at an angle of 20° with respect to the thruster axis, thus intercepting particles moving toward the thruster exit. The measurements were carried out both with and without a target.

The energy spectra of the particles that passed through the thruster channel were also investigated. For this purpose, a multigrid probe was mounted flush with the rear wall of the buffer; the axis of the probe was parallel to the thruster axis. The experiments were carried out at the working-gas (Xe) mass flow rate $\dot{m}_a$ = 1.5–2.5 mg/s and U = 200–300 V.

1063-780X/00/2608-0715$20.00

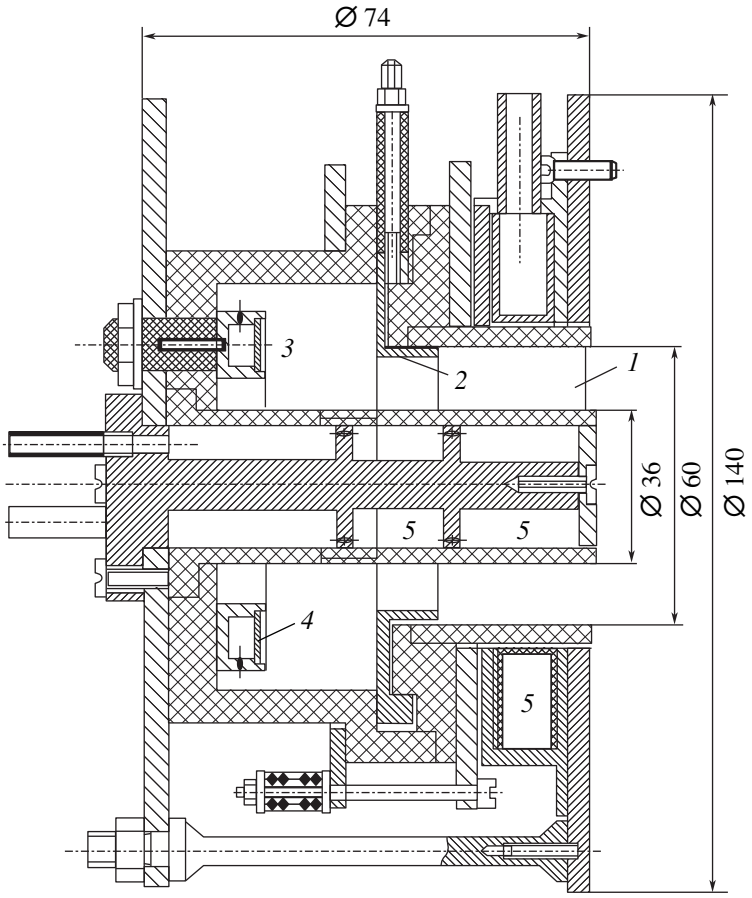

Fig. 1. Schematic of the ATON SPT: (*1*) accelerating channel, (*2*) anode, (*3*) buffer region, (*4*) gas distributor, and (*5*) magnetic coils.

3. ENERGY SPECTRA OF CHARGED PARTICLES AT THE ENTRANCE OF THE THRUSTER CHANNEL AND IN THE BUFFER VOLUME

Figure 2 presents the energy spectra of negatively charged particles without a target at the entrance of the thruster channel (Fig. 2a) and in the buffer volume (Fig. 2b) for $U = 300$ V and $\dot{m}_a = 2$ mg/s. It is seen from Fig. 2 that there is a group of negatively charged particles with an average energy of $\varepsilon \sim 6$ eV at the channel entrance. In accordance with the results of [8], this group is identified with electrons, which neutralize the ions flowing out of the thruster.

At the end of the buffer volume, the energy spectrum (Fig. 2b) has two peaks corresponding to slow electrons with energies of $\varepsilon \approx 6$ and fast electrons with energies of $\varepsilon \approx 38$ eV. The fast electrons are assumed to be responsible for the current related to the effect of a near-wall conductivity [9].

If a target is set into the thruster jet under the above operating conditions, then a second group of negatively charged particles with an average energy of $\varepsilon \approx 28$ eV is formed at the channel entrance (Fig. 3a). Since these particles appear only in the presence of a target, we assign them to negative ions. Variations in the discharge voltage slightly affect the average energy of slow electrons, whereas the energy of the negative ions changes appreciably (Table 1).

With a target, the spectrum of negatively charged particles in the buffer volume consists of three groups (Fig. 3b). A group of negatively charged particles whose energy corresponds to the discharge voltage appears at the rear wall of the buffer. Again, since this group appears only in the presence of a target, we assign them to negative ions. As the discharge voltage decreases, the energy of fast electrons and negative ions also decreases, whereas the energy of slow electrons changes only slightly (Table 2).

4. DENSITY OF NEGATIVELY CHARGED PARTICLES

There are two methods for calculating the density of charged particles using the measured collector current–voltage characteristics.

The first method is based on the measurements of the probe collector current. The density of the saturation current to the collector of a multigrid probe is

known to be $j_\alpha = \gamma e n v_\alpha$, where γ is the grid transparency and the other notation is standard. The value of v_α is taken from the measured energy spectrum.

The second method is based on the analysis of the particle distribution function. Having a distribution function of the particles of a given type, the particle density is calculated as

$$n_\alpha = \int f(v)dv.$$

The charged-particle densities presented in Table 3 were obtained from the ion saturation current measured with a plane electrostatic probe [10] and the positive-ion current measured with a multigrid probe [11]; the table also presents the results of this study.

The results of calculations shows that, in accordance with the results of [3, 8], the variations in the discharge voltage within 200–300 V (at $\dot{m}_a$ = const) slightly affect the densities of both fast and slow electrons. To calculate the density of negative ions, we should make some assumptions. The average mass of negative ions is supposed to be $m_i \approx 28$ amu. This assumption is based on previous results [4, 5, 12] and the experimental fact that a well-localized film is formed fairly fast on dielectric surfaces if a quartz plate (the main component is Si with the atomic mass $m_i \approx 28$ amu) was used as a target.

The average energy of negative ions can be determined from their distribution function (Fig. 3).

The density of negative ions is substantially less than the density of positive ions and electrons. As the mass flow rate of the working agent decreases from 2.5 to 1.5 mg/s, the density of negative ions n_i decreases from 8×10^{14} to 3×10^{14} m^{-3} at the thruster exit and from 6×10^{13} to 3×10^{13} m^{-3} in the buffer volume. The lowering of the discharge voltage from 300 to 200 V also leads to a decrease in n_i.

To verify the calculated values of the density of negative ions, we examined the rate at which the inner surfaces of the dielectric channel and the buffer are coated with a film. The thickness of the deposited film is $h = m/\rho S$, where ρ is the silicon specific mass density, S is the coated area, and $m = m_0 n_i v_i S t$ (here, m_0 is the Si ion mass; t is the deposition time; and n_i and v_i are the density and velocity of negative ions, respectively).

The calculated rate of coating for U = 300 V, $\dot{m}_a$ = 2 mg/s, and t = 4 h turned out to be

$$\dot{v} = h/t = n_i m_0 v_i/\rho \approx 0.05 \ \mu\text{m/h}.$$

This value is in good agreement with the rate determined from the measured thickness of the film on the insulator surface.

5. ANALYSIS OF EXPERIMENTAL DATA

According to numerous studies (see, e.g., [7]), the electron distribution function in the SPT channel is non-Maxwellian. It is formed mainly due to collisions

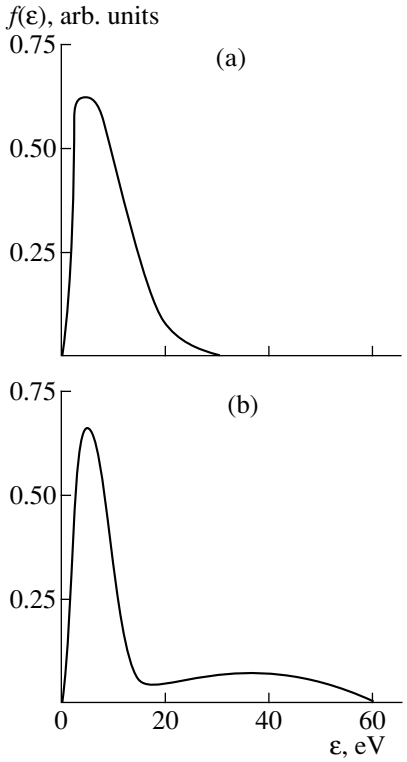

Fig. 2. Energy spectra of negatively charged particles without a target (a) at the thruster exit and (b) in the buffer volume for U = 300 V and $\dot{m}_a$ = 2 mg/s.

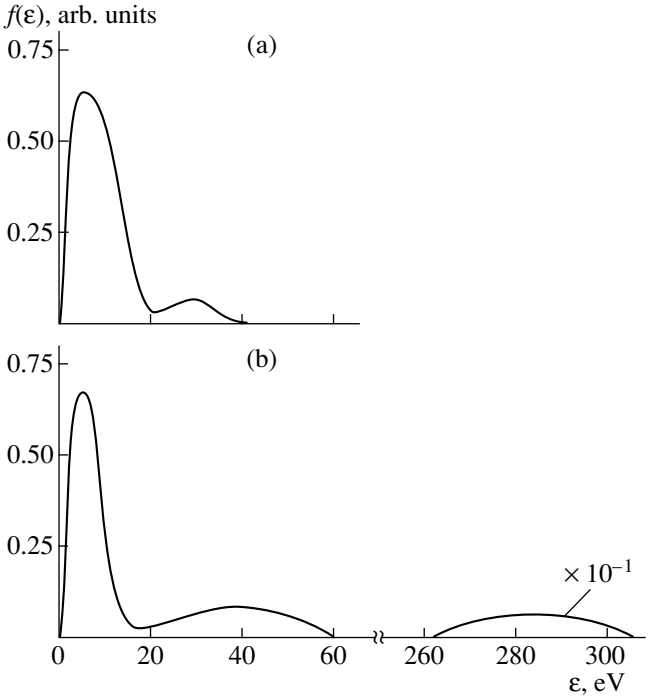

Fig. 3. Energy spectra of negatively charged particles with a target (a) at the thruster exit and (b) in the buffer volume for U = 300 V and $\dot{m}_a$ = 2 mg/s.

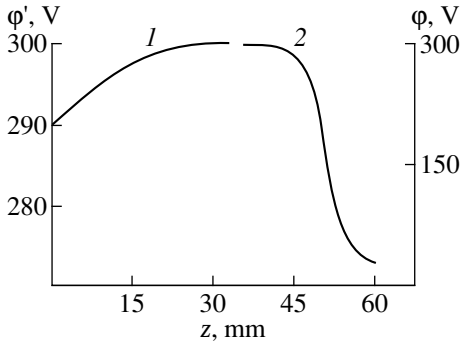

Fig. 4. Distribution of the potential along the thruster channel for U = 300 V and $\dot{m}_a$ = 2 mg/s: the profiles of (*1*) the potential φ' between the buffer rear wall (z = 0) and the anode (z = 26–36 mm) and (*2*) the potential φ between the anode and the thruster exit (z = 60 mm).

with the channel walls and can be represented by three electron groups, two of which are of interest for us.

The group of slow electrons trapped in the channel by the volume and near-wall fields is the largest. It determines the basic plasma parameters (density, temperature, fluxes, etc.) [7]. The second group consists of fast electrons. These electrons are created in the ionization zone and undergo elastic collisions with the walls. They are responsible for near-wall conduction and conduction across the magnetic field. Moving toward the anode, they acquire an energy corresponding to the potential drop between the ionization zone and anode [8].

The measurements carried out without a target show that, at the channel entrance, there is a group of the particles identified above as slow electrons. At the same time, the second group of electrons with the average energy ε ≈ 20–30 eV appears in the buffer volume. It may be seen from the potential distribution measured along the channel from the cathode to the anode (Fig. 4) that the potential drop between the ionization zone and the buffer corresponds to that value. Thus, the second group can be assigned to runaway electrons originating due to near-wall conduction.

We consider now the group of particles formed at the thruster exit in the presence of a target, assuming that it consists of negative ions. An analysis of data

Table 1. Energy of negatively charged particles in the presence of a target at the thruster entrance for $\dot{m}_a$ = 2 mg/s

Discharge voltage U, V	300	250	200
Energy of slow electrons ε, eV	6	5	5
Energy of negative ions ε, eV	28	25	22

Table 2. Energy of negative ions in the presence of a target in the buffer volume for $\dot{m}_a$ = 2 mg/s

Discharge voltage U, V	300	250	200
Energy of slow electrons ε, eV	5	4	4
Energy of fast electrons ε, eV	37	32	27
Energy of negative ions ε, eV	283	243	196

Table 3. Density of negatively charged particles in the buffer volume and the thruster jet for U = 300 V and $\dot{m}_a$ = 2 mg/s

		Density in the buffer n, m^{-3}			Density in the jet n, m^{-3}		
		1	2	3	1	2	3
Thruster without a target	a	3×10^{16}	–	–	1.6×10^{17}	–	–
	b	2×10^{16}	–	–	1.2×10^{17}	–	–
	c	3×10^{16}	7×10^{15}	–	1.3×10^{17}	–	–
	d	2×10^{16}	5×10^{15}	–	1.1×10^{17}	–	–
Thruster with a target	a	3×10^{16}	–	–	1.5×10^{17}	–	–
	b	3×10^{16}	–	–	1.2×10^{17}	–	–
	c	3×10^{16}	8×10^{15}	5×10^{13}	1.2×10^{17}	–	5×10^{14}
	d	2×10^{16}	5×10^{15}	4×10^{13}	1.0×10^{17}	–	7×10^{14}

Note: (1) slow electrons, (2) fast electrons, and (3) negative ions; (a) n is calculated from the current–voltage characteristic of an electrostatic probe, (b) n is calculated from the spectrum of positive ions, (c) n is derived from the formula $j_\alpha = \gamma e n v_\alpha$, and (d) n is derived from the formula $j_x = e\int v_x f_v(v) dv_x$.

available in the literature [13, 14] shows that negative ions with energies of 1–20 eV can appear if a surface is bombarded by ions with energies of ~200 eV. Consequently, when thruster jet ions with energies of 180–200 eV act upon a target, particles with energies of 10–30 eV are expected to appear at the channel entrance because the potential drop between the target and the point where the probe is set is equal to ~10 V. Slight variations in this value with changing operation conditions shift the maximum of the particle distribution function within the range 22–28 eV.

It is the accelerating electric field that governs the motion of negative ions in the channel. Apparently, the ions reaching the buffer must acquire an energy corresponding to the above potential drop. For $\dot{m}_a$ = 2 mg/s and U = 300 V, the potential drop between the anode and the thruster exit is ~270 V and that between the buffer and the anode is ~10 V. The energy of a negative ion measured at the buffer end should be about $\varepsilon \approx$ 280 eV (see Table 2 and Fig. 4). This is exactly the energy of the particles that have passed through the channel and that have been recorded in the buffer.

Therefore, identifying the third group of particles in the spectrum presented in Fig. 3b with negative ions is quite justified.

5. CONCLUSION

(i) The energy spectra of charged particles at the thruster exit and in the buffer volume are measured by a multigrid probe both in the absence and presence of a target that, being exposed to the plasma jet, emits negative ions.

(ii) The negative ions are shown to be involved in the measured spectra of charged particles if the jet acts upon a target.

(iii) The average energy and density of negative ions are determined under different operating conditions.

ACKNOWLEDGMENTS

This work was supported by INTAS, grant no. 96-2276.

REFERENCES

1. A. I. Bugrova, A. S. Lipatov, and A. V. Desyatskov, in *Theses of II German–Russian Conference on Electric Propulsion Engines and Their Technical Application, Moscow, 1993*, p. 40.
2. A. I. Morozov, A. I. Bugrova, A. V. Desyatskov, and V. K. Kharchevnikov, Fiz. Plazmy **22**, 333 (1996) [Plasma Phys. Rep. **22**, 302 (1996)].
3. A. I. Morozov, A. I. Bugrova, A. V. Desyatskov, *et al.*, Fiz. Plazmy **23**, 635 (1997) [Plasma Phys. Rep. **23**, 587 (1997)].
4. A. I. Bugrova, A. S. Lipatov, and A. I. Morozov, in *Proceedings of 24th International Electric Propulsion Conference, Moscow, 1995*, p. 107.
5. A. I. Bugrova, A. S. Lipatov, A. I. Morozov, and D. V. Churbanov, in *Proceedings of 24th International Electric Propulsion Conference, Moscow, 1995*, p. 105.
6. A. I. Morozov, A. I. Bugrova, and A. S. Lipatov, Fiz. Plazmy **21**, 650 (1995) [Plasma Phys. Rep. **21**, 614 (1995)].
7. J. P. Bugeat, D. Valentian, and A. V. Desyatskov, in *Theses of II German–Russian Conference on Electric Propulsion Engines and Their Technical Application, Moscow, 1993*, p. 39.
8. A. I. Morozov, A. I. Bugrova, and A. V. Desyatskov, Fiz. Plazmy **18**, 963 (1992) [Sov. J. Plasma Phys. **18**, 501 (1992)].
9. A. I. Morozov, Prikl. Mekh. Tekh. Fiz., No. 3, 19 (1968).
10. O. V. Kozlov, *Electric Probe in Plasma* (Atomizdat, Moscow, 1969).
11. M. I. Ionov, Zh. Tekh. Fiz. **34**, 769 (1964) [Sov. Phys. Tech. Phys. **9**, 591 (1964)].
12. A. I. Bugrova, A. S. Lipatov, I. V. Titov, and D. Valentian, in *Proceedings of 24th International Electric Propulsion Conference, Moscow, 1995*, p. 113.
13. V. V. Egorov, V. Kim, A. A. Semenov, and I. I. Shkarban, in *Ion Injectors and Plasma Accelerators* (Énergoatomizdat, Mocsow, 1989), p. 56.
14. M. Kaminsky, *Atomic and Ionic Impact Phenomena on Metal Surfaces* (Springer-Verlag, Berlin, 1965; Mir, Moscow, 1967).

Translated by N. Ustinovskiĭ